INVESTIGATION OF COORDINATION ENVIRONMENTS IN HETEROGENEOUS CATALYSIS

by

Elif Pınar Alsaç

A thesis
presented to the University of Waterloo
in fulfillment of the
thesis requirement for the degree of
Doctor of Philosophy
in
Chemistry

Waterloo, Ontario, Canada, 2022

Examining Committee Membership

The following served on the Examining Committee for this thesis. The decision of the Examining Committee is by majority vote.

External Examiner:	Byron Gates Professor Department of Chemistry, Simon Fraser University
Supervisor:	Rodney D. L. Smith Assistant Professor Department of Chemistry, University of Waterloo
Internal Member:	Linda Nazar Professor Department of Chemistry, University of Waterloo
Internal-External Member:	Michael Pope Associate Professor Department of Chemical Engineering, University of Waterloo
External Member:	Aicheng Chen Professor Department of Chemistry, University of Guelph

Author's Declaration

This thesis consists of material all of which I authored or co-authored: see Statement of Contributions included in the thesis. This is a true copy of the thesis, including any required final revisions, as accepted by my examiners.

I understand that my thesis may be made electronically available to the public.

Statement of Contributions

Prof. Rodney Smith as Elif Pınar Alsaç's supervisor assisted with the conceptualization of the projects, the creation of the data acquirement, and the analysis of the results. He also took part in writing and editing manuscripts published (Chapters 3 and 4) and submitted (Chapter 5) in peer-reviewed journals. The first drafts were written by Elif Pınar Alsaç, and he was involved in the editing process. The details of the contributions of the authors of the publications listed below. I am the sole author of the rest of the thesis.

Part of the work described in **Chapter 1** has been published as:
"Structure–property correlations for analysis of heterogeneous electrocatalysts"

Elif Pınar Alsaç, Nataraju Bodappa, Alexander W. H. Whittingham, Yutong Liu, Adriana de Lazzari, and Rodney D. L. Smith
Chem. Phys. Rev., **2021**, 2 (3), 031306.
https://doi.org/10.1063/5.0058704.

- I wrote the sections *'Strain'* and *'Electronic and Bonding Effects'* and involved writing and editing of the first draft.
- Nataraju Bodappa, Alexander W. H. Whittingham, Yutong Liu, and Adriana de Lazzari contributed to writing of the other sections.
- Prof. Rodney Smith and I completed the final draft with the contribution of other authors.

Part of the work described in **Chapter 3** has been published as:

"Probing the Role of Internalized Geometric Strain on Heterogeneous Electrocatalysis"

Elif Pınar Alsaç, Alexander Whittingham, Yutong Liu, and Rodney D. L. Smith**.**
Chemistry of Materials, **2019**, 31, 18, 7522–7530
https://doi.org/10.1021/acs.chemmater.9b02234.

- I performed the majority of the synthesis, physical and electrochemical testing of the materials.
- Dr. Rodney Smith acquired Near-infrared spectroscopy data, and completed DFT calculations
- Alexander Whittingham and Yutong Liu helped with electrochemistry experiments.

Part of the work described in **Chapter 4** has been published as:
"Identification of non-traditional coordination environments for iron ions in nickel hydroxide lattices"
Elif Pınar Alsaç, Keyu Zhou, Wen Rong, Soma Salamon, Joachim Landers, Heiko Wende, and Rodney D. L. Smith
Energy Environ. Sci., **2022**, 15, 2638-2652
https://doi.org/10.1039/D2EE00396A

- I performed the majority of the synthesis, characterization and electrochemical testing of the materials.
- Keyu Zhou and Wen Rong helped with the synthesis and acquiring FTIR spectroscopy data.
- Dr. Soma Salamon, Dr. Joachim Landers, and Prof. Heiko Wende completed Mössbauer Spectroscopy experiments and helped with the analysis of the results.

Part of the work described in **Chapter 5** has been submitted as:

"Linking Lattice Strain and Electron Transfer Kinetics in Crystalline Layered Double Hydroxides"

Elif Pınar Alsaç and Rodney D.L. Smith
Submitted to ACS Catalysis

- I performed all the synthesis, characterization, and electrochemical testing of the materials.
- I wrote the first draft, Prof. Rodney Smith and I completed manuscript.

The work described in **Chapter 6** has been prepared as a manuscript and will be submitted.

- I performed most of the synthesis, characterization, and electrochemical testing of the materials.
- Marlyn Mwita helped with the synthesis of the samples.
- Justine Bissonnette helped with the XRD measurements.
- Prof. Rodney Smith contributed to conceptualization of the project and analysis of the results.

Abstract

Increasing energy demand, environmental causes, and sustainable energy goals give rise to the study of energy conversion systems extensively. More efforts have been devoted to oxygen evolution reaction because of kinetic considerations and improving electrocatalytic behavior of a vast number of materials including both homogeneous and heterogeneous catalysis. In heterogeneous catalysis, a small number of catalytically active sites are believed to be involved in electrochemical reactions. The properties and coordination environments of these sites play a key role in the design of optimum electrocatalyst. However, direct analysis of the coordination environments is often challenging and requires more systematic analysis. This analysis can be done by a systematic perturbation of a system and measuring the structural and electrochemical response. This thesis focuses on the analysis of the identification of distinct coordination environments in nickel and cobalt hydroxides through structure-property analysis. Correlations between structure-activity and structure-property give information on the electrochemical activity and ultimately serve as a method to design more efficient and high-performance materials for various electrochemical energy conversion applications.

Chapters 3,4, and 5 focus on nickel hydroxide based electrocatalysts. **In chapter 3,** aluminum, iron, and gallium doped nickel hydroxides were fabricated by the photochemical deposition method. The effect of internalized geometric strain is investigated by employing density functional theory and near-infrared spectroscopy. Tensile and compressive strain is reproduced for all three composition series. Computational studies indicate that activation energy decreases in every set, but Fe doped nickel hydroxides significantly change electrokinetic parameters. With this study, we proposed that strain is not solely responsible for the improved catalytic activity in iron-doped nickel hydroxides.

Chapter 4 reveals the effect of synthetic methods on the structure and electrochemical behaviors of iron incorporated nickel hydroxides. Mössbauer and Raman spectroscopy directly identify two unidentical coordination environments for the samples synthesized in water environment, on the other hand only a single type of iron coordination site for the samples synthesized in presence of

formamide. Powder X-ray diffraction and X-ray absorption spectroscopy hint at the presence of a diverse coordination environment with the change in intermetallic distance. The second coordination environment is found to be ineffective on electrochemical properties and is suggested to be located atop the layered sheets of nickel hydroxide lattice. The study provides a piece of detailed structural information and their impact on oxygen evolution reaction to the scientific community to optimize synthetic protocols of this class of materials.

Chapter 5 focuses on hydrothermally synthesized NiFe hydroxides at different iron concentrations. The combination of multiple characterization techniques reveals the formation of three distinct iron coordination sites in nickel hydroxide lattice. Crystalline nickel-iron hydroxides have different electrochemical behavior from the same class of samples in amorphous form. The static pre-catalytic redox peaks across the composition series but a linear decrease in the Tafel slope shows that a sophisticated argument is needed to explain the electrokinetic behavior of this system. The correlation between O-M-O bond angle and Tafel slope is described by asymmetric Marcus-Hush theory.

Chapter 6 compares the structure and electrochemical behaviors of three sets of the cobalt hydroxides synthesized in aqueous pH precipitation in water and formamide and hydrothermal methods. Synthetic conditions impact cobalt and iron coordination and electrocatalytic activity. X-ray diffraction and X-ray absorption spectroscopy reveal that iron incorporation into cobalt hydroxide in hydrothermal series is the least among the three composition series. Cobalt hydroxides synthesized with co-precipitation in aqueous conditions partially oxidized into the cobalt oxyhydroxide phase. A layered double hydroxide structure is fabricated with the inclusion of formamide to the co-precipitation synthetic. Each series has characteristic lattice parameters and electrochemical characteristics, and the results indicate that cobalt hydroxide series show different characteristics from other brucite type materials such as nickel hydroxides even though they have the same crystal structure.

Acknowledgements

First and foremost, I would like to express my gratitude to my supervisor Professor Rodney Smith. He trusted and believed in me when we first met in CSC 2017 and accepted me as the first Ph.D. candidate in his research group. It has been a pleasure to learn from his knowledge, creativity, and experience over the course of my Ph.D. journey. I appreciate his mentorship, the fruitful discussions on the projects that I have been working on, and his dedication to science.

I am sincerely thankful to the examining committee members, Professor Linda Nazar, Professor Michael Pope, and Professor Aicheng Chen for their valuable time and feedback over the last four years. I would like to specifically thank the external examiner, Professor Byron Gates, for his time and feedback on my thesis.

I also would like to acknowledge my M.Sc. degree supervisor Professor Ferdi Karadaş for making me fall in love with the field I have worked in for eight years. He is always a great role model for me with his endless support, and encouragement to continue to walk on the academic path.

I would like to acknowledge Dr. Bruce Ravel from Brookhaven National Laboratory for accepting and testing our samples during the pandemic.

I would like to thank the University of Waterloo and the Waterloo Institute of Nanotechnology for their financial support. Special thanks to Dr. Laura Ingram, Dr. Howard Siu, and Sue Stathopoulos for their great mentorship. I thank Cathy van Esch and Kim Rawson for their assistance regarding departmental paperwork.

I would like to thank all the former and current members of Smith Group. My special thanks to my first friends in the group: Alex Whittingham and Yutong Liu. I will always appreciate your kind friendship and support. Another special thanks goes to Wen Rong for being an amazing lab-mate three years ago and being a best friend now. I would like to thank the rest of the Smith Group: Dr. Nataraju Bodappa, Andrew Jewlal, Adriana de Lazzari, Una Hogan, Xinran Liu, and Jixi Zhang for being very kind and friendly lab mates. Justine Bissonnette and Marlyn Mwita thank you for your last-minute help.

I am very thankful for my friends in Chemistry department: Dr. Cheryl Sturm, Xenia Medvedeva, Luke Menezes, Daniel Ramirez, and Lauren Blanc. Special thanks to Klinkova, Kleinke, and Nazar group members for their help and understanding when I needed to use their lab equipment in the Summer 2021.

I would like to thank my lifelong friends for their encouragement and feeling their cross-continental support: Canan, Pınar, Esra, Tuğçe, İzel, Aybegüm, Feride, Merve, Hilal, Seray, and Ebru. Thank you for being with me and growing together.

Last but not least, I would like to acknowledge my parents Meryem and Resul Alsaç for their sacrifices and patience throughout my education, and their unconditional love. To my sister Filiz, I say thank you for all of your support and understanding. I thank my bro Ümit and my sister-in-law Aysun for their all kinds of assistance and friendship. To my niece Elif, you have been my muse since you were born. Glad to have you all. Cheers to all the joys and difficulties that life brings us!

Dedication

Dedicated to headmaster Mustafa Kemal Atatürk, the founder of the independent, secular, and modern Republic of Turkey.

'Our true mentor in life is science.'

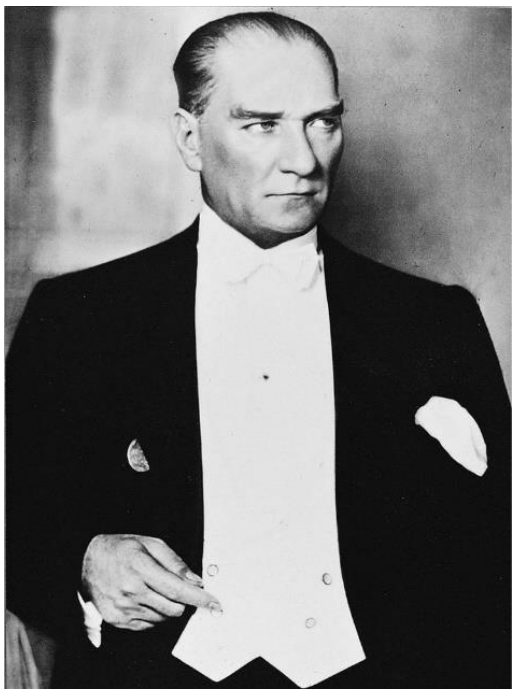

Mustafa Kemal Atatürk

(1881-1938)

Table of Contents

List of Figures

List of Tables

List of Abbreviations

A: Ampere

Å: Angstrom

AEM: Adsorbate Evolution Mechanism

A: Area

C: Coulomb

CA: Chronoamperometry

CV: Cyclic Voltammetry

DFT: Density Functional Theory

E: Potential

$E_{1/2}$: Half-wave potential

EIS: Electrochemical Impedance Spectroscopy

E^o: Standard redox potential

eV: Electron volts

EXAFS: Extended X-ray Absorption Fine Structure

FTIR: Fourier Transform Infrared Spectroscopy

FTO: Fluorine doped tin oxide

I: Current

i_o: Exchange Current Density

j_o: Current Density

LOM: Lattice Oxygen Mechanism

OER: Oxygen Evolution Reaction

PES: Potential Energy Surfaces

RDS: Rate-determining Step

RHE: Reversible Hydrogen Electrode

SEM: Scanning Electron Microscopy

TEM: Transmission Electron Microscopy

WT: Wavelet Transform

XANES: X-ray Absorption Near Edge Structure

XAS: X-Ray Absorption Spectroscopy

XPS: X-Ray Photoelectron Spectroscopy

XRD: X-Ray Diffraction

Δo: Octahedral Splitting

η: Overpotential

λ: Wavelength

μ: Micro

ν: Wavenumber

υ: Potential scan rate

Chapter 1
Introduction

1.1 Motivation

The world is dependent on fossil fuel resources such as coal, natural gas, and petroleum due to high energy density in spite of their detrimental effects on climate, desertification, and air pollution.[1,2] The rapid rise in universal energy need and negative climatic impacts caused by extensive consumption of carbon-based fossil fuels underline the requirement for clean and sustainable alternative energy resources.[3,4] The United Nations (UN) announced Sustainable Development Goals (SDGs) in 2015 to combat worldwide issues on education, equality, energy, and sustainability by 2030 for a better and sustainable future for the citizens of the world.[5] Especially, SDG 7 focuses on ensuring access to sustainable, modern, clean, and affordable energy sources for all. Among all possible energy alternatives, solar energy is the largest energy resource that is able to provide worldwide energy needs within eighty minutes of irradiation.[4,6] Nonetheless, solar-driven energy sources are often intermittent and highly dependent on time and location. For these reasons, solar energy requires efficient energy storage and energy transportation systems.[2] Among potential candidates for alternative energy resources, photoelectrochemical or electrochemical production of hydrogen (H_2) is a promising alternative with a high energy density with the absence of any adverse by-products. Hence a considerable amount of effort has been dedicated to investigating effective ways to split water into hydrogen and oxygen.

1.1.1 Water Splitting

Water splitting consists of the oxygen evolution reaction (OER) and the hydrogen evolution reaction (HER), which take place at the anode and cathode respectively. Depending on the reaction conditions the half-cell reactions can be written as in **Table 1.1**:

Table 1.1 HER and OER reactions at different pH levels

	HER	**OER**
Acidic medium	$2H^+ + 2e^- \rightarrow H_2$	$H_2O \rightarrow 2H^+ + 1/2O_2 + 2e^-$
Neutral medium	$2H_2O + 2e^- \rightarrow H_2 + 2OH^-$	$H_2O \rightarrow 2H^+ + 1/2O_2 + 2e^-$
Basic medium	$2H_2O + 2e^- \rightarrow H_2 + 2OH^-$	$2OH^- \rightarrow H_2O + 1/2O_2 + 2e^-$
	$\mathbf{E_{HER}}$= 0 V – 0.059 V*pH(vs. NHE)	$\mathbf{E_{OER}}$= 1.23 V– 0.059 V* pH(vs. NHE)
		$\mathbf{E_{water\ splitting}}$= -1.23 V

In order to achieve to split one mole of water into hydrogen and oxygen under standard conditions, a thermodynamic potential of 1.23 V, which corresponds to 237.1 kJ mol^{-1} energy input (ΔG^0) is required. While HER, involves in two-electron process as seen above, OER is being four-electron process. In addition, surface-adsorbed species as reaction intermediates contribute to the complexity of OER reaction. The complicated reaction mechanism attracts the scientific community to make a more detailed analysis by utilizing sophisticated characterization techniques to resolve fine details of OER reaction.

1.1.2 Oxygen Evolution Reaction (OER)

Electrocatalysis is an interdisciplinary subject where chemistry and physics are combined in pursuit of a mechanistic understanding of reaction kinetics. An electrocatalyst stabilizes reaction intermediates along the reaction pathways, which increases electron transfer kinetics by reducing the activation energy barrier. For these reasons, the design of electrocatalysts plays a key role in tuning reaction kinetics and pathways.

The OER half-reaction has been studied since 19^{th} century with the observation of electrically driven water splitting reaction by Paets van Troostwijk/Deiman and Nicholson/Carslie. Despite this, the reaction mechanism for OER remains a matter of debate.[7] Numerous studies have been devoted to understanding OER mechanism on heterogeneous catalysis particularly transition metal

oxide electrocatalysts. Several proposed mechanisms indicate that the metal centers play as electroactive sites and an optimum electrocatalyst should follow the Sabatier principle which states that key intermediates should have an optimum bonding strength, neither too strong nor too weak.[8,9] Optimum binding strength concept in electrocatalysis is experimentally demonstrated with a "volcano-plot" for hydrogen evolution reaction (HER) by Sergio Trasatti.[10] Numerous theoretical studies now focus on the activity of these volcanos and how the behavior of volcanos depends on descriptors.[11,12] Typically descriptors are based on the binding energies of the intermediates. Brønsted-Evans-Polanyi and linear scaling relations,[13,14] combines kinetics and thermodynamic parameters. Both statements show that thermodynamic parameters have a linear relation with kinetic parameters. The activation energy of a system can be correlated to the thermodynamic stability of intermediates. Hence, it can be concluded that reaction intermediates determine the overall mechanism of a reaction.[15] Numerous mechanism for OER has been proposed in both acidic and basic medium and some differences and similarities exist between each proposed mechanism. The majority of mechanistic studies showed OER mechanism consisting of single-electron charge transfer species with three adsorbate species which are OH*, O*, and OOH*. The formation of each adsorbed species differs in acidic and basic environment (**Figure 1.1**). Among proposed reaction mechanisms, M-O and M-OH are the most common intermediates and differences arise from oxygen forming reactions.

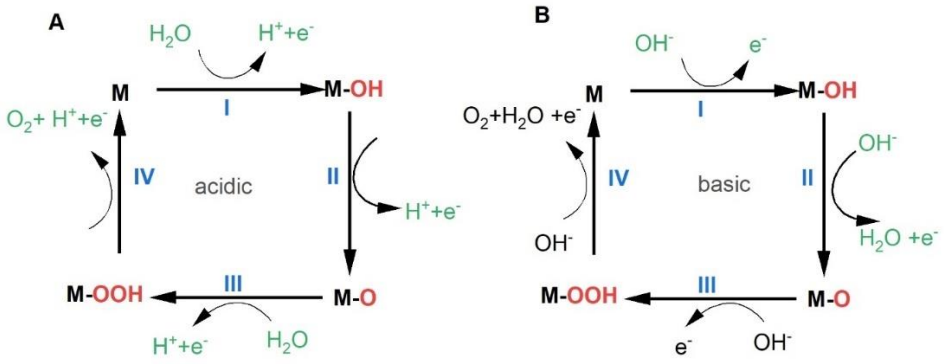

Figure 1.1 Possible oxygen evolution reaction mechanism of metal oxides in **(A)** acidic and **(B)** alkaline conditions.

Each elementary reaction in **Figure 1.1** has individual intermediate adsorption energy. Ideally, each elementary reaction should have 1.23 eV for each step (**Figure 1.2**). However, proposed mechanisms indicate that the binding strength of OOH* intermediate is weak and therefore the third step where peroxide intermediate is formed with Gibbs free energy of ΔG_3 is considerably higher than the other three elementary steps. Hence the third step is often counted as the rate-determining step. At the applied potential of *U=0*, where U represents electrode potential, both ideal and real catalysts are going upwards during the reaction series, and OER cannot process. At the reversible potential *i.e.*, *U=1.23*, ideal and real catalysts behave differently. The Gibbs free energies of the first and the second steps disappear, the third step has a positive, and the fourth step has positive chemisorption energies that indicate that the third step with ΔG_3 is the rate-determining step. At *U>1.23* all steps are going downwards so OER can proceed in this condition. These findings indicate that the energy of OOH* should be shifted to more negative values to complete OER reaction.

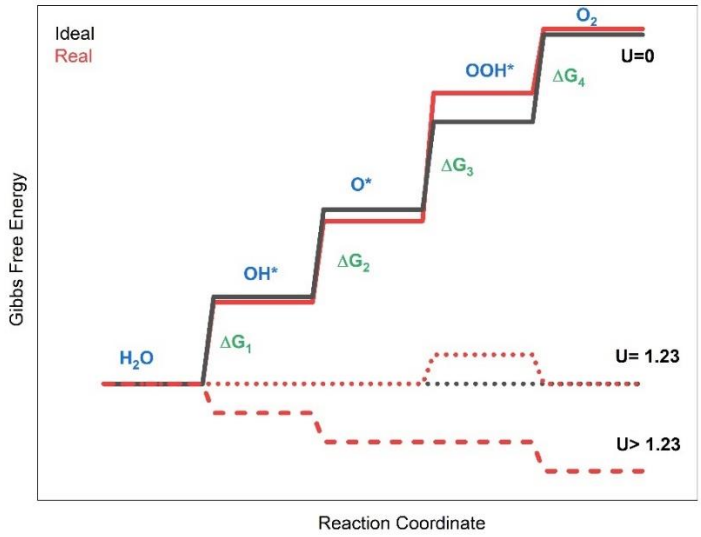

Figure 1.2 Gibbs free energy versus reaction coordinate of intermediate species of OER. Energetics of ideal and real catalysts are shown at three different potentials (at U= 0, +1.23, and

+1.23) by black and red colors, respectively. Figure adapted with a permission from WILEY-VCH Verlag GmbH&Co.[16]

The activity reaction mechanism trends in the literature indicate the existence of a different reaction mechanism than the conventional proposed mechanism. This type of mechanism is called the lattice oxygen oxidation mechanism (LOM) which involves the oxidation of oxygen ions in lattice.[7,17] Unconventional reaction mechanisms with lattice oxygen participation were proposed by Jovanovic[18], Bockris[19], and Heitbatum[20] approximately forty years ago. Afterward, several studies reported oxygens from metal oxide surfaces play a key role in OER. Binninger and co-workers proposed that both lattice oxygens and metal oxide dissolutions participate in OER according to thermodynamic potentials.[21] The number of reports on LOM for transition metal oxides, especially for perovskites, has increased recently.[22–27]

1.2 Layered Double Hydroxides (LDHs)

There are a number of experimental and theoretical studies made to find the optimum electrocatalysts in the literature on different classes of inorganic materials such as perovskites, two-dimensional materials, transition metal oxides, hydroxides, metal-organic frameworks.[28] Each class of catalysts has its own advantages and disadvantages over each other. Among these materials, transition metal oxides and hydroxides draw attention due to facile preparation, tunable structure, and high electrocatalytic activity.[29–34]

1.2.1 Structure of LDHs

Layered double hydroxides (LDHs) have the general formula of $[M^{2+}_{1-x}M^{3+}_{x}(OH)_2]^{x+}$ $[A^{a-}_{x/a}.nH_2O]$ where M^{2+} and M^{3+} are divalent and trivalent metal ions reside in edge-sharing MO_6 octahedra, respectively and A is the exchangeable anions confined between the layers to maintain charge balance.[35] LDHs are lamellar hydroxides, and they adopt a layered brucite structure $[Mg(OH)_2]$ which is naturally found as a mineral called theophrasite.[36] The crystal structure of brucite is a hexagonal close-packed (hcp) structure with trigonal symmetry (space group is $P\bar{3}m1$,

#164). The $M(OH)_6$ units form layers along the crystallographic c-axis and make a stacked three-dimensional structure where hydroxide ions (OH^-) are placed perpendicular to the plane of the layers. OH^- makes weak interactions with intercalated ions and water molecules that are present between the layers.[37] 2-dimensional projections in the ab and ac planes of the unit cell are shown in **Figure 1.3**:

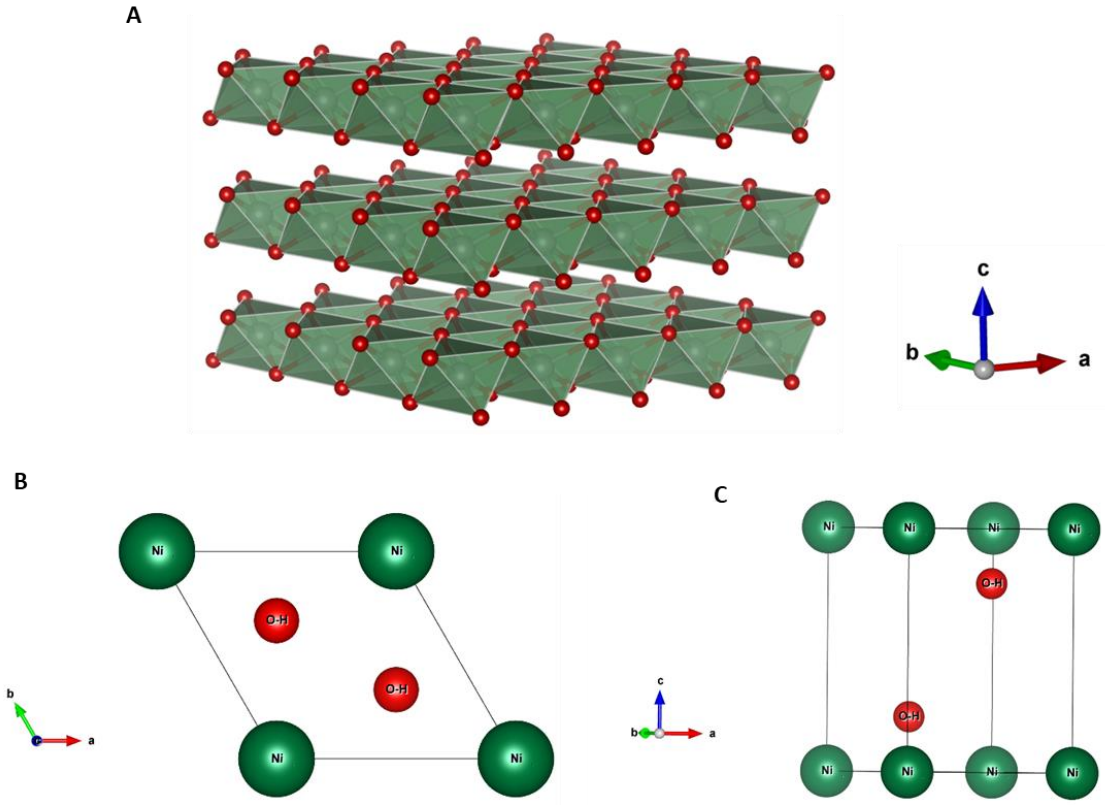

Figure 1.3 The crystal structure of β-nickel hydroxide from different points of view **(A)** layered **(B)** from ab plane **(C)** from the angled perspective. Structures are generated with VESTA software.[38]

A useful feature of the metal hydroxide structure is that many transition metals can be used to fabricate isomorphous LDH structures. Two of the most common LDH widely studied for electrocatalysis are nickel hydroxides and cobalt hydroxides. Both materials adopt either one of the two polymorphs denoted as alpha [α-$M(OH)_2$], and beta phase [β-$M(OH)_2$]. The difference

between α and β phases arise from the presence of intercalated water molecules and ions between the layers of metal hydroxides. The different phases of the same materials have the same bonding structures but varying lattice parameters. The unit cell parameters of α and β phases of nickel and cobalt hydroxide are listed in **Table 1.2**.

Table 1.2 Unit cell parameters of α and β phases of nickel hydroxides

		Lattice Parameters		Angles	
	Space group	a=b	c	α=β	γ
α-$Ni(OH)_2$	D_{3d} (#162)	3.08	8.01	90	120
β-$Ni(OH)_2$	D_{3d} (#164)	3.13	4.61	90	120
α-$Co(OH)_2$	D_{3d} (#166)	3.14	25.01	90	120
β-$Co(OH)_2$	D_{3d} (#164)	3.18	4.66	90	120

The electrochemical properties of the polymorphs of nickel hydroxide were initially analyzed by Bode.[39] According to the Bode cycle, highly crystalline β-$Ni(OH)_2$ can be oxidized to β-NiOOH. A disordered α-$Ni(OH)_2$ forms γ–NiOOH under oxidation. Furthermore, β-NiOOH can be further oxidized to γ-NiOOH but it can be converted back to β phase with a cyclic voltammetry experiment (**Figure 1.4**).

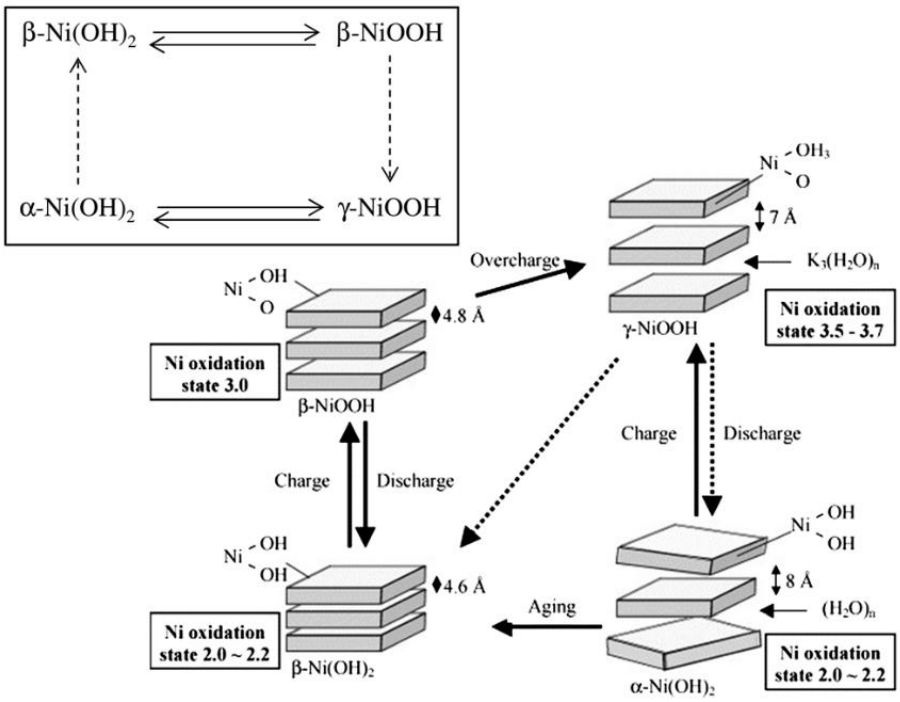

Figure 1.4 Bode cycle of nickel hydroxide and nickel oxyhydroxide phases. Reprinted with permission from Royal Society of Chemistry[3]

1.2.2 Layered Double Hydroxides as Oxygen Evolution Reaction Electrocatalysts

$Ni(OH)_2$ is the first metal hydroxide type material identified as an OER electrocatalyts.[40] The OER activity of nickel hydroxide is can be boosted with secondary and tertiary metal cations with variable valences.[41,42] Transition metals especially Co, Fe, Mn, and Ni based LDHs exhibit promising OER activity.

The activity trends between various transition metal hydroxides are reported as Ni > Co>Fe>Mn.[43] For this reason, nickel hydroxide, and cobalt hydroxide are the most widely studied metal hydroxides as OER electrocatalysts. Mixing with other types of cations with varying valences is shown to improve electrocatalytic behavior by changing redox potentials, reducing Tafel slopes and overpotentials for certain current density values.[44–47]

1.2.3 Modification of Layered Double Hydroxide Electrocatalysts

In order to increase the electrocatalytic activity of the LDHs variable modifications on the structure have been applied. These modifications can be either extrinsic or intrinsic enhancements.[48] Extrinsic modulation is a combination with other structures or components such as the addition of another phase, or atoms to create a heterostructure which is a layered structure that possesses an interface of different materials to increase the interaction between electrode and electrolyte. Heterostructures are designed to modulate the synergy between each component to improve the electrochemical behavior of the catalysts.[49] Intrinsic enhancement is the modulation of the structure by changing composition, morphology, dimension, thickness, and type of the intercalated ions between layers. Here, we focused on two intrinsic enhancements: composition and synthetic strategies to tune structure which are discussed in the following sections.

Doping Strategies

Tuning of the composition is one of the most common techniques to improve electrochemical behavior of the catalysts. Doping is an effective approach for altering electronic, optical, and structural properties of metal hydroxides. This has the potential to increase the number electrochemically active metal sites with decreased thickness, size of the particles, or increased surface area.[50,51] The replacement of an electroactive site with another element modifies the electronic structure and bonding environments. Therefore, it can be used to change the electron density on the electroactive sites donating or accepting electrons from the dopants. Mono, di, or trivalent ions intercalated into iron-oxo (hydroxo) or manganese-oxido complexes have a correlation with reduction potential with the Lewis acidity of the dopant cation.[52–55] This concept has also been applied to metal oxide catalysts with an observation of a shift in redox-peaks.[56]

Introducing a second or a third kind of cation into metal hydroxide lattice modulates its electronic structure and alters adsorbing properties of intermediate species.[57–60] It has been reported that when the combination of Fe(II) and Fe(III) is incorporated into nickel hydroxide lattice, the charge throughout the lattice is adjusted. Divalent iron modifies atomic structure when it is intercalated

into NiFe hydroxides. According to in-situ XAS, Fe-O-Fe moieties are formed at lower overpotentials which stabilizes high-valent metal sites during OER. Nickel hydroxides doped with both divalent and trivalent iron ions exhibit 195 mV overpotential at 10 mA cm^{-2}.[61]

Doping is often correlated with the electronegativity concept. For instance, trivalent Fe is a strong Lewis acid and according to the Coulometric titration experiments, the formation of tetravalent-Ni sites is induced. This situation promotes the OER activity by lowering the Tafel slope from 90 mv dec^{-1} to 30 mV dec^{-1} for NiB_i and electrodeposited NiFe hydroxide thin films respectively. According to Ni K-edge and electron energy loss spectroscopy (EELS) the electronegativity of iron sites enhances the covalency between Ni and oxygen and promotes the O-O bond formation during OER.[62] Similar inductive effect has been observed for iridium doped nickel hydroxides, the partial oxidation of nickel sites through the doping of iridium decreases Tafel slope from 100 mV dec^{-1} for undoped nickel hydroxide to 58.1 mV dec^{-1} for 4% Ir-doped analogue.[63]

The effect of doping is often explained by the effect of covalency that describes the charge-transfer and hybridization.[64,65] For instance, the covalency of metal-silicate hydroxides with the formula $M_3Si_2O_5(OH)_4$ where M is cobalt, iron, or nickel is shown with DFT calculations by the relative contributions of atomic orbitals to bonding orbitals. This study shows that the covalency is the highest with cobalt and with 58.6 mV dec^{-1} has the lowest Tafel slope. The slope values are increasing to an average value of 70 mV dec^{-1} for nickel and iron metals.[66] Vanadium incorporated CoFe hydroxides are shown as increasing M-O covalency that regulates the electronic structures. With the increasing covalency the Tafel slope transitions from 63.3 mV dec^{-1} to 41.4 mV dec^{-1} for CoFe hydroxides and CoFe-V hydroxides respectively.[67] Similarly, another study indicated that the charge transfer from cobalt and iron sites to vanadium in CoFe-V hydroxides regulates the p electrons delocalization and the adsorption strength of OH* intermediate, which indicates an improved catalytic activity with a Tafel slope of 39.1 mV dec^{-1}.[68] The covalency affects OER performance of NiFe hydroxides as well. XAS reveals that higher electronegativity of trivalent iron sites increases the covalency at nickel sites. According to operando analysis, the partial oxidation of oxide ions into oxyl ions promotes OER activity.[62] The following study supports this

idea of the enhanced redox reaction with improving hybridization between M 3d and O 2p orbitals according to XAS L-edge analysis of NiFe hydroxides.[69]

Synthetic Strategies on the Adjustment of Coordination Environment

Coordination environment of a catalyst can be tuned by several methods including defect engineering,[70–72] single-atom catalysts addition,[73,74] and synthetic treatments.[75,76] Defect engineering is one of the common ways to introduce oxygen and metal vacancies in LDH structures. Sun *et al.* reported that doping of Al(III) and Zn(II) cations into NiFe hydroxides followed by an alkaline etching process to form cation vacancy and changes intrinsic activity of the electrocatalysts. The defective catalysts were obtained with the addition of the tertiary cation dopants.[77] M(III) and M(II) vacancy with the addition of Al(III) and Zn(II) decreases overpotential requirement by 80 and 48 mV for NiFeAl and NiFeZn LDHs compared to their doped analogues without vacancy. The comparison of electrocatalytic activity of M(III) and M(II) indicates that M(II) defects more efficiently unsaturated oxygen coordination of Ni-O-Fe site. Similarly, another study showed that Al etching in NiFe hydroxides promotes the formation of defects and Ni(III) sites during OER.[78] Composition dependent behavior shows a volcano dependent trend between amount of doped Al in main lattice and OER current density. The results indicate that intercalated Al sites tailor the nickel coordination environment and provides a better kinetic behavior up to a certain threshold. Furthermore, Wang *et al.* reported CoFe LDHs synthesized via water-plasma-enabled exfoliation exhibit multiple vacancy sites.[79] Oxygen, cobalt, and iron vacant sites decreases coordination number and increases the disorder. An overpotential of 232 mV at 10 mA cm^{-2} is achieved with tailored coordination environments.

Non-traditional coordination environments can be obtained by anchoring single atoms to metal hydroxide lattice. Cui *et al.* reported iridium coordinated NiFe oxyhydroxides synthesized via in-situ cryogenic-photochemical reduction procedure show an excellent water oxidation activity with a 183 mV overpotential at 10 mA cm^{-2}.[80] The superior activity is attributed to modulated coordination sites through a modulated electronic structure of the iridium sites. Another study on Pt single atom intercalated NiFe hydroxides indicates that Pt increases the valency of the

electroactive nickel site after spatial confined electroreduction reaction increases intrinsic activity for OER.[81]

Layered double hydroxides can be synthesized by various techniques such as electrodeposition,[82–84] co-precipitation,[85] pulsed layer deposition,[86] hydrothermal,[87,88] solvothermal[89], and chemical deposition.[90,91] Each synthesis technique has their own advantages. For instance, hydrothermally synthesized LDHs can be prepared with different growth mechanisms that enable to fabricate samples with different sizes and crystal structures of the particles. While pulsed layer deposition provides intercalation of different interlayer anions,[92,93] co-precipitation method is fast and facile. Different experimental conditions such as temperature, and pH affects the characteristics of the samples. Lastly, deposition techniques, for instance, electrodeposition is another facile and inexpensive technique. With this technique, a better electrode-substrate binding is achieved. Furthermore, the film thickness can be easily tuned with electrodeposition time, and applied current or voltage. Each synthetic protocol yields nominally the same materials, however with varying coordination environments.

Two-dimensional structure with a few nanometers thickness is considered as the ideal structure for an electrocatalyst. LDHs in nanosheet morphology attract attention due to improved electroactive surface area and thus expected to have improved catalytic behavior. Exfoliation of a pristine layered double hydroxide is a promising technique to delaminate LDH.[94] Amino acids and surfactants are common exfoliating agents, but the technique is expanded with the usage of different types of intercalated ions and surfactants to obtain a desirable interlayer distance.[95] Previously, Adachi-Pagano *et al.* reported exfoliation process with dodecyl sulfate as a surfactant and butanol as the dispersant.[96] Following studies indicate several successful exfoliation process using formamide molecules.[97–99] Since exfoliation requires either pre-intercalation of large anions or mechanical forces, exfoliation requires time, and intense laboring, several strategies were developed to directly synthesize single-layer nanosheets to simplify synthetic procedures such as co-precipitation,[100,101] micro-emulsion,[102] and laser ablation.[103] In co-precipitation technique, formamide is used as a solvent together with water. Formamide is proposed to be adsorbed on the

LDH surface and diminishes the interaction between layers and inhibits material to grow in Z-direction.[101] NiFe hydroxides synthesized with this method yield a more uniform distribution of Fe(III) compared to hydrothermal and aqueous co-precipitation.[85]

The use of different types of intercalated ions between the sheets of layered double hydroxides enables changing electrochemical behaviors. Hunter *et.al.* reported a variety of intercalated anions between the sheets of NiFe LDH and they observed a correlation between the basicity of the intercalated anion and onset overpotentials and this behavior is attributed to a base-assisted deprotonation step. Monovalent anions are reported as weaker proton acceptors than divalent anions.[92] Comparison of fluoride that has a high standard reduction potential has a higher overpotential and Tafel slope compared to the anion hypophosphite with a lower standard reduction potential.[104] The change in electrochemical activity is often attributed to a change in the electronic structure of the catalysts. NiFe LDH intercalated with chloride and sulfate anions changes the electroactive surface area, but similar electronic structures according to XPS yield similar electrocatalytic performance. Dodecyl sulfate, on the other hand, increases the interlayer distance and positively impacts the catalytic activity. This behavior is attributed to changes in pK_a across different intercalated anions.[105] The following study from Carrasco *et.al.* shows a systematic change in the chain length in intercalated anions and reported a direct proportion between the interlayer distance and catalytic activity. It is reported that NiFe LDH with the maximum basal spacing of 31.6 Å, yields the lowest Tafel slope of 27 mV dec^{-1}.[106]

Solution additives is another method found to modify the activity and reaction intermediate properties of LDHs.[107] Iron incorporated nickel hydroxides electrochemical activity is dependent on the size of the cations in the electrolyte. Comparison of different electrolyte cations shows an increasing trend from Li(I) to Cs(I). According to in-situ Raman analysis, the $NiOO^-$ intermediate is stabilized by the size of the cation.[108] Furthermore, Michael *et al.* reported a Raman analysis showing synergy between alkali-metal electrolyte dependent Ni-O stretch and electrocatalytic performance.[109] NiFe oxyhydroxide electrocatalysts tend to increase overpotential in the presence of alkaline-earth metal cations in electrolyte compared to alkaline metal cations. The study

reported that the increase in the overpotential is a result of changing bond strength and adsorbate-adsorbent interactions.[110] Moreover, tetraalkylammonium ions also tune catalytic activity on NiFe oxyhydroxides by shifting pre-catalytic redox peaks and increasing the Tafel slope to 90 mV dec^{-1} compared to the slope of 60 mV dec^{-1} for potassium cation. The authors attribute this behavior to the increased interaction between the cation and oxygen due to deprotonation during OER.[111]

NiFe hydroxides reveal different mechanistic results depending on the different morphologies. According to Pourbaix diagrams of such catalysts, the reaction order with respect to the specific intermediate can be determined. The reaction order with respect to hydroxide ions is determined as 3 for amorphous nickel hydroxide,[82] 2 for NiFe LDHs,[112] and 1.8 for FeOOH-NiOOH hybrid structure.[112] Another study on γ-NiOOH prepared from nickel foam indicates a covalent bond between FeOOH sites on the terrace sites of nickel oxyhydroxides.[113] This unusually coordinated catalyst exhibits 248 mV overpotential at 100 mA cm^{-2} current density.

1.3 Structure-Property Correlations

As seen in the examples in previous sections, the strategy of catalyst modification requires tuning kinetic properties and elementary reactions. However, the complexity of these modifications increases with the presence of multiple parameters regarding material properties. The computational studies, Brønsted–Evans–Polanyi relations and scaling relations, demonstrate the correlations between multiple effects. However, the direct observation of these correlated features is often complicated with experimental work. AOM indicates that the adsorption energy of the intermediate should be optimized to increase electrocatalyst performance. Volcano-shaped plots as in Trasatti's volcano plot is a clear description of this argument. Some experimental studies indicate that correlations of more complex electrocatalysts are in agreement with the volcano plot and at the same time some catalysts have non-volcano shaped trends between experimental parameters. The aim of this thesis is to observe such correlational behaviors across variations of nickel and cobalt based hydroxide electrocatalyst.

Correlational analysis is the comparison and harmonization of multiple experimental and theoretical descriptors regarding the structure of electrocatalysts. In order to effectively screen all correlative parameters, a systematic perturbation of the structure is required. This can be done by fabricating the series of materials by systematic alteration of the desired property. However, these changes in the system can cause diverse effects on the system and make it hard to control. For instance, direct information on the catalytically relevant species can be limited by the convolution of defect and bulk sites as electrocatalysis happens only on the surface species. Moreover, sometimes modulation of a single parameter is impossible as substitution of an additional metal cation into the host lattice can create structural distortions, strain, or change in the electronic structure. Hence, the multiple convoluted effects on the structure should be considered when a correlational analysis is made. This type of analysis can be done by both synthetic and analytical strategies such as environmental factors, strain, defects, and electronic factors.

OER involves multiple elementary steps and the overall behavior of the reaction series is determined by the kinetic and thermodynamic behaviors of each step. A general electron transfer reaction can be written as:

$$O + e^- \rightarrow R \qquad \textbf{(1.1)}$$

Nernst equation shows the equilibrium conditions **(equation 1.2)**:

$$E = E^{0'} - \frac{RT}{F} ln \frac{\Gamma_R}{\Gamma_O} \qquad \textbf{(1.2)}$$

where $E^{0'}$ is the formal reduction potential, R is the gas constant, T is temperature, F is Faraday's constant and Γ_R and Γ_O are the surface concentrations of the electroactive species. The rates of the anodic and cathodic reactions are described as:

$$\nu_a = \frac{i}{FA} = k_a \Gamma_R \qquad \textbf{(1.3)}$$

$$\nu_c = \frac{i}{FA} = k_c \Gamma_O \qquad \textbf{(1.4)}$$

The rate of anodic and cathodic reactions changes with the applied voltage. The Butler-Volmer approach is the most widely used to describe the kinetics of electrocatalytic reactions. The essence of Butler-Volmer formula is to treat all redox reactions as a single electron transfer. The 'α' parameter is defined as the transfer coefficient which can be between 0 and 1. Generally, it is assumed as 0.5 for both anodic and cathodic reactions. Steady-state electrokinetic information can be obtained with the slope of $\frac{F}{2RT}$ when the reverse reaction is insignificant. The slope is converted to base 10 logarithms and has the unit of mV dec^{-1} and named as Tafel slope (for more detailed information: **Chapter 2.2.8**).

The combination of thermodynamic and kinetic information about the elementary steps yields information on the rate-determining step of OER. Herein, the target is to demonstrate how correlational analysis is effective in detailed OER mechanistic analysis. **Equations 1.5-1.8** shows the single electron transfer steps on the metal hydroxide electrodes.

$$M^{II}(OH)_2 + OH^- \rightarrow M^{III}O(OH) + e^- + H_2O, \quad \textbf{(1.5)}$$
$$M^{III}O(OH) + OH^- \rightarrow M^{IV}O_2 + e^- + H_2O, \quad \textbf{(1.6)}$$
$$M^{IV}O_2 + OH^- \rightarrow M^{II}O(OOH)^-, \quad \textbf{(1.7)}$$
$$M^{II}O(OOH)^- + OH^- \rightarrow M^{II}(OH)_2 + 2e^- + O_2 \quad \textbf{(1.8)}$$

In this section, two possible rate-limiting steps and their effects on the reaction mechanism will be discussed. When **equation 1.6** is the RDS the intermediates of **equation 1.7** and the products of **equation 1.8** will not accumulate on the electrode surface. The total surface concentration (C_t) will belong to $M(OH)_2$ and MO(OH) species. As seen in **Figure 1.5A**, the concentration of $M(OH)_2$ will change from 99% to 1, and this change is associated to a change in Tafel slopes. The logarithm of current density increases as E_2 is shifting cathodically since the rate-determining step is the second electron transfer so the effect of E_1 is negligible in this case. **Figure 1.5B** shows the changes in oxidation state, and the MO(OH) intermediate becomes observable in and after the transition. Furthermore, a comparison of Tafel slope and oxidation state (**Figure 1.5C**) indicates that the

change in oxidation state is only observed where Tafel slop is readily changing as in the example where Tafel slope transitions from 40 to 120 mV dec^{-1}.

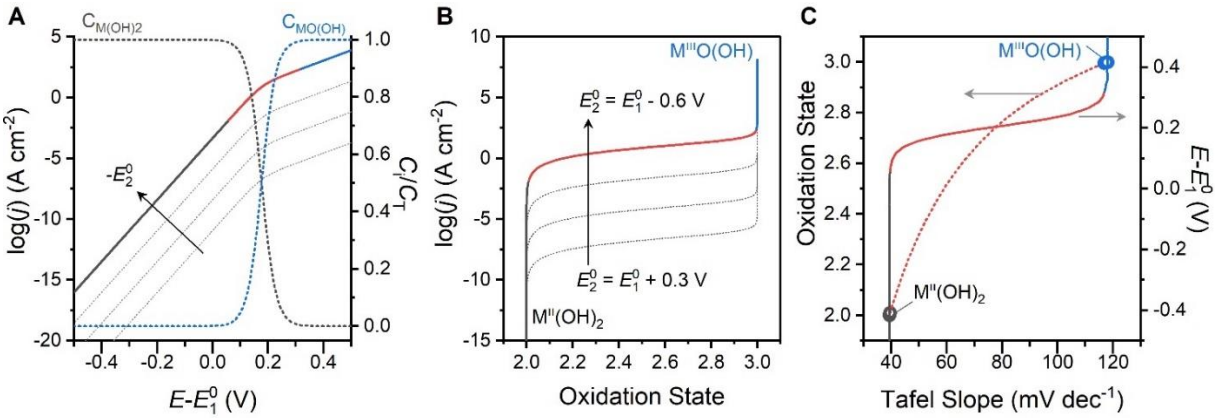

Figure 1.5 Electrocatalytic behavior and relative surface speciation for the situation where equation (1.7) is rate limiting for OER. **(A)** Predicted Tafel plots and relative concentration of reactants and intermediates. **(B)** Catalytic performance as a function of transition metal oxidation state. **(C)** Oxidation state and voltage as a function of Tafel slope with hollow black and blue circles signifying oxidation states within their respective colored regions. Dotted lines in panels **(B)** and **(C)** indicate changes in current as a function of E^0_2. Black, red, and blue segments demonstrate the same regions across the three panels. Figure re-printed with a permission from AIP Publishing.[15]

On the other hand, if **equation 1.7** becomes the RDS, the complexity of the mechanism increases. In this case the O-O bond formation has the highest activation energy barrier. Like the previous case (**Figure 1.6**), the intermediates start to accumulate on the electrode surface when Tafel slope readily changes. The mechanism indicates that transitions happen in two stages but as the second steps voltage sweep to more negative potentials, the first transition broadens, and the relative concentration of MO(OH) becomes weaker.

As seen in these two cases, reaction kinetics and thermodynamics are based on the steady-state or minor equilibria conditions where the reaction system has a semi-logarithmic behavior when the change in concentrations of the intermediate species is negligible. Relying on equilibrium conditions sometimes masks some important information and limits to obtaining instant

information on the reaction system. Because intermediate behaviors are changing in this transition region (red lines shown in **Figures 1.5 and 1.6**), and accordingly only a small portion of the catalyst can be counted as electrochemically active site.

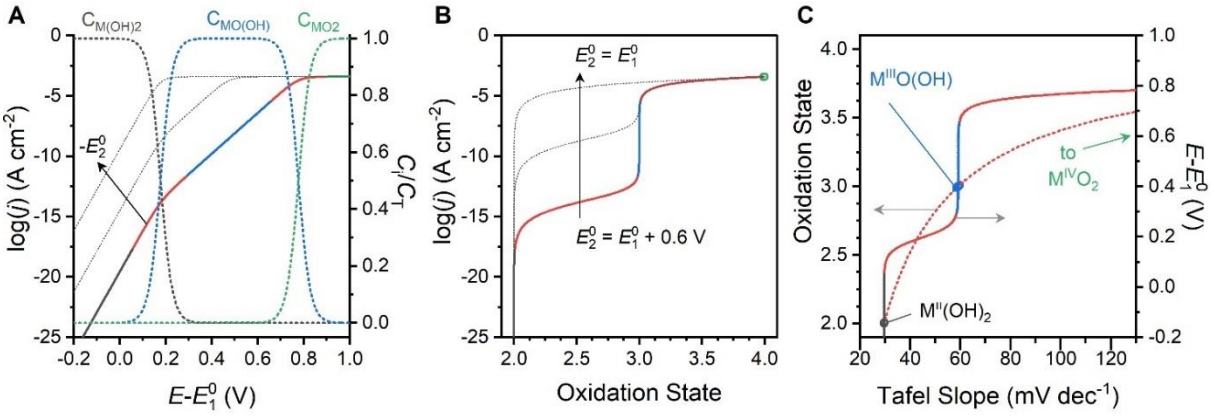

Figure 1.6 Electrocatalytic behavior and relative surface speciation for the situation where equation (1.8) is rate limiting for OER. **(A)** Predicted Tafel plots and relative concentration of reactants and intermediates. **(B)** Catalytic performance as a function of transition metal oxidation state. **(C)** Oxidation state and voltage as a function of Tafel slope with black and blue circles signifying all points captured within their respective regions. Dotted lines in panels **(B)** and **(C)** indicate changes in current as a function of E^0_2. Figure re-printed with a permission from AIP Publishing.[15]

For these reasons, an effective way to analyze such transitions is required to gain insight into reaction mechanisms and ultimately catalyst design. Structure-property or correlational analysis becomes a part of testing reaction sites of materials. Systematic perturbations of the system yield consistent changes in the behavior of the active site. These changes yield sometimes a defective, strained site that behaves differently than bulk. Therefore, constructing correlations between the behavior of the system and its surroundings and electrochemical behaviors can expand our understanding on catalysts mechanisms and thermodynamic interpretations.[15] In this thesis, our target is to make a structure-property analysis on iron doped nickel and cobalt hydroxides by utilizing several characterization techniques and investigating the effect of structural variations on electrochemical behaviors (**Figure 1.7**).

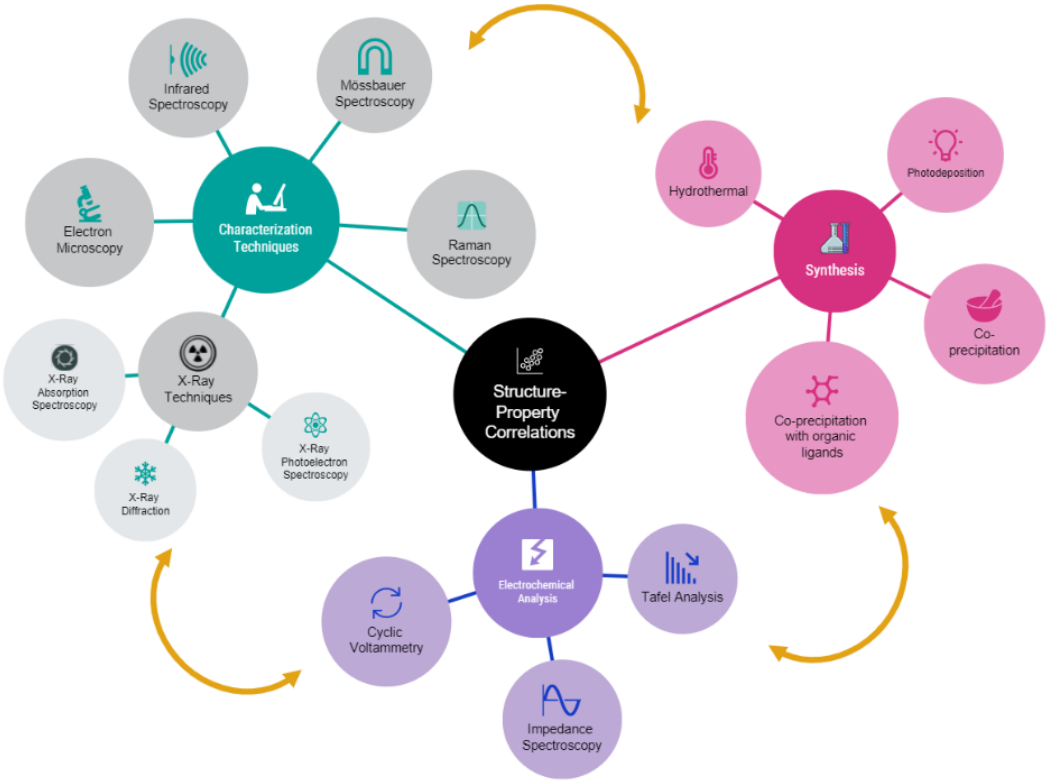

Figure 1.7 Structure-property correlations of the materials described in this thesis.

1.4 Scope of the Thesis

Linking of structure and electrochemical behaviors of heterogeneous catalysis provides a deeper understanding towards optimize electrochemical behavior for energy conversion applications. In this thesis, we highlight how synthetic protocols affect the structure and electrochemical performances of metal hydroxide catalysts.

Chapter 2 summarizes background and theoretical information about each synthesis and instrumental techniques operated in the studies throughout the thesis are explained thoroughly.

Chapter 3 expands the effect of geometric strain on iron, gallium, and aluminum-doped nickel hydroxides fabricated with photochemical route on the electrocatalytic oxygen evolution behavior are presented. Near-infrared spectroscopy, density functional theory, and potential energy diagrams of such systems are explained in detail.

Chapter 4 summarizes iron incorporated nickel hydroxides are synthesized with traditional co-precipitation and co-precipitation with the presence of formamide as OER electrocatalysts. Structure-property analysis is done with a detailed analysis of multiple characterization techniques including Mössbauer, X-ray absorption, Raman spectroscopy, X-ray diffraction, and electrochemical experiments.

Chapter 5 describes structural differences in iron incorporated nickel hydroxides synthesized with hydrothermal method. Structural analysis, phase segregation, and iron coordination environment are investigated.

Chapter 6 expands on the impact of synthetic conditions on the electrochemical performances of iron incorporated cobalt - (oxy)hydroxides are prepared with three different synthetic techniques: co-precipitation, co-precipitation with the presence of formamide, and hydrothermal method. Structural and electrocatalytic properties are extensively investigated and discussed.

Chapter 7 A general summary of the studies presented in this thesis and an outlook on nickel and cobalt hydroxides as electrocatalysts for oxygen evolution reaction is presented.

Chapter 2

Synthesis and Characterization Techniques

Several syntheses and characterization techniques were used to synthesize LDH materials to explore the influence of the systematic changes in experimental conditions on structural and electro(chemical) behaviors. In this section, different types of synthesis techniques employed for the synthesis of different types of LDH will be introduced. In the following sections, background information and the several types of analysis and characterization techniques used for these materials for structural analysis are introduced.

2.1 Synthesis Techniques

Various synthetic approaches have been developed for the synthesis of LDHs, including co-precipitation,[114–116] hydrothermal,[117] sol-gel,[118] reverse microemulsion,[119] urea hydrolysis,[88] electrodeposition,[84,120] photochemical deposition,[121] and atomic layer deposition.[122] The fabrication technique is highly effective in structural properties such as morphology, size, and surface area pore size.[123] We focused on four different synthetic routes to compare structural variances, and electrochemical behaviors of catalysts prepared by photochemical deposition, co-precipitation with aqueous and with the presence of organic molecules, and hydrothermal synthesis.

2.1.1 Photochemical Deposition

A photochemical deposition technique also known as photochemical metal-organic deposition (PMOD), involves the deposition of a metal-organic precursor on a substrate and subsequent UV

irradiation. This technique is a convenient way to obtain thin and smooth films.[124,125] UV light source is used for activation of precursor coordination complex solutions.[126] PMOD requires a stable substrate that is not affected by UV irradiation and the formation of stable thin films during the spin coating process. With the photolysis process, ligands and residues diffuse out of the film and transition metal oxides are formed after extrusion.[127] The fabrication of films involves the deposition of a single precursor and therefore the technique draws attention to the synthesis of different types of metal oxides because of simplifying the synthetic process.[91,126,128–130] Materials synthesized with this technique are highly disordered materials and reminiscent of LDHs and a thickness of a few hundred nanometers scale.[121,131]

Photodeposition technique is an effective way to control the kinetic formation mechanism of such materials. The decomposition mechanism of the ligand is previously studied by the two-dimensional Fourier-Transform correlational spectroscopy (2D-COS).[132] In this study, the formation mechanism of metal oxides from several metal-organic complexes is shown. The authors showed that the binding mode of the ligand initially changes from monodentate to chelating modes, and the decomposition process begins in chelating mode. The rate constant of the formation mechanism is shown as a V-shaped correlation with pKa or electronegativity. This relation is explained by the Sabatier principle, based on the binding strength of the carboxylate ligand.

In this technique, metal-organic complexes such as nickel (II) 2-ethyl hexanoate, iron (III) 2-ethyl hexanoate are used as precursors for the synthesis of amorphous metal hydroxides **(2.1)**. Metal complexes with desired concentration are firstly dissolved in a solvent such as ethanol, and solutions are spin-coated onto FTO films and put into UV-irradiation chamber for 24 hours.

$$Metal\ 2-ethyl\ hexanoate\ precursor \xrightarrow{UV,25^0C} amorphous\ metal\ oxide + CO_2(\mathrm{g}) + C_xH_y\ (\mathrm{g}) \quad \textbf{(2.1)}$$

2.1.2 Co-precipitation

Co-precipitation method for the synthesis of LDHs is the concurrent precipitation of hydroxides of M(II) and M(III) where M(II) and M(III) salts are precursors. The co-precipitation technique is one of the most convenient and rapid techniques for the synthesis of metal hydroxides such as nickel hydroxides or cobalt hydroxides blended with other cations. Co-precipitation allows yielding high-purity and crystalline products. The crystallinity of the LDH can be tuned with several experimental parameters including pH of the medium, concentration, type of the solutions, reaction speed and temperature, metal concentration, and the ratio between metals.[133]

The co-precipitation method can occur at either constant pH or increasing or decreasing pH values. The advantage of this method is in variability in choosing metal salts, reaction environment, pH, and the stoichiometric ratio between different metal sites.[134] The drawback of this technique is hard to control the size and distribution of materials which results in larger particles.

The general strategy for synthesizing transition metal (oxy)hydroxides present in this thesis is as follows:

Aqueous pH precipitation was carried out by dissolving appropriate amounts of ferric chloride and nickel or cobalt chloride hexahydrate to obtain a desired total metal ion concentration with the desired stoichiometric ratios varied from 0% to 30% of Fe. While the aqueous solution was stirred under N_2 environment, a 1M NaOH was added dropwise until pH of the solution was around 12. The solution was stirred for 10 minutes and followed by a centrifugation process. The final product is washed with water and acetone several times and oven-dried in an oven at 75 ℃ overnight. The color of the powder samples of nickel and cobalt hydroxides have green and pink, respectively. As iron is doped the colors turn brownish-green and pink.

2.1.3 Co-precipitation with the presence of organic molecules

2-dimensional LDHs are attractive due to their anisotropy, higher surface area, and conductivity properties.[135] Thus, several methods have been proposed to prepare LDHs in this morphology and increase the distance between layers to increase the number of electrocatalytically active sites and

tune the charge density of the sheets.[136–139] Modulation of anionic species between LDHs induces the formation of single-layer nanosheets. The most common method to synthesize LDHs in nanosheet form is exfoliation of the sheets with the help of organic molecules or simply adding them to reaction solvent during the synthesis.[101,137,140,141]

Precipitation from aqueous solutions in the presence of organic molecules such as formamide, sodium dodecyl sulfate, ethyl sulfate, octyl sulfate, hexadecyl sulfate, and octadecyl sulfate has been reported for the synthesis of two-dimensional layered double hydroxides.[101,136,138,142] The thickness of the sheets and the interlayer distances synthesized with this method are reported as approximately 13 Å, and 8-22 Å, respectively.[138,143] Materials synthesized with this technique exhibit a high number of defects and structural distortion in the lattice that favors OER activity.

The process developed for alkaline precipitation was modified following a literature protocol to fabricate colloidal solutions of individual 2-dimensional nanosheets. Aqueous solutions containing 30% v/v formamide and a total 0.35 M metal ion concentration with an appropriate ratio of nickel chloride and ferric chloride were titrated by NaOH solution. Aggregated particles were removed and individual nanosheets were collected by centrifugation of the remaining supernatant colloidal suspension. The final product is washed with two 10 ml aliquots of water, then with three 10- ml aliquots of acetone, and dried in an oven at 75 ℃ overnight.

2.1.4 High Temperature Synthesis

High temperature synthesis or hydrothermal synthesis is often employed to prepare crystalline materials.[37,144] An electrocatalysts fabrication using high temperature methods can be accomplished by either using an autoclave or boiling the content. The synthesis of LDH type materials with these techniques is very common since these methods offer higher crystallinity of products and larger scale of the products.[134]

Hydrothermal synthesis of transition metal (oxy) hydroxides reported in this thesis follows this experimental procedure: The aliquots of ferric chloride and nickel chloride hexahydrate were prepared in 5 M KOH. Solutions were added to a Teflon reactor with desired stoichiometric ratios

and a total metal ion concentration of 0.6 M. The reactor was heated to 140 ^{0}C at 5 ^{0}C min^{-1} and held for 16 hours, after which the supernatant fluid was removed. The solid was rinsed with H_2O, then added to the reaction vessel with 40 ml of H_2O and heated to 170 ^{0}C at 10 ^{0}C min^{-1}. After 16 hours the final product was collected by vacuum filtration. The samples were then rinsed with H_2O until pH was between 7.5 and 8.5 then washed with ethanol and oven dried at 200 ^{0}C for 2 hours. The final color of nickel hydroxides was green, and pink powders are obtained with cobalt hydroxide synthesis.

2.2 Characterization Techniques

2.2.1 Electromagnetic Spectrum

Electromagnetic energy is in waveform and spans a spectrum from shorter gamma waves to longer radio waves. The eyes of humans can only detect a smaller region of the spectrum that is visible lights. Different instruments detect specific regions of the spectrum, and they are listed in **Figure 2.1**. In this thesis, several characterization techniques that span nuclear, chemical, and molecular energy levels and their details are explained in the following sections.

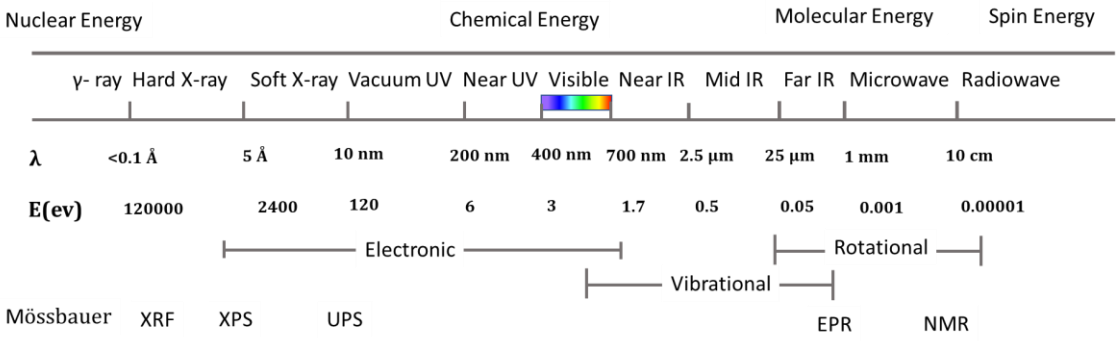

Figure 2.1 Electromagnetic spectrum and their corresponding energies, wavelengths, and characterization techniques associated with different regions of the spectrum.

2.2.2 Powder X-ray Diffraction (P-XRD)

Powder XRD is a common technique for analyzing crystal structures with long-range order and the identification of different types of phases. The technique was investigated by Sir W.H. Bragg

and Sir W.L. Bragg in 1913.[145–147] XRD measures the periodicity of the atomic structure of crystals. It is a useful technique to detect the quantitative and qualitative properties of the samples. Quantitatively, the interlayer distances, spacing between atoms in the same row, determining the orientation of grain or the crystal structure, measuring size, strain, and shape of the materials that are being tested. Qualitatively, the crystal structure of an unknown chemical can be determined with the help of the XRD technique since each material has a unique peak position and intensity in XRD experiments.

The electrons in an atom consistently scatter light and the intensity of the scattering light is proportional to the number of electrons around the atom. The atoms in the crystal structures are located periodically and therefore they can diffract light. X-rays scattered from an atom produce an X-ray diffraction pattern that contains information on the atomic arrangement of the crystal structure. Crystal structures are associated with symmetry elements to characterize the atomic arrangement of the samples. Peaks in an XRD pattern are associated with the planes of the atoms and Miller indices (*hkl*) which define the reciprocal of the axial intercept are used to identify these planes. The location of a peak is measured by the length of the parallel planes of the atom. XRD's working principle can be explained by Bragg's law in **equation (2.2)**:

$$n\lambda = 2d \sin\theta \qquad \textbf{(2.2)}$$

where d is the distance between layers, and n is the integer that refers to the order of diffraction (**Figure 2.2**). and lambda (λ) is the wavelength of the incident X-ray beam:

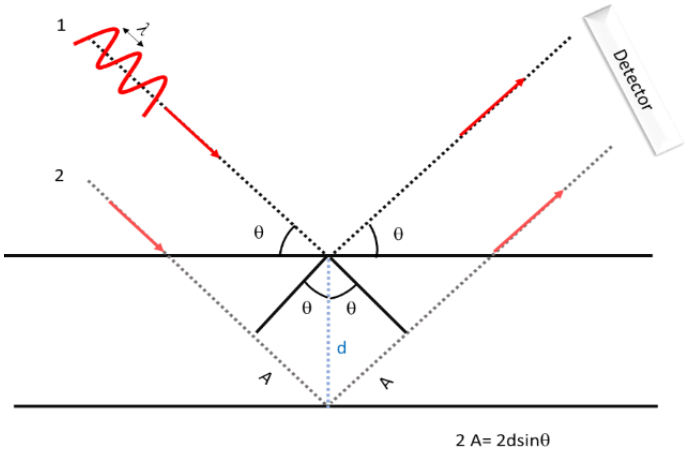

Figure 2.2 Schematic representation of Bragg's Law.

Bragg's Law informs the angle where constructive interference occurs as they produce the diffraction peak. The arrangement of atoms in the crystal structure determines the intensity of the diffraction peak. X-rays are scattered by the electrons around nuclei, a scattering factor is taken into account to derive the intensity of the diffracted beams without any assumptions. With this, the number and the position of specific atoms can be determined (**equation 2.3**):

$$F_{hkl} = \sum_{i=1}^{j} N_i f(r_i) e^{i2\pi(hx_i+ky_i+lz_i)} \qquad \textbf{(2.3)}$$

where F_{hkl} is the sum of the scattering from all atoms in the unit cell to form the diffraction peak from (*hkl*) plane, x_i, y_i, and z_i are the fractional coordinates that represent the locations of the atoms on the (*hkl*) plane, f is the scattering factor that depends on scattering angle and atom type, and N_i is the fraction of the equivalent positions occupied by the atom.

Several approaches are employed to measure an XRD pattern of a sample. The first one is referred to as the Laue technique in which the angle of incidence is fixed, but the wavelength is variable. The second approach is a more traditional way that uses monochromatic X-rays for a fixed wavelength and variable angle. There are two common geometries for this technique. The most often encouraged one is using a flat-plate geometry that is called as Bragg-Brentano geometry. In

this technique, the diffraction vector is normal to the sample surface. The incident angle is half of the detector angle. Two common ways are employed to measure the XRD patterns. In the first approach, the X-ray tube is fixed, and the sample and detector rotate at θ^0 and $2\theta^0$ rotates respectively per minute. In the second approach, called as Debye-Scherrer geometry, the sample is fixed, and the X-ray tube and detector rotate by the incident angle at the same rate in opposite directions.

XRD patterns in this dissertation were measured by using a PANalytical Empyrean diffractometer with Cu K_α radiation (λ = 1.5405 Å) and 2θ angles between 10-80 degrees at a step size of 0.0250^0. The Bragg–Brentano geometry equipped with a PIXcel bidimensional detector with a Ni K_β filter was used.

2.2.3 X-ray Absorption Spectroscopy

X-ray absorption spectroscopy (XAS) is complementary to XRD, providing a way to analyze the local coordination environment and electronic structures of the materials. XAS involves electronic transitions; an X-ray photon interacts with a core electron in the K or L edges. The electron excites and moves to an unoccupied state above the Fermi level. An electron from the higher energy level decays into the core-hole created by the excited electron and emits a photon or an Auger electron is emitted from the energy of the higher energy level. Absorption of X-rays can be explained by the Beer-Lambert law which shows the exponential relation between the intensity of the incident radiation (I_0) and the radiation after passing through the sample (I_t) (**equation 2.4**):

$$I_t = I_o\, e^{-\mu d} \qquad \textbf{(2.4)}$$

where μ is the absorption coefficient and d is the thickness of the sample. μ has dependence on energy of incident radiation (E_o), density of the sample (ρ), atomic number (Z) and mass (A):

$$\mu(E) \sim \frac{\rho Z^4}{A E_0^3} \qquad \textbf{(2.5)}$$

When the energy of electron in core levels of atom is equal to the incident photon energy absorption coefficient dependency starts to deviate and a sharp rise in the absorption called absorption edge (E_0) is observed. Absorption jump occurs when incident beams excite the core electrons of the absorbing atom to one of the unoccupied states in the valence shell. The location of E_0 is element specific and depends on Z^2 and the intensity depends on sample thickness and concentration of the absorbing atom.

A typical XAS spectrum can be divided into two main regions. These two regions reveal different details of the absorber atom, yet they are complementary to each other. The first region called as the X-ray absorption near-edge structure or near-edge X-ray absorption fine structure (XANES or NEXAFS) region consists of shoulders and peaks near the absorption edge (**Figure 2.3**). XANES analysis gives information on the molecular, electronic structure, symmetry of coordination environments, and oxidation state of the element being measured.

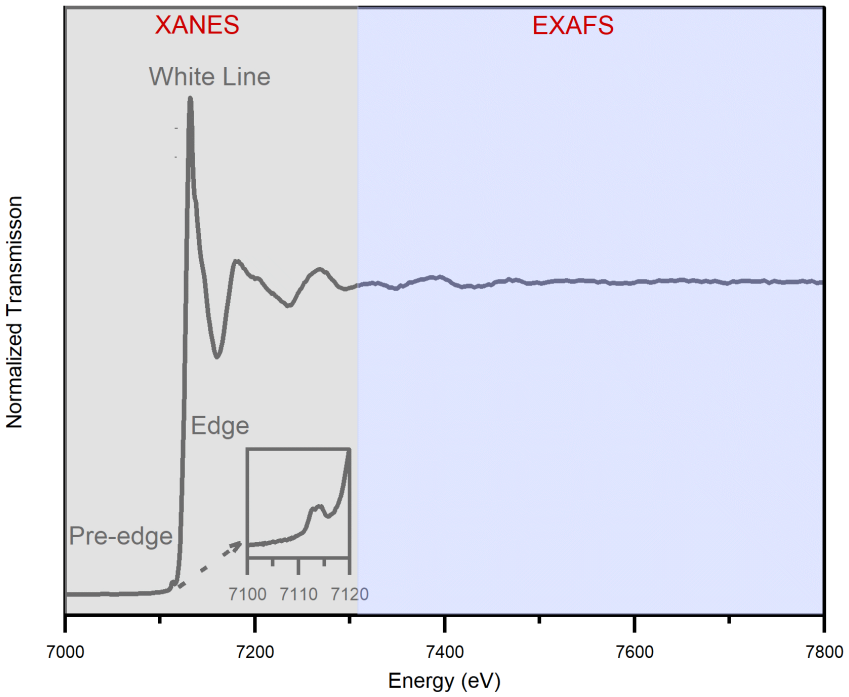

Figure 2.3 A typical XAS spectrum shows XANES and EXAFS regions.

XANES includes electronic transitions from the ground state to localized state, and dipole-allowed transitions to localized states yield prominent and large peak called *white line*, especially in L and M edges. In K-edge, the s-d transition is dipole-forbidden and therefore the quadrupole transitions are very weak in pure metals, so a sharp white line is not observed for such species. Furthermore, *pre-edge* feature before white line and edge regions is observed due to hybridization effect, as the vacant d-states may assume p-states characters, so the transition becomes dipole-allowed.[148] Pre-edge features are often useful to distinguish symmetry and distortions.

The second region is the post-edge is called as extended X-ray absorption fine structure (EXAFS) that extends a few keV above the E_0. EXAFS oscillations are a result of the interaction between photoelectron from the core level of the absorbing atom and the electrostatic potentials of the atoms near absorbing atom. EXAFS gives information on the distance between absorbing atoms and their neighbors. Neighboring atoms affect the absorption probability and therefore we observe an oscillatory structure of the measured spectrum. For these reasons, EXAFS region requires a background elimination and normalization steps (**equation 2.6**):

$$\chi(E) = \frac{\mu(E)-\mu_0(E)}{\Delta\mu_0(E_0)} \qquad \textbf{(2.6)}$$

where $\chi(E)$ is the normalized spectrum, $\mu(E)$ is the measured spectrum, $\mu_0(E)$ is the background function and $\Delta\mu_0(E_0)$ is the difference between pre-edge and post-edge regions background calculated as E_0 and called absorption jump. E_0 represents the minimum energy to excite the photoelectron to higher energy levels.

After background subtraction and normalization process the EXAFS signal needs to be converted to k-space (photoelectron wavenumber) from energy space by the relation in **equation 2.7**:

$$k=\sqrt{\frac{2m_e(E-E_0)}{\hbar^2}} \qquad \textbf{(2.7)}$$

where $\hbar$ is the reduced Planck's constant, and m_e is the electron mass. Photoelectron wavevectors have destructive and constructive interference. The condition for a constructive interface is shown in **equation 2.8**:

$$2R\text{-}n\lambda \quad \textbf{(2.8)}$$

where R is the reduced distance between the absorbing atom and neighboring atoms, λ is the wavelength, and 2 factor represents that electron travels between the absorber atom and its neighbor in two directions. Since photoelectron is a wavefunction, reaches a maximum value when a constructive interference occurs, and it can be written as:

$$\chi(k) \propto \cos\left(\frac{2\pi 2D}{\lambda}\right) \propto \cos(2kR) \quad \textbf{(2.9)}$$

However, the **equation 2.9** does not reflect EXAFS fully since for an elastic scattering bond distance, the identity of the element and wavevector are effective parameters on the scattering. Therefore, a probability function is needed to incorporate in **equation 2.10:**

$$\chi(k) \propto f(k)\cos(2kR) \quad \textbf{(2.10)}$$

where *f(k)* is the proportionality function or scattering amplitude that is calculated during the simulation process. Furthermore, EXAFS focuses on the atoms within 5-10 Å of the absorbed atom hence the radial distribution of atoms around the absorbing atom needs to be considered. The distances in EXAFS are called as coordination shells and the closest distances are named first coordination shells. Shells are comprised of identical atoms' places at a uniform radial distance from the absorbing atom. EXAFS signal is the combination of the scattering paths of possible photoelectron interactions and can be represented as:

$$\chi(k) = \sum_i f_i(k)\cos(2kR_i) \quad \textbf{(2.11)}$$

where the subscript i represents each individual coordination shells. However, the **equation 2.11** does not include the contributions of degeneracy or stoichiometry. The term N_i is incorporated into **equation 2.12** to consider the effect of degeneracy.

$$\chi(k) = \sum_i N_i f_i(k) \cos(2kR_i) \quad \textbf{(2.12)}$$

As photoelectrons are ejected from the absorber atoms they move in a uniform as spherical waves. These spherical waves interact with the electron density of neighboring atoms and introduce a phase shift, $\delta_i(k)$. It compensates for the movement of electron orbitals. EXAFS equation becomes as **equation 2.13** after incorporation of phase shift:

$$\chi(k) = \sum_i N_i \frac{f_i(k)}{kR_i^2} \sin(2kR_i + \delta_i(k)) \quad \textbf{(2.13)}$$

kR_i^2 term is incorporated into 2.13 since photoelectrons move in spherical waves. In addition, the cosine function in **equation 2.13** is replaced by the sine function to unite the phase shift parameter $[\delta_i(k)]$. In addition to these factors, there is no defined border between XANES, and EXAFS region and it is associated with the mean free path of the excited electron [λ(k)]. Mean free path affects the lifetime of the core-hole and inelastic interactions. Since EXAFS region involves high energy interactions λ(k) dramatically decreases and the interactions are limited by a few neighboring atoms. For these reasons, EXAFS inform on the local environment of absorbing atom and affected by R_i and shown as:

$$\chi(k) = \sum_i N_i \frac{f_i(k)}{kR_i^2} e^{-\frac{2R_i}{\lambda(k)}} \sin(2kR_i + \delta_i(k)) \quad \textbf{(2.14)}$$

As the core hole affects the interaction between ground and excited states after the photoexcitation in an element characteristic way, the amplitude of the signal decreases. For this reason, the amplitude reduction factor (S_0^2) is incorporated into EXAFS equation becomes as **equation 2.15**:

$$\chi(k) = S_0^2 \sum_i N_i \frac{f_i(k)}{kR_i^2} e^{-\frac{2R_i}{\lambda(k)}} \sin(2kR_i + \delta_i(k)) \quad \textbf{(2.15)}$$

EXAFS represents an average of the coordination shell around absorbing atom, however, the disorder including static, and thermal disorders weakens the oscillations. The effect of disorder is incorporated into EXAFS equation with the mean square displacement parameter (σ^2) (**equation 2.16**):

$$\chi(k) = S_0^2 \sum_i N_i \frac{f_i(k)}{kR_i^2} e^{-\frac{2R_i}{\lambda(k)}} e^{-2\sigma_j^2 k^2} \sin(2kR_i + \delta_i(k)) \quad \textbf{(2.16)}$$

2.2.3.1 XAS Measurement

An XAS measurement is performed by measuring the XAS absorption coefficient as a function of incident X-ray photon energy. This requires the ability to scan X-rays over a range of 1-2 keV, and to acquire high signal-to-noise ratio data for analysis of EXAFS oscillatory.

XAS is traditionally performed at synchrotron facilities, where magnets force electrons traveling relativistic velocities to turn shedding energy as broadband radiation. Single-bending magnet synchrotrons are adequate to produce radiation for typical XAS experiments. For more complex experiments that require higher X-ray radiation such as time-resolved or dilute samples, special insertion devices for example wiggler and undulator insertion devices are used. In essence, insertion devices are periodic magnetic arrays that are installed as either linear or circular way, and hence XAS beams with wiggler or undulator yield highly polarizable radiation with a superior brightness over a wide range of energy.

The most common XAS setup consists of mirrors to collimate the beam and remove the unnecessary part of the emitted radiation, a rotatable monochromator that consists of two single crystals, with a specific orientation for the desired wavelength, and inert gas filled ionization chambers as detectors that measure the X-ray intensity of sample and the reference. A metal foil of the same absorbing element is often placed behind the sample and used for the alignment of instrument. X-rays passing through the ionization chambers, ionize the gas molecules, which are

subsequently detected as a current which is proportional to the X-ray intensity. In order to convert current into signals as voltage current amplifiers are used to reach a detectable current.

Three common methods for measuring XAS are transmission, fluorescence, and total electron yield techniques. In the transmission mode the quantification of the absorption can be made by comparing the incident and transmitted beam for the transmission mode (**equation 2.17**):

$$I_t = I_0 e^{-\mu(E)d} \qquad \textbf{(2.17)}$$

where d is the thickness, I_0 and I_t is the X-ray intensity before and after the sample. XAS measurements in transmission mode generally have a good signal-to-noise ratio with a good quality of samples with appropriate concentration and thickness of the absorbing atom and the homogeneity of the sample.

XAS in fluorescence mode measures the fluorescent X-ray from the excited atom that fills the core hole. In fluorescence mode, the detector is placed orthogonal to the incident beam to reduce elastic scattering from the sample and the background. In order to minimize the self-absorption effect in fluorescence mode thin and less concentrated samples are preferred. Under these conditions the fluorescence intensity becomes **equation 2.18**:

$$\mu(E) \sim \frac{I_f}{I_0} \qquad \textbf{(2.18)}$$

The third mode of XAS measurement is total electron yield mode. The geometry is similar to fluorescence mode, but the Auger electrons are measured in total electron yield mode instead of photons. As only the electrodes being ejected from a few nanometers deeper than the thin surface of the materials are detected with this method, total electron yield mode is highly sensitive to atoms near the surface.

Synchrotron facilities have a broad range of collimated energy, high flux, and small size of the source. All synchrotron facilities have a storage ring, and the electromagnetic radiation is emitted into beamlines. Each beamline has its specific experimental conditions that are optimized with its

optics. As electrons pass through a beamline X-rays are generated with the help of bending magnets for steering electrons to beamlines and generating photons and wigglers that have very high dipole moments and undulators that are similar to wigglers but with shorter magnet periods and smaller distances. In this thesis, XAS experiments were conducted at Brookhaven National Laboratory (BNL) synchrotron facility. All the Ni and Co K-edge samples were recorded in transmission mode, Fe K-edge data was recorded in both fluorescence and transmission modes since iron absorber is dilute in the sample series which prevents obtaining a desirable edge step.

2.2.3.2 EXAFS Simulations

The background function, normalization steps, and E_0 value affect the shape of EXAFS spectrum. Hence, a systematic data reduction process is very important for analyzing a series of samples. Path parameters are the mathematical expressions of the parameters in the EXAFS equation. The results and fit quality are highly dependent on these parameters:

N is the path degeneracy, and it is used for the determination of coordination numbers. $\mathbf{So^2}$ is the amplitude reduction factor. It is used for modifying the path intensity of the fitting model. It cannot be a negative value. The concentration of vacancies, dopants, and coordination numbers are effective factors in the determination of amplitude reduction factor. $\mathbf{\Delta E_0}$ is used for correcting E_0 for correcting the wavenumber. ΔE aligns the grids of wavenumber or energy of data to theory. **ΔR** is used to adjust the length of the half path. This value modulates the interatomic distances of a single scattering path. It is a function of R_{eff} which is the calculated bond distance of the specific shell. $\mathbf{\sigma^2}$ is called as Debye-Waller factor which is the mean square variation in the path length. It represents thermal or static disorder at the path. It cannot be a negative value. Phase correction is done before Fourier transform to eliminate the contributions of the absorber and the scattered atom which is why we observe different lengths in the simulation results. **R- factor** and $\mathbf{X^2}$ are the statistical values that give information on the quality of modeling. R-factor is the uncertainty of the correlations between parameters used in fitting the materials. To be more specific, it is the percent misfit between experimental data and EXAFS theory. In general, a good fit has an R-factor

value of less than 0.02. X^2 is the statistical parameter. A good fit is expected to have a X^2 value that is close to 1. However, X^2 itself is not enough criterion to evaluate modeling quality.

2.2.3.3 Wavelet Transform Analysis

Wavelet transform (WT) recently attracts attention since it provides a clear description of neighbor-specific interactions. By using a continuous wavelet transform, we can distinguish between the noise and multiple scattering pathways at various R-spaces. While a typical EXAFS analysis consists of Fourier Transform (FT) process in which a complex wavefunction is converted from k- space to R-space. However, due to the nature of FT some information while the conversion may not be very clear like the nature of the various peaks.

The maxima of different shells in k-space information are not obvious as a result of FT and this can be solved by using wavelet analysis. In WT the wavefunction is multiplied by a Gaussian function and the wave becomes weighted towards a particular part of the k-space and that is multiplied through the spectrum (**Figure 2.4**). In a WT spectrum, we can tell that a specific peak in the radial distribution function corresponds to a certain part in the k-space spectrum.

$$W_f^{\psi}(a,k') = \frac{1}{\sqrt{a}}\int_{-\infty}^{\infty}\chi(k)\psi(\frac{k-k'}{a})dk \qquad \textbf{(2.19)}$$

where $\chi(k)$ is the EXAFS data, ψ is the mother wavelet. The mother wavelet is often selected to be either Morlet wavelet or Cauchy wavelet. The Morlet wavelet is represented as:

$$\psi(k) = \frac{1}{\sqrt{2\pi}\sigma}e^{i\omega k}e^{-\sigma_0^2 k^2}\ , \int_{-\infty}^{\infty}\psi(k)dk = 0 \text{ and } a = (\frac{\eta}{2R}) \qquad \textbf{(2.20)}$$

where σ and η are two adjustable parameters of the frequency of the wave and the shape of the Gaussian (**Figure 2.4**). These two parameters are effective in the resolution of WT spectra in two-dimensional space. The resolution of k space and R space is inversely related to each other, and it can be represented as Heisenberg's boxed as in **equations 2.21 and 2.22**:

$$[k \mp \Delta k]\ x\ [R \mp \Delta R] \qquad \textbf{(2.21)}$$

$$\left[k \mp \frac{\eta\sigma}{\sqrt{2}R}\right] x \left[R \mp \frac{R}{\sqrt{2}\eta\sigma}\right] \quad \textbf{(2.22)}$$

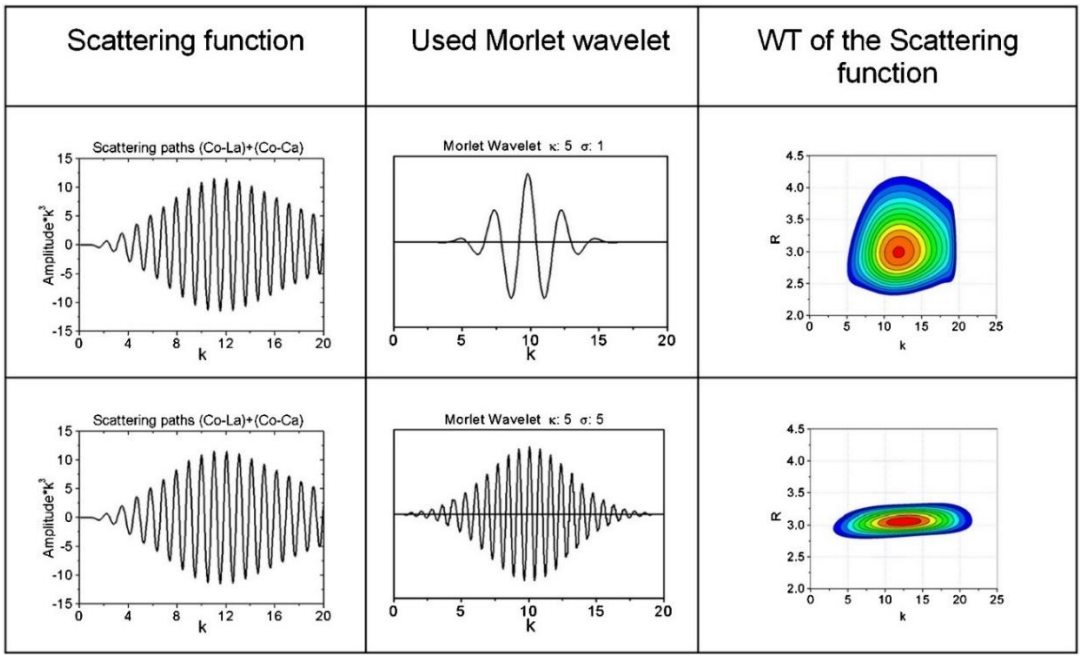

Figure 2.4 Sample Morlet Wavelet Transform analysis on $La_{0.5}Ca_{0.5}CoO_{3-\delta}$ shows continuous wavelet transform and the effect of parameters on the WT spectrum. Reprinted with permission from AIP Publishing.[149]

2.2.4 X-ray Photoelectron Spectroscopy (XPS)

XPS is a useful technique for the determination of the electronic structure such as oxidation state of the elements, ionization energies and relative surface compositions, and valence band structures. In XPS, X-ray beam is irradiated on the surface of the sample and kinetic energy and the number of electrons ejected from the inner shells of the sample as photoelectrons are quantified. This phenomenon is called the photoelectric effect. These ejected electrons have kinetic energies which are used to determine the chemical composition and the electronic structure of the sample. While kinetic energy is independent of X-ray energy, the scale of binding energy and peak positions of Auger electrons is dependent on the X-ray source (**equation 2.23**):

$$E_{kinetic} = E_{photon} - E_{binding} - \phi_{spec} \quad \textbf{(2.23)}$$

where $\mathbf{E_{kinetic}}$ is the kinetic energy of the ejected photoelectrons $\mathbf{E_{photon}}$ is the energy of the incident X-ray, $\mathbf{E_{binding}}$ is the binding energy and $\boldsymbol{\phi_{spec}}$ is the work function of the element. Work function describes the minimum energy needed to remove an electron from a solid. Apart from electrons ejected by the X-ray, Auger electrons can also be detected with XPS. Auger electrons are emitted when an electron-hole is created in lower energy shells such as K, and the hole is filled by another electron from a higher energy shell. The energy of this process ejects another electron and that is the Auger effect.

A typical XPS instrument consists of an X-ray source, an Ar ion gun, neutralized, vacuum system, and an electron energy analyzer. Ultrahigh vacuum system where the pressure is less than 10^{-7} Pa. Due to the spin-orbital splitting, two separate peaks are observed for s, p, and d orbitals. Spin orbital splitting is a characteristic feature of an element. The value of the splitting of the core level of an element is the same in various compounds. Another important parameter in XPS spectra is the peak area ratio, and this value is also expected to be the same for an element in different compounds. Spin orbital splitting and peak area ratio are used to identify an element in a compound. The ratio of $s_{-1/2}$ and $s_{+1/2}$ is 1/2, 2/3, and 3/4 for p, d, and f orbitals respectively.

Sampling depth is another important parameter for an XPS measurement. The value of the sampling depth depends on the kinetic energy of the photoelectron and the type of material. XPS spectrum is generally represented as the intensity versus binding energy or the kinetic energy. In an XPS measurement, chemical shift value is reported, and it is defined as the response of a material by changing the core electron binding energy caused by the change in chemical bonding of the element. The essence of the chemical shift is the electrostatic interaction between the electron and nucleus. When oxidation happens, the binding energy increases and for the reduction, it's vice versa.

XPS technique is an advantageous technique in terms of its surface sensitivity, being non-destructive, and providing information on chemical bonding.

2.2.5 Vibrational Spectroscopy Techniques

Vibrational spectroscopy techniques are useful for the determination of the structural and electronic and mechanistic properties of the materials. In the structural aspect, the characteristic properties of vibrations, detection of functional groups, isotope shifts, and normal coordinate analysis can be done with infrared, Raman, and resonance Raman spectroscopy. Electronic information can be extracted by resonance Raman spectroscopy for the identification of electronic transitions, bonding properties, and excitation profiles. Mechanistic information, such as time-resolved intermediate profiles can be extracted with the combination of other characterization techniques such as electrochemistry. These techniques are complementary to other techniques.

2.2.5.1 Factor Group Analysis

Factor group analysis (FGA) helps to derive the irreducible representation of each crystallographic site in a lattice. It was introduced by Bhagavantam and Venkatarayadu in 1939. With the help of FGA, the vibrational properties at k=0 (the center of the Brillouin zone) of a crystal structure can be investigated. The process consists of identifying the point group and identifying the site symmetries in the unit cell. It is followed by correlating the site symmetry and the lattice symmetry, and the determination of the irreducible representation per site.

FGA helps to estimate infrared and Raman active modes of crystal lattices. Selection rules apply for the determination of these modes. The linear characters and quadratic characters in the character table represent infrared and Raman active modes respectively. According to FGA of brucite, four Raman and four infrared active modes exist. (**Figure 2.5 and 2.6**).

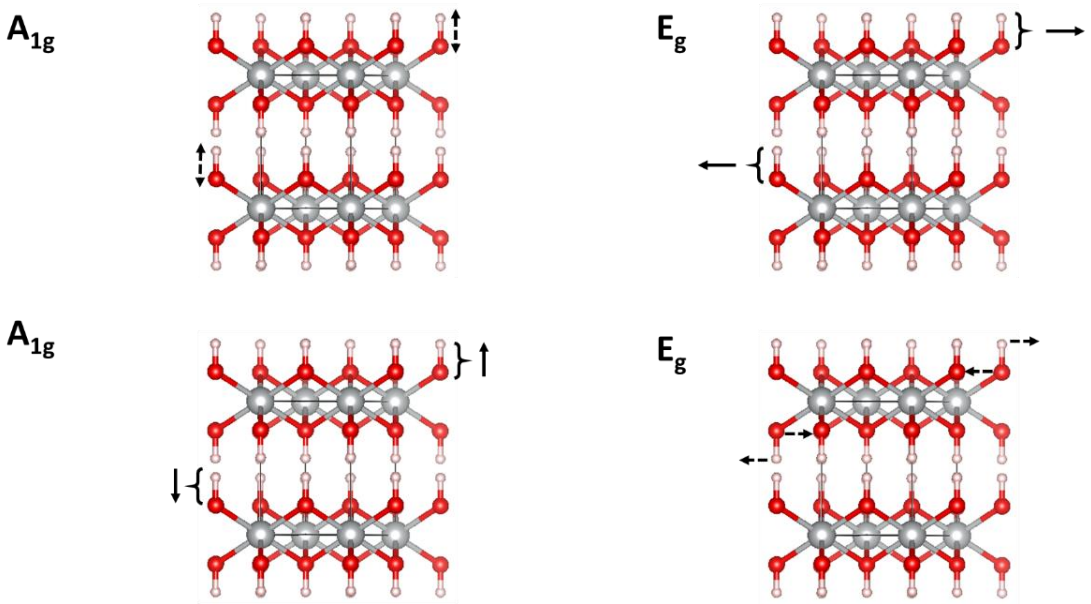

Figure 2.5 Raman active modes of brucite β-Ni(OH)$_2$. Solid and dashed arrows represent translational and rotational lattice modes respectively. Figure is adapted from[150]

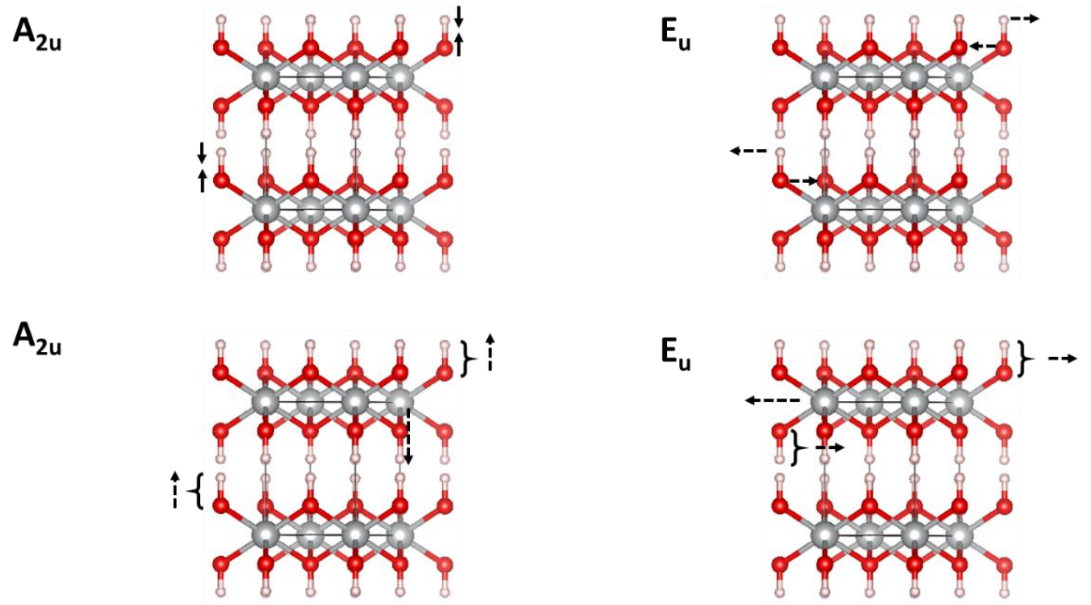

Figure 2.6 Infrared active modes of brucite β-Ni(OH)$_2$. Solid arrows and dashed arrows represent translational and rotational lattice modes respectively. Figure is adapted from[150]

2.2.5.2 Raman Spectroscopy

Raman spectroscopy reveals vibrational and rotational transitions of materials and assesses the structural defects in materials. It is complementary to FTIR spectroscopy, the difference between FTIR and Raman spectroscopy arises from differences in the selection rules.

In Raman spectroscopy a laser as the monochromatic light source is shining on the sample of interest and scattered light from the sample is detected and analyzed. Different laser frequencies can be used in a Raman experiment. However, fluorescence occurs when a photon absorbs and then re-emitted by the sample. Raman scattering involves inelastic scattering collision. Raman-active vibrations change the polarizability of a molecule when they are exposed to a vibrational motion. A molecule in its ground state with the energy of $h\upsilon$ accepts energy from a photon and is excited to a higher energy level (virtual energy state) $h(\upsilon_{ex}-\upsilon_{vib})$ and in the meantime, incident radiation scatters with energy. The frequency of the scattered energy ($\upsilon_{ex}-\upsilon_{vib}$) is called as *Stokes line*. (**Figure 2.7**) Furthermore, when this molecule returns to its ground state has an extra energy $h\upsilon$, and the photon scatters with the frequency of $h(\upsilon_{ex}+\upsilon_{vib})$. This frequency line is called the *anti-Stokes line*. According to the Boltzmann distribution, and the population of the vibrational levels the intensity of the anti-Stokes line is lower compared to the Stokes line. Rayleigh scattering occurs when light and the energy of the sample interacts, and the frequency of the scattered light remains the same. In this situation, the electron in the molecules oscillates at the same frequency and the oscillating dipole radiates the energy in each direction. Rayleigh and Raman scattering processes are generally not very efficient. To make this process efficient, a very strong laser beam is required.

Raman measurements were performed using a Renishaw inVia Reflex confocal Raman microscope. A 532 nm (Renishaw DPSSL, 50 mW) laser, filtered to 1% of maximum intensity unless otherwise stated, was used in conjunction with 1800 lines/mm diffraction grating. Raman data were processed and analyzed by Renishaw WiRE 5.3 software package. Processing of spectra includes subtraction of baseline, spectrum normalization, and curve fitting.

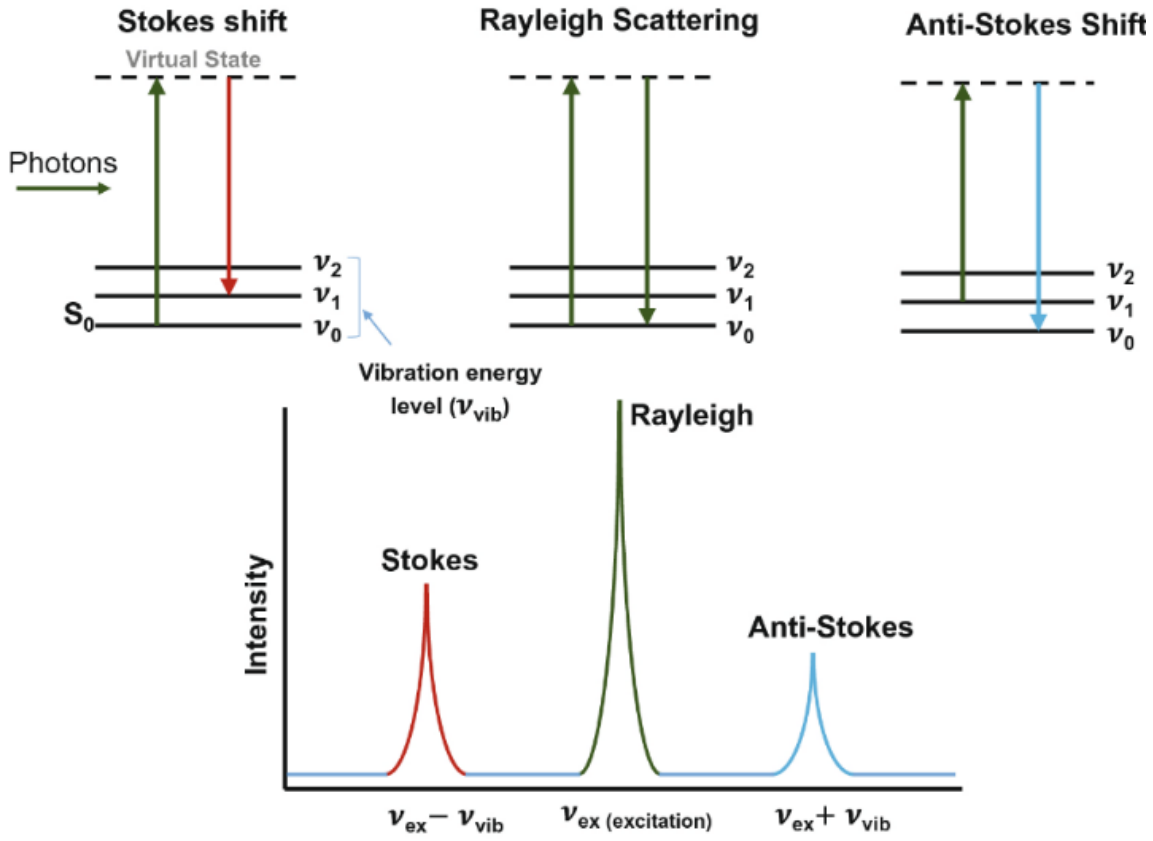

Figure 2.7 Schematic representation of Stokes, Rayleigh, and Anti-Stokes scattering. Reproduced with permission from Springer Nature.[151]

2.2.5.3 Fourier-Transform Infrared Spectroscopy (FTIR)

FTIR is one of the most popular techniques for mostly organic and inorganic scientists. It is used for the determination of chemical and structural behaviors of the materials such as organic functional groups, fingerprinting of an unknown organic and inorganic compound, and determination of the conformation of molecules, their stereochemistry, and measuring optical conductivity. Solid, liquid, and gas phases can be tested with FTIR spectroscopy.

The source of infrared radiation is heat or thermal radiation and molecular vibrations happen when the frequency of applied infrared radiation is equal to the frequency of the vibration of the sample. If a molecule absorbs the infrared radiation, there should be a change in dipole moment by vibrations and rotations.

Infrared spectroscopy covers *ca.* 1 meV to 1 eV energy region and it is divided into three areas in the electromagnetic spectrum. Near-IR spans 4000-14000 cm^{-1}, mid-IR spans 500-4000 cm^{-1} and far-IR spans 5-500 cm^{-1}. Rotational level energy changes happen below 100 cm^{-1} wavenumber regions. Vibrational levels are quantized, and the vibrational energy levels of most molecules typically correspond to the mid-IR region. Molecular vibrations can be classified as stretching and bending. Stretching vibration points out a change in the interatomic distance on the axis of the bond, on the other hand bending vibrations represent a change in bond angle. There are four types of bending vibrations which are scissoring, wagging, rocking, and twisting.

Wavenumbers are typically shown as the x-axis of an FTIR spectrum since it is directly proportional to the energy of infrared absorption. Percent transmittance (T%) or absorbance is commonly used for the y-axis of the spectrum. Transmittance (T) is the ratio between the transmitted intensity by the sample and the intensity of infrared radiation:

$$T = \frac{I}{I_0} \quad \textbf{(2.24)}$$

Transmittance of a sample is often represented with the percentage:

$$T\% = \frac{I}{I_0} x100 \quad \textbf{(2.25)}$$

The relation between absorbance and transmittance is given by the Beer-Lambert Law (**equation 2.26**)

$$A = -\log(T) \quad \textbf{(2.26)}$$

The combination of the **equations (2.25** and **2.26)** yields **equation 2.27**:

$$A = 2 - log_{10}(\%\, T) \qquad \textbf{(2.27)}$$

Attenuated total reflection (ATR) is a fast and easy way to measure FTIR spectrum of a sample. In this technique, infrared light passes through a crystal and the molecular information is obtained by the interaction with the sample and infrared beam. It is a non-destructive process. It is suitable for a wide variety of samples such as powders, pellets, liquids, oils, and pastes. Limitations of FTIR spectroscopy are the transparency of the background and molecule activity in the infrared region.

2.2.6 Mössbauer Spectroscopy

Mössbauer spectroscopy, named after Rudolph L. Mössbauer, is the absorption of recoilless nuclear gamma rays by nuclei. Prof. Mössbauer was awarded Nobel Prize in physics due to his discovery and contributions to recoilless nuclear resonance fluorescence (*i.e.*, Mössbauer effect). Mössbauer spectroscopy is a valuable technique for different areas of science including physics, chemistry, earth sciences, and biology, and informs experimenters about the chemical environment, valency, electric field gradient, and magnetic properties of samples being tested.

The nuclear transitions because of the γ-rays absorption from the sample, nuclear spin quantum numbers of the atom change. The absorption depends on the electron density of the nucleus. The numbers and shapes of the peaks give structural information. The theory of the Mössbauer effect is that an element (emitting atom) that has excited state energy ($\mathbf{E_e}$) transitions into ground state energy ($\mathbf{E_\gamma}$) by emission of gamma quantum energy. Accordingly, this gamma quantum energy is absorbed by the same type of element (absorber atom) that is in its ground state. The second element undergoes resonance absorption. During these processes, the recoil effect is eliminated with the absorption and emission of γ-rays. (**Figure 2.8**)

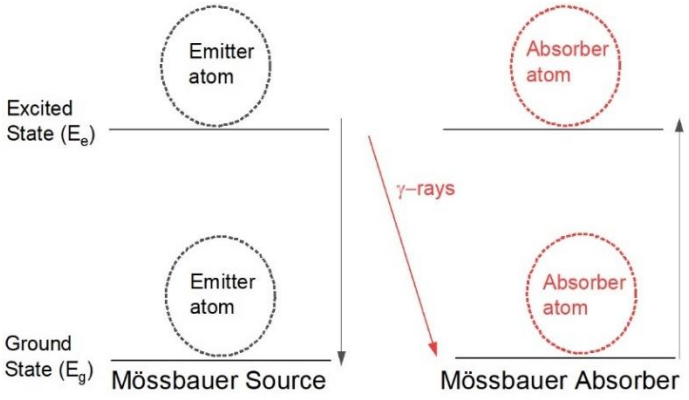

Figure 2.8 Schematic representation of working principle of Mössbauer spectroscopy.

Recoil effect **(E_R)** is defined as an atom or a molecule that undergoes an emission or absorption of γ-quanta (**E_γ**) is affected by a recoil effect (**equation 2.28**):

$$E_R = \frac{E_\gamma^2}{2mc^2} \qquad \textbf{(2.28)}$$

The Mössbauer effect can be observed in more than forty elements in the periodic table (**Figure 2.9**). The most commonly used Mössbauer nuclide is ^{57}Fe.

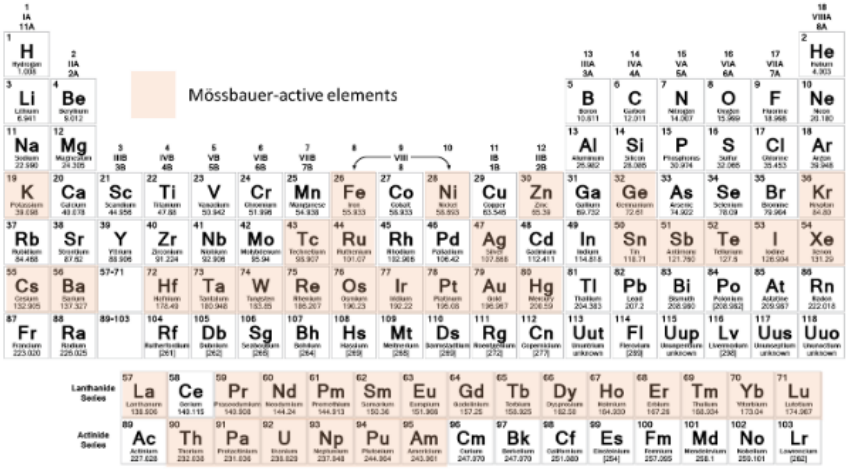

Figure 2.9 Mössbauer active elements across the periodic table.[152]

There are three important interactions of nuclei with their chemical environment that changes the absorption energy. (**Figure 2.10**). The first parameter is isomer shift (δ) from changes in the electron environment. It arises from a change in the size of the radius and is shown in **equation 2.29**:

$$\delta = (e_0/5)\,(Ze^2R^2)\,(\Delta R/R)\,[|\psi_s(\text{absorber})|^2 - |\psi_s(\text{source})|^2] \qquad \textbf{(2.29)}$$

where $\mathbf{e_0}$ is the permittivity of free space, **Z** is the atomic number, **e** is the charge of an electron, **R** is the radius and **ΔR** is the difference in radius of an atom between excited and ground state, and $|\boldsymbol{\psi_s}|$ is the s- electron wavefunctions of the nuclei in absorber and source.

Isomer shift values show a dependence on the oxidation state of the element tested. For instance, Fe(II) has larger isomer shifts than Fe(III) since isomer shift is associated with electron density at the nucleus. Isomer shift is mostly sensitive to s- orbital electron density since the wavefunction of s-orbital has its maxima at the nucleus and p, d, and f orbitals have zero wavefunctions. Furthermore, it is affected by the screening nucleus by p and d orbital electrons. For ^{57}Fe, an increase in electron density of 3d orbital increases the isomer shift but an increase in 4s orbital decreases the shift.

The second parameter is the electric quadrupole splitting ($\mathbf{\Delta E_Q}$) which describes the interaction between the nuclear quadrupole moment and the electric field gradient in the sample. It informs about the molecular symmetry, oxidation state, and bond characters of the nuclei environment. In order to be an electric quadrupole interaction occurs, at least one of the nuclear states should have a quadrupole moment (**eQ**) and inhomogeneous electric field in the nuclei. $\mathbf{\Delta E_Q}$ is measured by the energy difference between two resonance lines *i.e.,* I= ½ and I= 3/2 (**Figure 2.10**). Shape and the symmetry of the ligand field around the atom are under the effect of the quadrupole splitting (**equation 2.30**):

$$\Delta E_Q = \frac{1}{2} eQV_{ZZ} \left(1 + \frac{\eta^2}{3}\right)^{\frac{1}{2}} \quad \textbf{(2.30)}$$

where $\boldsymbol{V_{ZZ}}$ is the electric field gradient, and $\boldsymbol{\eta}$ is the asymmetry parameter which is an additional parameter for nuclei with non-axial symmetry.

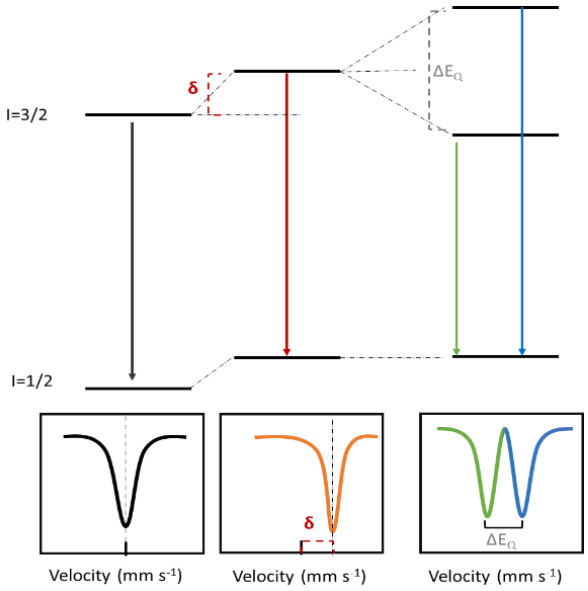

Figure 2.10 Schematic representations of isomer shift and quadrupole splitting parameters.

The shape of the nuclear charge distribution is affected by the electric field gradient. Such as symmetric molecules and symmetric d orbital electron distribution produce a singlet, but when the ligand field is not symmetric a singlet peak is formed. In ^{57}Fe Mössbauer spectroscopy, a doublet peak forms when electric quadrupole interaction occurs in the absence of magnetic dipole interactions.

The third interaction is magnetic splitting ($\boldsymbol{\Delta E_M}$) which is the magnetic dipole interaction between the magnetic dipole moment and the magnetic field. This interaction enlightens the magnetic properties of the materials such as ferromagnetism and anti-ferromagnetism.

2.2.7 Transmission Electron Microscopy (TEM)

TEM is a high-resolution imaging technique that is used to analyze the fine details of the materials such as shape, size, composition, and defects. The technique was developed in the 1930s by Knoll and Ruska.[153,154] TEM uses a highly energetic electron beam to shine on the thin sample and tests the interactions between electrons and atoms. The shorter wavelength of the beam enables to obtain high-resolution TEM images. With the recent developments, a TEM is capable of *ca.* 0.04 nm spatial resolution and *ca.* 4.2 meV high energy resolution.[155] The electron beam passes through the specimen to provide a contrast and produce a TEM image. The atomic scale information can be obtained with the combination of energy-dispersive X-ray spectroscopy (EDX) and electron energy-loss spectrometry (EELS). For these reasons, the local structure of a catalyst can be identified. TEM works under ultra-high vacuum conditions and therefore specimen preparation has a great impact on the formation of the image. The thickness, component, and structure of the specimen are important factors for image quality. Samples can be prepared by direct coating on TEM grids or cutting with gallium or argon beams.

A Hitachi HD2000 microscope was used for scanning transmission electron microscopy (STEM). Approximately 5 mL of an ethanol suspension of the sample synthesized in formamide was coated on a carbon grid using an Eppendorf pipette. A gentle stream of N_2 was directed over the grid for about 3 minutes to remove the solvent. The STEM was operated at 200 kV using secondary electron imaging.

2.2.8 Electrochemical Techniques

Electrocatalytic properties of the individual materials were investigated by a series of diverse electrochemical experiments. Cyclic voltammetry, chronoamperometry, and electrochemical impedance spectroscopy are the most common techniques used for the materials in this thesis. Subsections will give more detailed information on each technique.

2.2.8.1 Cyclic Voltammetry

Cyclic voltammetry (CV) is one of the most common electrochemical analysis techniques to probe the redox process of the material. It investigates the current response of an electrocatalyst with respect to potential and time. In a typical CV experiment potential is swept in one direction and followed by a sweep in the reverse direction. The investigation of electron transfer is done with the help of CV experiment. Thermodynamic behavior of electron transfer reactions is dictated by the Nernst equation which describes the equilibrium of the redox process:

$$E = E^0 + \frac{RT}{nF} ln \frac{C_{ox}}{C_{red}} \quad \textbf{(2.31)}$$

where $\mathbf{E^0}$ is standard electrode potential, $\mathbf{C_{ox}}$ and $\mathbf{C_{red}}$ are the concentrations of oxidized and reduced species respectively, **F** is the Faraday's constant, **R** is the gas constant, **n** is the number of electrons and **T** is temperature. However, in a CV experiment the transition between one equilibrium to another as potential sweeps from one end to another. Therefore, mass transfer and electron transfer kinetics play an important role in the investigation of the electrochemical properties.

During an electrochemical experiment, a concentration gradient is formed since electron transfer reactions occur only on the electrode surface. A CV experiment provides mechanistic information both quantitatively such as determination of rate constant from scan-rate dependence and qualitatively such as peak shapes.

2.2.8.2 Chronoamerometry

Chronoamperometry is one of the controlled-potential techniques. It involves the stepping of the potential and observing the current-time response of the Faradaic process. Since a gradual growth of the diffusion layer occurs as the concentration of the reactants diminishes and that causes current decay over time. The current at the planar electrode is explained by the Cottrell equation **(equation 2.32)**:

$$i(t) = \frac{nFAC\sqrt{D}}{\sqrt{\pi t}} \quad \textbf{(2.32)}$$

where **n** is the number of electrons, **F** is Faraday constant, **A** is surface area of the electrode, **C** is concentration, **D** is diffusion coefficient and **t** is time. The current in the Cottrell equation refers to mass transfer limited currents. The magnitude of the current depends on the flux of the species from bulk solution to the electrode surface.

Chronoamperometry is often used to extract Tafel slopes of electrocatalysts to study electron transfer kinetic information on the electrocatalytic process. Tafel analysis helps to elucidate the mechanistic behavior of multi-step energy conversion systems. Tafel analysis was performed using a multi-step potential step experiment starting from before the pre-catalytic redox peak observed in CVs to after Faradaic process with specific potential steps and time. The current density of each step is taken as steady-state current density. **Figure 2.11** represents a sample chronoamperometry experiment for extracting Tafel slope.

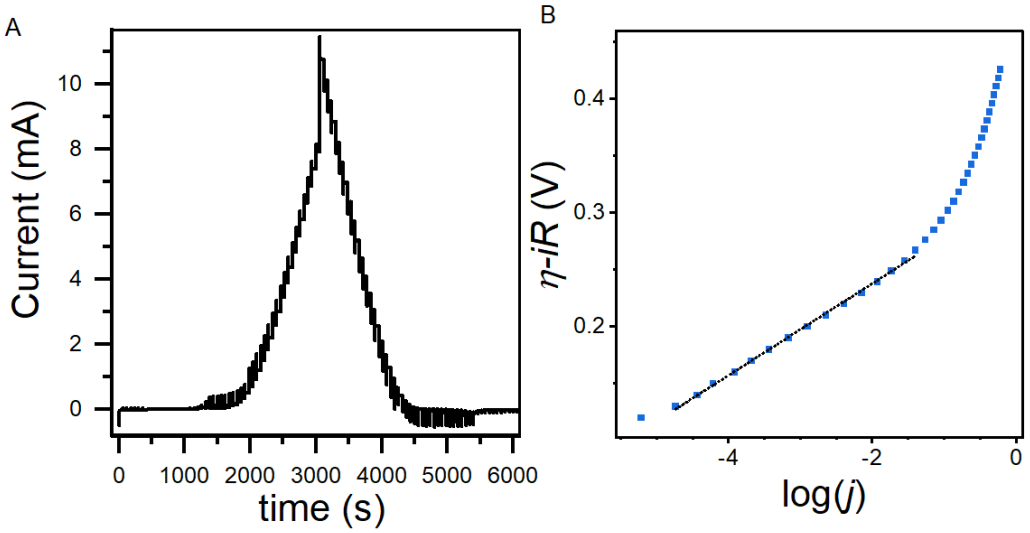

Figure 2.11 Electron transfer kinetics experiments. **(A)** Sample potential step (chronoamperometry) experiment stepped in both oxidation and reduction reactions. **(B)** Sample Tafel slope analysis, the linear region is used to calculate the slope.

The Butler-Volmer equation (**equation 2.33**) specifies the current potential characteristic of a system:

$$i = FAk^0\left[C_O(0,t)e^{-\alpha f\left(E-E^{0'}\right)} - C_R(0,t)e^{(1-\alpha)f\left(E-E^{0'}\right)}\right] \quad \textbf{(2.33)}$$

where $f = \frac{F}{RT}$

The Tafel equation **(equation 2.34)** is the simplified version of the Butler-Volmer equation. It only considers one direction of the reaction.

$$\eta = a + b \log j \quad \textbf{(2.34)}$$

$$b = \frac{2.303\,RT}{\alpha nF} \quad \textbf{(2.35)}$$

where **b** defines Tafel slope, η is overpotential which is defined as the difference of the energy between experimental and thermodynamic conditions ($E-E_0$), **j** is current density, α is transfer coefficient.[156]

All experiments were carried out with 1 M KOH electrolyte solutions in a single-compartment polyethylene cell. A Biologic SP-300 was used in conjunction with a Gaskatel HydroFlex reversible hydrogen electrode (RHE) as the reference electrode, a platinum mesh as the counter electrode, and FTO or carbon fiber paper as the working electrode. Electron transfer kinetics were measured by chronoamperometry experiments in both the anodic and the cathodic directions. The voltage was stepped from 0.9 to 1.7 V vs RHE in 10 mV, 60 s steps. The current density at the end of each step was taken as the steady-state catalytic current. Cell resistances were measured by impedance spectroscopy prior to electrochemical experiments with values on the order of 15 Ohms for FTO and 5 Ohms for carbon fiber paper measured for all samples. All experiments were performed without resistance correction; the voltage axis of Tafel plots was corrected for resistance unless otherwise stated:

$$E = E_{ref} - iR_u \quad \textbf{(2.36)}$$

2.2.9 Density Functional Theory (DFT)

Theoretical studies are widely used in chemistry to extract information on the electronic density and the electronic energy of the compounds. The simulations based on quantum physics help us to obtain information on dipole moments, charge distribution, and with the help of potential energy surfaces bond energies, and molecular geometry. DFT in material science is used to investigate vibrational, optical, structural, and magnetic properties of matter according to theoretical methods derived from the fundamental equations. In this thesis, calculations were performed with plane-wave-based density functional theory (DFT) in the Quantum ESPRESSO package.[157]

Chapter 3
Effect of Geometric Strain on Nickel Hydroxides

3.1 Introduction

Incorporation of the trivalent iron into the nickel hydroxides dramatically improves electrochemical OER activity. The effect of iron induced enhancement can be observed by decreasing onset overpotentials, lowering Tafel slopes, and anodic shifts in the pre-catalytic redox peak potentials.[36,42,158–160]

The main role of iron in nickel hydroxides is a point of debate and proposed arguments on the catalytic activities can be classified as:

i) Nickel sites are activated with the presence of iron sites[62,121]

ii) Iron sites are electrochemically active sites and partially oxidized[80, 142] or tetravalent under operating conditions[162–164]

iii) Iron is dissolved in nickel hydroxide lattice and promotes OER upon aging[165]

Upon these proposals, several reports support each of the above proposals with evidence showing that Fe cations either are[164,166] or are not[167–169] electrochemically oxidized during OER. However, each of these mechanistic studies provides indefinite support for these arguments. Strain engineering in heterogeneous catalysis draws attention as another option to tune the catalytic activity of the materials. Several examples show strain has on electronic structure and electrochemical behavior.[170–177] These studies point out that strain can be a parameter to modulate electrochemical performances.[178] A correlation between electrocatalyst activity and the binding strength of the OER intermediates to the electrode surface has already been studied for a wide variety of materials.[28,179,180] These correlations play an important role on the optimization of the

electrocatalytic performances of the OER electrocatalysts. For instance, experimentally measuring antibonding orbital populations in perovskite family[181] or theoretical study on the prediction of the thermodynamic properties such as binding energy calculations of the intermediate species demonstrate the direct correlation between two parameters.[182] The volcano plot shows the relation of the activity versus binding energy, however, relies on several assumptions, primarily stating that the structure and the mechanism of the electrocatalysts remain stable under operation. The limitation of this approach has been shown with experimental and theoretical studies: the amorphous or disordered materials as OER electrocatalysts,[125,183] the experimental evidence of the reversible and irreversible changes during the reaction,[184–186], a surprising finding that basal-plane MoS_2 vacancies serve as very active sites,[170] and computations that show the situations where these assumptions are not valid under operando conditions.[180]

In this chapter, we investigated the effect of the geometric strain for photochemically deposited highly disordered nickel (oxy)hydroxide electrocatalysts. The purpose is to highlight the effect of strain in trivalent aluminum, gallium, and iron-doped nickel hydroxides on the structure and electrochemical properties. Electrocatalytic activity and electronic structure of the catalysts are under the effect of the effective ionic radii of the blended ions. Structural distortions of the composition series were identified by using near-infrared spectroscopy and DFT calculations conducted for obtaining electronic structure and producing potential energy surfaces (PES) of the blended electrocatalyst. A combination of all results from several techniques indicates that while strain is reproduced for all three systems by their shift in pre-catalytic redox peak potentials, however, the electrocatalytic activity of iron incorporated nickel hydroxide is ruled out from their aluminum and gallium doped analogues.

3.2 Results

We fabricated three thin films series of Fe(III), Al(III), and Ga(III) incorporated nickel oxides with the formula of $M_xNi_{100-x}O_y$ where x is varied between 0 and 30 with in step of 5. The secondary cations are intentionally selected for investigating the effects of geometric strain on the

electrocatalytic OER behavior. The reasons for choosing these metals specifically are based on four main points:

i) all three metals are compatible with layered double hydroxide structure when incorporated to nickel hydroxide,[35,187,188]

ii) the effective ionic radii of these metals provide a gradient between Ni(II) and Ni(IV)[189] (**Figure 3.1**)

iii) all of them are trivalent for providing an equivalent electrostatic charge, and

iv) standard reduction potential (E^0) of these metals do not fall into the working voltage range. Especially for the possibility of oxidation of Fe(III) higher valences are ruled out since it happens at higher potentials than our employing voltage range.[93,164,166]

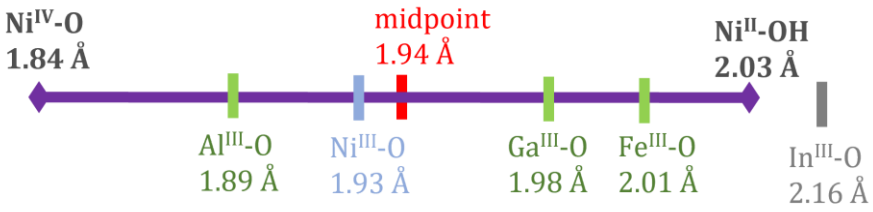

Figure 3.1 Comparison of bond distances between nickel and trivalent secondary cations sites blended into nickel hydroxide.

We prepared uniform films of three composition series of iron, gallium, and aluminum doped nickel hydroxides on fluorine-doped tin oxide (FTO) with spin coating technique. The precursor solutions are photochemically reactive materials and they form disordered nickel hydroxides after irradiating UV light. This fabrication protocol yields films with a highly disordered structure that are *ca.* 150 nm thick. X-ray diffraction has been shown to be ineffective in characterizing these materials,[42,125] but X-ray absorption spectroscopy indicates a disordered structure related to layered double hydroxides in which all nickel sites are electrochemically accessible. These films have been shown to achieve complete coverage and be highly uniform in their as-deposited state, with morphological changes yielding increased surface roughness after electrochemical testing.[42]

3.2.1 Electrochemistry

Voltammetric characterization of the Al−Ni, Ga−Ni, and Fe−Ni composition series reveal identical trends in precatalytic behavior but disparate electrocatalytic performance (**Figure 3.2**). A precatalytic redox process decreases in size and shifts anodically at a rate of 2.5 mV per percent addition of Fe in the Fe−Ni series (**Figure 3.2**A). The precatalytic redox process is variably assigned to a Ni(II) to Ni(III)[36,41,159] or a Ni(II) to Ni(IV) [121,168] transition for nickel oxyhydroxides, likely owing to differences in fabrication and characterization protocols. We assign a Ni(II) to Ni(IV) transition as indicated by a recent analysis of photochemically deposited $Fe_yNi_{100-y}O_x$.[121] The subsequent exponential rise in currents is electrocatalytic OER. This feature exhibits a significant cathodic shift following addition of Fe, with the majority of the shift occurring within the first 5% Fe addition. This behavior is characteristic of the material and is in agreement with all of the past studies on iron−nickel (oxy)hydroxides.[36,121,159] The precatalytic redox process for both Ga−Ni (**Figure 3.2**B) and Al−Ni (**Figure 3.2**C) series exhibits a 2.6 mV anodic shift per percent of additional metal but no clear catalytic gains as seen in the Fe−Ni series. The well-defined precatalytic redox peaks observed for all three composition series show no signs of shouldering or peak splitting, suggesting a homogeneous distribution of the dopant cations. The identical behavior of the precatalytic redox process in all composition series suggests preservation of the nature of the precatalytic electron transfer process despite differences between the additive elements.

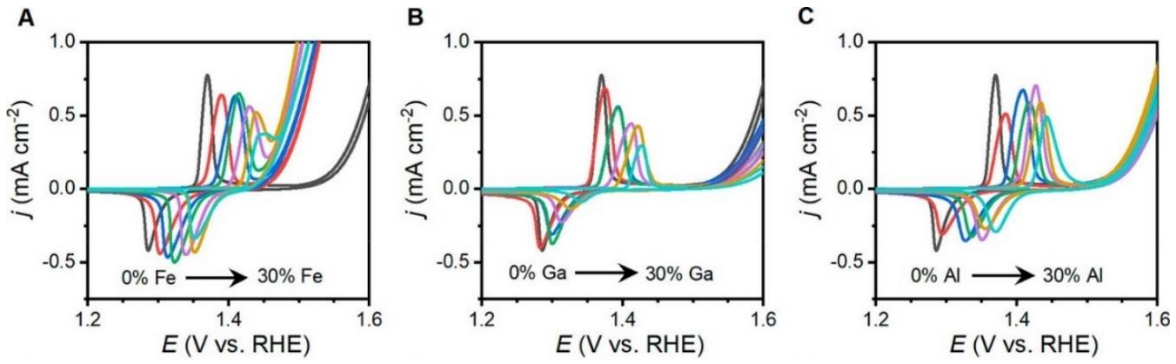

Figure 3.2 Cyclic voltammetric behavior of the **(A)** Fe-Ni, **(B)** Ga-Ni, and **(C)** Al-Ni composition series acquired at 1 mV s^{-1} in 1 M KOH.

This overall behavior is in excellent agreement with that previously reported for the Fe–Ni composition series deposited on glassy carbon electrodes,[121] suggesting that no electrode substrate effects are at play. Neither of these characteristic changes is observed for the Al–Ni or Ga–Ni composition series, where the Tafel slopes gradually change by *ca.* 10 mV dec^{-1} and η_{onset} slightly increases. The differences in electrocatalytic behavior observed here support the assertion that electrocatalytic OER and the precatalytic process are fundamentally decoupled and not a linear series of events.

Electrokinetic activity of the three-sample series was evaluated by Tafel slope analysis. Tafel slopes were obtained through chronoamperometry experiments in both anodic **(Figure 3.3A)** and cathodic **(Figure 3.3B)** directions. The voltage is stepped from 0.9 to 1.7 V vs RHE with one minute and 10 mV steps. Steady-state current density values for each step is determined at the end of each step. Tafel plots of Al, Ga, and Fe doped sample series are shown in **Figure 3.3C-E.**

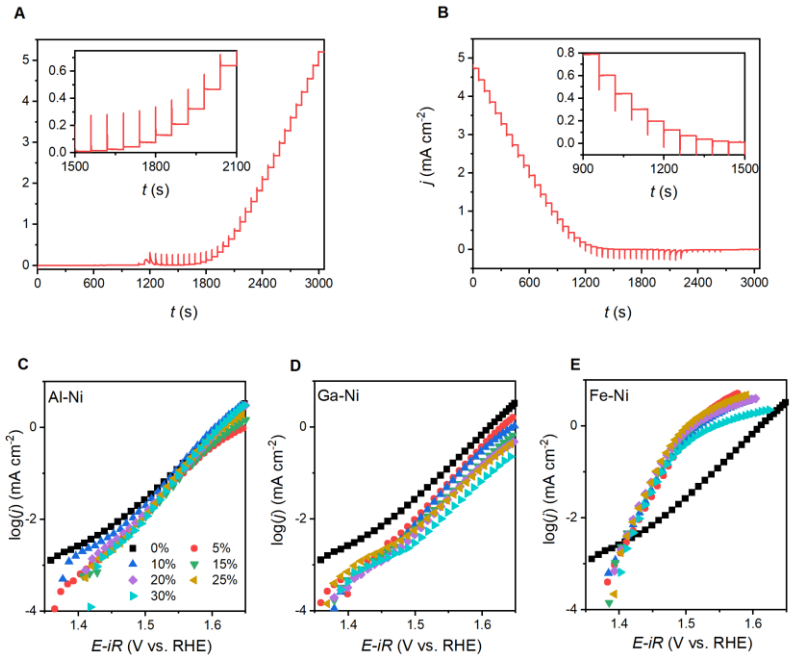

Figure 3.3 Steady-state electrokinetic analysis of three sample series. Sample chronoamperometry experiments of **(A)** anodic and **(B)** cathodic directions. Tafel plots produced from cathodic chronoamperometry of **(C)** Al-Ni **(D)** Ga-Ni and **(E)** Fe-Ni hydroxide sample series.

Incorporation of iron into nickel hydroxide yields the characteristic changes in electrocatalytic OER activities: a sudden decrease in the onset overpotential **(Figure 3.4A)** for electrocatalytic OER (η_{onset}), defined here as the onset of linearity in Tafel plot **(Figure 3.4B-C)**, and a stepped decrease in the measured Tafel slope.

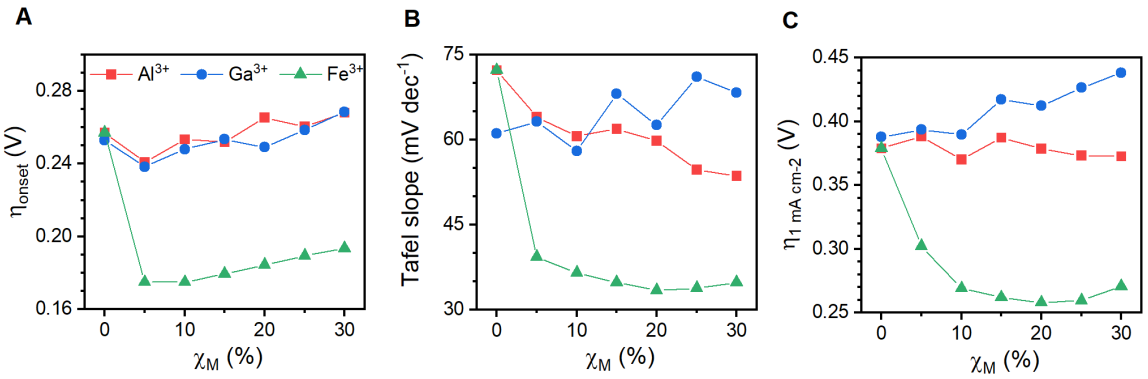

Figure 3.4 Composition dependent electrokinetic properties. **(A)** Onset overpotential (η_{onset}). **(B)** Tafel slopes and **(C)** onset overpotential for 1 mA cm^{-2} current density.

Evidence that changes observed in electrochemical behavior for the Al and Ga series are not due to incidental incorporation of Fe come from electrochemical behavior when Fe is intentionally incorporated **(Figure 3.5A-B)**. Addition of 1% Fe content during fabrication of 5% Ga and 10% Ga electrodes induces the characteristic decrease in Tafel slope for electrocatalytic OER, as does the analysis of a 15% Ga electrode analyzed in a 1 M KOH solution that had not been subjected to the purification procedure (**Figure 3.5C-D**).

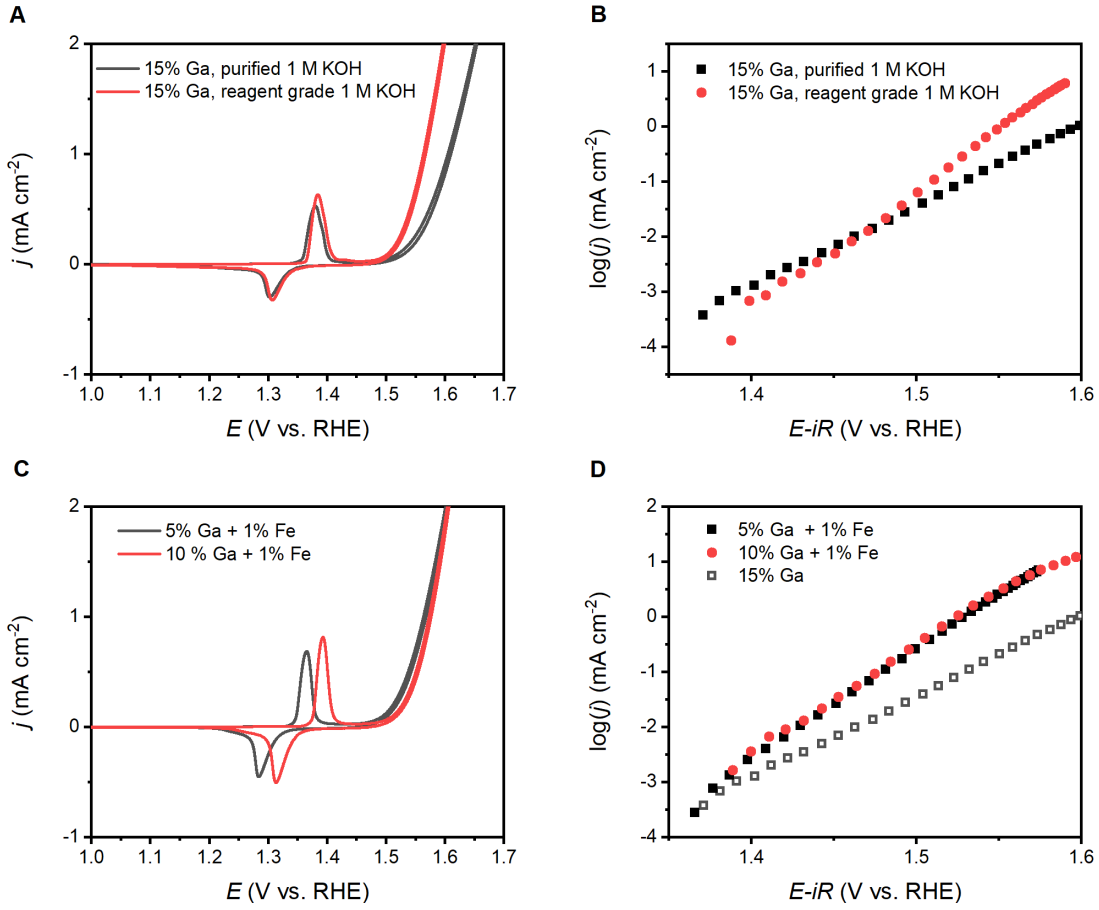

Figure 3.5 Cyclic voltammetric behavior of Ga-containing films intentionally contaminated with Fe. **(A)** Cyclic voltammetric and **(B)** steady-state currents for $Ga_{15}Ni_{85}O_x$, in purified and unpurified 1 M KOH solutions. **(C)** Cyclic voltammetric and **(D)** steady state currents for $Fe_1Ga_5Ni_{94}O_x$ and $Fe_1Ga_{10}Ni_{89}O_x$. All CVs show stabilized voltammetric acquired at 1mV s^{-1}.

3.2.2 X-ray Photoelectron Spectroscopy (XPS)

The surface compositions of the 20% Ga and 20% Al samples were examined by X-ray photoelectron spectroscopy (XPS) before and after electrochemical testing. High resolution XPS scans in the Fe 2p region show no Fe in either sample (**Figure 3.6**).

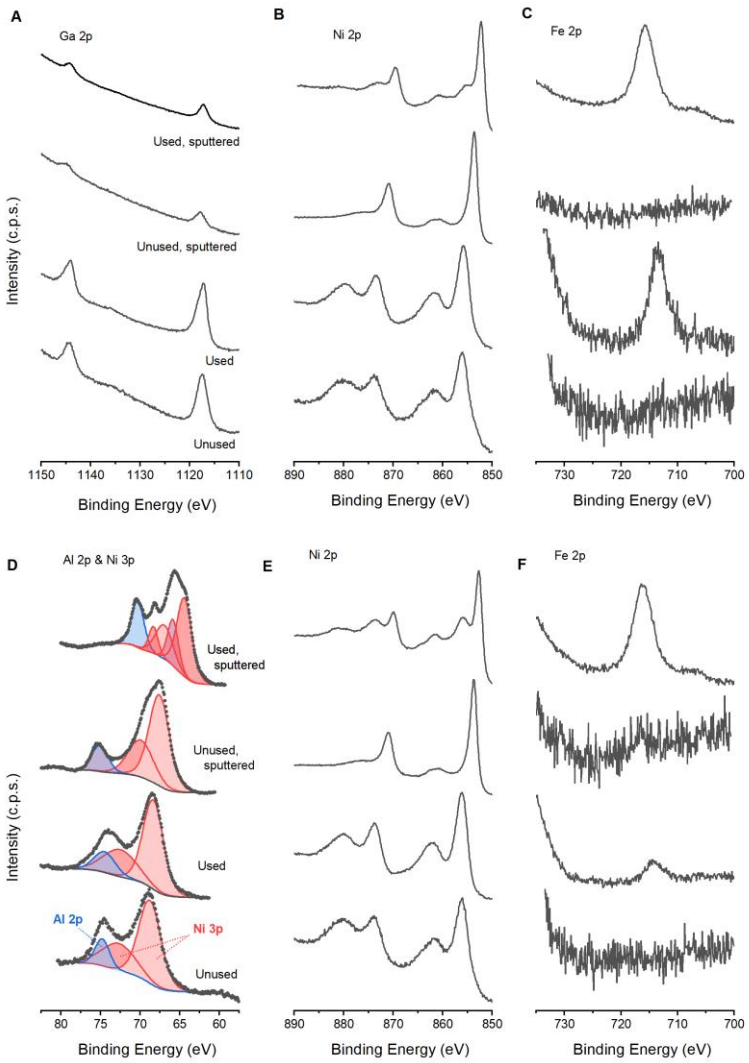

Figure 3.6 High resolution X-ray photoelectron spectra for the **(A)** Ga 2p, **(B)** Ni 2p, **(C)** Fe 2p regions for $Ga_{20}Ni_{80}O_x$ and the **(D)** Al 2p and Ni 3p, **(E)** Ni 2p and **(F)** Fe 2p regions for $Al_{20}Ni_{80}O_x$. Data is shown for unused electrodes and electrodes used for electrochemical testing, both before and after Argon sputtering for 600 seconds.

3.2.3 Near-Infrared Spectroscopy

Synchrotron-based studies have been indispensable in revealing the bonding structure for disordered metal (oxy)hydroxides such as those studied here,[131,190–193] but limited accessibility to suitable facilities inhibits research progress. Such studies have consistently indicated that nickel (oxy)hydroxide materials possess a defective layered structure comprised exclusively of bis-μ-(hydr)oxo Ni−M motifs, even after incorporation of secondary transition metal ions. This consistency makes $M_yNi_{100-y}O_x$ an effective family on which to test alternative characterization techniques. Transition metal ions in an octahedral environment experience a splitting of d orbitals to yield a t_{2g}-e_g electron configuration, but a trigonal distortion of the nickel coordination environment is known for both well-crystallized β-$Ni(OH)_2$ and disordered Fe−Ni oxyhydroxide.[37,121] The resultant D_{3d} symmetry of Ni(II) coordination environments has d^8 electronic configuration and it is expected to split the triply degenerate t_{2g} orbitals into a nondegenerate orbital, a_{1g}, and a doubly degenerate set of orbitals, e_g. Two e_g orbitals will be separated as antibonding(e_g^*) and bonding (e_g) orbitals **(Figure 3.7)**. According to the electronic configuration of Ni(II) a_{1g} and e_g orbitals are expected to be fully occupied and e_g^* orbitals will be partially occupied. When in oxidized form, Ni(IV) has d^6 electronic configuration, it is expected that the e_g antibonding orbitals will be unoccupied. The NIR spectra of all $M_yNi_{100-y}O_x$ films exhibit a broad absorbance band at approximately 9000 cm^{-1} and a sharp band at approximately 6000 cm^{-1} when in the reduced state (**Figure 3.7A** and **Figure A.1**).

Upon electrochemical oxidation, the high-energy feature splits into two well-resolved bands and the low-energy band experiences a red shift and grows in relative intensity (**Figure 3.7B**). We assign the high-energy bands to the two distinct d−d transitions expected for the D_{3d} coordination environment (**Figure 3.7C**).

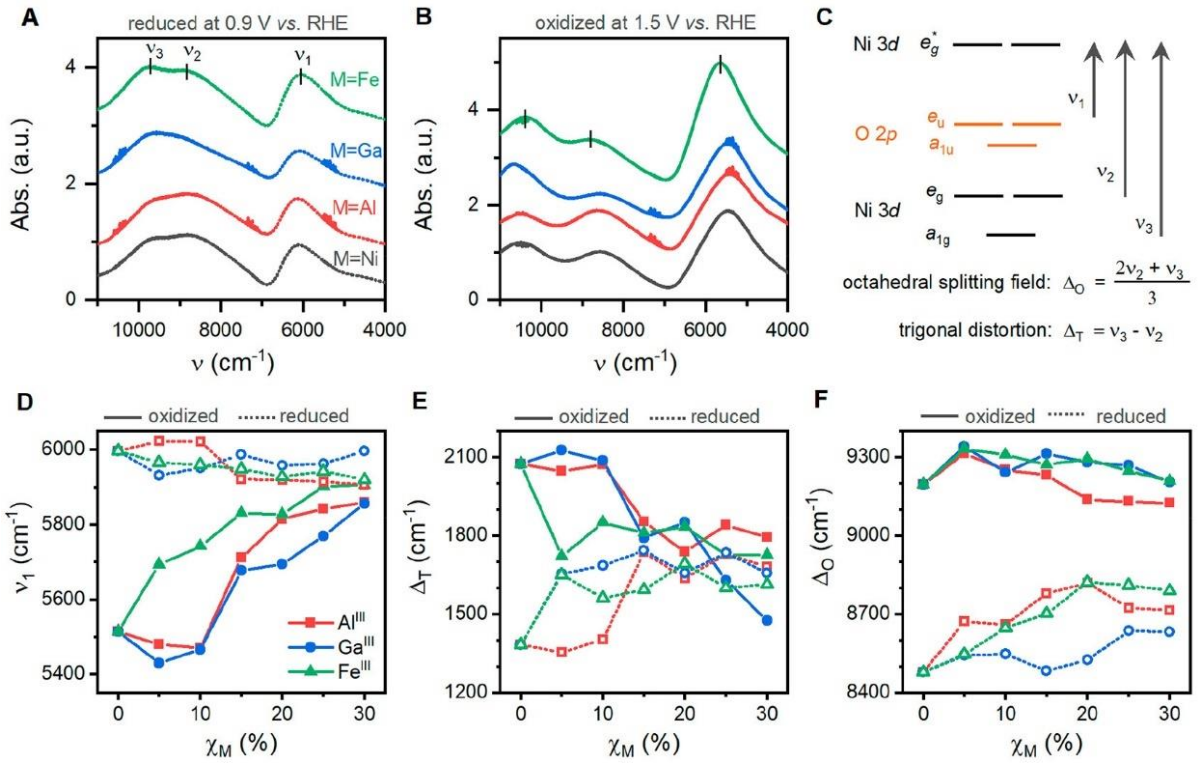

Figure 3.7 Near-infrared spectra of $M_{10}Ni_{90}O_x$. Spectra for **(A)** the electrochemically reduced and **(B)** the electrochemically oxidized phases for M being Fe, Ga, Al, and Ni. **(C)** Proposed electronic structure and assignments for absorbance processes are employed to track **(D)** the location of the low-energy absorbance, **(E)** the splitting due to trigonal distortion, and **(F)** the octahedral splitting field as a function of relative stoichiometry for each composition series.

A broad absorbance band between 6000 and 7800 cm^{-1} was previously assigned as a second harmonic of the fundamental O−H vibration in nickel-containing layered double hydroxides.[194,195] The low energy feature is orders of magnitude more intense than the O−H vibrations in the materials studied here and exhibits a dependency on nickel oxidation state (**Figure 3.8**), however, ruling out the assignment as a vibrational overtone.

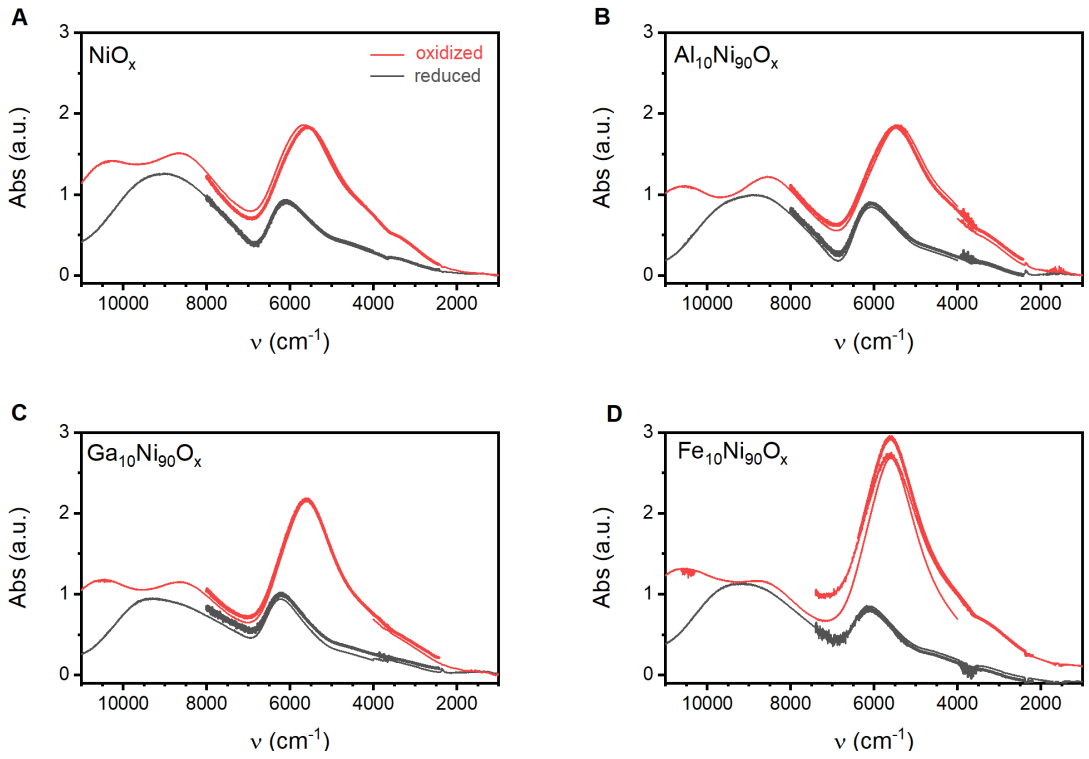

Figure 3.8 Comparison of absorbance bands in the mid-infrared and near-infrared regions for **(A)** NiO_x, **(B)** $Al_{10}Ni_{90}O_x$, **(C)** $Ga_{10}Ni_{90}O_x$, and **(D)** $Fe_{10}Ni_{90}O_x$. Data was acquired on an FTIR spectrometer using combinations of an infrared light or white light source with an InGaAs near-infrared detector or a DTGS mid infrared detector. Bolded lines are datasets acquired with a white light source and DTGS detector.

3.2.4 Density Functional Theory Calculations

Calculations were performed with plane-wave-based density functional theory (DFT) in the Quantum ESPRESSO package.[157] The precatalytic process was shown to be a Ni(IV) to Ni(II) transition for materials related to those studied here.[121] Structural models were therefore chosen as $[Ni_9(OH)_{18}]$and $[Ni_9O_{18}]$ for the pure nickel composition and $[M_1Ni_8O(OH)_{17}]$ and $[M_1Ni_8O_{18}]^-$ for the Al(III), Ga(III), and Fe(III) containing materials. Relaxations of periodic slabs were initiated using a single 2-dimensional sheet of β-$Ni(OH)_2$ containing nine cations and 15 Å of vacuum between layers. Projector augmented wave pseudo-potentials with PBE exchange-

correlated functionals were used with planewave cutoff values of 50 and 500 Ry. A 10 × 10 × 1 Monkhorst−Pack grid was employed, with Hubbard-U terms fixed at 6.6 eV for Ni and 3.5 eV for Fe to maintain consistency with past reports. The in-plane unit cell dimension was systematically increased relative to β-NiOOH to model tensile strain on the oxidized phases or decreased relative to β-$Ni(OH)_2$ to introduce compressive strain on the reduced phases. Each series of calculations involved 8 distinct calculations with a fixed unit cell, from 0 to 7% strain, and one with a variable unit cell. The computationally predicted R_{Ni-M} distances are slightly larger than experimentally measured values for the reduced phase and smaller for the oxidized phase. We therefore limit ourselves to a qualitative analysis of trends as rigorously accurate structural models are impossible for the disordered material being studied here.

Projected density of states (PDOS; **Figure 3.9 and Figure A.2-4**) plots from DFT calculations on both the reduced and the oxidized states show orbitals with Ni d_z^2 character to be lowest in energy. Orbitals with character of the remaining Ni d orbitals are split into two degenerate sets: an e_g located slightly above the d_z^2 orbitals and an e_g^* above the Fermi level (**Figure 3.9**). Orbitals with O 2p character are located between the e_g and the e_g^* orbitals. These calculations lead us to tentatively assign ν_1 as a charge transfer process. The consistency with past reports for β-$Ni(OH)_2$,[44] the molecular orbital ordering indicated by DFT models, and recent reports detailing the splitting of nickel d orbitals in $LaNiO_3$ by biaxial strain[175] bolster confidence in these assignments. The nickel d−d transitions in the NIR region, therefore, confirm a trigonal distortion of nickel coordination environments in all samples. Comparison of the composition-dependent trends in the NIR spectra with DFT-generated models provides insight into the influence of Al, Ga, and Fe on the bonding framework and electronic structure of the host $Ni(OH)_x$ material. The location of ν_1 shows the location of orbitals with oxygen 2p character relative to Ni-based e_g^* orbitals as a function of material composition (**Figure 3.7B**), the spacing between ν_2 and ν_3 approximates the magnitude of d-orbital splitting due to the trigonal distortion (**Δ_T; Figure 3.7C**), and the weighted average of ν_2 and ν_3 yields the octahedral splitting field (**Δo; Figure 3.7C**). In

the reduced state, v_1 decreases slightly while Δ_T and Δ_O increase with M content for each composition series; in the oxidized state, v_1 increases, Δ_T decreases, and Δ_O slightly decreases.

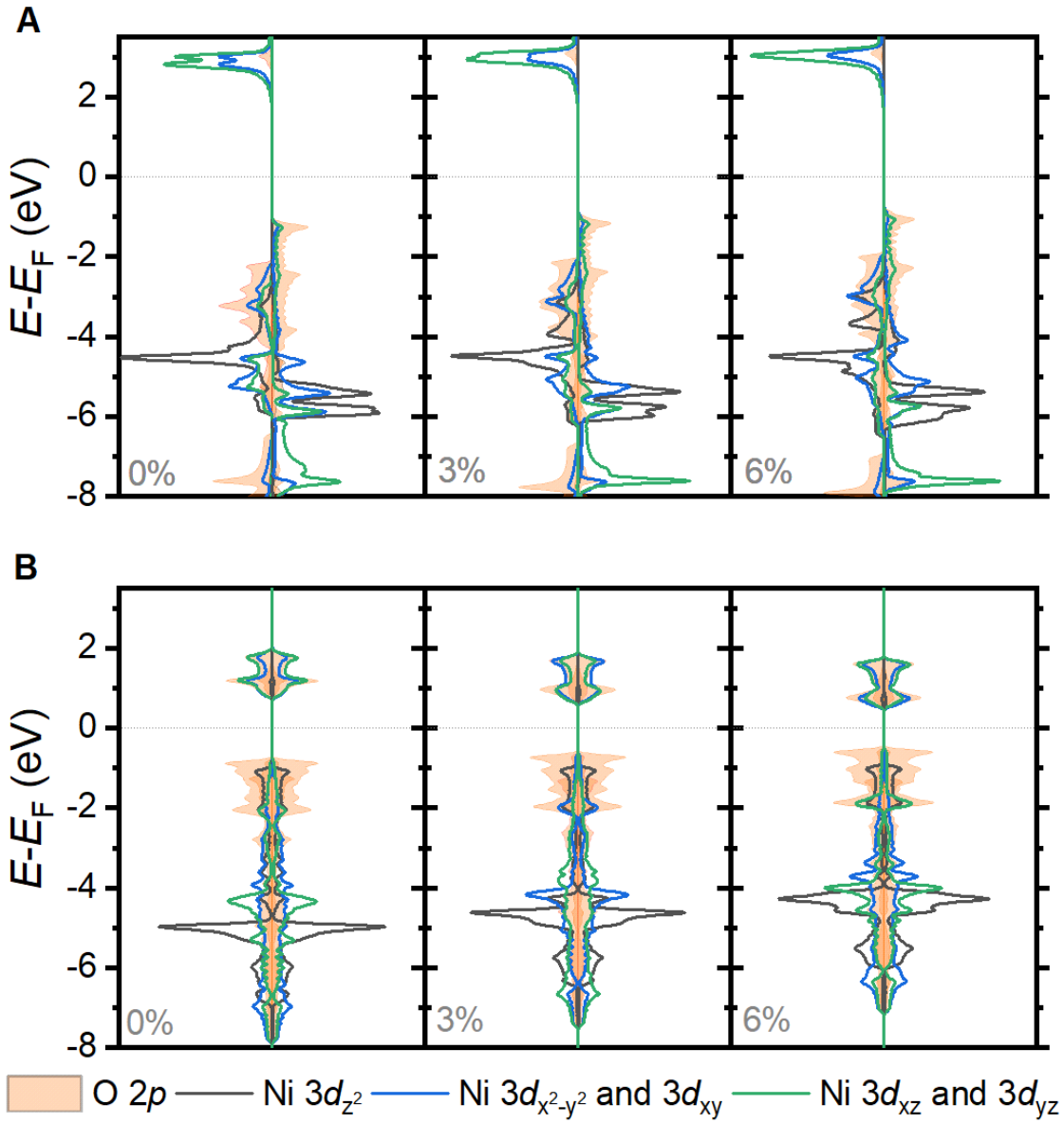

Figure 3.9 The influence of strain on the projected density of states for nickel oxyhydroxide. PDOS are shown for 0, 3, and 6% **(A)** compressive strain on the reduced phase and **(B)** tensile strain on the oxidized phase.

By defining and varying the unit cell size, DFT calculations provide insight into the effects of compressive or tensile lattice strain on the electronic structure of the reduced and oxidized forms of nickel hydroxide, respectively. These calculations indicate that tensile strain on the oxidized state destabilizes the a_{1g} orbitals and stabilizes the e_g* orbitals (**Figure 3.9B**). In contrast, compressive strain on the reduced state has little effect on the a_{1g} orbitals and slightly destabilizes the e_g and e_g* orbitals (**Figure 3.9A**). Agreement between the computationally predicted trends and the experimentally observed ones support the assertion that the incorporation of suitably sized cations into the $Ni(OH)_2$ lattice influences the electronic structure by modulating geometric strain. Reaction coordinate diagrams generated from the above DFT calculations provide a microscopic description for the observed changes in the electrochemical behavior.

The Butler− Volmer approach to analyzing electron transfer kinetics positions potential energy surfaces (PES) for the oxidized and reduced phases on a suitable reaction coordinate. Application of a voltage changes the kinetic rate constants for the electron transfer reaction by stabilizing or destabilizing one PES curve relative to the other. Two parameters are required to mathematically describe electron transfer kinetics: the standard rate constant (k°) is defined by the activation energy at the standard reduction potential, and the transfer coefficient (α) is the magnitude of voltage-induced change to the cathodic rate constant relative to the applied overpotential. We generate PES diagrams for the oxidized and reduced states by varying cell dimensions for the slab used in DFT calculations (**Figure 3.10A**).

The average Ni−M distance (R_{Ni-M}) in bis-μ-(hydr)oxo structural motifs within the slab is used as the reaction coordinate because the $Ni(OH)_2$ lattice is known to contract upon oxidation and expand upon reduction; the parabola arising from mathematical fits of the computed stabilities are shifted to position their minima at zero energy, as would be observed at the standard reduction potential. An additional PES that simulates the application of a 300 mV overpotential is also shown in **Figure 3.10A**.

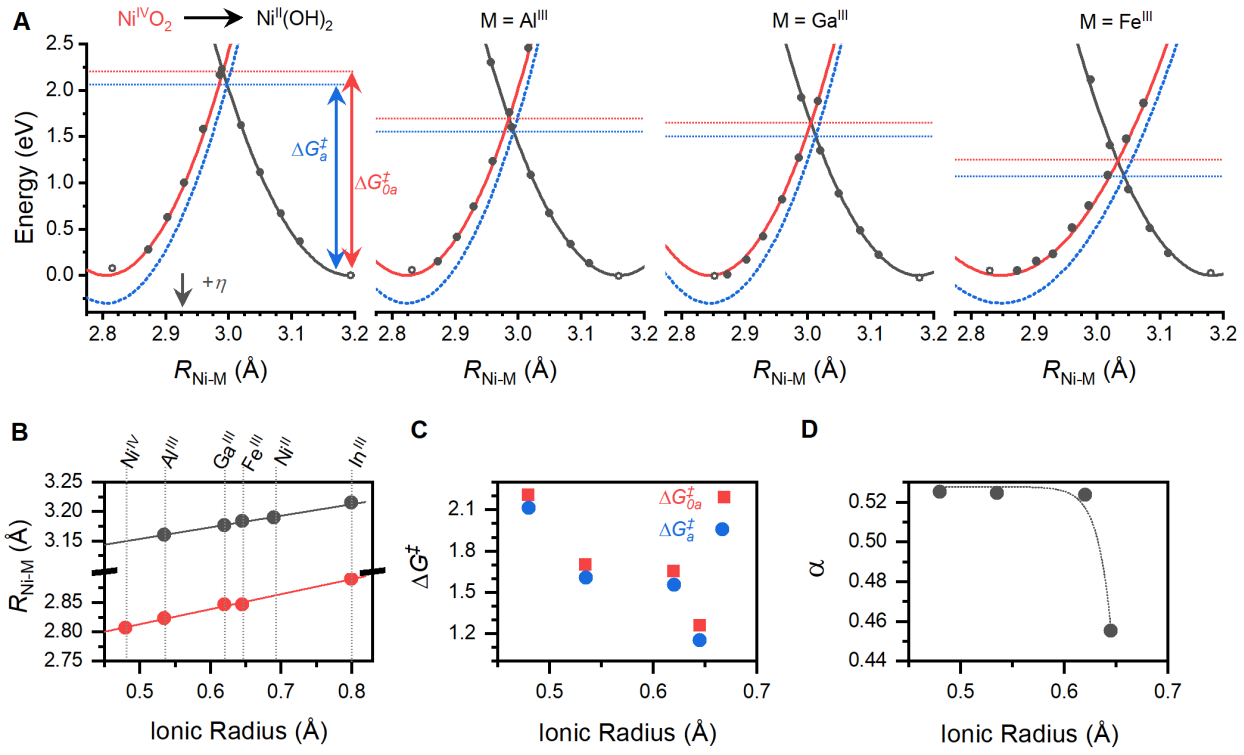

Figure 3.10 Reaction coordinate diagrams and parameters for electron transfer kinetics for M-containing nickel oxyhydroxide. **(A)** Potential energy surfaces as a function of the Ni-M distance in bis-μ-oxo Ni-M structural motifs for the reduced phase (red curves) and the oxidized phase at overpotentials of 0 V (black curves) and 0.3 V (blue curves) for M being Ni (II/IV), Al (III), Ga(III), Fe (III). Variable-cell relaxation results are indicated by the hollow data point. **(B)** The energy minima from the potential energy surface parabola, **(C)** activation energies for electrochemical oxidation, and **(D)** the electrochemical transfer coefficient are given as a function of the effective bond length of the dopant metal.

These diagrams predict that $R_{Ni–M}$ is linearly correlated to the effective ionic radii of the additive metals in both the reduced and the oxidized phases **(Figure 3.10B)**. The ionic radius mismatch brings the PES curves closer together on the reaction coordinate, effectively inducing a decrease in activation energy for electron transfer **(Figure 3.10C)**. Repeating the computations with In(III) as a significantly larger dopant predicts that the lattice will expand for both the oxidized and the reduced states, inducing an increase in activation energy **(Figure 3.11)**.

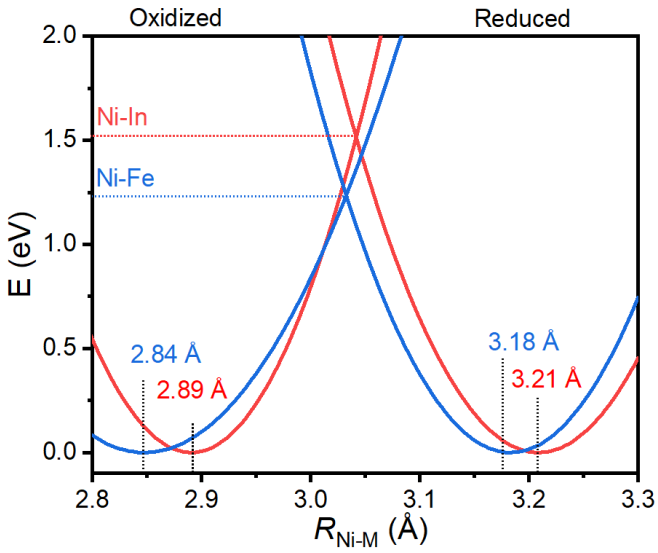

Figure 3.11 Reaction coordinate diagrams generated from DFT calculations on $[M_1Ni_8O(OH)_{17}]$ and $[M_1Ni_8O_{18}]^-$ slabs with M = Fe (III) (blue lines) and M = In (III) (red lines).

This computational model suggests that the decrease in activation energy is unique to dopants with an ionic radius between those of the oxidized and reduced forms of nickel. Attempts to experimentally confirm the prediction were impeded by an inability to synthesize a Ni−In composition series. The relative shape of the PES curves remains essentially unchanged for Al and Ga dopants, but the oxidized PES broadens substantially for Fe. This asymmetric change results in a decrease in α **(Figure 3.10D)**. Such a change would favor oxidation reactions by making changes that affect the anodic rate constant more significantly than the cathodic rate constant. This analysis predicts that the incorporation of ions with a radius between Ni(II) and Ni(IV) into a $Ni(OH)_2$ lattice will decrease the activation energy for electron transfer and decrease the electron transfer coefficient by asymmetrically distorting the PES once beyond a certain threshold.

3.2.5 Discussion

The agreement between trends in DFT models and experimental results suggest that the addition of selected cations, namely Al(III), Ga(III), and Fe(III), to a nickel hydroxide lattice can be

structurally modeled by limiting the extent to which the host nickel hydroxide lattice can expand and contract. A static Fe−O bond distance in $Fe_yNi_{100-y}O_x$ was previously shown to reside between that of Ni(II)−O and Ni(IV)− O at voltages up to 1.6 V vs RHE,[121] effectively distorting the structure by inhibiting the oxidative compression and reductive expansion of the host nickel hydroxide lattice. The DFT models generated here predict that the Ni−M distance and O−Ni−O bond angles in bis-μ-(hydr)oxo motifs are influenced by the effective ionic radius of the secondary metal ion **(Figure 3.10)**. The PDOS diagrams in **Figure 3.9** indicate that tensile strain in the oxidized state of $Ni(OH)_2$ would decrease both the octahedral splitting field (Δ_O) and the trigonal distortion (Δ_T); an increase in both parameters would arise from compressive strain in the reduced state. The NIR spectra show composition-dependent trends in both Δ_O and Δ_T that match this predicted behavior, suggesting that the additive metals increase internal strain within the $M_yNi_{100-y}O_x$ materials **(Figure 3.7)**.

The similarity in anodic shift rate for redox peaks in all composition series provides clear evidence that the precatalytic redox process is fundamentally decoupled from electrocatalysis. The consistency of anodic shift rate for all composition series in spite of variable electronegativity for each of the additive metals suggests that inductive effects or changes in Ni−O bond strength are not responsible for the behavioral change. The predicted linear relationship between effective ionic radii and average R_{Ni-M} in bis-μ-(hydr)oxo motifs shown in **Figure 3.10D** suggests that the overall strain present in the system may be the key consideration underlying this behavioral feature. It is well established that the oxidation of $Ni(OH)_2$ induces a reversible contraction in R_{Ni-M};[121,161,167,169,193] the models here predict a decrease in the magnitude of this contraction when secondary metals are incorporated. As the thermodynamics for an electron transfer reaction are based on the energetics of both the oxidized and the reduced states, we propose that the opposing strain present in the oxidized and reduced states is responsible for the anodic shift. Such an interpretation is supported by the observed shift of redox processes when shape-memory alloys have been used to apply compressive or tensile strain[176,177] and when elastomer substrates have been used to apply a gradient of tensile strain.[170] The assignment is also in line with past work on

metal alloys, where the d band of pseudomorphic monolayers has been shown to be destabilized by tensile strain and stabilized by compressive strain.[172,173] This strain-induced effect has been shown to shift electrochemical redox processes cathodically when compressive strain is applied and anodically when tensile strain is applied.[174]

The results here suggest that the precatalytic process is highly dependent on the total strain within the material, while the catalytic process either is decoupled from strain or presents a nonlinear correlation that cannot be discerned from the present data set. A decrease in the Tafel slope is the primary catalytic change observed following incorporation of Fe into nickel hydroxide. Experimentally observed Tafel slopes are a function of reaction mechanism and identity of the rate limiting step:[19,196] rate-limiting steps involving electron transfer present a Tafel slope that is scaled by α for that reaction, chemical steps present as constant slopes, [19,196] and pushing the rate-limiting step later in a catalytic cycle results in a decreased Tafel slope (in mV dec^{-1}). The stepwise change observed for the Fe−Ni composition series implies either a shifting of the rate-limiting step later in the catalytic cycle or a change in dominant reaction mechanism. The gradual change in the Tafel slope following incorporation of Ga or Al suggests that the rate-limiting step for OER in these samples is an electron transfer step rather than a chemical reaction. The assumption that the trends in our computational model apply to catalytically relevant sites leads to the conclusion that

(i) there is a threshold of strain to trigger the behavior observed in the Fe−Ni case, which is alluded to by the PES distortions captured in **Figure 3.10**,

(ii) the d orbitals in Fe enable a synergistic combination of geometric strain and bonding effects in the Fe−Ni series, or

(iii) a secondary reaction mechanism such as the electrochemical oxidation of Fe(III) to higher oxidation states becomes dominant.[93,161]

We note that previous systematic studies on cation dopants such as Ti, Mn, and Co into nickel hydroxide lattices have not revealed any correlations in precatalytic behavior with comparable Fe−Ni compositions.[158,197] The correlations reported here for Al−Ni, Ga−Ni, and Fe−Ni thus confirm the need for the selection criteria discussed earlier to study the type of internalized

geometric lattice strain analyzed here. These criteria provide an unfortunate limit on the number of elements suitable for use in replicating the catalytic properties of the Fe−Ni materials through simple compositional tuning. The development of tunable substrate-based approaches, such as those based on shape-memory alloys,[176,177] may provide a means to overcome this limitation.

3.3 Conclusion

We studied binary Al−Ni, Ga−Ni, and Fe−Ni hydroxides to explore the role of internalized geometric strain on electrocatalytic water oxidation by nickel hydroxide-based materials. The Al−Ni and Ga−Ni series replicate the well-documented composition-dependent anodic shift of the precatalytic redox process for the Fe−Ni series but did not significantly influence electrocatalytic water oxidation. Near infrared spectroscopy and DFT models provide evidence that asymmetric distortions in the oxidized and reduced states can be achieved by the incorporation of cations with a suitable ionic radius into a nickel-based lattice. The computational models indicate that all three composition series shift the potential energy surfaces to decrease the activation energy barrier for oxidation of nickel sites but that only Fe significantly alters the electrochemical transfer coefficient that would manifest as lower Tafel slopes. We attribute the composition-dependent anodic shift of precatalytic redox processes in nickel hydroxide materials to asymmetric strain in the oxidized and reduced states of the nickel hydroxide lattice. Failure to emulate the electrocatalytic performance of Fe−Ni hydroxides using other compositions suggests that geometric strain is not solely responsible for improved catalysis.

3.4 Experimental

3.4.1 Materials and Sample Preparation

Nickel(II) 2-ethylhexanoate (78% in 2-ethylhexanoic acid, Strem Chemicals Inc.), iron 2-ethylhexanoate (6% solution in mineral spirits, Strem Chemicals Inc.), aluminum(III) 2,4pentanedionate (Alfa Aesar), gallium(III) acetylacetonate (99.99%, Sigma-Aldrich), indium(III) acetylacetonate (98%, Alfa Aesar), and indium(III) acetate (099.99%, Alfa Aesar)

were used as received. Fluorine-doped tin oxide glass (FTO; TEC-7 grade, Hartford Glass) was cleaned immediately prior to use by sequential ultrasonication in a detergent solution, milli-Q H_2O, and then isopropanol. The surface was dried under a stream of N_2 and placed in a custom UV irradiation chamber (GHO18T5VH lamp, Atlantic Ultraviolet) for 15 min. Aqueous 1 M KOH solutions were prepared using milli-Q H_2O and reagent grade KOH (>85%, Sigma-Aldrich). Iron impurities were removed from these electrolyte solutions by aging over $Ni(OH)_2$, as previously described.[36] Catalyst films were fabricated by dissolving precursor complexes in ethanol with the relevant stoichiometry and a total metal concentration of 0.3 M. The solutions were spin coated (Laurell WS-650 mz-2nNPP model) onto freshly cleaned FTO and placed in a UV-irradiation chamber (Atlantic Ultraviolet G18T5) for 24 h.[121,125] Attempts to synthesize nickel−indium compositions were unsuccessful due to the insolubility of indium compounds in solvents suitable for spin coating precursor films.

3.4.2 Electrochemical Experiments

All experiments were carried out with 1 M KOH electrolyte solutions in a single-compartment polyethylene cell. A Biologic SP-300 was used in conjunction with a Gaskatel HydroFlex reversible hydrogen electrode (RHE) as the reference electrode, a platinum mesh as the counter electrode, and catalyst-coated FTO as working electrodes. Cyclic voltammetry experiments consisted of 5 cycles between 0.9 and 1.7 V vs RHE at a rate of 1 mV s^{-1}. Reproducible voltammograms were obtained after 2 or 3 cycles; data shown represents the stabilized behavior. Electron transfer kinetics were measured by a chronoamperometry experiments in both the anodic and the cathodic directions. The voltage was stepped from 0.9 to 1.7 V vs RHE in 10 mV, 60 s steps. The current density at the end of each step was taken as the steady-state catalytic current. Cell resistances were measured by impedance spectroscopy prior to electrochemical experiments with values on the order of 15 Ohms measured for all samples.

3.4.3 X-ray Photoelectron Spectroscopy

Measurements were performed on a Thermo-VG Scientific ESCALab 250 microprobe using a magnesium X-ray source. Survey scans were performed using a pass energy of 50 eV and high-resolution scans with 30 eV. All measurements were performed on films deposited on FTO glass with a small strip of conductive carbon tape to make electrical contact. Films that were employed for electrochemical experiments were thoroughly rinsed with Milli-Q H2O and allowed to air dry before loading into the sample chamber. Argon sputtering was performed for a period of 600 s. Quantification was performed on the high-resolution scans using CasaXPS and the following relative scaling factors (r.s.f.). The 20% Ga sample was analyzed using the Ni 2p (r.s.f. = 13.92 and 7.18 for $2p_{3/2}$ and $2p_{1/2}$) and Ga 2p (20.47 and 10.56 for $2p_{3/2}$ and $2p_{1/2}$) regions. Overlap of Al- and Ni-based photoelectrons in the 20% Al required deconvolution of the Al 2p (0.5735) and Ni 3p (1.36 and 0.701 for $3p_{3/2}$ and $3p_{1/2}$) features. The area of the Ni $3p_{1/2}$ component was constrained to be one-half that of the Ni $3p_{3/2}$ component during deconvolution. Argon sputtering of 20% Al sample that was electrochemically conditioned induced a change in speciation of the nickel within the film (**Figure 3.6**), necessitating the use of four peaks to describe the Ni 3p component. Spectra were calibrated by shifting the adventitious carbon 1s peak to 285.0 eV.

3.4.4 Near-Infrared Spectroscopy

Near-infrared region measurements were performed on a Nicolet 6700 FTIR equipped with a Pike Technologies VeeMAX III variable-angle reflection accessory. An InGaAs detector and a white light source were used to acquire near-infrared spectra on all samples. Spectra from 4000 to 800 cm^{-1} were recorded on a subset of samples using a DTGS detector with an infrared light source. Spectra were acquired from 8000 to 2500 cm^{-1} on this subset samples with a white light source and DTGS detector to ensure the accurate comparison between the mid-and near-infrared regions.

Chapter 4

Identification of Diverse Iron Coordination Environments in Nickel Hydroxide Lattices

4.1 Introduction

It is remarkable that iron-doped nickel hydroxide shows exceptional performance towards the oxygen evolution reaction (OER) regardless of how the solid-state material is synthesized. Electrocatalysts such as rutile IrO_2, the perovskite $LaNiO_3$, and the spinel Co_3O_4 all show substantial changes in electrocatalytic performance when fabrication protocols are adjusted.[198–200] The inclusion of iron ions into $Ni(OH)_2$ consistently shows a dramatic decrease in Tafel slope that yields a benchmark-setting catalyst regardless of fabrication protocols – even simple physical mixing of FeOOH with $Ni(OH)_2$ yields exceptional behavior.[201,202] The two-dimensional bonding structure within this family of materials poses a limitation to the quality of structural analysis that can take place, particularly considering that disordered forms are the preferred phase. XRD is frequently used to identify the phase and measure spacing between individual sheets, EXAFS has become a critical technique for analyzing changes in structure both operando and ex-situ, and Raman spectroscopy has served to track changes in nickel-oxygen bonds. Each of these techniques, however, produces a small number of measurable signals to enable analysis of nuanced structure changes: Bragg peaks rapidly broaden and shrink as iron-content increases and ions migrate into the interlayer region, EXAFS results frequently only provide two easily resolved coordination shells, and Raman spectra similarly produce two peaks in the low frequency region. With the

resilience of fundamental electrochemical behavior of this family of materials and the limitations in structural analysis that can be performed, it is not surprising that multiple proposals have been made to describe the electrocatalytic behavior. Such proposals for iron ions include that they activate electrocatalysis by replacing nickel cations at edge[203,204] or corner sites,[164,205] work with nickel to establish a binuclear reaction site for OER,[206] serve as a direct reaction site for OER,[161,207] as supported by observation of tetravalent[164,166] or hexavalent iron centers,[93] during OER, force deprotonation of the nickel hydroxide lattice and promote formation of metal-oxo species,[62,208] or induce lattice distortions that activate nickel ions for catalysis.[121,209] Considering the breadth of results, the possible existence of catalytically relevant coordination environments that have not been directly observed is a consideration that should be explored.

Significant global efforts to develop improved catalysts in recent years have shown *in-operando* structural changes and revealed that coordination environments other than those within the 2-dimensional bonding framework of $Ni(OH)_2$ are viable.[15] The electrochemical stability and catalytic activity of LDH materials is controlled by exsolution and redeposition mechanisms, where the stability of individual ions in specific coordination sites has been probed by analysis of surface coverage and adsorption energies.[210] It is well established that ferric ions are rapidly incorporated into LDH materials by simple exposure.[160,197] These ions have been shown to accumulate at the periphery of nickel(oxy)hydroxide.[203] Long-term tests have also shown that the iron ions experience a continual dissolution and redeposition process–essentially an equilibrium that is subject to the concepts of self-repair and self-healing in electrocatalysts.[211] The concept of amorphization has become prominent in the literature,[185,186,184,212–217] and the resulting increase in grain boundaries or edge sites has been suggested to be important.[218] Parallel studies have identified non-traditional coordination sites in nominally LDH materials, including iron ions situated outside of the 2-dimensional framework in $Co(OH)_2$,[131] iron ions on terrace sites of γ-NiOOH,[113] and iridium ions anchored to the basal plane of $Ni(OH)_2$.[80] Changes in behavior have also been achieved by mixing of nickel hydroxide and iron oxyhydroxide,[113] inclusion or exchange of anions between the LDH layers,[92,219,220] and through combination of anion exchange with

immobilization of single Pt atoms.[81] The diversity of possibilities motivated us to explore variations in fabrication protocols as a means to study small changes in composition-dependent structure in an effort to identify non-traditional coordination environments in nickel-based layered double hydroxides.

Herein, we describe the structural analysis of two related families of iron-doped nickel hydroxide and identify a secondary iron coordination environment. Comparisons of Mössbauer and Raman spectra for the two series of samples provide direct evidence for the co-existence of two distinct iron centers in samples fabricated by conventional alkaline precipitation. Both XRD and EXAFS results show similar structural features as frequently reported, but close analysis reveals that the composition-dependent changes in structural parameters are inhibited at compositions where this second coordination environment exists. Correlations of structural parameters to electrochemical behavior suggest that changes in lattice strain are responsible for the anodic shifting of precatalytic redox peaks, and that the series of samples synthesized in the presence of formamide exhibits improved kinetics compared to traditionally synthesized samples.

4.2 Results

4.2.1 Sample Preparation

Two analogous layered double hydroxide composition series were fabricated using variations of a pH precipitation protocol. Conventional aqueous pH precipitation was carried out by dissolving appropriate amounts of ferric chloride and nickel chloride in Milli-Q® water to obtain a total metal ion concentration of 0.35 M with the desired stoichiometry to obtain $Fe_xNi_{1-x}(OH)_2$, where *x* was varied from 0 to 0.214. A 1 M aqueous NaOH solution was added dropwise to the solution while stirring under N_2 environment until a pH of 12 was reached. Stirring was maintained for 10 additional minutes before the solid product was collected by centrifugation. The solid was washed twice by suspending in 10 mL aliquots of water, three times in 10 mL aliquots of acetone, then dried overnight at 75 °C to remove residual bulk solvent. The fabrication protocol was modified for the second sample series by addition of formamide to the reaction solution, which has

previously been reported to produce single-layered "nanosheets."[101] An identical protocol was employed for this sample series as the aqueous samples, with the exception that the precursor solutions were prepared in aqueous solutions containing 30% v/v formamide. Electron microscopy indicates that samples synthesized in the presence of formamide continue to show a stacked structure, rather than individual nanosheets **(Figure B.1).** The two composition series are referred to here as the water series and the formamide series.

4.2.2 Mössbauer Spectroscopy

Zero field ^{57}Fe Mössbauer spectroscopy reveals two unique iron coordination environments in the iron-doped nickel hydroxide samples. A large paramagnetic doublet is present in all compositions from both sample series (**Figure 4.1A** and **Figure 4.1B**). This primary feature is associated with a coordination environment that will be referred to as $\mathbf{Fe_A}$. The spectroscopic feature for $\mathbf{Fe_A}$ exhibits an isomer shift (δ) of *ca.* 0.34 mm s^{-1} and quadrupole splitting (Δ) values between 0.41-0.48 mm s^{-1} for all samples (**Figure 4.1C** and **Figure 4.1D**). These values are consistent with those previously reported for Fe ions residing on Ni sites within the $Ni(OH)_2$ lattice.[44] The consistency of Δ and δ across compositions for both fabrication protocols indicates successful substitution of Ni with Fe ions. A second paramagnetic doublet appears in spectra acquired on samples synthesized in aqueous conditions (**Figure 4.1A**). Labeled $\mathbf{Fe_B}$, this feature is most easily observed at low Fe content, while above 15.3% Fe, stronger superposition of both contributions hinders precise evaluation of the $\mathbf{Fe_B}$ subspectrum. Curve fits restricted only in the width of the $\mathbf{Fe_B}$ peaks, however, suggest that $\mathbf{Fe_B}$ spectral area remains relatively constant at 14% (**Figure 4.1E**).

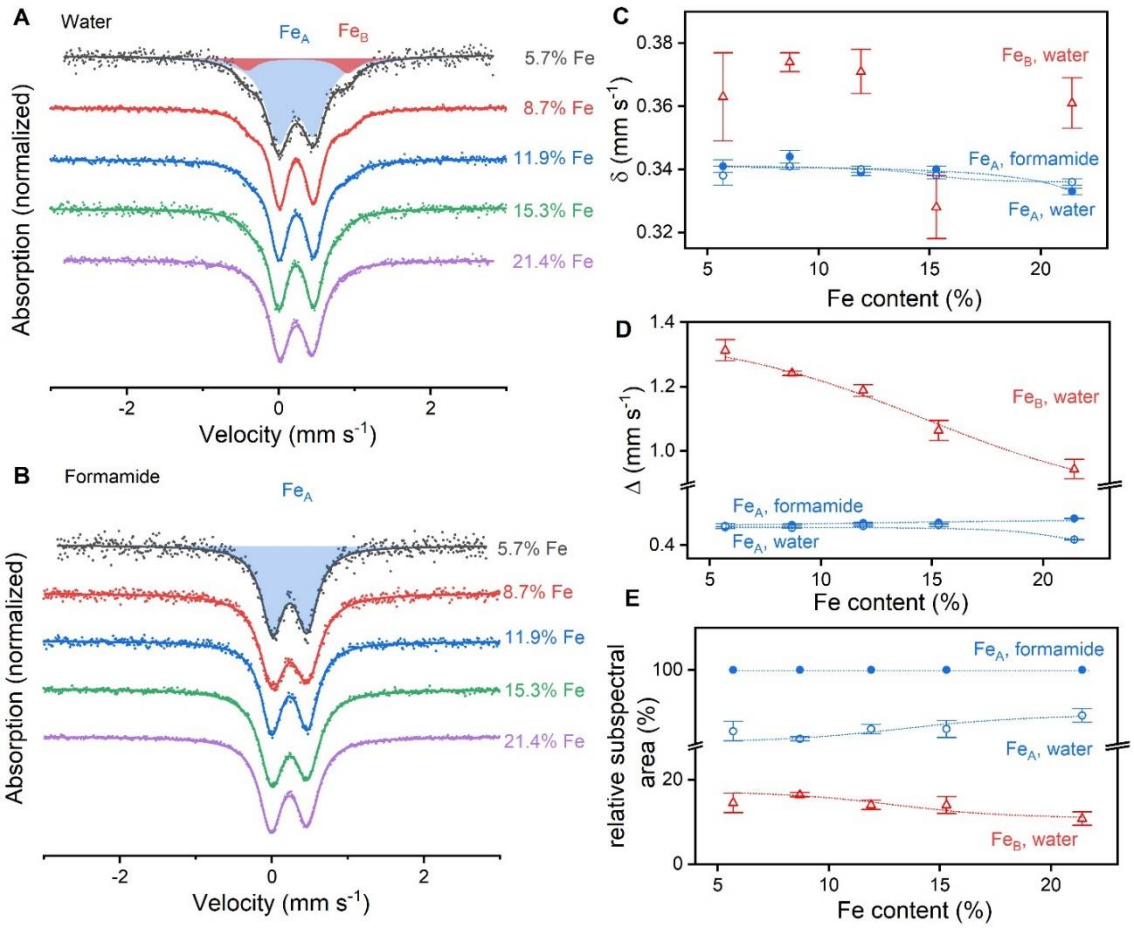

Figure 4.1 Zero-field ^{57}Fe Mössbauer spectroscopy for two $Fe_xNi_{1-x}(OH)_2$ composition series. Spectra for samples synthesized by **(A)** aqueous co-precipitation in 1M NaOH solutions and **(B)** 1 M NaOH containing 30% v/v formamide. **(C)** Isomer shift and **(D)** quadrupole splitting values obtained through curve fitting as a function of Fe-content. **(E)** Relative subspectral areas of Fe_A and Fe_B coordination environments.

The δ values for **Fe$_B$** are relatively constant near 0.36 mm s^{-1} (**Figure 4.1C**). Isomer shifts for both **Fe$_A$** and **Fe$_B$** are consistent with values expected for high spin Fe(III) ions.[44,164] A change in isomer shift is generally associated with a change in covalency between Fe ions and its first coordination shell.[221–223] The δ value and lack of an observed trend in isomer shift suggest that iron ions remain trivalent across the sample series. Quadrupole splitting values, which are affected by the strength

of electric field gradient at the Fe nuclei and distortions in iron coordination environments, decrease from 1.31 mm s^{-1} to 0.94 mm s^{-1} as the iron content increases (**Figure 4.1D**). The substantial increase in splitting compared to $\mathbf{Fe_A}$ indicates that the coordination environment for $\mathbf{Fe_B}$ is initially substantially different than that for $\mathbf{Fe_A}$, but the two environments become more similar at high Fe-content.

4.2.3 Raman Spectroscopy

Similarities are observed in features assigned as M-O and O-H vibrational modes for both sample series. Factor group analysis predicts $2A_{1g}$ and $2E_g$ vibrational modes for β-$Ni(OH)_2$, but one E_g is commonly not observed (**Figure 2.5**).[150,224,225] These modes tend to be preserved following disruption of the interlayer stacking to yield α–$Ni(OH)_2$.[37] Here, the Fe-free samples exhibit the expected peaks near 300 (E_g), 445 (A_{1g}) and 3580 (A_{1g}) cm^{-1} under both synthetic conditions (**Figure 4.2A**). The mode near 300 cm^{-1} involves anti-symmetric tilting of oxygen atoms on the top and bottom of each LDH layer.[150] The peak experiences a *ca*. 22 cm^{-1} red shift in both sample series as Fe-content increases (**Figure 4.2B**). A more rapid shift is observed for the formamide series, but both series ultimately attain the same value. The mode near 445 cm^{-1}, assigned as M-O stretching along the crystalline c-axis,[226] undergoes a *ca*. 11 cm^{-1} blue shift as Fe-content increases. Increasing the Fe-content induces a decrease in intensity of the major A_{1g} O-H stretching vibration at 3580 cm^{-1}, suggesting deprotonation within the lattice to accommodate the change in positive charge.[37,227] Both sample series contain a sharp peak at 3680 cm^{-1} that behaves in a similar fashion. This feature has been associated with the antisymmetric A_{2u} O-H stretching vibration.[228] This vibration is not expected to be Raman active but is commonly seen in samples with stacking disorder.[37,229–231] An additional sharp peak is observed at 3601 cm^{-1} for the water series, and a broad one at *ca*. 3650 cm^{-1} for the formamide series. These features are consistent with stretching of surface hydroxide motifs,[37,232] an assignment that is supported by two O-H stretching vibrations observed in FTIR spectroscopy (**Figure 4.3**).

New peaks that behave in a composition- and fabrication-dependent manner emerge in the low frequency region of the spectra upon incorporation of iron. A peak at *ca*. 520 cm^{-1} appears immediately upon addition of Fe to both sample series (**Figure 4.2A**). This peak's intensity increases with Fe-content to rapidly become the strongest peak in the spectra. Peak growth is paired with a *ca.* 10 cm^{-1} blue shift for both sample series. This peak's prevalence in all Fe-containing samples, and its dependence on Fe-content, suggests that it is associated with the $\mathbf{Fe_A}$ feature seen in the Mössbauer spectra. A peak reported at *ca*. 508 cm^{-1} in disordered α-$Ni(OH)_2$ has been used to probe disorder within crystalline $Ni(OH)_2$.[37,150] The intensity observed in such studies, however, is considerably lower than that observed here. A significant peak has been reported to emerge at *ca*. 510 cm^{-1} following substitution of Ni(II) with trivalent ions,[62] which was proposed to be caused by deprotonation splitting the A_{1g} vibration into Ni-OH and Ni-O vibrations. This latter explanation is consistent with the data here, where the intensity of the *ca*. 510 cm^{-1} peak increases as the intensity of O-H stretching vibrations decrease. The emergence and growth of this peak is therefore assigned to a deprotonation of hydroxide groups caused by charge imbalance from $\mathbf{Fe_A}$.

The aqueous sample series contains a peak in the M-O region that is never observed in the formamide samples. The Raman peak red shifts from 601.0 cm^{-1} at 0.5% Fe to 586.6 cm^{-1} at 15.3% Fe at a rate of 1 cm^{-1} per percent iron, then becomes indistinguishable at higher Fe-content (**Figure 4.2C**). The appearance and disappearance of this feature at the same compositions as for $\mathbf{Fe_B}$ in the Mössbauer spectra supports the co-existence of two unique Fe coordination environments in the aqueous sample series and suggests that the two spectroscopic features are linked.

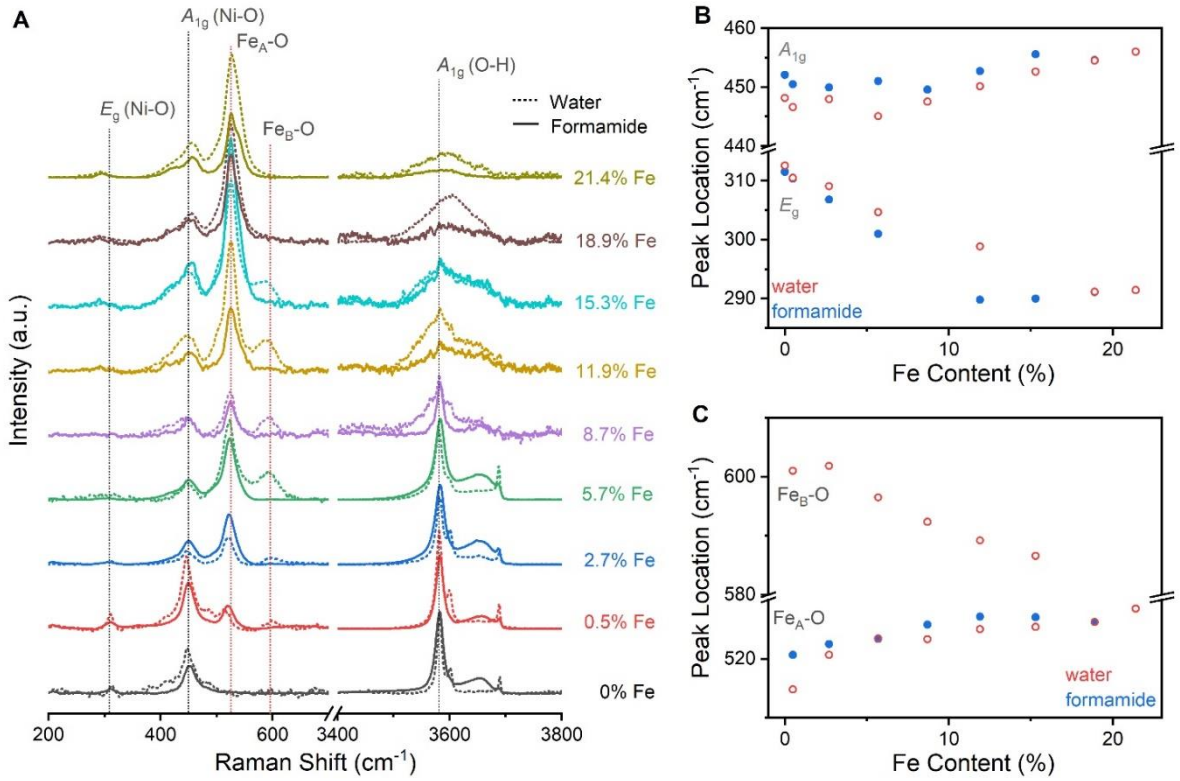

Figure 4.2 Raman spectroscopy for two $Fe_xNi_{1-x}(OH)_2$ composition series. Raman spectra acquired on **(A)** the water series (dotted lines) and the formamide series (solid lines). **(B)** Iron-induced changes in frequency of Raman vibrations for M-O vibrational modes that are present in the absence of Fe, and **(C)** M-O vibrational modes that emerge upon incorporation of Fe.

4.2.4 FTIR Spectroscopy

Infrared spectra confirm that Fe-incorporation induces deprotonation of the $Ni(OH)_2$ lattice and suggest that formamide may be bound to transition metal centers. Spectra acquired on both the water series and the formamide series contain (**Figure 4.3A**): (i) an O-H stretching mode at 3643 cm^{-1},[37] (ii) a stretching mode for O-H groups hydrogen-bonded to water at 3480 cm^{-1},[233] (iii) a bending mode for intercalated H_2O at 1630 cm^{-1},[224] and (iv) a stretching mode for intercalated carbonate ions between 1360-1380 cm^{-1}.[234]

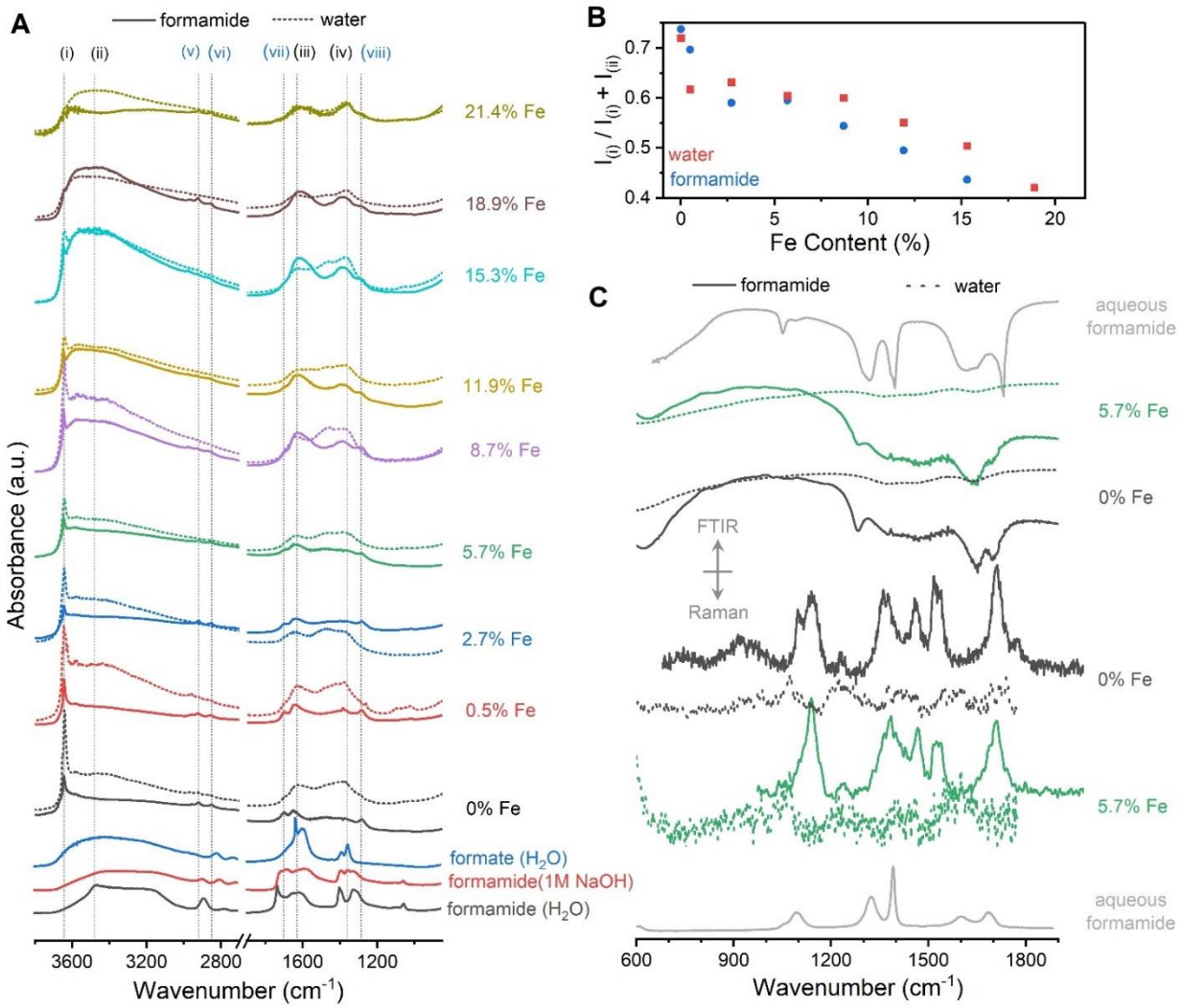

Figure 4.3. Infrared spectroscopy for two $Fe_xNi_{1-x}(OH)_2$ composition series. **(A)** FTIR spectra acquired for the water series (dotted lines) and formamide series (solid lines) with spectra for reference compounds above. **(B)** Intensity ratio of hydroxide vibrations that suggest Fe-induced deprotonation. **(C)** Comparison of FTIR and Raman spectra of an aqueous formamide solution with spectra for 0% and 5.7% Fe samples synthesized using both approaches.

LDH phases are known to have sufficient affinity for carbonate ions to scavenge CO_2 from the atmosphere unless handled in controlled atmospheres.[92] The carbonate ions therefore likely originate from atmospheric CO_2. Peak (i) decreases as Fe-content increases (**Figure 4.3B**),

suggesting that the strong Lewis acidity and trivalent charge of the iron ions leads to deprotonation of hydroxide, consistent with past reports.[227] The formamide sample series shows additional peaks at (v) 2921, (vi) 2850, (vii) 1, and (viii) 1287 cm^{-1} (**Figure 4.3A**). Three reference spectra were acquired to assign these features (**Figure 4.3A**). Neutral aqueous solutions of formamide contain peaks at 2886, 2769, 2688, 1731, 1614, 1396, 1319, and 1051 cm^{-1}. Alkaline solutions of formamide shift the peaks to 2894, 2800, 2711, 1677, 1581, 1384, 1349, 1319, 1052, and 763 cm^{-1}. Sodium formate, which may form by hydrolysis of formamide, exists as a deprotonated carboxylate with peaks at 2817, 2730, 2657, 1633, 1596, 1384, 1351, and 769 cm^{-1}. The observation of peak (vii) in the samples confirms that molecules present contain a carbonyl species, precluding assignment to deprotonated formamide ions residing in the interlayer spacing. This carbonyl peak is not perfectly matched with formamide or formate solutions, being respectively red-shifted by 32 cm^{-1} and blue-shifted by 98 cm^{-1}. Comparisons of the Raman and FTIR spectra of formamide in this region with the samples show similarities that do suggest the presence of formamide, but the frequencies for all peaks are shifted. Such a shift could arise from formamide ions displacing hydroxide ions within the lattice or, more likely, to the differences in dielectric properties of the interplanar region on $Ni(OH)_2$ relative to aqueous solutions.

4.2.5 X-ray Diffraction

All samples exhibit powder X-ray diffraction patterns that are consistent with a disordered form of nickel hydroxide. All observed Bragg peaks can be indexed using the *P-3m1* space group **(Chapter 1.2.1)** adopted by β-$Ni(OH)_2$ (ICSD 169978). Well-formed 2-dimensional layers in low Fe-content samples are revealed by sharp and well defined Bragg peaks for lattice planes that do not involve the crystalline c-axis, such as the (100) and (110) planes (**Figure 4.4A**). Stacking disorder is evident in these samples by the width of Bragg peaks for lattice planes involving the c-axis, such as the (001) and (101) planes. The (001) plane is notably split into two Bragg peaks for $Ni(OH)_2$ synthesized in the presence of formamide, with one shorter and one longer than the single peak that is observed for $Ni(OH)_2$ synthesized in water. Formamide is known to intercalate

between the layers of layered double hydroxide lattices[235] and the observed behavior is reminiscent of previously reported interstratified stacking structures.[85,236] The (001) splitting is therefore assigned to presence of formamide between a fraction of layers in the material. Increasing the Fe-content results in broadening of all Bragg peaks for both sample series, particularly those involving the c-axis. Such broadening indicates increased structural disorder and may indicate either increased variation in interatomic distances within the material or a decrease in coherent crystallite size. The two (001) Bragg peaks in the formamide series move in opposite directions from one another as Fe-content increases, with the shorter (001) shifting to larger 2θ and the longer (001) shifting to significantly smaller 2θ (**Figure 4.4B**). Similar behavior is observed for the water series of samples for Fe-contents above 8.7% Fe, but lower Fe-content samples in this series show greater stability in interlayer spacing. The larger (001) equilibrates at a distance near 8 Å for both sample series, consistent with maximal distance before exfoliation of individual sheets,[99] and the shorter (001) distance equilibrates near 4 Å.

Composition-dependent shifts of Bragg peaks suggest that the two sample series exhibit similar unit cells but different structural distortions. A characteristic distance often reported for this class of electrocatalyst is the distance between metal ions within edge-sharing polyhedra ($d_{M\text{-}M}$),[121,161,201,237] which is equivalent to the unit cell *a* parameter. This distance can be readily calculated using the (110) plane through **(equation 4.1)** or, based on the space group, through the (100) plane using **(equation 4.2)**

$$a = 2 \times d_{(110)} \qquad \textbf{(4.1)}$$

$$a = d_{(100)} / \cos(30^{o}) \qquad \textbf{(4.2)}$$

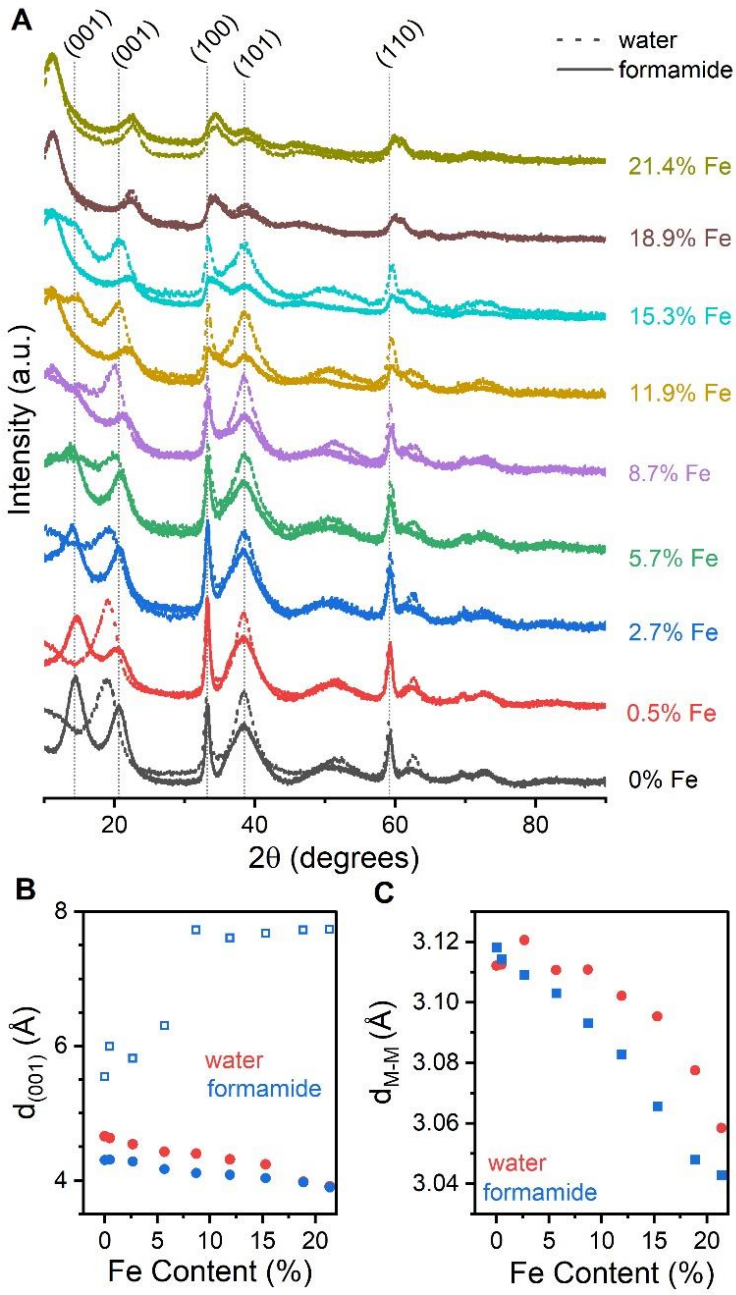

Figure 4.4 Powder X-ray diffraction results for two $Fe_xNi_{1-x}(OH)_2$ composition series. **(A)** Diffraction patterns for the water series (dotted lines) and the formamide series (solid lines). Composition-dependent changes in **(B)** spacing of (100) lattice planes, and **(C)** distance between metal ions in edge-sharing structural motifs ($d_{M\text{-}M}$).

This $d_{M\text{-}M}$ distance continually contracts in the formamide sample series as Fe-content increases (**Figure 4.4C**). This contraction arises due to the smaller ionic radius of Fe(III) relative to Ni(II), as has been reported for doping of $Ni(OH)_2$ with Fe and other cations.[209,238] The water sample series differs in that $d_{M\text{-}M}$ is static until 15.3% Fe, after which a similar contraction occurs. The composition range where $d_{M\text{-}M}$ is stable is synchronized with the composition range where Mössbauer spectra contain the feature for **Fe$_B$** (**Figure 4.1**) and Raman spectra contain the vibrational mode at *ca*. 600 cm^{-1} (**Figure 4.2**). This increased stablity suggests that the **Fe$_B$** coordination environment does not reside within the 2-dimensional bonding framework of $Ni(OH)_2$.

4.2.6 X-ray Absorption Spectroscopy

X-ray absorption near-edge spectra (XANES) show stability in the Ni K-edge structure but composition dependent trends in the Fe K-edge structure. The K-edge from both spectra contain two primary features: a small pre-edge peak that corresponds to the symmetry forbidden 1*s* to 3*d* electronic excitation, and the primary absorption peak (**Figure 4.5A**). The pre-edge and the primary peak for the Ni K-edge are both remarkably stable throughout both series of samples. The K-edge location is static at 8341.40 ± 0.08 eV across both sets of the samples (**Figure 4.5B**). The intensity of the "white line" of the Ni K-edge systematically increases as Fe-content increases for the formamide series (**Figure 4.5A**). The pre-edge feature in Fe K-edge XANES is split into two distinct peaks near 7112.7 eV and 7114.5 eV (**Figure 4.5C**). The intensity of this pre-edge feature increases with increasing Fe-content for both series of samples, with the intensity in the formamide sample being consistently higher than the same composition in the water series. Oxidation state, spin state, and geometry of the Fe coordination site affect the location, splitting and intensity of the pre-edge feature.[239] Splitting of the pre-edge peak into two peaks occurs in high spin Fe(III) sites due to the d^5 electronic structure and crystal field splitting.[240] Increased intensity in this feature has been interpreted as a relaxation of symmetry selection rules due to greater mixing of metal 3*d* and oxygen 4*p* orbitals.[239] Extraction of Fe K-edge location using the half-height method suggests a *ca*. 0.5 eV shift to lower energies as Fe-content increases (**Figure 4.5D**). A shift in edge

position is often assigned as a change in average oxidation state, but such an interpretation assumes that no changes occur in bonding symmetry or ligand identity and the shift typically occurs as an energy shift for the entire edge.[62,113,167,169] Inspection of the edge structure here shows that the Fe K-edge shifts in a non-uniform fashion: the lower portion of the edge shifts towards lower energies while the upper portion shifts towards higher energies (**Figure 4.5C**). Further, the peak intensity of the white line decreases as Fe-content increases. Changes in edge shape are known to occur with changes in coordination environment, and research on photosystem II has clearly shown that *K*-edge position is not purely related to oxidation state.[241] These efforts draw attention to the importance of geometry and coordination number on the measured XANES edge positions, with the changes in either feature inducing changes in edge shape and position. In more direct relevance to the current work, changes in the shape and intensity of the Fe K-edge have been previously observed using *in-situ* spectroelectrochemical XANES measurements on iron-nickel hydroxide films and been assigned to a modification of coordination environment for Fe sites.[167] The changes in structure of the pre-edge and K-edge features observed here thus suggest that Fe(III) ions experience a change in symmetry of the coordination environment as Fe-content increases.

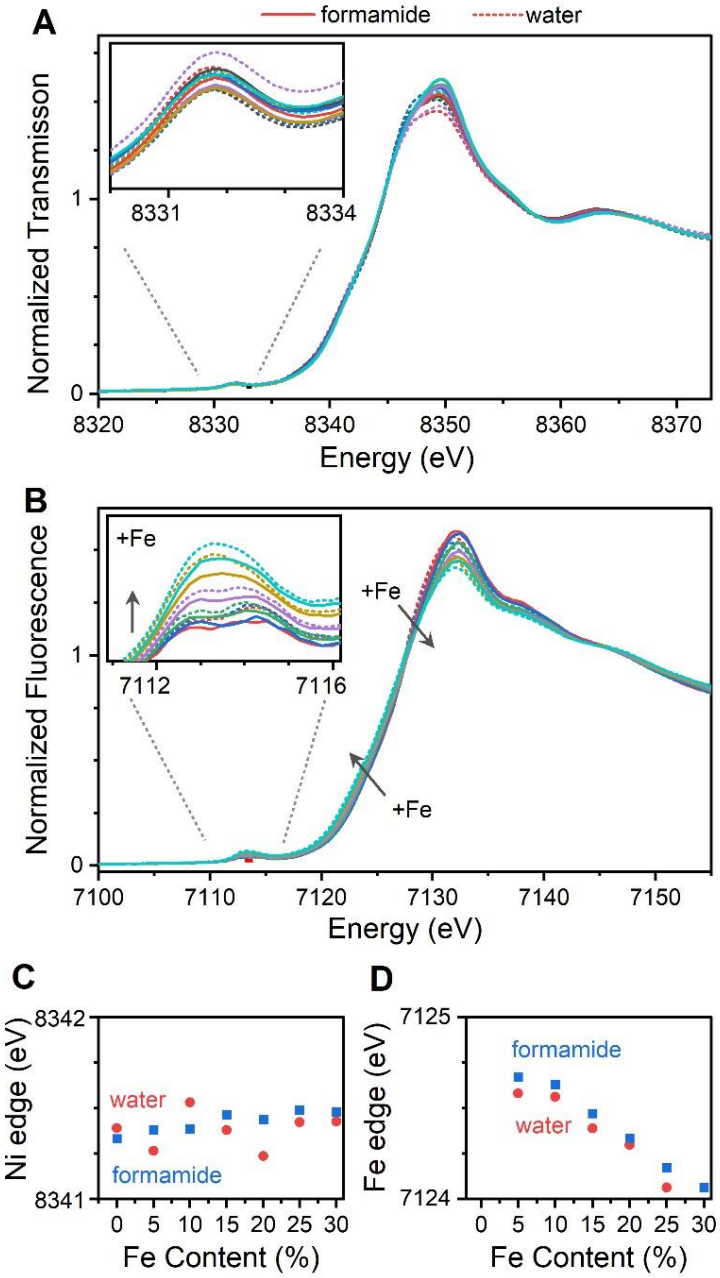

Figure 4.5 X-ray absorption near edge spectra for two $Fe_xNi_{1-x}(OH)_2$ composition series. **(A)** Nickel K-edge XANES spectra with enlarged view of pre-edge feature (inset). **(B)** Changes in nickel K-edge location as a function of Fe-content. **(C)** Iron K-edge XANES spectra. **(D)** Changes in iron *K*-edge location as a function of Fe-content. Color scheme for individual samples matches those from previous figures.

EXAFS confirms a high degree of order within the bonding framework, with differences between the coordination environments and composition dependent changes for Fe and Ni ions. Spectra for the Fe and Ni edges show the expected features for LDH materials, with major features in Fourier transform plots at reduced *R* values near 1.8 and 2.9 Å (**Figure 4.6A** and **Figure 4.6B**). These features correspond to M-O bonds and di-μ-(hydr)oxo linkages that define the characteristic edge-sharing polyhedral motifs. A much smaller feature near 6 Å arises from a combination of the 2nd and 3rd M-M coordination shells. This minor feature becomes indistinguishable from noise in disordered samples,[121,242] but is well resolved from the noise level of the experiments here. Simulations of the data indicate that Ni-O bonds are stable at 2.058 Å across both composition series (**Figure 4.6C**), and that Fe-incorporation decreases Ni-M distances in di-μ-(hydr)oxo motifs more rapidly in the formamide series than the water series (**Figure 4.6D**). Such an occurrence–the decrease of Ni-M distances without affecting Ni-O bond distances–requires distortion of nickel bonding environments. In contrast, both the Fe-O and Fe-M distances decrease as Fe-content increases (**Figure 4.6C** and **Figure 4.6D**). These values are *ca*. 0.02 Å shorter than those observed in the Ni data. This contraction, combined with the fact that EXAFS examines local structure while XRD examines long-range order, explains the slight discrepancies between nickel-specific $R_{\text{Ni-M}}$ values from EXAFS and the structural averaged $d_{\text{M-M}}$ values from XRD. Plots of the difference in Ni-M distance for the two fabrication techniques, $\Delta R_{\text{Ni-M}}$ ($R_{\text{Ni-M,formamide}} - R_{\text{Ni-M,water}}$), against composition (**Figure 4.6E**) clearly demonstrate the same delay in structural changes for the water series that was observed in Mössbauer spectroscopy, Raman spectroscopy and XRD.

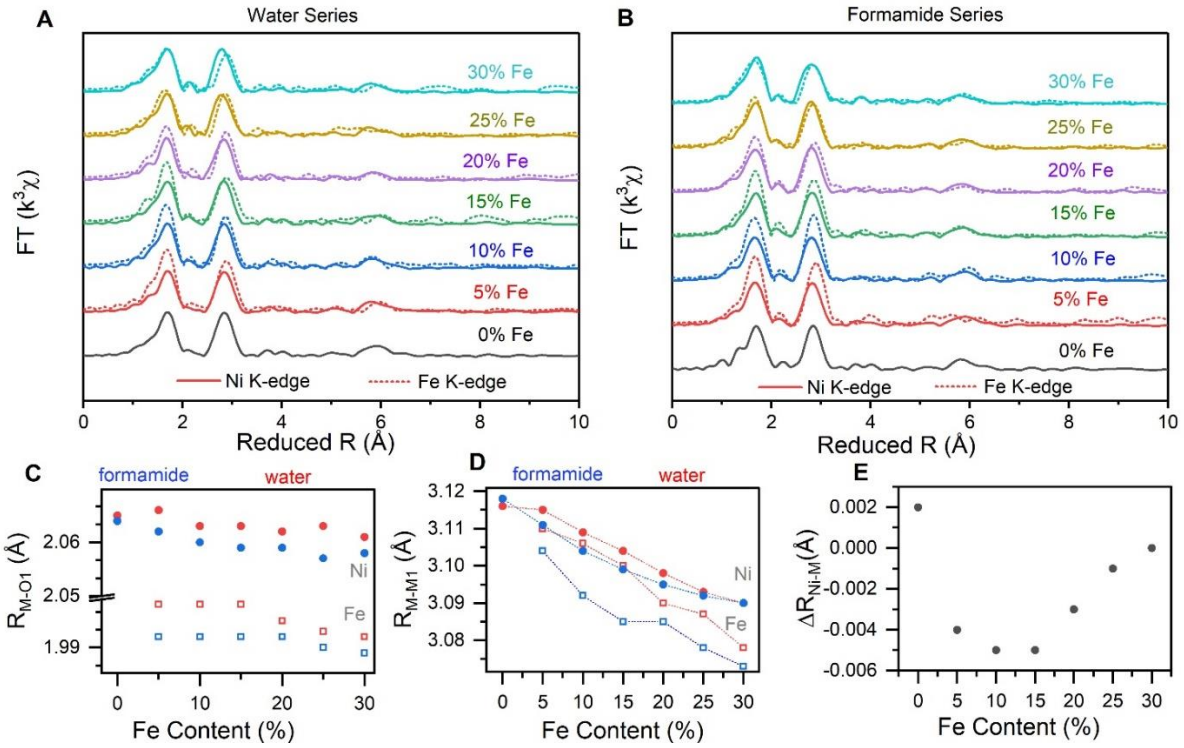

Figure 4.6 Extended X-ray absorption fine-structure spectra for two $Fe_xNi_{1-x}(OH)_2$ composition series. Fourier transformed EXAFS results for **(A)** the Ni K-edge and **(B)** the Fe K-edge. Composition-dependent changes in bond lengths for **(C)** Ni-O and Fe-O, and **(D)** Ni-M and Fe-M. **(E)** Differences between di-μ-(hydr)oxo distances for Ni-M and Fe-M coordination environments.

4.2.7 Electrochemical Behavior

Qualitatively comparable composition-dependent changes in electrochemical behavior for both sample series mask differences in electron transfer kinetics. Both sample series exhibit a single set of pre-catalytic redox peaks that shrink and shift anodically at a rate of 3.3 mV $\%Fe^{-1}$ for the water series and 4.3 mV $\%Fe^{-1}$ for the formamide series (**Figure 4.7A**). Similarities in electrocatalytic performance trends exist between the two sample series, but the formamide series consistently shows higher performance (**Figure 4.7B**). As is characteristic of all Ni-Fe OER electrocatalysts, Fe-incorporation yields a rapid change decrease in Tafel slope that leads to improved electrocatalytic OER performance (**Figure 4.7C**). Pure $Ni(OH)_2$ synthesized using both techniques

yield Tafel slopes of 130 mV dec^{-1}. These values decrease to 58 mV dec^{-1} for both series upon addition of 0.5% Fe, then shift gradually to 30 mV dec^{-1} for 21.4% Fe (**Figure 4.7C**). Despite a synchronized change in Tafel slopes and normalization of the data by electroactive nickel sites, the onset of linearity in Tafel plots (η_{onset}) for the formamide series are consistently *ca*. 70 mV cathodic of those for the aqueous sample series (**Figure 4.7D**). The overall performance is therefore higher for the formamide series (**Figure 4.7E**). This performance gain cannot be attributed to increased surface areas because the results are normalized by redox active nickel sites, which represent the portion of the material exposed to the electrolyte solution. The only interpretation within the confines of the Butler-Volmer formalism for electron transfer kinetics[243–245,196] is that the formamide series must be characterized by a higher intrinsic catalytic capability, denoted by either the standard rate constant (k^o) or the exchange current (i_o) for electron transfer.

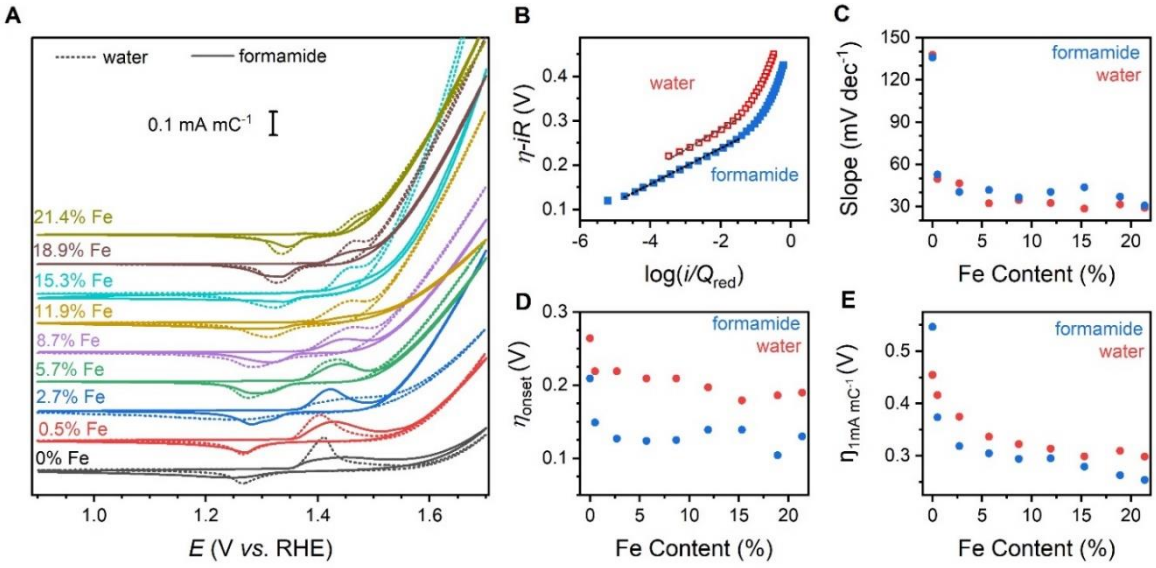

Figure 4.7 Electrochemical characterization of the two $Fe_xNi_{1-x}(OH)_2$ composition series. **(A)** Cyclic voltammograms acquired at 10 mV s^{-1} for all samples. **(B)** Sample Tafel plots for the 2.7% Fe samples synthesized in formamide (blue) and water (red). The full dataset is available in Figure B.3. Composition dependent trends in **(C)** Tafel slope, **(D)** onset of linearity in Tafel plots, and **(E)** overpotential required for a current of 1 mA mC^{-1}. All currents are normalized by charge under the pre-catalytic cathodic redox peak in cyclic voltammograms.

4.2.8 Correlational Analysis

Complementary characterization techniques confirm that the two unique iron coordination environments have different effects on structure, and ultimately on electrochemical behavior. The contraction of the $Ni(OH)_2$ lattice following iron substitution is well-documented and frequently observed as a decrease in $R_{M\text{-}M}$ by XAFS, or $d_{M\text{-}M}$ by XRD.[121,246] The precise nature of this contraction has not been examined in detail. Uniform contraction of the crystal lattice following compositional substitution should preserve relative interatomic distances, such as the $d_{Ni\text{-}O}/d_{Ni\text{-}Ni}$ ratio of 0.67 observed for β-$Ni(OH)_2$ (ICSD 109390).[247] A direct measure of $d_{M\text{-}M}$ is obtained by XRD (**Figure 4.4C**), which can be compared to $d_{Ni\text{-}O}$ values approximated by application of Badger's rule to M-O Raman stretching vibrations:

$$d_{Ni-O} = 5.66\left(\frac{\mu}{\upsilon}\right)^{1/3} + 0.259 \qquad \textbf{(4.3)}$$

Where ν is the frequency of the Raman peak and μ is the reduced mass for Ni-O bonds. Comparison of these two distances shows deviation from the expected linear slope of 0.67 (**Figure 4.8A**). This is an imperfect comparison, however, because Badger's rule is known to underestimate M-O distances in solid state materials[248–251] and $d_{M\text{-}M}$ measured by XRD captures the average for both nickel and iron environments. A more direct measure of these distances for nickel sites is obtained from EXAFS models, where plots of $R_{Ni\text{-}O}$ against $R_{Ni\text{-}M}$ yield similar behavior (**Figure 4.8B**). This deviation from uniform contraction necessitates the distortion of nickel bonding environments following iron substitution. Plots of the interatomic distance ratios to Fe-content show that the formamide series experiences a continual change in magnitude of distortion while the water series shows initial stability and distortions beginning near 15% Fe-content (**Figure 4.8C**). This region of stability exists in the composition range where $\mathbf{Fe_B}$ was observed in all characterization techniques above. It is thus apparent that both contraction and distortion of the $Ni(OH)_2$ lattice are achieved by $\mathbf{Fe_A}$ sites, while $\mathbf{Fe_B}$ sites exert little direct structural influence.

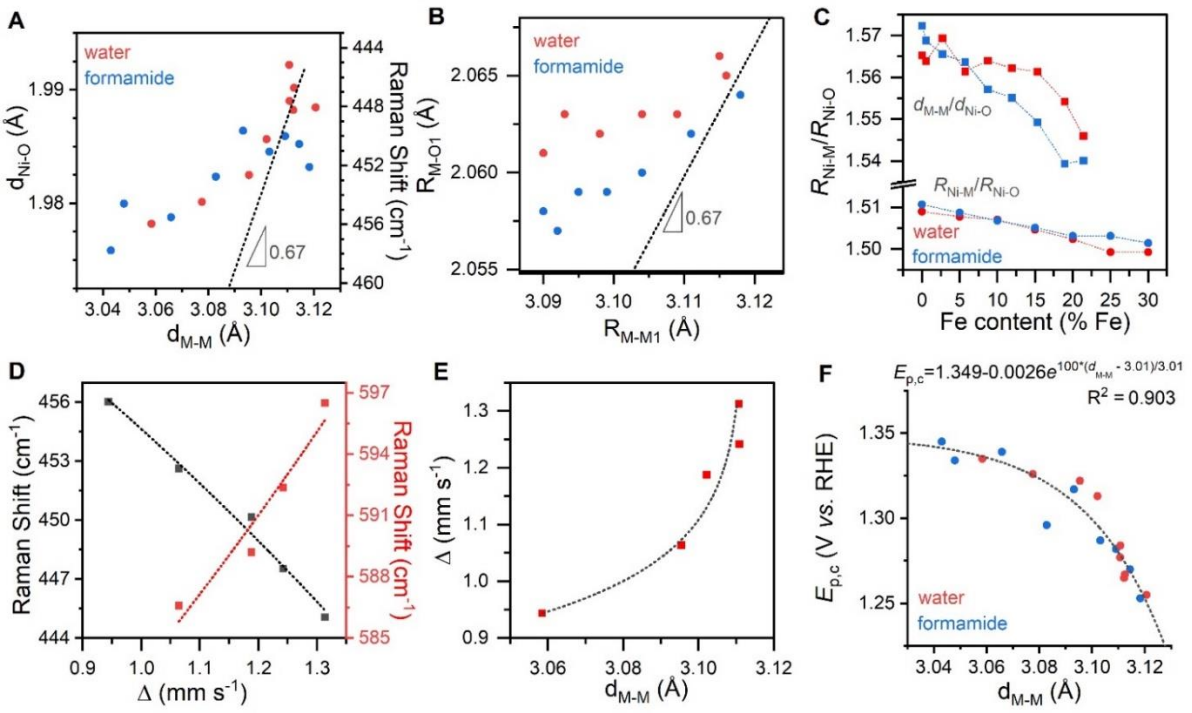

Figure 4.8 Structure-structure and structure-property correlations. Relationship between M-O bond lengths and di-μ-hydr(oxo) distances as **(A)** estimated by Raman spectroscopy and XRD, and **(B)** measured by XAFS. Dashed lines represent the ratio expected for a volume change without structural distortion. **(C)** Effect of Fe-content on the ratio of interatomic distances as measured by XAFS. **(D)** Correlation between Mössbauer quadrupole splitting and the frequency of Raman vibrations for the Fe_A-O (black points; left axis) and Fe_B-O (red points; right axis) coordination environments. **(E)** Correlation between Mössbauer quadrupole splitting of Fe_B and di-μ-hydr(oxo) distances measured by XRD. **(F)** Exponential relationship between location of the pre-catalytic Faradaic peaks and the d_{M-M} spacing.

The composition and fabrication dependence of the unique signatures for **Fe_B** led us to assign it as an octahedral species that sits atop the 2-dimensional sheets, linked to the sheets by di-μ-oxo bonds. The fact that **Fe_B** features in Mössbauer, and Raman spectra are not consistent with known iron oxide or nickel-iron oxide crystalline phases, combined with a lack of unexplained peaks in XRD or XAS results, rule out the possibility that **Fe_B** is a contaminant phase. The largest quadrupole splitting and intensity for the **Fe_B** Mössbauer doublet is at the lowest Fe-content (*ca.* 5%), it systematically decreases as Fe-content increases, and seems to merge into **Fe_A** at high Fe-

content. The Raman spectroscopy feature similarly red shifts towards the **Fe$_A$** feature and disappears at high Fe-content. We rule out assignment of **Fe$_B$** to the co-existence of $Fe_xNi_{1-x}(OH)_2$ platelets with different Fe-content because such a situation would induce step-changes rather than smooth composition-dependent trends, both **Fe$_A$** and **Fe$_B$** would be expected to remain visible for all compositions, and **Fe$_B$** would be expected in some subset of the formamide sample series. The similarities in Mössbauer and Raman spectroscopic features for **Fe$_B$** and **Fe$_A$**, and the invisibility of **Fe$_B$** in EXAFS and XRD results, suggest that the two environments are similar to one another. Viable options include internal 'bulk' sites (Fe fully surrounded by Ni ions), edge sites, or a previously unreported site. We are not aware of any experimental technique capable of measuring the relative proportion of Fe ions residing in bulk sites and edge sites, but it is highly unlikely that the formamide sample shows exclusively one or the other. We therefore conclude that **Fe$_B$** is a secondary coordination site and propose that it exists as an edge-sharing site atop the $Ni(OH)_2$ lattice (**Figure 4.9**). This contrasts with the previous assignment of a minor paramagnetic doublet in Mössbauer spectra to Fe ions residing in kinks that may form in the bonding framework at boundaries between α-$Ni(OH)_2$ and β-$Ni(OH)_2$ segments of the material.[44] The viability of such out-of-plane ions is nonetheless supported by the entirety of data presented here, and by recent reports for tetrahedral iron sites atop cobalt hydroxides,[131] iron oxide clusters atop nickel hydroxides,[113] and iridium ions atop nickel hydroxides.[80]

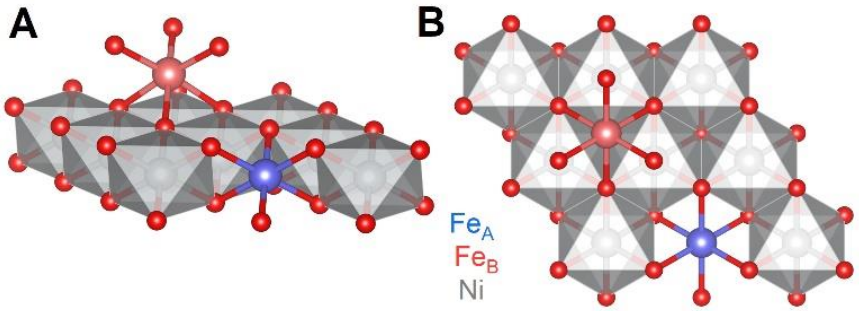

Figure 4.9 Proposed Fe_A and Fe_B coordination environments in relation to the $Ni(OH)_2$ host lattice in $Fe_xNi_{1-x}(OH)_2$ from a **(A)** side view and **(B)** top view.

Iron ions sitting atop the 2-dimensional sheets in the proposed fashion would be strained/distorted due to longer Ni-O bonds within the 2-D sheets creating an effective lattice mismatch for the shorter Fe-O bonds of **Fe$_B$** sites atop the sheets; maximal distortion in **Fe$_B$** sites would be expected at low Fe-content. Such a distortion is consistent with Δ values being larger for **Fe$_B$** than **Fe$_A$** (**Figure 4.1D**), and with the shift in frequency of M-O stretching vibrations in Raman spectra. Increasing Fe-content yields a decrease in unit cell dimensions (**Figure 4.4C**), which strains the $Ni(OH)_2$ lattice but relieves strain in **Fe$_B$** sites. This is observed as opposing shifts in M-O stretching vibrations attributed to **Fe$_A$** and **Fe$_B$** (**Figure 4.2**), and in opposing correlations of Δ with the frequency of these two Raman spectroscopic features (**Figure 4.8D**). Further support for this proposal is that XRD-derived $d_{M\text{-}M}$ values, which correlate to the amount of iron incorporated into **Fe$_A$** sites (**Figure 4.3**), exhibit an exponential relationship with the Mössbauer Δ values (**Figure 4.8E**). This proposal reveals how the **Fe$_B$** environment has been overlooked in the past: all features representing **Fe$_B$** become indistinguishable from **Fe$_A$** at high Fe-content due to their structural similarity, and the linkage of **Fe$_B$** by di-μ-oxo bridging makes the feature blend into the first M-M coordination shell in XAFS results.

Composition-dependent changes in electrochemical behavior of these two composition series appear to be linked exclusively to **Fe$_A$** sites. An anodic shift of pre-catalytic redox peaks is characteristic of the iron-nickel hydroxide system.[159,197,252,121,209,207,61,81] A more detailed perspective is acquired here, with the peak locations being found to be exponentially related to $d_{M\text{-}M}$ values (**Figure 4.8F**). This correlation spans both series of samples, indicating that the anodic shift in pre-catalytic features is attributable to the presence of **Fe$_A$**. Lattice distortions caused by ionic radius mismatch have been reported following iron incorporation into $Ni(OH)_2$,[121] and a transition between compressive strain in the reduced phase and tensile strain in the oxidized phase was identified and demonstrated by exact replication of the composition-dependent shift with non-iron substituents.[209] The exponential relationship between $d_{M\text{-}M}$ and $E_{p,c}$ exactly reveals how the inversion of lattice strain affects this peak. Addition of Δw, a term describing the difference in strain energy in the oxidized and reduced phases, to the Nernst equation yields:

$$E = E^0 + \Delta w + \frac{RT}{nF} ln(K) \quad \textbf{(4.4)}$$

This term will depend upon the magnitude of strain in each phase, ε_i, which will be associated with the amount of **Fe$_A$** in a given sample. This strain can be represented as a percent change in $d_{M\text{-}M}$ in **equation (4.5)**:

$$\epsilon_i = 100 \frac{(d_{M-M} - d_0)}{d_0} \quad \textbf{(4.5)}$$

Considerations of stresses, strains and displacements in all three dimensions are necessary to generate a quantitative model. The experimentally fitted equation, however, suggests a simplified relationship involving a limiting voltage ($E_{p,c}^{0'}$), strain as an exponential coefficient (c), and a single term describing strain. This fitted equation captures the average strain present in the oxidized and reduced phases, with d_0 residing near the midpoint of the expected $d_{M\text{-}M}$ distances for reduced (≈ 3.12 Å) and oxidized (≈ 2.84 Å) forms of pure $Ni(OH)_2$,[113,121,161,169,193,253] and $E_{p,c}^{0'}$ being a limit attained at high Fe-content. The exponential coefficient of 2.6 mV is exactly equal in magnitude to the rate of anodic peak shift observed upon incorporation of Fe(III), Ga(III) and Al(III),[209] suggesting that it captures the *change* in work energy between the oxidized and reduced phases. These results provide confirmation that the changes in pre-catalytic peaks are primarily associated with inversion of strain following electron transfer. The similar Tafel slopes for electrocatalytic OER indicates that the absence of **Fe$_B$** does not degrade the catalytic performance. The onset of OER and overpotential requires to pass 1 mA mC^{-1} of current are consistently lower for the formamide samples even with the use of a current normalization protocol based on electroactive nickel sites. This suggests that **Fe$_A$** may cause an increase in inherent catalytic activity. We note, however, that the changes in electrocatalytic OER performance are very abrupt, and the maximum current attained is slightly higher for water samples with intermediate Fe content **(Figure B.1)**.

The **Fe_B** site is clearly not critical to good OER performance, but it is difficult to draw a conclusive interpretation on the exact effect that **Fe_B** has on OER.

4.3 Conclusion

Two unique coordination environments were identified for iron ions in $Fe_xNi_{1-x}(OH)_2$ by comparison of the structure and behavior of two related composition series. A sample series fabricated by aqueous precipitation in the presence of formamide resulted in uniform atomic distribution of the dopant ions, as judged by the presence of only one subspectrum in Mössbauer spectra, theoretically expected peaks in Raman spectra, and through monotonic changes Bragg peaks in XRD patterns and in interatomic nickel-metal distances measured by EXAFS. Samples prepared by conventional aqueous pH precipitation show additional features, including a second minor paramagnetic doublet appearing in Mössbauer spectra, and a Raman vibration near 600 cm^{-1}. A synchronized delay also emerges in composition-dependent changes to lattice parameters measured by XRD, and in interatomic distances measured by EXAFS. A continual distortion of nickel coordination environments in the formamide series is revealed by analysis of composition-dependent changes in interatomic distances measured by XRD and EXAFS; these distances remain constant below 15% Fe-content for the water sample series before showing similar distortions. An exponential relationship between interatomic Ni-M distances and location of precatalytic redox peaks spans both sample series. This relationship suggests that inversion of lattice strain upon oxidation, from compressive to tensile, yields predictable changes in thermodynamics for electron transfer. The secondary iron coordination environment has no discernable impact on precatalytic redox, and no beneficial influence over electrocatalytic OER performance. These results not only demonstrate the existence of a second coordination environment for dopant ions in $Ni(OH)_2$ lattices, but identify several experimental techniques that are capable of directly identifying their presence. These results provide additional structural information that will help to deconvolute the electrochemical behavior of doped nickel hydroxide materials, while the experimental capabilities will support community efforts to optimize fabrication protocols.

4.4 Experimental

4.4.1 Materials and Sample Preparation

Nickel chloride hexahydrate ($NiCl_2.6H_2O$) (Fisher Chemical), ferric chloride ($FeCl_3$) (Fisher Chemical), sodium hydroxide, and potassium hydroxide (NaOH and KOH) (Sigma-Aldrich), and reagent grade formamide (CH_3NO) (Sigma-Aldrich) were used as received. All H_2O used during fabrication was Milli-Q® H_2O (18.2M **Ω**).

4.4.2 Electrochemistry

A Biologic SP-300 potentiostat was used for all the electrochemical experiments. Experiments were conducted in a single compartment polyethylene cell. A Gaskatel HydroFlex reversible hydrogen electrode (RHE) was used as reference electrode, platinum mesh as the counter electrode, and Toray carbon fiber paper as a substrate for the working electrode. 1M KOH solution is used as the electrolyte. Cell resistances were recorded at open circuit potential with impedance spectroscopy at the beginning of each experiment, the values were on the order of 5 Ohms for all the samples. Cyclic voltammetry experiments were recorded between 0.9 and 1.7V vs RHE electrode at 5 mV sec^{-1} scan rate with two cycles, and the second cycle of each sample was compared. The stability of the samples is shown with the comparison of cyclic voltammograms acquired before and after chronoamperometry experiment **(Figure B.1).** All currents are normalized by charge passed under the cathodic redox peak in cyclic voltammograms to effectively normalize electrochemical results to the number of electroactive nickel centers. Electrokinetic parameters were extracted from chronoamperometry experiments. Chronoamperometry experiments were recorded in both anodic and cathodic directions between 0.9 V and 1.7 V in 10 mV and one-minute steps. A sample chronoamperometric experiment for both directions are shown in **Figure B.3**. Since chronoamperometry of oxidation reaction includes species from the previous reaction, we used cathodic chronoamperometry for further analysis. EC-Lab program was used to integrate the cathodic peak of cyclic voltammograms with baseline correction (**Table B.1**).

Catalyst Modified Electrode Preparation

A suspension of 5 mg of catalysts, 780 µL of ethanol, 200 µL of water, and 20 µL of 0.5% Nafion® solution was sonicated, and 20 µL of this solution was drop-cast onto carbon fiber paper. The electrodes were dried at room temperature overnight.

4.4.3 Mössbauer Spectroscopy

In this thesis, room temperature Mössbauer spectra were recorded in transmission geometry on *ca.* 20-50 mg powder samples, utilizing a ^{57}Co(Rh) γ-ray source mounted on a constant-acceleration driving unit. All spectra were evaluated with the "*Pi*" program package.[254] Lorentz curve profiles were used to curve fit the experimental data and extract hyperfine parameters. For the additional minor doublet subspectrum present in the aqueous sample series the width of the minor peaks was restricted to typical values observed for the dominant doublet peaks.

4.4.4 X-ray Absorption Spectroscopy

XAS experiments were performed at the Beamline for Materials Measurements (BMM) at the National Synchrotron Lights Source II (Brookhaven National Laboratory, NY, USA) using a Si(111) monochromator. Data were collected in transmission mode for the Ni K-edge of all samples, and in both transmission and fluorescence mode (4 element Si drift detector) for Fe K-edge data. The Athena software package was used for standard baseline subtraction and normalization of XAS spectra.[255] The K-edge locations were determined by applying the half-height method to the normalized spectra. (**Table B.2**)[256] The Artemis software package was used to generate structural models by simulation of k^3 weighted EXAFS results from k of 3 to 15 $Å^{-1}$ (**Figure B.4**). The goal of obtaining accurate interatomic distances led us to try two different simulation approaches. Both simulation approaches were performed using fixed amplitude reduction factors (S_0^2) and coordination numbers (N_j) of 6 for the M-O and M-M coordination shells, consistent with the $Ni(OH)_2$ structure indicated by XRD. The preliminary model fitted E_O, Debye-Waller factors (σ^2_j), and R_{M-O} and R_{M-M} for the observed shells (**Tables B.3-B.6**). The second model was similarly fitted, but with E_o fixed at the average value obtained per sample series

in the first attempt to minimize the influence of correlation between E_o and R_j values (**Tables B.7-B.10**). All analysis is performed using the second, final model.

XAS measurements were performed on a separate sample series, using 5 % (atomic) Fe-content increments between 0 to 30% iron. Powder samples were characterized with XRD and Raman spectroscopy to ensure comparability of the sample series with original results (**Figures B.5-B.7**).

4.4.5 FTIR Spectroscopy

Fourier transform infrared (FTIR) spectroscopic measurements were performed on a Nicolet 6700 FTIR in the transmission mode using KBr powder as pellet press materials. Microscope mode was used for liquid formamide, and the data was recorded between 4000-650 cm^{-1} wavenumber range. The data was then converted into absorbance by OMNIC 9 software.

4.4.6 X-ray Diffraction

Experimental details of the powder XRD experiment are stated in **Chapter 2.2.2**

4.4.7 Raman Spectroscopy

Experimental details of the Raman spectroscopy measurements are stated in **Chapter 2.2.5.2.**

Chapter 5

Effect of Lattice Strain on Electron Transfer Kinetics

5.1 Introduction

Iron-doped nickel hydroxides rank as one of the best oxygen evolution reaction (OER) electrocatalysts in alkaline environment and a large range of synthetic protocols have been developed to prepare these materials.[257] Easily prepared by pH-induced precipitation,[85,258] materials exhibiting layered hydroxide type structures can be prepared by anodic electrodeposition,[84,62,208] cathodic electrodeposition,[83,120,207] photochemical deposition,[42,121,125,209] anodization of metallic electrodes,[259–261] hydrothermal techniques,[262–264] and precipitation in the presence of various small organic molecules.[136,99] Efforts at improving the catalytic properties of this family of materials have focused on tuning morphology[252,265], adding dopants, introducing carbon additives,[117,266] acting as a support for single atoms,[80,267,268] or using alternative materials such as metal organic frameworks as synthetic precursors.[269] Such a wide variety of fabrication and processing protocols yields variations in overall catalytic performance, but the incorporation of even trace amounts of around 1 ppm of Fe(III) into $Ni(OH)_2$ type materials consistently yields the same abrupt changes in electrocatalytic response.[270] Structural analyses are commonly performed by a mixture of XRD and XAFS, with each approach typically identifying the same minimal set of structural features for all synthetic approaches **(Chapter 4)**. With such diversity in synthetic techniques, however, it is highly probable that variations in structural features exist that are hidden behind the abrupt changes in OER activity. Careful analysis of the quantitative changes in structure and performance are necessary to identify any such variations.[15]

Modern efforts to identify individual coordination environments that are particularly active for electrocatalytic OER have identified several specific structures that may be of importance. The undercoordination of ions residing along the edge, or at corners, of the layered double hydroxide structure are often viewed as the catalytically relevant sites.[164,203,204] Variations in measurement strategies have revealed unexpected tetrahedrally coordinated sites that potentially affects the catalytic performance.[47,93] Another study reported the ability for elements such as iron and iridium to reside atop the basal plane of $Ni(OH)_2$. The increased catalytic activity is originated from the synergy between anchored Ir sites and $Ni(OH)_2$.[80] Systematic variations in nickel and iron electronic structures is found to be important parameter to modulate OER capability of the electrocatalysts.[62,271,272] Redox activity of the iron sites is also considered for the improved catalytic activity.[161] Due to ionic radius differences between nickel and iron coordination environment, lattice strain is formed.[121,209] The diversity between statements on the structure and coordination environments on LDHs requires more sophisticated methods to analyze the structural varieties. Analysis using advanced operando techniques has yielded some success in identifying sites that may have catalytic relevance.[81,210,273–275] Identification of such non-standard sites, however, has been relatively restricted to individual lines of research due to reliance on specialized characterization and analytical techniques. An understanding of the prevalence of such structural features, the role of synthetic conditions in their effective concentrations will assist in optimizing electrocatalysts performance and stability.

Metal oxyhydroxides synthesized with a hydrothermal route yield more crystalline structures than fabrication techniques such as electrodeposition, co-precipitation.[85,275] This approach has a risk of producing contaminating phases, such as the spinels Co_3O_4, Fe_3O_4 or $NiFe_2O_4$,[44,276] or disordered platelets as seen in Zn(II) doped aluminum hydroxides.[277] Nonetheless, hydrothermal approaches have also yielded the highest quality crystals of β-$Ni(OH)_2$ reported to date.[225] Highly crystalline forms of nickel hydroxide historically serve as alkaline battery cathode materials due to their exceptionally poor ability to catalyze OER; the catalytic capabilities increase dramatically upon introduction of structural disorder.[42,82,125] Previous report demonstrated that the electrocatalytic

activity of iron incorporated nickel hydroxides prepared with this techniques remains comparable after 5% iron incorporation.[169] This situation points out the presence of multiple catalytically active or inactive sites. This change in behavior marks hydrothermally synthesized samples of interest for studying critical structural features through structure-property analysis, particularly if the degree of structural disorder can be systematically affected.

This chapter covers structural and electrocatalytic characteristics of a $Fe_xNi_{1-x}(OH)_2$ composition series fabricated using hydrothermal techniques. Structural analysis using Raman spectroscopy, XRD, and XAFS show that Fe(III) within $Ni(OH)_2$ yields localized structural distortions, where Ni-sites retaining long-range order while Fe-sites show no order beyond *ca.* 3.5 Å. Peaks that emerge in Raman spectra show correlations to structural features that enables Raman spectroscopy to serve as a rapid diagnostic tool. A linear correlation is observed between Tafel slope for OER and bond angles within the material. This behavior deviates from the commonly reported step-wise change in Tafel slope that is commonly reported for iron-nickel hydroxide materials. This trend cannot be explained by the traditional Butler-Volmer model for electron transfer kinetics, but asymmetric Marcus-Hush theory serves to link the trend to increasing lattice strain with increasing Fe-content.

5.2 Results

5.2.1 X-ray Diffraction

XRD patterns for the $Fe_xNi_{1-x}(OH)_2$ series are consistent with a well-crystallized structure similar to brucite **(Chapter 1.2.1)**, with Fe(III) ions inducing structural disorder. (**Figure 5.1A and Chapter 4.2.5**).[37] Addition of Fe(III) to the reaction flask induces progressive shrinkage and broadening of Bragg peaks that signify decreased long-range structural order. Successful incorporation of iron ions into the $Ni(OH)_2$ lattice is confirmed by a monotonic shift in the (100) reflection, which represents Ni-Ni distances across di-μ-hydroxo linkages ($d_{M\text{-}M}$). Rietveld refinements show this distance contracts from 3.124 Å for 0% Fe to 3.111 Å for 30% Fe (**Figure 5.1B**). The unit cell *c* parameter represents the spacing between 2-dimensional sheets and is static

near 4.61 Å until *ca*. 10% Fe content, after which it decreases towards 4.56 Å (**Figure 5.1C**). The increased disorder and absence of a concerted contraction of both *a* and *c* suggests that iron dopants induce localized distortions in the lattice. The distortion arises when these two values do not decrease linearly with each other. These parameters undergo different rates of contraction and thus structural distortion happens.

An iron oxide phase contaminant emerges as the amount of iron added to the reaction vessel increases. Bragg peaks at 31, 36, 44, and 57° become visible in the XRD at 10% Fe-content and continually increase in intensity as Fe-content increases (**Figure 5.1A**). These peak locations are consistent with the strongest reflections expected for either magnetite[278] (Fe_3O_4; ICSD #49549) or maghemite[279] (γ-Fe_2O_3; ICSD #35643). Due to similarities between the two structures, it is not possible to conclusively identify which is present by XRD. Rietveld refinements using β-$Ni(OH)_2$ and Fe_3O_4 components provide a measure of the phase fraction of the iron oxide contaminant, confirming that its concentration steadily increases with Fe-content (**Figure 5.1D**). The calculations of the stoichiometry from Rietveld refinements are presented in (**Appendix C**, page 175) The stoichiometry of iron successfully incorporated into the $Ni(OH)_2$ lattice is therefore not equivalent to the stoichiometry added to the reaction flask, with the observed behavior suggesting that a solubility limit for Fe(III) in the $Ni(OH)_2$ lattice exists.

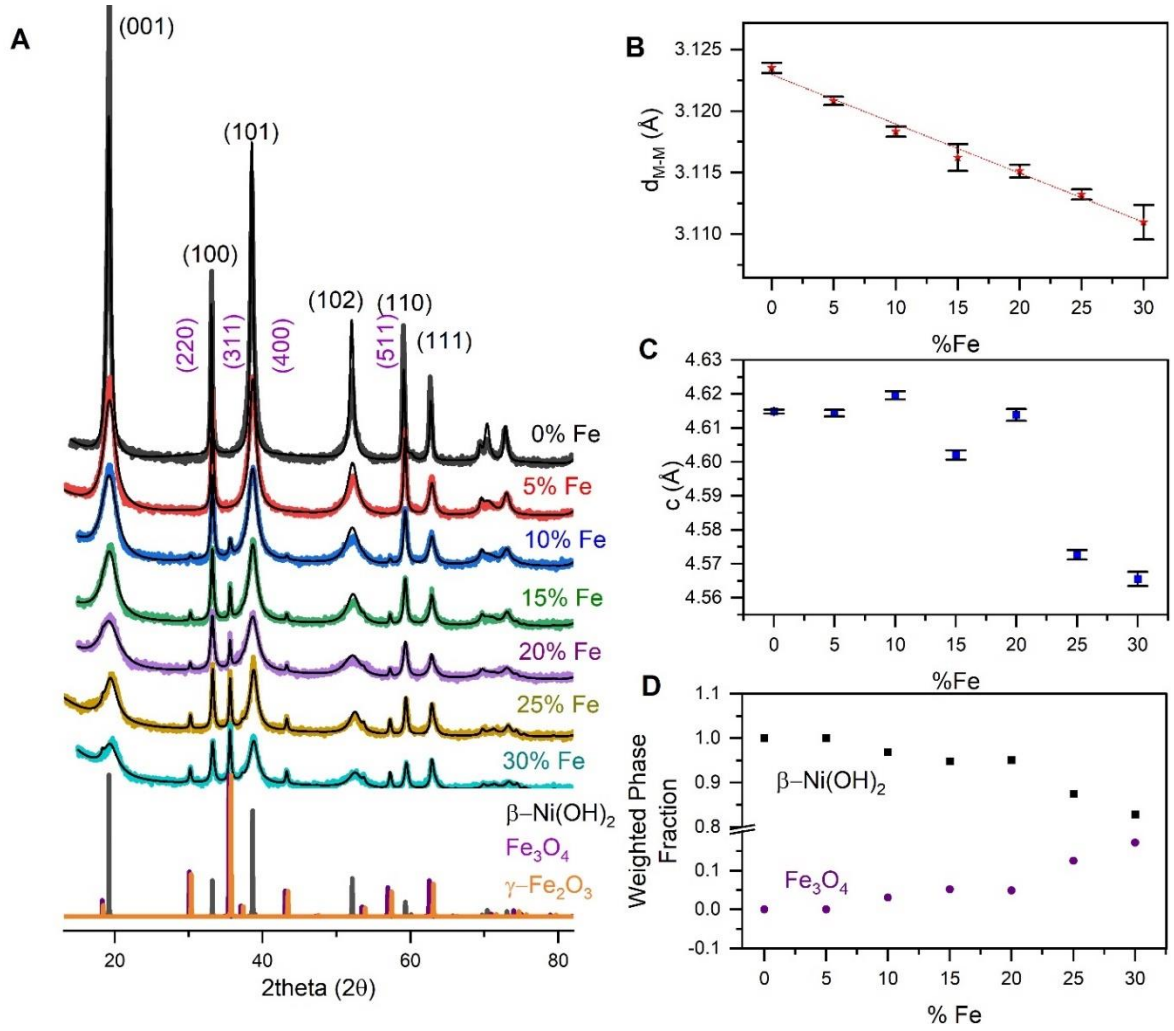

Figure 5.1 P-XRD analysis of $Fe_xNi_{1-x}(OH)_2$. **(A)** Experimental XRD patterns (data points) and Rietveld refinement fits (lines) for the composition series. **(B)** Composition dependence of the unit cell a parameter, which represents metal-metal distances in edge-sharing polyhedral. **(C)** Composition dependence of interlayer spacing**. (D)** Relative weighted phase fractions determined by Rietveld refinement using β-$Ni(OH)_2$ and magnetite (Fe_3O_4).

5.2.2 Raman Spectroscopy

Raman spectra on the sample series are consistent with a decrease in long-range order upon Fe-substitution and reveal systematic deprotonation of hydroxyl groups. The brucite structure is expected to yield two A_{1g} and two E_g Raman active modes, but one E_g mode is not observed.[150,224] The pure $Ni(OH)_2$ sample here shows the three commonly observed modes, with an E_g mode at 313 cm^{-1}, an A_{1g} mode at 446 and a second A_{1g} mode at 3580 cm^{-1} (**Figure 5.2A**). Incorporation of Fe(III) ions causes the peak for the E_g mode, an antisymmetric movement of oxygen ions on either side of the metal hydroxide layers, to broaden substantially but remain at a static frequency (**Figure 5.2B**).[150] The peak for the low frequency A_{1g} mode, a symmetric stretching of M-O bonds, exhibits broadening and an apparent blue shift following incorporation of Fe(III) ions (**Figure 5.2B**). The apparent blue shift of this A_{1g} peak may be attributable to the overlap of two poorly resolved bands, evidenced by the clear emergence of a low-frequency peak with a shoulder in the 30% Fe-content sample (**Figure 5.2C**). The second A_{1g} mode at 3580 cm^{-1} broadens as Fe-content increases, suggesting deprotonation of hydroxyl groups.[37,227] Such deprotonation is consistent with a strengthening of M-O bonding that is supported by the observed blue shift of the A_{1g} M-O stretching vibration. Additional O-H vibrations are observed at 3600 and 3687 cm^{-1}. The former is a sharp peak on the high frequency shoulder of the A_{1g} hydroxide stretch that has been previously assigned to surface hydroxide vibrations, while the latter to has been assigned as an A_{2u} O-H stretching vibration that become visible due to disorder in layer stacking.[37]

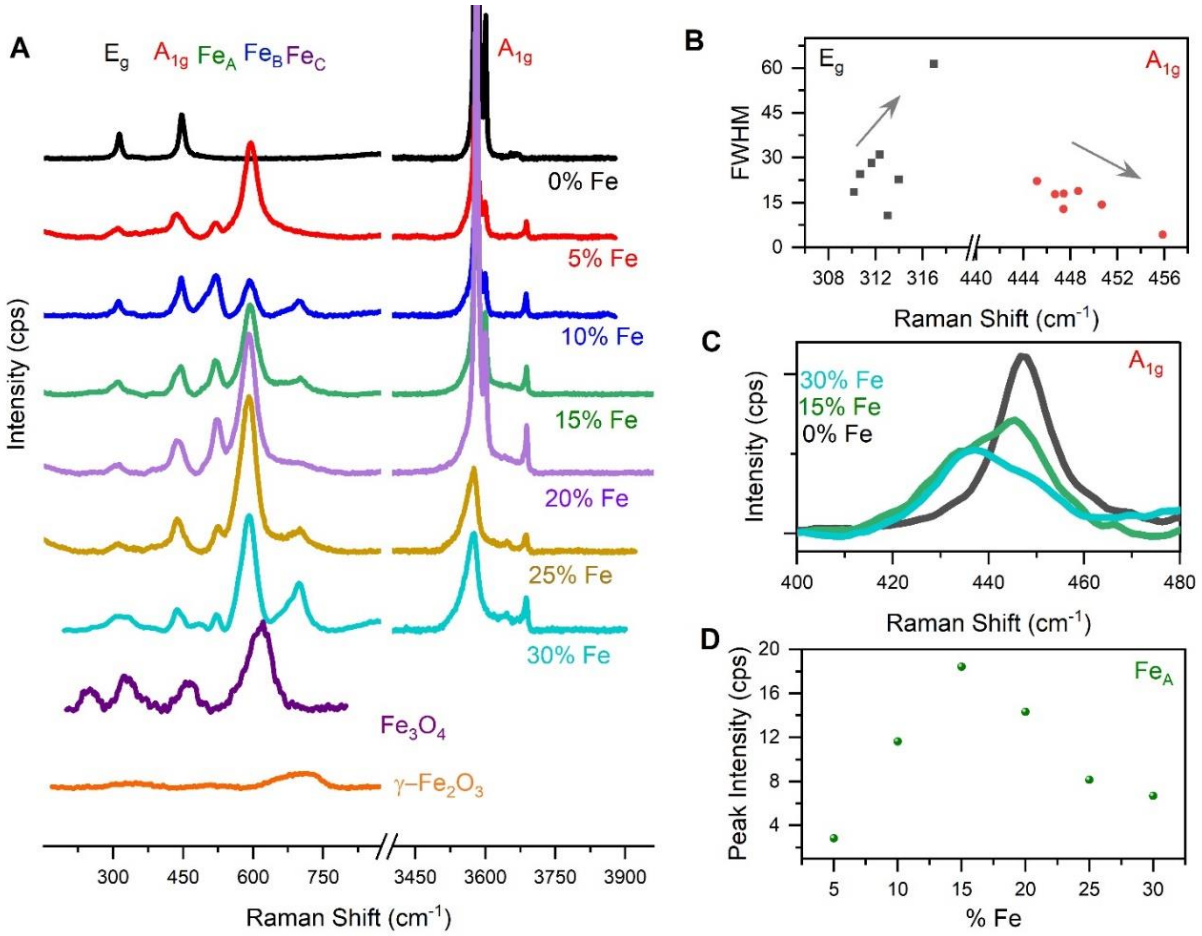

Figure 5.2 Structural analysis of $Fe_xNi_{1-x}(OH)_2$ with Raman spectroscopy. **(A)** Raman spectra of composition-dependent $Fe_xNi_{1-x}(OH)_2$ series with magnetite and maghemite references. **(B)** Composition dependent Ni-O vibrations. **(C)** Shape transformation of the peak observed for the A_{1g} stretching vibration. **(D)** Composition-dependent intensity of the peak at *ca.* 518 cm^{-1} that is labelled as Fe_A.

The emergence of several additional Raman peaks upon introduction of iron reveals the composition-dependent structural evolution in the material. A peak at *ca*. 518 cm^{-1} (**Fe_A**; **Figure 5.2A**) appears immediately upon addition of iron and blue shifts with increased Fe-content. Previous reports indicate that this feature is an M-O stretching mode that arises following substitution of Ni(II) with trivalent cations due to deprotonation.[232] The **Fe_A** peak grows in

prominence until 20% Fe before shrinking due to growth of two other peaks, located at *ca.* 600 and 700 cm^{-1}. XRD results demonstrated that the proportion of Fe ions successfully incorporated into the $Ni(OH)_2$ lattice was near quantitative below 20% Fe content, and a linear trend exists between Fe-content and intensity of **Fe$_A$** in this composition range (**Figure 5.2D**). The intensity of the **Fe$_A$** feature therefore provides a measure of Fe ions successfully incorporated into the lattice. The peak at *ca*. 600 cm^{-1} (**Fe$_B$**; **Figure 5.2A**) is intense immediately upon addition of Fe to the samples and grows even more prominent at 20-30% Fe. Our past results suggest that the **Fe$_B$** peak arises due to a second coordination environment for Fe(III) in $Ni(OH)_2$ samples, which sits atop the two dimensional sheets.[280] The intensity of this peak is significantly greater at low Fe-content values here than previously reported, suggesting that these secondary sites are more favored through hydrothermal synthesis than the previous alkaline precipitation methods due to the induced localized strain with iron addition. The final additional peak that emerges upon introduction of Fe is visible at *ca.* 700 cm^{-1} between 10-30% Fe (**Fe**C; **Figure 5.2A**). The location of this peak is consistent with γ-Fe_2O_3, [281,282] which XRD analysis identified as a potential contaminating phase for these compositions.

5.2.3 X-ray Absorption Spectroscopy

Composition-dependent changes in the Ni and Fe K-edge XANES show a distortion of coordination environments. The K-edge spectra for both elements consist of a pre-edge peak and an edge leading to a prominent peak (the *"white line"*). The former is a symmetry-forbidden electronic transition from 1*s* to 3*d* orbitals while the subsequent edge and peak are the symmetry allowed 1*s* to 4*p* transition.[239,240,283,284] The pre-edge peak is stable throughout the composition series in the Ni K-edge spectra (**Figure 5.3A**), but increases in intensity in the Fe K-edge spectra as Fe-content increases (**Figure 5.3B**). The pre-edge peak in the Fe K-edge data consists of distinct peaks at 7112.2 and 7114.5 eV at low Fe-contents, which is consistent with high spin Fe(III) ions.[239] The two peaks merge into a single, more prominent peak near 7113.3 eV as Fe-content increases. The trend in intensity may be indicative of greater orbital mixing of the iron 3*d* and oxygen 4*p* orbitals,[239,240,283] but increased influence of the iron oxide contaminant can't be ruled

out due to its expected pre-edge peak near 7113 eV.[285] Both of maghemite and magnetite phases are expected as a single peak centered as 7113 eV.[286] The proximity of the centers of the pre-edge peaks of magnetite, maghemite and FeNi hydroxides prevents to determine the exact identity of the secondary phase from XANES. The K-edges themselves show evidence of changes in coordination environments. The edge location appears to shift negatively by *ca*. 0.8 eV, which would often be interpreted as a decrease in average oxidation state (**Figure 5.3C**, **Table C1**). The Raman spectra and XRD patterns suggest that γ-Fe_2O_3 or Fe_3O_4 is the contaminant phase, however, suggesting that this apparent shift is an artefact of a change in either geometry or spin-state. A distinct change in shape of the Fe edge as Fe-content increases supports the assessment that the apparent shift is unlikely a change in oxidation state as discussed in **Chapter 4 (Figure 5.3B)**. The Ni edge shows the same behavior, but in a much less pronounced fashion (**Figure 5.3A**). The estimated K-edge location shifts negatively by 0.33 eV (**Figure 5.3C**), which is also likely to arise due to changes in the coordination environment rather than the nickel oxidation state.

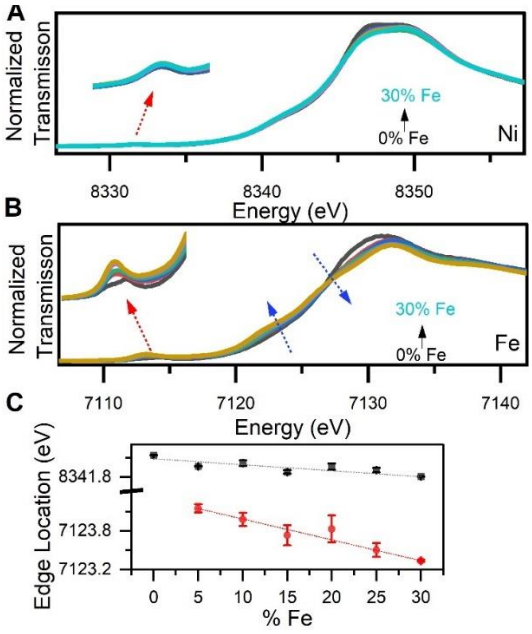

Figure 5.3 X-ray absorption near-edge spectra for $Fe_xNi_{1-x}(OH)_2$. **(A)** XANES spectra of Ni K-edge of $Fe_xNi_{1-x}(OH)_2$ sample series. **(B)** XANES spectra of Fe K-edge of $Fe_xNi_{1-x}(OH)_2$ sample series. **(C)** Composition dependent Ni-K and Fe-K edge locations.

Wavelet transform (WT) analysis was found to be capable of revealing the iron oxide phase contamination, but could not differentiate between Ni and Fe ions residing within the $Ni(OH)_2$ lattice. WT offers improved resolution of scattering paths with when R-values are similar but oscillations are present in different *k*-space.[287,288] The strongest features in WT of k^3-weighted data are maxima corresponding to M-O and edge-sharing M-M shells (**Figure 5.4**).

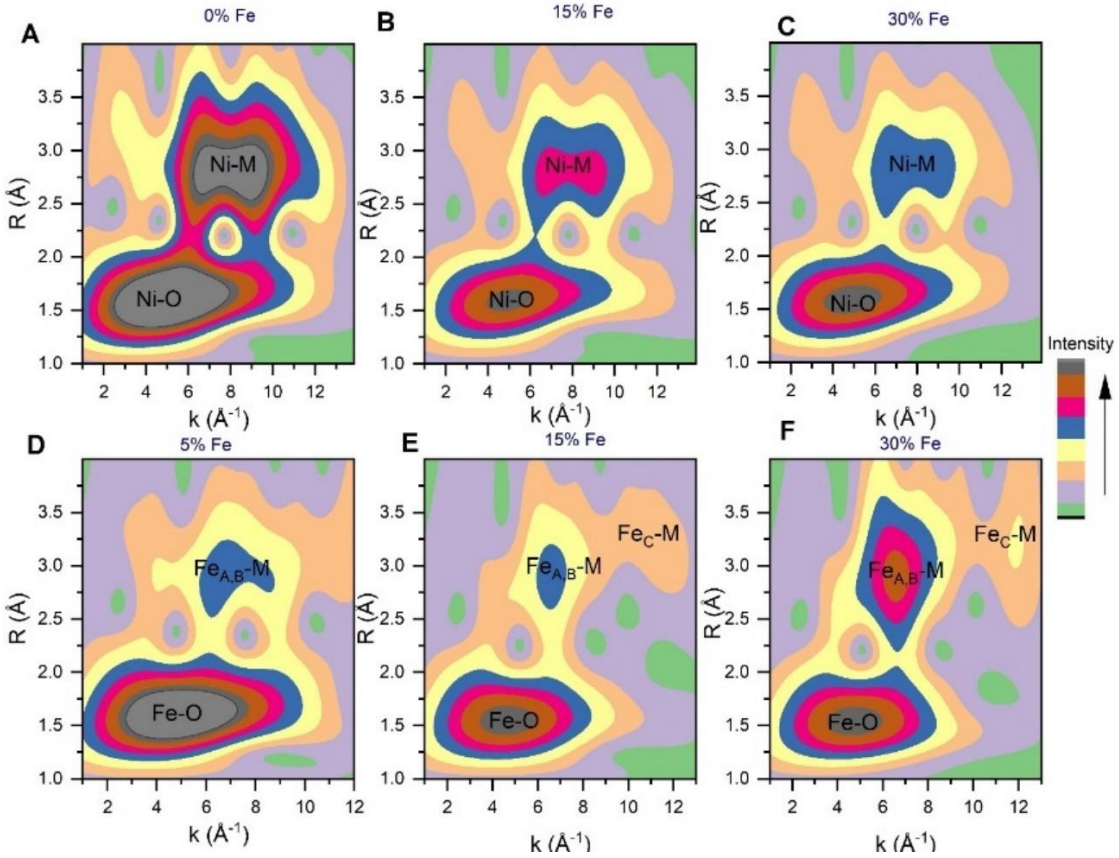

Figure 5.4 Wavelet transform analysis of $Fe_xNi_{1-x}(OH)_2$. Continuous wavelet transforms performed using a Morlet wavelet on k^3 weighted data for the Ni K-edge in **(A)** 0% Fe, **(B)** 15% Fe, **(C)** 30% Fe, and for the Fe K-edge in **(D)** 5% Fe, **(E)**15% Fe, **(F)** 30% Fe.

The M-O shells predominantly reside in the low-*k* portion of the data, while the M-M shell resides in the mid-*k* region. The intensity of the Ni-M feature decreases as Fe-content increases, which is

consistent with disorder arising from increased variation of bond distances. The Fe-M feature is instead very weak at low Fe-content and increases with Fe-content in the samples (**Figure 5.4D-F**). This growth shows two features that are separated in both *k*-space and *R*-space and are not observed in the Ni K-edge data, confirming the addition of at least two new Fe-M coordination shells.[203] This perspective on the data shows that the increased structural disorder in the nickel sites of $Fe_xNi_{1-x}(OH)_2$ samples arises due to fundamentally different structural modifications than in the Fe sites.

EXAFS reveal the differences in the Fe and Ni coordination environments and provide a secondary quantitative measure of iron distribution. Fourier-transforms of k^3 weighted data for the Ni K-edge show the features expected for a well-defined layered double hydroxide (**Figure 5.5A**): peaks at reduced *R* values of 1.85 and 2.90 Å correspond to Ni-O and Ni-M coordination shells. A peak at *ca.* 6 Å is the third M-M distance within the $Ni(OH)_2$ lattice, and the feature near 4 Å is a multi-leg path.[121,242] These features are only observable in $Ni(OH)_2$ samples that exhibit substantial long-range order. The Fe K-edge data contains the first Fe-O and Fe-M peaks but is notably missing all of the higher distance features, even for the 5% Fe which contains no observable phase contamination (**Figure 5.5B, Table C3-4**). The observation of measurable long-range order in the Ni environments but not the Fe environments demonstrate that Fe ions successfully incorporated into $Ni(OH)_2$ induce distortions that are highly localized within the lattice.

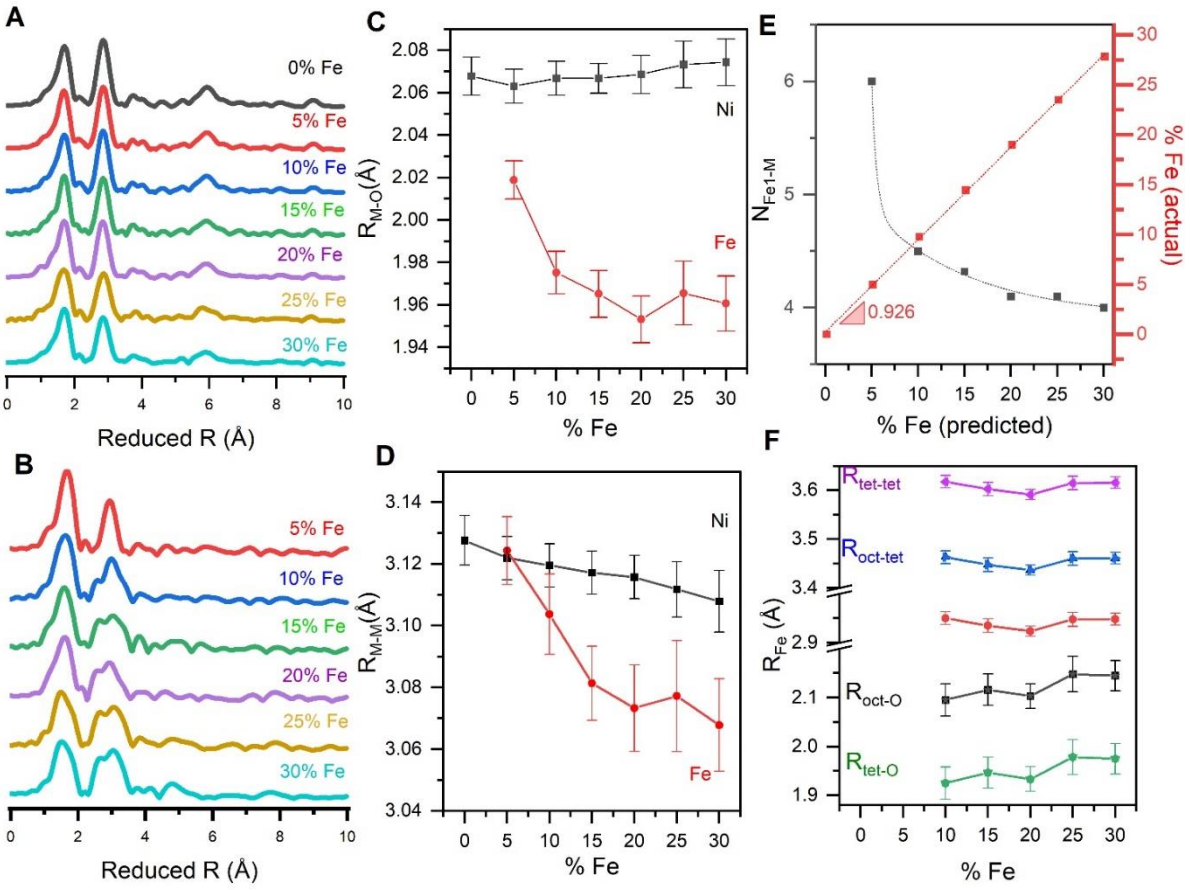

Figure 5.5 Fourier transformed EXAFS spectra of the **(A)** Ni K-edge and **(B)** Fe K-edge. Composition dependent changes in **(C)** M-O bond lengths and **(D)** M-M bond lengths for ions within the $Ni(OH)_2$ lattice. **(E)** Composition dependent coordination numbers (N) of nickel hydroxide and comparison between the theoretical and measured Fe-content within the $Ni(OH)_2$ lattice. **(F)** Composition dependent bond distances of magnetite phase.

Simulation of Ni K-edge EXAFS data provide a secondary means to quantify phase contamination across the sample series. The R_{Ni-M} shell decreases from 3.13 to 3.11 Å as Fe content increases, consistent with XRD trends (**Figure 5.1**), but the R_{Ni-O} distance shows a subtle increase from 2.068 to 2.074 Å (**Figure 5.5C and Figure 5.5D**). The Fe K-edge data is more complex due to phase contamination, with the Fe-M shell near 3 Å splitting into multiple features at 10% Fe content. Simulation of the Fe data using the brucite and magnetite crystal structures simultaneously enables

a form of linear combination analysis. In this technique, the most prominent shells expected for each crystalline material present were selected and their coordination numbers linked according to the expected crystalline stoichiometry. The coordination numbers for the octahedrally coordinated M-O shells in each of the two structures were then linked to each other, with the restriction that they sum to 6.0 between the two crystal structures. A direct measure of the weighted average of each crystal structure within the material can then be obtained through the relative coordination numbers between these octahedral shells; the Fe-M shells were similarly analyzed and found to yield consistent results. Coordination numbers are highly correlated to both the amplitude reduction factor and the Debye-Waller factors, so both were fixed for all samples. Simulations on the Fe sites show a coordination number of 6.0 for the $M(OH)_2$ structure, confirming the XRD, Raman spectroscopy and WT judgements that 5% Fe contains no detectable phase contamination. This coordination number gradually decreases to 4.0 for 30% iron content due to the formation of the contaminating phase (**Figure 5.5E**). The weighted average values can serve to quantify the amount of Fe that is successfully incorporated into the $Ni(OH)_2$ lattice (**Figure 5.5E**).

Comparisons of bond distances from the EXAFS simulations support the assertion that Fe ions induce highly localized distortions. The M-O and M-M distances are consistent between the Fe and Ni K-edge data only for the 5% Fe sample. Clear and strong trends in bond distances are observed for Fe ions within the $Ni(OH)_2$ lattice, with $R_{Ni\text{-}O}$ decreasing from 2.02 Å to 1.95 Å and $R_{Ni\text{-}M}$ shell decreasing from 3.12 to 3.06 Å. These values signify a large deviation from those in the Ni K-edge data. This is consistent with Fe ions inducing highly localized strain within the lattice. The distances between Fe atoms within the contaminating phase show only minor variations (**Figure 5.5F**), which both supports the validity of the linear combination analysis approach on the iron doped nickel hydroxides and maghemite phase and indicates that the contaminant is not intimately interfaced with the nickel hydroxide lattice.

5.2.4 Electrochemical Analysis

Cyclic voltammograms of the composition series are qualitatively comparable to commonly reported behavior **(Chapter 4.2.7)**, but notable quantitative differences exist. Voltammograms

contain a single set of pre-catalytic Faradaic peaks (**Figure 5.6A**). Structurally disordered iron-nickel hydroxide samples, such as those synthesized by anodic electrodeposition, aqueous precipitation, or photochemical decomposition, exhibit systematic anodic shift of *ca*. 2.5 mV per percent Fe for both the anodic and cathodic peaks upon Fe incorporation.[207,121,209,289] Such a shift is not observed in the hydrothermally prepared sample series here (**Figure 5.6A**). Rather, these Faradaic peaks broaden and remain approximately static with a half-peak potential of 1.38 V vs. RHE. The electrocatalytic OER capabilities of the sample series are also different, revealing a smooth composition-dependent trend rather than the frequently reported abrupt change.[121,201,209] The Tafel slope for the 0% Fe sample is measured to be 70 mV dec^{-1}, with the value linearly decreasing towards 33 mV dec^{-1} for 30% Fe (**Figure 5.6B**). Onset overpotentials show a similar linear trend, steadily decreasing from 0.2 to 0.1 V (**Figure 5.6C**). These more defined electrokinetic parameters offer a potential means to resolve structural features responsible for the classically observed decrease in Tafel slope.

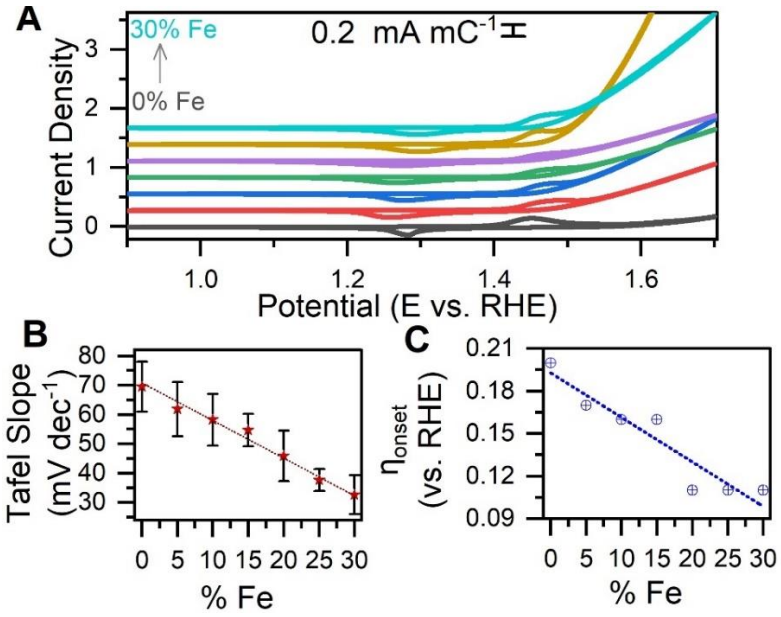

Figure 5.6 Electrochemical behavior of $Fe_xNi_{1-x}(OH)_2$. **(A)** Cyclic voltammograms of $Fe_xNi_{1-x}(OH)_2$. Composition dependent trends in **(B)** Tafel slopes and **(C)** onset overpotentials. Tafel slopes are given as the average between distinct electrodes and error bars represent their standard deviation.

5.3 Discussion

Multiple complementary techniques indicate successful incorporation of Fe(III) ions into the $Ni(OH)_2$ lattice while also providing evidence for ions in secondary phases and coordination environments. Powder XRD confirms that a single contaminating phase, attributable to either Fe_3O_4 or γ-Fe_2O_3, appears and grows in prevalence as nominal Fe-content increases (**Figure 5.1D**). Raman spectra for the sample series contain three composition-dependent peaks that are consistent with expectations for the $Ni(OH)_2$ lattice (**Figure 5.2**).[37,232] Three distinct peaks become prominent after iron is introduced: a peak at *ca.* 500 cm^{-1} that is assigned as M-O stretching following deprotonation (**Fe$_A$**; **Figure 5.2**),[232] a peak at *ca.* 700 cm^{-1} that identifies the phase impurity as γ-Fe_2O_3 (**Fe$_C$**; **Figure 5.2**),[282,290] and a peak at *ca*. 600 cm^{-1} (**Fe$_B$**; **Figure 5.2**).This third peak has been variably assigned as a second-harmonic of the E_g mode at *ca*. 300 cm^{-1},[37] to the presence of cation vacancies,[78] and to Fe(III) ions residing in a coordination environment atop the 2-dimensional sheets within $Ni(OH)_2$.[280] We assigned this Raman vibration at *ca*. 600 cm^{-1} to the presence of Fe(III) ions residing atop $Ni(OH)_2$ sheets. The details of this feature have been discussed in **Chapter 4.2.4.**

An upper bound for the stoichiometry of iron ions successfully incorporated into the $Ni(OH)_2$ lattice can be established. The phase fraction of the two crystalline species obtained by Rietveld refinement provides a measure of the distribution of Fe(III) ions in these phases, which enables calculation of Fe(III) ions successfully incorporated into the $Ni(OH)_2$ lattice (**Figure 5.7A**). This approach suggests that the real stoichiometry is *ca*. 1-2% lower than the nominal concentration (*e.g.*, 29.7% measured vs. 30% nominal). A secondary estimate of the real stoichiometry can be obtained by a restricted simulation of EXAFS results to accomplish a linear combination analysis (**Figure 5.5**). This approach provides values that are consistent, albeit slightly lower (*e.g.*, 27.8% measured vs. 30% nominal) than the values provided by XRD (**Figure 5.7A**). The calculations to derive these values include only Fe(III) ions within either $Fe_yNi_{1-y}(OH)_2$ or Fe_3O_4; an inability to

quantitatively measure the number of Fe(III) ions in the secondary site (**Fe_B**) means that these values are an overestimation.

Composition dependent structural changes measured by XRD and EXAFS indicate that Fe(III) induces a non-uniform structural compression of $Ni(OH)_2$. The metal-metal distance across di-μ-hydroxo linkages can be directly measured as the unit cell *a* parameter by XRD ($d_{M\text{-}M}$) and as the second coordination shell in EXAFS ($R_{Ni\text{-}M}$). These two measures are in excellent agreement with each other, both showing a linear contraction of 0.02 Å across the series (**Figure 5.7B**). The magnitude of contraction is notably smaller than for samples prepared by synthetic protocols that exhibit greater structural disorder, which showed a linear contraction of nearly 0.07 Å up to 21% Fe.[121,169] Uniform contraction of the crystal lattice would necessitate a concerted decrease in these di-μ-hydroxo motifs and in Ni-O distances, but Ni-O bond distances measured by EXAFS exhibit a slight increase across the composition series (**Figure 5.5C**). Direct comparison of $R_{Ni\text{-}O}$ to $R_{Ni\text{-}M}$ reveals a trend (**Figure 5.7C**) that is only possible if the coordination environments are progressively distorted with increased Fe-content. Calculation of the O-Ni-O bond angles within the 2-dimensional sheets using $R_{Ni\text{-}O}$ and $R_{Ni\text{-}M}$ values which reveals the distortion to be an increased bond angle (**Figure 5.7D**).[121,291]

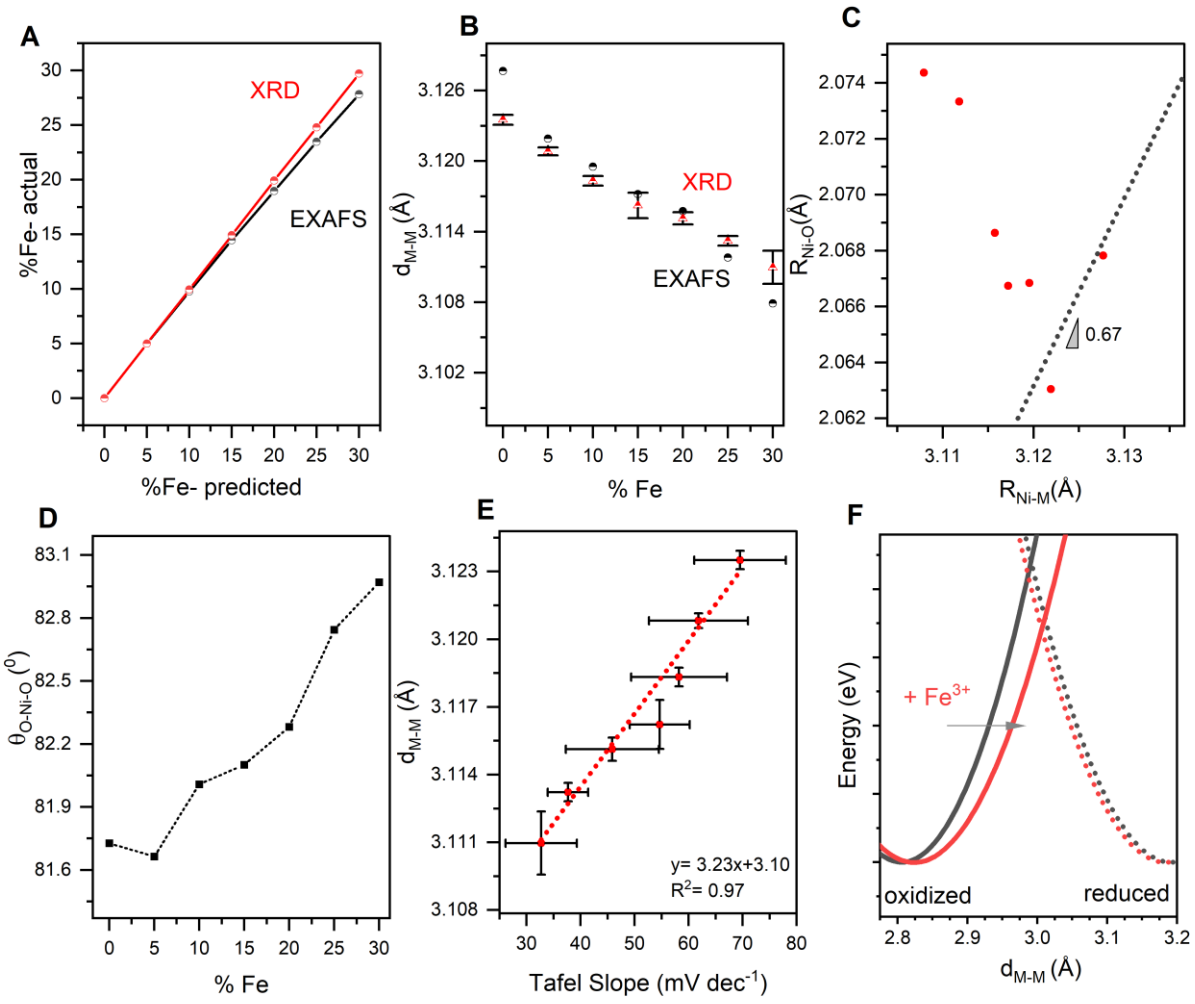

Figure 5.7 Correlational analysis with different characterization techniques. **(A)** $d_{M\text{-}M}$ comparison calculated by Rietveld refinements and EXAFS simulations. **(B)** %-actual- Fe calculations by Rietveld refinements and EXAFS simulations. **(C)** The relationship between $R_{M\text{-}M}$ and $R_{M\text{-}O}$ obtained from EXAFS. **(D)** The angles of edge-sharing O-M-O of Ni and Fe sites. **(E)** Correlation between $d_{M\text{-}M}$ and Tafel slope. **(F)** Potential energy surfaces of $Ni(OH)_2$ and $Fe_xNi_{1-x}(OH)_2$.

While the composition dependent structural features in this sample series are qualitatively comparable to those frequently reported in the literature, their effect on electrochemical behavior is notably different. The two most prominent changes in electrochemical behavior commonly reported for Fe(III)-doped $Ni(OH)_2$ are an anodic shift in the pre-catalytic redox peaks and a

stepped decrease in Tafel slope for electrocatalytic OER. The shift in redox peak has been documented for sample series prepared by anodic electrodeposition,[289] cathodic electrodeposition,[252] and photodeposition,[121,209] occurring at a rate of *ca.* 2-4 mV per percent Fe added, but appears somewhat dependent on fabrication protocol.[292] In the present study, this peak differs by showing remarkable stability. The second expected change is a strong decrease in Tafel slope towards *ca*. 30 mV dec^{-1}, which has been shown to occur even by simple exposure to Fe(III) impurities in the electrolyte solution at a parts-per-billion levels.[36,160] Existing reports show this transition to be essentially an on-off switch, providing little means to study the transition in detail. In the present study, the Tafel slope is found to linearly decrease as a function of metal-metal spacing across di-μ-hydroxo linkages (**Figure 5.7E**); because $d_{M\text{-}M}$ and the O-M-O bond angles are themselves linearly correlated, this relationship also links Tafel slope to bond angle changes. This relationship is not compatible with traditional microkinetic analyses of electron transfer reactions, which relate a static Tafel slope to a rate limiting steps.[19,196,293] A more advanced model of electron transfer kinetics is required to understand this behavior.

The observed linear trends in Tafel slope necessitates a systematic change in the relative activation energy for the oxidizing and reducing half-reactions with increased Fe-content. The Butler-Volmer formalism, which oversimplifies reality by approximating potential energy surfaces to be linear, captures this concept through an empirical fraction, α. Asymmetric Marcus-Hush theory has emerged as a more complex, but physically meaningful model. This approach uses a more realistic parabolic shape for potential energy surfaces (PES) and formalizes the original a parameter:

$$\alpha(E) = \frac{1}{2} + \gamma\left(\frac{1}{4} - \frac{1.267}{\Lambda + 3.353}\right) \qquad \textbf{(5.1)}$$

where Λ is the reorganization energy from Marcus-Hush theory and γ is a fraction representing the relative shape of the two parabolic PES.[294–297] A broader PES surface for the PES of the oxidized state, which has been predicted to arise upon Fe-doping,[209] would yield a negative value for γ. The

observed linear decrease in Tafel slope may therefore be attributable to a systematic increase in lattice strain as Fe-content increases. This relationship is of interest because it provides a practical system which can be used to explore the utility of asymmetric Marcus-Hush theory in electrokinetic analyses in solid-state electrochemistry. It also provides a viable explanation for the observed differences between ordered and disordered $Fe_xNi_{1-x}(OH)_2$ sample series: the localized nature of lattice strain induced by Fe(III) ions is not experienced by most nickel centers in well-crystallized materials, while the smaller platelet size expected for more disordered phases makes strain effects prominent at much lower Fe(III) concentrations.

5.4 Conclusion

A hydrothermal approach was used to fabricate a well-crystallized composition series of $Fe_xNi_{1-x}(OH)_2$, which exhibited similar structural features to their commonly reported disordered counterparts but different electrochemical behavior. Raman spectroscopy, XRD and XAS revealed that the majority of Fe(III) ions were successfully incorporated within the $Ni(OH)_2$ framework, with minor distribution into an iron oxide phase impurity and a secondary coordination site atop the 2-dimensional $Ni(OH)_2$ framework. Qualitatively similar composition-dependent changes in structure and electrochemical characteristics were similar to those commonly reported for disordered forms of $Fe_xNi_{1-x}(OH)_2$, but were markedly different in a quantitative sense. The pre-catalytic redox peak showed little movement following Fe(III) incorporation and, more importantly, the Tafel slope showed a linear decrease with respect to both M-M spacing and to O-Ni-O bond angles. This unexpected behavior is rationalized using asymmetric Marcus-Hush theory, where lattice strain induced by Fe(III) ions alters the relative symmetry of potential energy surfaces for the oxidized and reduced states of the material. These results identify a system that is of interest for advancing more complex theories of electron transfer kinetics in solid state materials while simultaneously rationalizing the significant differences in behavior between well-crystallized and disordered forms of $Fe_xNi_{1-x}(OH)_2$.

5.5 Experimental

5.5.1 Materials

Nickel chloride hexahydrate ($NiCl_2.6H_2O$) (Fisher Chemical), ferric chloride ($FeCl_3$) (Fisher Chemical), sodium hydroxide, and potassium hydroxide (NaOH and KOH) (Sigma-Aldrich) were used as received. All H_2O used during fabrication was milli-Q H_2O (18.2M Ω).

5.5.2 Hydrothermal Synthesis

A total metal concentration of 0.6 M of appropriate amounts of nickel chloride hexahydrate and ferric chloride and 40 ml solution of 5 M potassium hydroxide is added into a Teflon autoclave. The reactor was first heated to 140 ^{0}C with 5 ^{0}C/min increments and held for 16 hours. Then, the supernatant is removed, and solid particles were washed with Milli-Q water and added into an autoclave with 40 ml of Milli-Q water and heated to 170 ^{0}C with 10-degree/min increments and held for 16 hours. The final product is vacuum filtrated and rinsed with water and ethanol. Powder products were obtained after samples were dried in an oven at 200 ^{0}C for two hours.

5.5.3 Electrochemistry

All of the instrumental information, experimental details are the same with **Chapter 4.4.2**.

5.5.4 X-ray Diffraction

Experimental details of the powder XRD experiment are stated in **Chapter 2.2.2.**

5.5.5 Raman Spectroscopy

Experimental details of the Raman spectroscopy measurements are stated in **Chapter 2.2.5.2.**

5.5.6 X-ray Absorption Spectroscopy

The instrumental information can be found in **Chapter 4.2.6**.

Ni and Fe K-edge locations were determined by half-height method (**Table C.1**). The Artemis software package was used to generate structural models by simulation of k^3 weighted EXAFS

results from k of 3 to 15 $Å^{-1}$ and 3 to 13 $Å^{-1}$ for Ni K- edge and Fe K edge respectively (**Figures C.2-3**). All simulations were performed with an amplitude reduction factor of 0.8 for all of the samples. Fixed coordination number (N_i) of 6 was used for the Ni shell and varying values between 6-4 for the incorporated Fe site and from 0 to 2 for the Fe_3O_4 phase (**Tables C.2-3**). The Debye-Waller factor (σ^2) was fixed at 0.006 $Å^2$ for nickel and iron shells and 0.004 $Å^2$ for oxygen shells for the nickel shell. The σ^2 values for Fe shells are 0.011 and 0.007 for layered double hydroxide and 0.002 and 0.0035 for magnetite Fe-M and Fe-O shells respectively. A constant value of Eo is used for Ni 8113 eV and iron 7112 eV.

MorletE program is used for Wavelet transform (WT) analysis. In WT expression η and σ are two adjustable parameters for the resolution of spectra. Typically, $\eta . \sigma \approx 2R$ where r is the magnitude of the region of interest in the R-space. We used 30 for η and 0.2 for σ following the values in the literature.[298] The k-ranges are 1-14 $Å^{-1}$ for Ni K-edge and 1-12 $Å^{-1}$ for Fe K-edge. The R-ranges are between 1-4 Å for both edges.

Chapter 6

Correlating Structure and Activity of Cobalt Hydroxides

6.1 Introduction

Cobalt-based materials are one of the most extensively studied inorganic materials as electrocatalysts. Among those, cobalt hydroxides are regarded as one of the prime candidates along with their isostructural materials such as nickel and iron hydroxides for water splitting application owing to their tunable electronic structure, morphology, and a large number of electroactive sites. $Co(OH)_2$ adopts brucite structure and upon iron doping, they become isostructural with hydrotalcite. Iron incorporation into cobalt and nickel hydroxide host lattices converts ordinary electrocatalysts into one of the best in alkaline medium for OER.

Iron doped $Co(OH)_2$ is studied with in-situ and operando techniques to gain a more detailed understanding of material behavior during the reaction. Liu and co-workers presented that during OER, tetrahedral sites become more suitable than octahedral sites in spinel Co_3O_4 for the formation of electroactive CoOOH.[299] Another study demonstrated that electroactive cobalt sites are found to be mainly trivalent but partly tetravalent states in electrochemically deposited amorphous hydrated cobaltates (Co-Pi) that are akin structures to $Co(OH)_2$ with their CoO_6 octahedra layers.[190,217,300–303] Formation of tetravalent Fe sites detected by Mössbauer and XAS spectroscopy is shown the promotion of OER through cobalt sites.[304] Single crystalline β-$Co(OH)_2$ has trivalent cobalt sites that condensed at the edge sites of the platelets.[305] Photodeposited $Co(OH)_2$ films have multiple electroactive sites that directly and indirectly affect the OER mechanism.[131] Diverse

arguments on the evolution of the electrocatalytically active sites increase in importance of the formation of diversified coordination sites is an important descriptor for determining the mechanisms. Stability tests demonstrated self-healing and self-repairing processes take place as iron sites continually dissolved and redeposited during OER in cobalt-based catalysts.[211,306] Several coordination environment tuning strategies are suggested to improve OER performance of cobalt based electrocatalyst, including the formation of oxygen vacancies[307], amorphization[308], phase controlling synthesis[309], and composition tuning.[131,310–312] Studies focused on the direct effect of iron on the electrochemical activity CoFe LDHs show diverse arguments: iron replaces electroactive cobalt sites[312,313], or FeO_6 acts as electroactive sites in CoOOH[314], or synergistic effect between Co and Fe sites.[315] The diversity of the structure and drawn conclusions on the critical role of iron in the cobalt hydroxides require a more systematical analysis of the structure and its reflection on the electrocatalysis.

Herein, we fabricated the nominal composition of iron incorporated cobalt hydroxides [$Fe_xCo_{1-x}(OH)_2$] with hydrothermal, co-precipitation in aqueous and formamide solution environments and investigated their OER activities. While samples synthesized with the presence of formamide adopt a LDH structure and have the highest rate of iron incorporation into the lattice, the iron incorporation is the smallest, and therefore electrochemical performance is limited by the partial iron incorporation for the hydrothermal series. Moreover, water series is affected by the stability limit of the cobalt sites and are inclined to oxidize into CoOOH structure when iron amount is less than 20%. Compared with other brucite structures, these results suggest that $Co(OH)_2$ differs from other LDH type materials because of their stability limits, electronic structures, iron incorporation, and electro catalytic behaviors.

6.2 Results

We fabricated three series of powder $Fe_xCo_{1-x}(OH)_2$, where x is varied from 0 to 0.3 in steps of 0.5 with aqueous pH co-precipitation, pH co-precipitation with 30% v/v formamide solution, and hydrothermal methods. These methods were intentionally tried to see the effect of the fabrication technique on the structure and electrocatalytic performance of the materials. The samples were

tested with XAS at Brookhaven National Laboratories (BNL) one month after their synthesis because they were shipped from the University of Waterloo to the synchrotron facility. All the samples were confirmed in metal hydroxide structure in the initial assessment with XRD immediately after the synthesis. All samples in the formamide series and most of the water and hydrothermal series preserve their LDH structure over a month under ambient conditions. However, some samples in water and hydrothermal series were found to oxidize into CoOOH under ambient conditions during sample transportation and after XAS experiments. All results and discussion in the following sections are based on the final structures for all samples.

6.2.1 X-ray Diffraction

Powder X-ray diffraction patterns of three sample series exhibit distinct structural aspects (**Figure 6.1A-C)**. Before sending all samples to BNL for XAS characterization, all samples were in α or β–$Co(OH)_2$ morphology. Hydrothermal and water series have β-$Co(OH)_2$[316] (ICSD: 88940) with hydrothermal series having higher crystallinity than water series (**Figure 6.1A-B**). One month after synthesis, XRD patterns of the sample series reveal that 5% Fe in hydrothermal synthesis and the first four lowest Fe incorporated in the water series are partially oxidized. The main crystal structure becomes CoOOH[317] (ICSD: 22285). Partial oxidation typically occurs in $Co(OH)_2$, especially at higher cobalt substances.[318–321] The samples in the water series have the combination of both β-$Co(OH)_2$ and CoOOH phases for 20, 25 and 30% Fe concentrations with β-$Co(OH)_2$ is the prominent phase. (**Figure 6.1D**). Samples after $Fe_{0.1}Co_{0.9}(OH)_2$ have an additional peak at 11^0 which is reminiscent of α-$Co(OH)_2$ (003) plane. Two distinct interlayer distance values point out the presence of stacking fault disorders for the water series.

The formamide sample series yields a diverse arrangement and less crystalline structure than the other two series **(Figure 6.1C).** XRD patterns of the formamide series are consistent with α-$Co(OH)_2$ structure and comparable with each other across the data set. α-$Co(OH)_2$ is isostructural with hydrotalcite-like structure which is consist of positively charged cobalt layers and charge balancing anions[76] (ICSD: 86655).

Apart from these features, the hydrothermal series has additional peaks at 31, 36, 44^0. The intensity of these peaks increases as Fe content increases beyond $Fe_{0.1}Co_{0.9}(OH)_2$. [**Figure 6.1**A, shown with an asterisk (*)]. Peak locations are consistent with the three most intense peaks of either magnetite[322] (Fe_3O_4, ICSD: 49549) or maghemite[323] (γ-Fe_2O_3, ICSD: 35643) phases. The crystal structure of the two compounds is similar to each other and therefore, the certain identity of this phase is not certain according to XRD patterns. According to the relative intensities of the contaminant phase, iron sites in the hydrothermal sample series do not fully incorporate into the cobalt lattice after $Fe_{0.05}Co_{0.95}(OH)_2$ iron. The characteristic of the contamination is similar in NiFe hydroxides synthesized in hydrothermal conditions in **Chapter 5** (**Figure 5.1**)

The crystal structure of both $Co(OH)_2$ and CoOOH structures consists of octahedrally coordinated through di-μ-(hdr)oxo bonds. Two essential unit cell parameters, *a* and *c*, provide bond distances and interlayer spacing. CoOOH consists of trivalent metal species so intermetallic distances (d_{M-M}) are shorter than $Co(OH)_2$ structure. The distances are measured corresponding to the positions of $d_{(110)}$ plane with **equation 4.1 (Chapter 4.2.5)**.

The hydrothermal sample series possesses the longest d_{M-M} distance, which is stabilized at around 3.18 Å. A single sample, $Fe_{0.05}Co_{0.95}(OH)_2$, oxidized such that it has an intermetallic distance of 2.86 Å. The distance did not show a strong correlation between the iron amount added during the synthesis. Similarly, the water series has 2.85 Å for undoped CoOOH, and the value slightly increases to 2.86 Å for $Fe_{0.15}Co_{0.85}(OH)_2$. A step change in distance to 3.17 Å is seen for $Fe_{0.2}Co_{0.8}(OH)_2$, after which a stable at 3.16 Å is observed (**Figure 6.1E**). The formamide sample series experiences a unique change in metal-metal distances from 3.08 Å to 3.13 Å for 0 to 20% Fe incorporation. The distance maintains at around this value with higher iron concentrations.

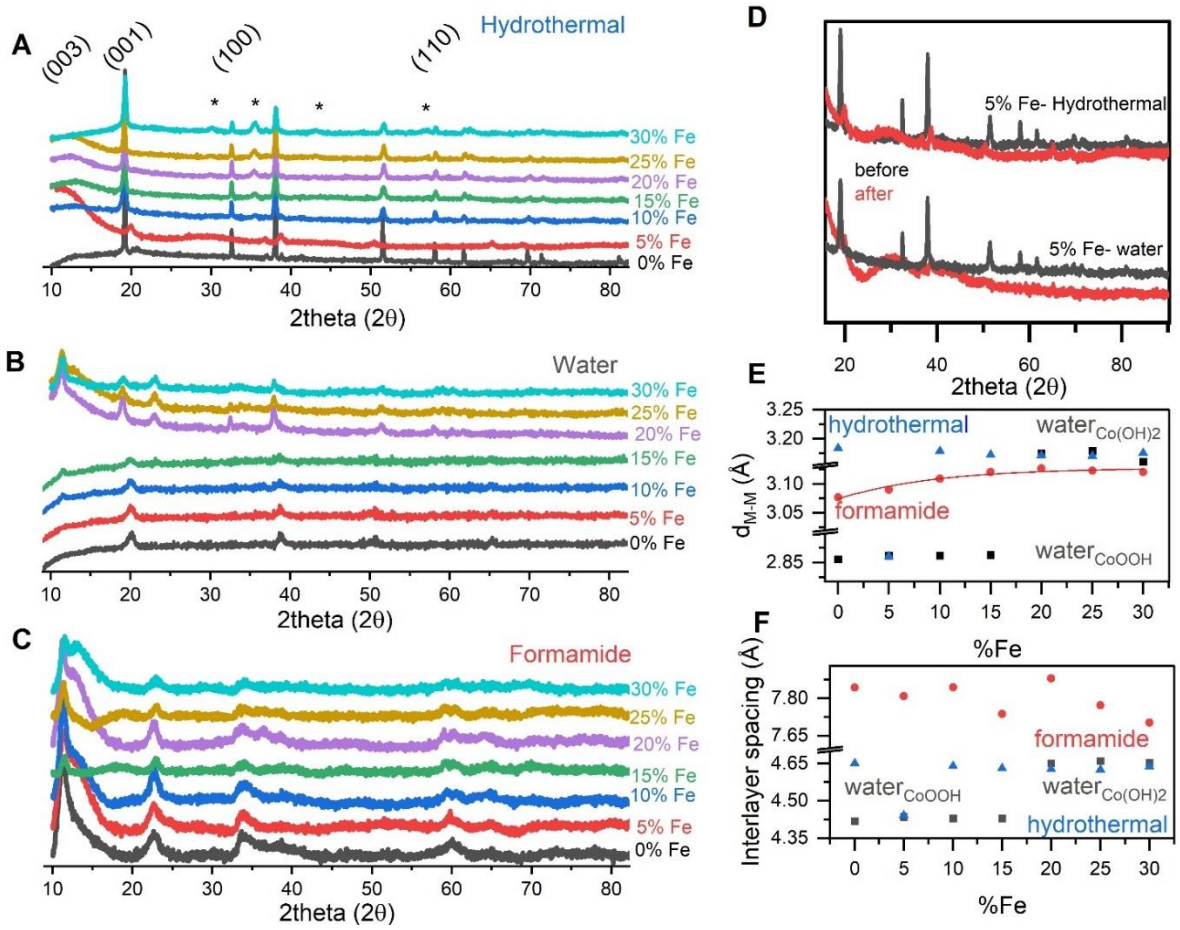

Figure 6.1 P-XRD analysis of $Fe_xCo_{1-x}(OH)_2$. Experimental XRD patterns for **(A)** hydrothermal, **(B)** water, and **(C)** formamide composition series. **(D)** Comparison of the XRD patterns of $Fe_{0.05}Co_{0.95}(OH)_2$ for water and hydrothermal series before and after synchrotron. **(E)** Composition dependence of metal-metal distances (d_{M-M}) in edge-sharing polyhedra. **(F)** Composition dependence of interlayer spacing (d_{001}). Iron oxide peaks are shown with an asterisk (*).

The *c*-parameter determines the basal spacing of these structures. CoOOH and hydrotalcite structures have (003) plane in XRD pattern, and $Co(OH)_2$ has (001) plane. After the stabilization of three sample series the interlayer distance of water and hydrothermal sets are steady at *ca.* 4.45 Å and 4.65 Å for CoOOH and $Co(OH)_2$ phases respectively. (**Figure 6.1E**). The formamide sample series has a transition from 7.85 to 7.65 Å for undoped and 30% Fe doped samples

respectively. The decreasing trend indicates that the increasing iron content decreases the positive charge and therefore interlayer attractions weaken.[321]

6.2.2 Raman Spectroscopy

Raman spectra of all three samples reveal a complex mixture of $Co(OH)_2$, CoOOH and/or spinel Co_3O_4. The blend of multiple phases limits to make a systematic peak analysis specifically for water and hydrothermal series. Raman spectra of cobalt hydroxide[324,325] and CoOOH are further complicated by their tendency to be transformed into the spinel Co_3O_4 with laser irradiation. The similar effect has been observed for CoO rock salt oxidation into Co_3O_4 due to energy transfer and therefore local heating with applied laser.[324] In order to avoid these issues, patterns were acquired under weak laser powers still, comparison with XRD patterns indicates that some samples might be transformed into Co_3O_4.

The predicted vibrations of $Co(OH)_2$ are located at *ca.* 455 cm^{-1} which is previously assigned as OCoO bending vibrations.[326] The next peak is the most intense vibration located at 520 cm^{-1}, attributed to A_{1g} CoO symmetric stretching vibrations.[315,327] In addition to these vibrations, another stretch at *ca.* 470 cm^{-1} is also reported for $Co(OH)_2$ related vibrations.[328] Hydroxide stretching vibrations (υ_{OH}) are located at 3570 cm^{-1}. Most of the samples across three different sample series support the formation of $Co(OH)_2$ as the major phase (**Figure 6.2**).

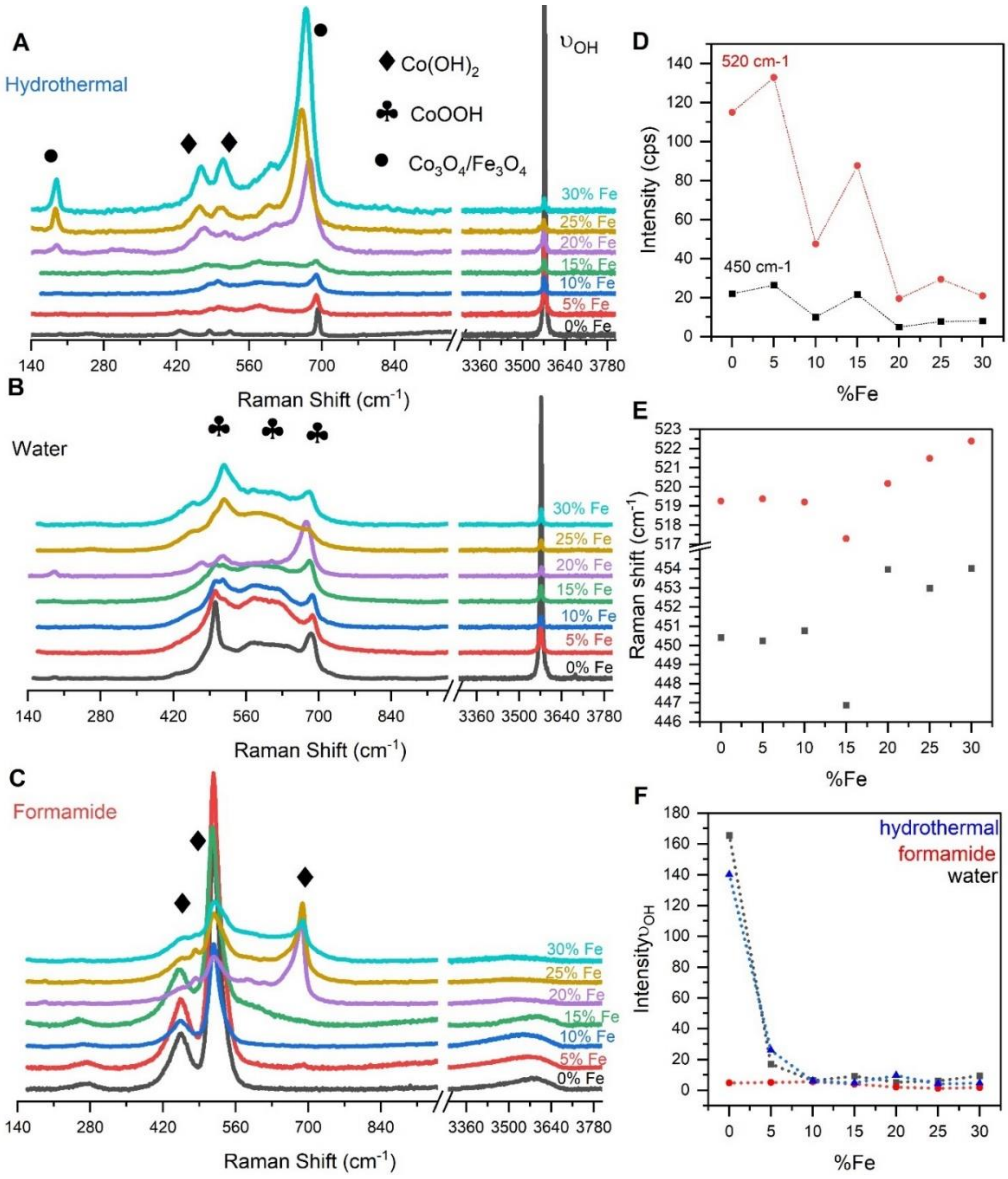

Figure 6.2 Raman spectra of $Fe_xCo_{1-x}(OH)_2$ for **(A)** hydrothermal, **(B)** water, and **(C)** formamide composition series. Composition dependence of **(D)** peak intensity and **(E)** peak locations of 450 and 520 cm^{-1} vibrations of formamide series. **(F)** Composition dependence of hydroxide vibrations (ν_{OH}) intensity.

The most prominent $Co(OH)_2$ peaks are observed in the formamide sample series. As the peaks are easily identified in formamide series, the peak locations and peak intensity changes reveal

composition dependent changes (**Figure 6.2C**). The intensity of both peaks decrease as more iron is introduced to the host lattice and the peak at 520 cm^{-1} peak is more under the influence of composition (**Figure 6.2D**). Both peaks are approximately 4 cm^{-1} blue-shifted with iron incorporation (**Figure 6.2E**). Both of these properties are likely due to the deprotonation of $Co(OH)_2$ caused by Fe^{3+} incorporation. After 20% Fe, an intense peak arises at 689 cm^{-1}, this peak may be either an A_{1g} mode of amorphous $Co(OH)_2$[329,330] or of the spinel Co_3O_4 structure. Characteristic Co_3O_4 peaks are located at 194, 480, and 688 cm^{-1}. The peak at 194 cm^{-1} is F_{2g}, the most intense peak located at 686 cm^{-1} peak is A_{1g}, and 480 cm^{-1} is the E_g mode of the spinel phase.[326,331] The intensities of peaks at 480 and 194 cm^{-1} are typically more intense for the 688 cm^{-1} peak. The lack of peaks at 194 and 480 cm^{-1} therefore suggest that the peak at 688 cm^{-1} indicates the presence of disordered $Co(OH)_2$ rather than the spinel structure. Iron incorporation causes deprotonation of the $Co(OH)_2$ lattice and therefore the formation of a more disordered structure is not surprising.

The water sample series exhibit both CoOOH and $Co(OH)_2$ associated vibrations (**Figure 6.2B**). Samples that have iron concentration of less than 20%, exhibit mainly CoOOH peaks. The most intense peak of CoOOH is at around 503 cm^{-1}. The other typical CoOOH vibrations are located at around 570, 640 and 705 cm^{-1}.[326] After 20% Fe, peaks at around 450 and 520 cm^{-1} prevail. These values are attributable to $Co(OH)_2$. Corresponding to these assignments water sample series are mainly CoOOH at lower iron concentrations. At higher concentrations, it is a mixture of $Co(OH)_2$ and CoOOH, as confirmed by XRD patterns and XAS simulations in the following sections.

The hydrothermal sample series has the combination of $Co(OH)_2$, spinel Co_3O_4, or Fe_2O_3 phases. The magnitude of cobalt or iron oxide peak increases with the increasing iron concentration (**Figure 6.2A**). However, the most intense A_{1g} peak location is not coherently shifted from 690 cm^{-1} to 665 cm^{-1}. The inconsistency between these peaks indicates that the hydrothermal set may have more than oxide phases. As noticed in XRD and XAS magnetite or maghemite is formed as a contaminant phase at higher iron concentrations and the peak at 670 cm^{-1} for 30% iron is pairs with the most intense peak of Fe_2O_3.[332]

In addition to these variations, hydroxide stretching vibrations for formamide series reveal differences from the other two sample series. β-$Co(OH)_2$ has υ_{OH} vibrations at 3571 cm^{-1}, for the formamide sample it is dramatically less intense and broad (**Figure 6.2**). The formamide hydroxide vibrations exhibit typical α-$Co(OH)_2$ υ_{OH} characteristics. Furthermore, the peak intensity of υ_{OH} significantly diminishes as iron start to integrate into the host lattice and becomes steady after $Fe_{0.05}Co_{0.95}(OH)_2$ in water and formamide series (**Figure 6.2E**). The difference in the peak intensity can be attributed to iron induced deprotonation of the $Co(OH)_2$ lattice.

6.2.3 X-ray Absorption Spectroscopy

6.2.3.1 XANES

Composition dependent trends in Co and Fe K-edge XANES indicate a change in the electronic and geometric structure of Co and Fe coordination environments. The pre-edge locations of all species are determined by the first derivative of the XANES spectra. Cobalt pre-edge features are consistently located at 7709 eV for all three sets of the samples (**Figure 6.3A-C-insets**). Pre-edge features are associated with 1s to 3d transitions and the peak at 7709 eV is attributed to transitions of cobalt. In addition to this peak, for some specific samples another peak arises at 7706 eV, it is previously assigned as trivalent octahedrally coordinated cobalt species, 1s to 3d e_g transition[333] or the second 1s to 3d transition with greater oxygen 2p orbital mixing.[334] Since these peaks are the most intense for 30% Fe samples in water and formamide series which do not have trivalent cobalt species, we assigned this peak to the latter assignment. Fe pre-edge features for the water and formamide series are similar to each other (**Figure 6.3E-G**). The pre-edge peak for lower iron incorporated water and formamide series splits into two peaks at 7112.7 and 7114.2 eV. Peaks start to combine and centered with higher intensity at 7113.4 eV for iron percentages higher than 20%. However, values are steadily placed at 7113.2 eV for the hydrothermal series and the shape of the peak becomes sharper than the other two series. Differences in pre -edge location and peak shape indicates differences in geometric structures of iron sites in hydrothermal set. Moreover, all

Fe pre-edge peaks have composition dependent intensity, and this is attributed to the greater 3d-4p mixing with higher iron concentration.

Cobalt K-edge locations show distinct features, firstly, water edge locations have a decreasing trend from 7721.0 eV to 7718.1 eV for iron-free and $Fe_{0.2}Co_{0.8}(OH)_2$ samples respectively (**Figure 6.3D**). The edge location is directly proportionate to the oxidation state. The location of the edge shifts to higher energy as the oxidation state increases. The pure cobalt hydroxide sample synthesized in the water has the highest value, at 7721.0 eV, which matches previously reported values for trivalent cobalt samples such as $LiCoO_2$ (7721.2 eV) and CoOOH (7721 eV).[335] Decreasing trends point out the mixed valency, and confirm the hybrid structure of $Co(OH)_2$ and CoOOH . The step-by-step decrease in the edge energy indicates that cobalt cations are stabilized in a divalent state with iron incorporation. Previous reports demonstrate that a 2.3 eV shift is expected per oxidation state change at cobalt centers.[131,335] According to this relation, we observed a change in the oxidation state of 0.8 in the transition region. The change in the oxidation state of cobalt sites confirms the presence of $Co(OH)_2$-CoOOH hybrid structure. After 20% Fe, Co ions are stabilized at *ca.* 7718 eV, which confirms the presence of mostly divalent cobalt in $Co(OH)_2$ structure. The hydrothermal and formamide sample series edge locations are mainly located at 7718 eV, and except for $Fe_{0.05}Co_{0.95}(OH)_2$ in the hydrothermal series. The lack of composition dependent trends in Co K-edge also confirms the stability of Co(II) in these samples.

Iron K-edge locations have a composition dependent decreasing trend in all three sets of the samples (**Figure 6.3H**). The rate of decrease is 0.033, 0.014, and 0.012 eV per percent of iron for formamide, hydrothermal, and water series, respectively. While the hydrothermal sample series yield lower K-edge values at around 7123.5 eV, it is at 7124.5 eV for $Fe_{0.05}Co_{0.95}(OH)_2$, and 7123.5 eV for $Fe_{0.3}Co_{0.7}(OH)_2$ incorporated sample for the formamide series. K-edge locations for the water series are in the middle region between the formamide and hydrothermal series. They have similar values to the formamide series in the mid composition region. Fe K-edge structures in these sample series have a non-uniform trend similar to that seen for NiFe samples described in **Chapters 4-5**. The changes in edge shape indicate that the sample series are under the effect of changes in the

coordination environment rather than oxidation state changes. The changes in pre-edge and edge shapes suggest that iron coordination sites undergo a change in the symmetry upon addition of iron into cobalt hydroxide lattice.

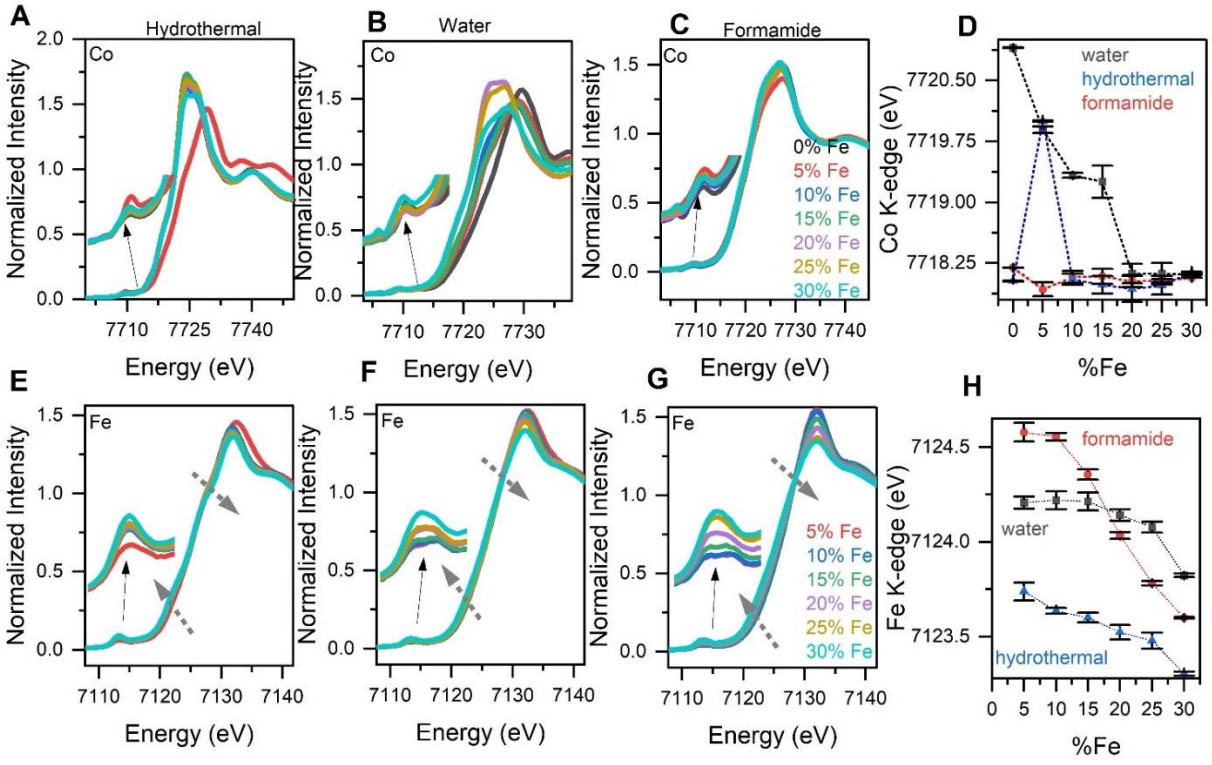

Figure 6.3 X-ray absorption near-edge spectra for $Fe_xCo_{1-x}(OH)_2$. XANES spectra of Co K-edge of **(A)** hydrothermal, **(B)** water, **(C)** formamide sample series. **(D)** Composition dependent trends in Co-K edge locations. XANES spectra of Fe K-edge of **(E)** hydrothermal, **(F)** water, **(G)** formamide sample series. **(H)** Composition dependent trends in Fe-K edge locations.

6.2.3.2 EXAFS

Extended X-ray absorption fine-structure (EXAFS) spectra of Co and Fe K-edge reveal the differences in coordination environments across three composition series. The general strategy of the fitting process is the group fitting approach in which fixing the Debye-Waller factor (σ^2) for M-O and M-M shell, amplitude reduction factor (S_o^2), and E_o to specific numbers for Co and Fe

K-edges and fitting R_{M-O}, R_{M-M}, $N_{M-O,}$ and N_{M-M} for each sample in the composition series (**Table D.2-Table D.7**). Fourier transformed k^3-weighted spectra for Co K-edge confirms the formation of $Co(OH)_2$ or CoOOH structures for all three sets of the samples (**Figure 6.4A-C**). Most of the samples are in $Co(OH)_2$ form, with two main coordination shells at 2.10 Å for M-O and 3.15 Å for M-M shells. Exceptions are the samples that noted to oxidize, including the $Fe_{0.05}Co_{0.95}(OH)_2$ hydrothermal sample, and 0-15% Fe samples in water series. These samples are CoOOH, with 1.90 Å for the M-O and 2.85 Å for the M-M coordination shells. Only hydrothermal series in LDH structure have additional peaks at around 4 Å which indicates the second coordination shells and long-range order in cobalt environments (**Figure 6.4A**). In these samples Co-O and Co-M shells are located at *ca.* 2.10 Å and 3.18 Å respectively. Co-M shells slightly decrease to 3.16 Å upon Fe incorporation **(Figure 6.4B and E)**. The formamide series reveals that there are two main peaks for both cobalt and iron K-edges (**Figure 6.4C and F**). Simulations on both Co and Fe K-edges edges show that the sample series are well-matched with LDH structure. Composition dependent trends show that M-M distances transitions from 3.09 to 3.11 Å for pure and 30% Fe samples respectively.

Fe K-edge spectra in R space indicate three diverse Fe coordination environments in three synthetic approaches. The Fe-O and Fe-M shells in the formamide series consistently match with Co-O and Co-M shells, indicating the proper incorporation of iron cations into the host lattice. The hydrothermal series has several Fe-O distances at 1.94, 2.06, and 1.79 Å and Fe-M distances at 3.02, 2.95, 3.46 and 3.62 Å. These multiple values for each shell indicate the contaminant phase as observed in XRD and Raman spectroscopy. According to the coordination shells of the segregated phase, the extra iron environment belongs to the magnetite structure, confirming XRD and Raman spectra. Magnetite structure has the combination of divalent and trivalent iron environments. Therefore, two Fe-O exist for tetrahedrally coordinated with a distance of 1.79 Å and octahedrally coordinated at 2.06 Å. Similarly, three Fe-M distances are expected for the second shell. The distances are 2.95 Å for tetrahedral-tetrahedral, 3.62 Å for octahedral-octahedral, and 3.46 Å for tetrahedral-octahedral scattering paths. The series can be fitted as a mixture of brucite

and Fe_3O_4, indicating that iron incorporation is not effective after 5% Fe for hydrothermally synthesized $FeCo(OH)_2$. Iron environments for the water series, on the other hand, have two Fe-O distances at 1.97 and 2.03 Å and 2.88 and 3.10 Å for Fe-M shell. Although one main peak for Fe-O shell is observed for all sample series, peak shapes of Fe-O shells of 10, 15 and 30% Fe samples is different than Co-O shells. When iron concentration increases, coordination shells start to match with the LDH structure. Fe and Co shells at higher iron concentrations exhibit similar properties.

Wavelet transform diagrams of the sample species of these samples could not successfully resolve the fine details of the diverse Co and Fe coordination sites since the atomic mass of cobalt and iron is very close to each other **(Figures D.2-D.3).** Simulations of the EXAFS spectra nonetheless support the formation of the composition-dependent unique structural motifs around Co and Fe local coordination environments for three sample series.

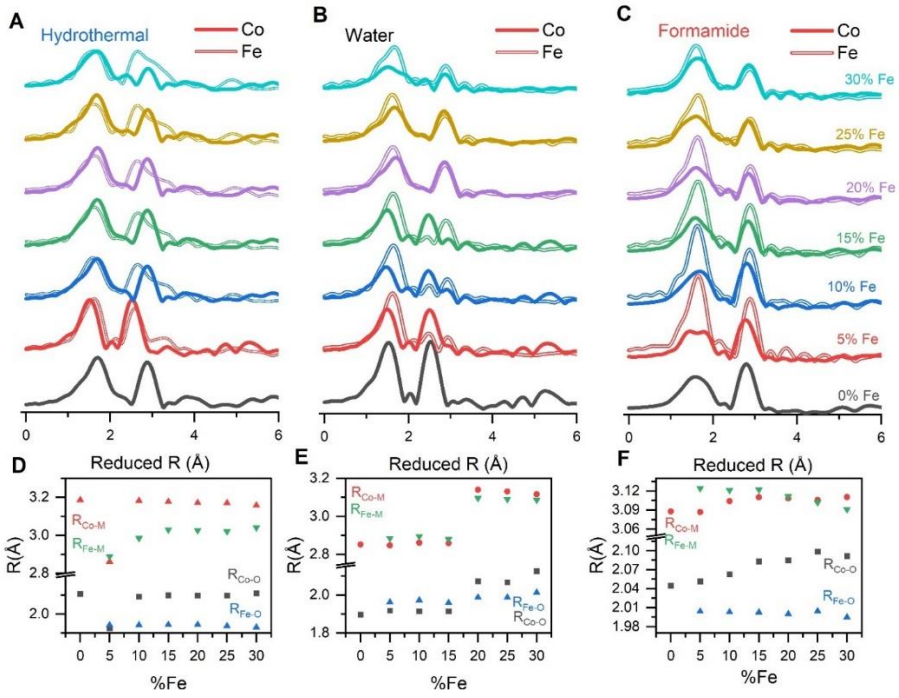

Figure 6.4 Extended X-ray absorption fine-structure spectra for three $Fe_xCo_{1-x}(OH)_2$ composition series. Fourier transformed EXAFS results for **(A)** hydrothermal, **(B)** water, and **(C)** formamide sample series. Composition dependent trends in R_{M-M} and R_{M-O} in **(D)** hydrothermal, **(E)** water, and **(F)** formamide sample series.

6.2.4 Electrochemical Behavior

Cyclic voltammograms were acquired at a 10 mV sec^{-1} scan rate with 10 cycles. The experiments reveal composition and synthetic dependent redox behaviors. The samples have two oxidation peaks *ca.* at 1.15 (a_1) and 1.45 V (a_2) and two reduction peaks at *ca.* 1.04 (c_1) and 1.48 V (c_2) vs RHE. These redox transitions are attributed to Co(II)-Co(III) and Co(III)-Co(IV) redox processes respectively. Comparison of the first and last cycles reveals that all sample species undergo an irreversible reconstruction process. (**Figure 6.5A-C**). The differences in charge accumulated under pre-catalytic redox peaks between the first and tenth cycles are higher in water and formamide series. The charge accumulated under the first oxidation peak(a_1) of the first cycle is generally higher than the last cycle. The comparison of the peak locations of the first and second redox processes indicates that hydrothermal reduction happens first and is followed by water species and lastly formamide set (**Figure 6.5D**). CVs indicate that formamide and water series have comparable activity and are followed by hydrothermal series with higher onset overpotentials (**Figure 6.5E**).

Electrokinetic analysis is completed by steady-state Tafel analysis (**Figure 6.5F**). The 0% Fe samples have the highest Tafel slopes, with values decreasing upon iron addition until stabilizing at a comparable slope for formamide and water series. The hydrothermal sample series slopes change less significantly than the other two series and the series exhibits a higher Tafel slope at around 50 mV dec^{-1}. The water series starts with a 61 mV dec^{-1} and decreases to 28 mV dec^{-1} for 30% Fe. The trend decreases from 47.2 to 36.5 mV dec^{-1} for the formamide series (**Figure 6.5G**). These values are in line with the previously measured Tafel slopes for cobalt (oxy)hydroxide samples.[315,336,337]

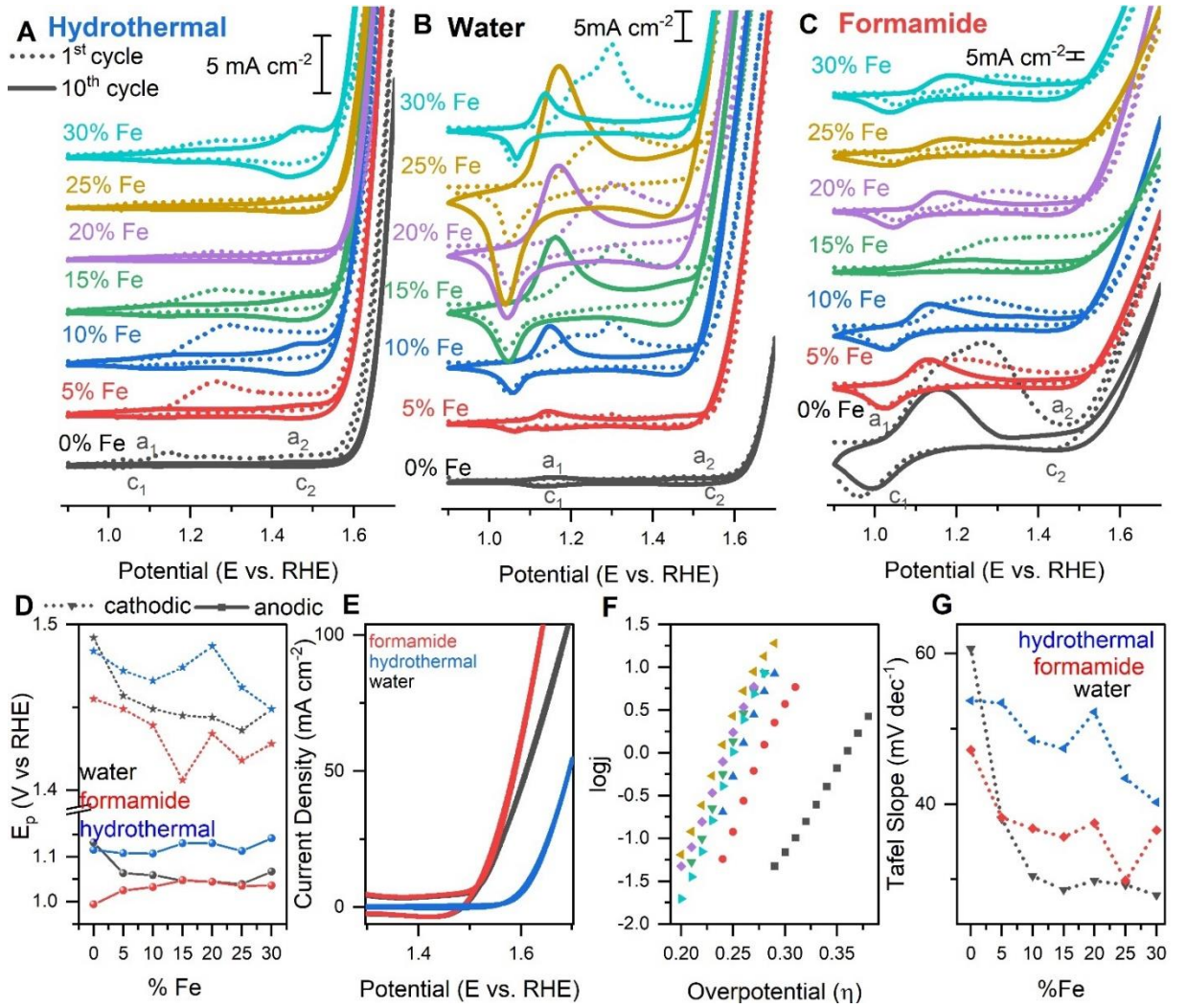

Figure 6.5 Electrochemical behavior of $Fe_xCo_{1-x}(OH)_2$. Cyclic voltammograms of **(A)** hydrothermal, **(B)** water, and **(C)** formamide sample series. **(D)** Composition dependent trends in pre-catalytic redox peak locations. **(E)** Comparison of onset potentials of $Fe_{20}Co_{80}(OH)_2$ in three series. **(F)** Sample Tafel slopes of cathodic chronoamperometry of $Fe_xCo_{1-x}(OH)_2$ water series. **(G)** Tafel slopes were obtained from cathodic chronoamperometry of three sample series. All sample series Tafel plots are demonstrated in **Figure D.4.**

6.3 Discussion

In this study, we fabricated three sets of $Co(OH)_2$ samples via hydrothermal and pH co-precipitation in aqueous and formamide environments. We observed that the structure of $Co(OH)_2$ is dependent on the synthetic method employed. The properties of the sample series deviate from the properties typically observed in other brucite-type metal hydroxides.

Raman spectroscopy, XANES, and EXAFS confirm hybrid $Co(OH)_2$-CoOOH for the lower iron content samples in the water series. The amount of trivalent cobalt sites is related to the charge accumulated under the first pre-catalytic redox peak. The amount of charge of a_1 and c_1 (**Figure 6.5B**) after 20% Fe is higher than the lower content iron species this could arise from the metal hydroxide structure. The hydrothermal series has an almost stable Tafel slope of *ca.* 50 mv dec^{-1} and onset overpotential of 0.2 V after 5% of Fe which indicates that not all of the iron sites are incorporated into $Co(OH)_2$ lattice. Furthermore, Raman spectroscopy, EXAFS, and XRD identified the presence of a second phase. The locations of Raman vibrations and bond distances from EXAFS reveal that the structure of the contaminated phase is reminiscent of Fe_3O_4. The secondary phase has no impact on the key electrocatalytic parameters.

$Co(OH)_2$ is known to be isostructural with brucite metal hydroxides (space group: $P\bar{3}m1$) such as $Ni(OH)_2$ which is one of the most widely studied electrocatalysts for OER. The electrocatalytic performance of both of the systems are further boosted with incorporated iron cations. Although the similarities in structure and catalytic properties, the chemistry behind coordination environments and catalytic descriptors like pre-catalytic redox peak potentials and kinetic parameters are often overlooked. Electronic factors *i.e.,* oxidation state of the catalytically relevant sites is an important parameter of the structure of materials. The differences between electronic structures of cobalt and nickel sites cause diversities: molecular orbital diagrams of nickel and cobalt cations in LDH structure with D_{3d} symmetry indicate that divalent nickel but trivalent cobalt sites are the stabilized form (**Figure 3.7C)**. The changes in the oxidation states directly affect R_{M-M} and R_{M-O} which are two important parameters used to evaluate the structure of the materials. Both of these values decrease with iron incorporation into nickel hydroxides. However, the change

in the bond distances of Ni-O and Ni-Ni distances are different. Therefore, the structure is distorted and changes coordination environments upon iron addition into the host lattice. On the other hand, $Co(OH)_2$ behaves differently: smaller decrease in bond distance with Fe incorporation for the water and hydrothermal series, and a slight increase in the formamide series. Even these sample series exhibit a reverse trend in the bond distances, the value of the ratio between $\frac{R_{M-M}}{R_{M-O}}$ do not change in cobalt hydroxides. The previously reported value of the ratio varies between 1.46 and 1.51 with an average value of 1.497.[76,316,317] Herein, the average ratio of all the sample series calculated from EXAFS simulations is 1.500 **(Figure 6.6A)**. This small difference in the ratio indicates that the structural distortion in $Co(OH)_2$ is negligible despite iron incorporation. The reflection of lattice distortion on electrocatalysis of $Ni(OH)_2$ is explained by a well-defined exponential relation between pre-catalytic redox peak potentials and $R_{M\text{-}M}$ (**Figure 4.8E**).[280]

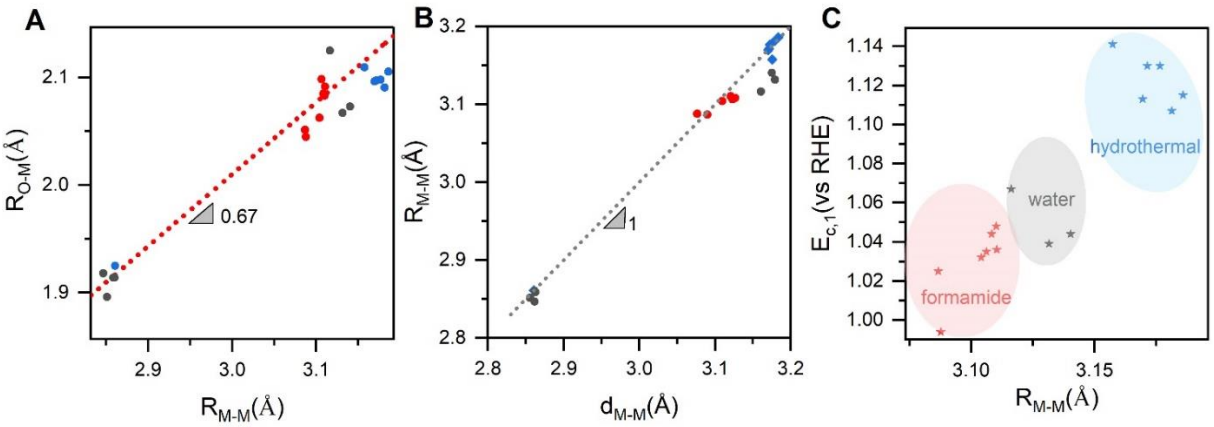

Figure 6.6 Correlational analysis of the three $Fe_xCo_{1-x}(OH)_2$ sample series. **(A)** The correlation between $R_{M\text{-}M}$ and $R_{M\text{-}O}$ calculated from EXAFS simulations. The line with the slope of the 0.67 indicates previously reported ratio of $R_{M\text{-}O}/R_{M\text{-}M}$. **(B)** The correlation between intermetallic distances connected through di-μ-(hdr)oxo bridge calculated by XRD ($d_{M\text{-}M}$) and XAS($R_{M\text{-}M}$). The line with the slope of 1 indicates 100% correlation. **(C)** Relation between the pre-catalytic redox peak potential ($E_{c,1}$) and $R_{M\text{-}M}$ distances.

However, FeCo hydroxide series does not follow the expected same trend instead they exhibit an opposite trend of increasing $E_{c,1}$ with increasing R_{M-M}. The absence of strain is reflected by the minimal shift of the pre-catalytic redox peaks of $Co(OH)_2$. The observed peak shifts are 3.3, 4.3, and 2.5 mV $\%Fe^{-1}$ for nickel hydroxides synthesized in aqueous pH precipitation in water, formamide, and hydrothermal methods respectively (**Chapters 4.2.7** and **5.2.4)**. The shift for the samples discussed in this chapter is 1.0 mV $\%Fe^{-1}$ for all the sample series. The dramatic difference between the values shows that the geometric strain is inconsequential in cobalt hydroxides.

The strong correlations between d_{M-M} and R_{M-M} values indicate that both XRD and XAS are convenient techniques to analyze coordination environments of cobalt hydroxides **(Figure 6.6B)**. Rather than strain, we identified synthetic techniques that strongly affect electrochemical and structural features. **Figure 6.6A** show that the first pre-catalytic redox peak located between 1-1.15 V vs. RHE are clustered at different voltage regions depending on the synthetic routes as well as intermetallic distances. Since the water series has a hybrid $Co(OH)_2$ and CoOOH structure at lower concentrations, the first four samples are unsuitable for the correlational analysis. This relation indicates that synthetic routes have an impact on the electrochemistry and structure of these models.

6.4 Conclusion

In conclusion, the combination of multiple characterization techniques shows that the nominal same materials synthesized with different techniques can structurally vary from each other. The structure directly affects the electrochemical activity of such systems. The combination of bond distances from XAS simulations and the first redox peak in cyclic voltammograms show a clear description of the structural properties of these materials. The hydrothermal sample series has the highest R_{M-M} values and $E_{c,1}$ potential on the other hand formamide series has the lowest. Furthermore, $Co(OH)_2$ is ruled out from other brucite materials due to their preferred electronic structure and its effect on electrochemical properties. For these reasons, more efforts are required to analyze iron doped cobalt hydroxides in a more systematic way to rationalize the essential role of iron on structure and electrochemical behavior.

6.5 Experimental

6.5.1 Materials

Cobalt chloride hexahydrate ($CoCl_2.6H_2O$) (Fisher Chemical), ferric chloride ($FeCl_3$) (Fisher Chemical), sodium hydroxide, and potassium hydroxide (NaOH and KOH) (Sigma-Aldrich), and reagent grade formamide (CH_3NO) (Sigma-Aldrich) were used as received. All H_2O used during fabrication was milli-Q H_2O (18.2M **Ω**).

6.5.2 Synthesis

pH precipitation: Two analagous layered double hydroxide composition series were fabricated using variations of a pH precipitation protocol. Conventional aqueous pH precipitation was carried out by dissolving appropriate amounts of ferric chloride and cobalt chloride hexahydrate in milli-Q water to obtain a total metal ion concentration of 0.35 M with the desired stoichiometry to obtain $Co_xFe_{1-x}(OH)_2$, where *x* was varied from 0 to 0.3. A 1 M aqueous NaOH solution was added dropwise to the solution while stirring under N_2 environment until a pH of 12 was reached. Stirring was maintained for 10 additional minutes before the solid product was collected by centrifugation. The solid was washed twice by suspending in 10 mL aliquots of water, three times in 10 mL aliquots of acetone, then dried overnight at 75 °C. The fabrication protocol was modified for the second sample series by the addition of formamide to the reaction solution, which has previously been reported to produce single-layered "nanosheets."[101] An identical protocol was employed for this sample series as the aqueous samples, with the exception that the precursor solutions were prepared in aqueous solutions containing 30% v/v formamide. The two-composition series are referred to here as the water series and the formamide series.

Hydrothermal Synthesis: A total metal concentration of 0.6 M of appropriate amounts of cobalt chloride hexahydrate and ferric chloride and a 40 ml solution of 5 M potassium hydroxide is added into a Teflon autoclave. The reactor was first heated to 140 °C with 5 ^{0}C increments and held for 16 hours. Then, the supernatant is removed, and solid particles were washed with Milli-Q water and added into an autoclave with 40 ml of Milli-Q water and heated to 170 °C with 10-degree

increments and held for 16 hours. The final product is vacuum filtrated and rinsed with water and ethanol. Powder products were obtained after samples were dried in an oven at 200 °C for two hours.

6.5.3 X-ray Absorption Spectroscopy

The instrumental information can be found in **Chapter 4.2.6**.

Co and Fe K-edge locations were determined by half-height method (**Table D.1**). The Artemis software package was used to generate structural models by simulation of k^3 weighted EXAFS results from k of 3 to 14 $Å^{-1}$ and 3 to 12 $Å^{-1}$ for Co K- edge and Fe K edge respectively (**Figure D.1**). All simulations were performed with a fixed amplitude reduction factor, the Debye-Waller factor (σ^2), and Eo for Co and Fe shells for all of the samples in composition series. The coordination numbers (N_i) and R_{eff} were fitted. The σ^2 and E_0 values can be found in **Tables D.2-7**. A constant value of E_o is used for Co 7709 eV and iron 7112 eV.

6.5.4 Electrochemical Analysis

All of the experimental procedures, catalyst preparation is the same with **Chapter 4.4.2.**

6.5.5 X-ray Diffraction

Experimental details of the powder XRD experiment are stated in **Chapter 2.2.2.**

6.5.6 Raman Spectroscopy

Experimental details of the Raman spectroscopy measurements are stated in **Chapter 2.2.5.2.**

Chapter 7

Conclusion and Outlook

This thesis presents a variety of transition metal hydroxides as oxygen evolution reaction electrocatalysts. Nickel hydroxide and cobalt hydroxides turn into remarkable OER electrocatalysts when the iron is incorporated into the host lattice. Several studies provide diverse proposals on the role of iron, including iron being catalytically active or inactive sites, iron-induced strain, and diverse coordination environment. More comprehensive information can be obtained through a systematic analysis of such systems. In this thesis, we focused on the structural analysis of these samples employed to get an insight into the role of iron in catalytic performance and the structure of materials. Depending on the purpose of each study different approaches are used to study to make a comprehensive analysis of the structure-property correlations.

Iron doped nickel hydroxides undergo a potential dependent geometric strain. The first part of the study investigates the effect of internalized strain in gallium, aluminum, and iron-doped nickel hydroxides that are fabricated with photochemical deposition route. Samples synthesized with this technique is highly disordered and therefore the structure of these materials prevents making a direct crystallographic analysis because of the limited accessibility to synchrotron facilities, we focused on near-infrared spectroscopy and computational studies. Near-infrared spectroscopy together with potential energy surfaces obtained through DFT calculations reveals that all sample series are under tensile strain in oxidized form and the compressive strain takes place when they are reduced. The results indicate that strain is reproducible for aluminum and gallium doped nickel hydroxides as their iron-doped analogues. Electrochemical activity of iron-doped samples, on the other hand, rule out from other two series. Correlations between electrokinetic parameters point to the existence of another parameter for boosting the electrochemical activity of the iron-doped sample series.

Building on the concept of the strain in iron-doped nickel hydroxides, a more detailed analysis is done in the second part of the project. Synthetic conditions have been previously reported as an important strategy to optimize catalytic activity. Synthetic-dependent structural diversities often yield different interpretations of the structure and catalysts' performance. Starting from this point, we investigated the effect of fabrication protocols on the structure and the reflection of the structure on the electrochemical behavior. Two sample series were fabricated with a conventional pH co-precipitation method with the presence of water and 30% v/v formamide-water as solvent. Mössbauer spectroscopy and Raman spectroscopy directly identify the formation of a second iron-related coordination environment for the samples synthesized in the absence of formamide. only one iron coordination site is formed when formamide is involved during the synthesis. XRD and XAS are not able to detect the second coordination sites but changes in crystallographic a parameter and intermetallic bond distances support the formation of the second iron site. The comprehensive structure-property analysis of the two sets of the samples provides a sophisticated way to optimize catalyst properties.

The next part of the project focuses on iron incorporated nickel hydroxide series synthesized with hydrothermal method. Crystalline form of nickel hydroxides exhibits three diverse iron coordination sites: incorporated to lattice successfully, bound to atop of the layers, and segregated iron oxide phase. Furthermore, electrocatalytic behaviors diverge from the same materials prepared as disordered form. Asymmetric Marcus Hush theory is used to explain the static pre-catalytic redox peak locations but linear decrement in the Tafel slope. The linear correlation between bond angle and Tafel slope points out the improved electrocatalytic behavior in hydrothermally prepared materials.

The last part of the thesis focuses on synthetic-dependent behaviors of iron-doped $Co(OH)_2$. The comparison of three sample series that are prepared with co-precipitation with and without formamide and hydrothermal techniques reveals dramatic structural diversities. The hydrothermal sample series have iron incorporation threshold after 5% iron. The rest of iron sites participate in the formation of iron oxide contaminants. Therefore, iron has the minimum effect on

electrocatalytic performance. Water sample series undergoes partial oxidation to CoOOH phase, but this situation does not alter electrochemical properties across the compositional series. The addition of formamide assists the formation of hydrotalcite-like materials with the highest iron incorporation rate. The correlations between structural parameters indicate that cobalt hydroxides behave differently than other metal hydroxides in electrocatalytic behaviors.

All in all, the result of this study provides a comprehensive understanding of structure-property correlations on various kinds of metal hydroxide electrocatalysts. The rational design of electrocatalysts for energy conversion applications necessitates comprehending structural diversities and chemistry behind them. Extensive research on the layered double hydroxide family highlights the structural diversities, however, the discussion on the structural variations across the literature is limited. This inhibits to optimization of the catalytic behavior of heterogeneous catalysis. Therefore, we focused on a systematic analysis of nickel and cobalt-based hydroxides which are the two most effective transition metal hydroxide electrocatalysts in oxygen evolution reaction and the two most affected materials by iron doping. For these reasons, working in this class of electrocatalysts can develop a point of view on improving catalytic performance. The correlations between structure and activity and the property provide an understanding of disordered and ordered heterogeneous electrocatalysts. The establishment of synthetic control over the coordination environments on electroactive sites is a constructive approach to improving the catalytic behaviors of the materials.

References

1 N. S. Lewis and D. G. Nocera, *Proc. Natl. Acad. Sci. U.S.A.*, 2006, **103**, 15729–15735.
2 B. You, M. T. Tang, C. Tsai, F. Abild-Pedersen, X. Zheng and H. Li, *Adv. Mater.*, 2019, **31**, 1807001.
3 R. L. Doyle, I. J. Godwin, M. P. Brandon and M. E. G. Lyons, *Phys. Chem. Chem. Phys.*, 2013, **15**, 13737–13783.
4 B. M. Hunter, H. B. Gray and A. M. Mü, *Chem. Rev.*, 2016, **116**, 14120–14136.
5 A. Miola and F. Schiltz, *Ecol Econ.*, 2019, **164**, 106373.
6 B. You, G. Han and Y. Sun, *Chem. Commun.*, 2018, **54**, 5943–5955.
7 E. Fabbri and T. J. Schmidt, *ACS Catal.*, 2018, **8**, 9765–9774.
8 P. Sabatier, *La catalyse en chimie organique*, Librairie polytechnique, Paris et Liege, 1920.
9 A. A. Balandin, in *Advances in Catalysis*, eds. D. D. Eley, H. Pines and P. B. Weisz, Academic Press, 1969, vol. 19, pp. 1–210.
10 S. Trasatti, *J. electroanal. chem. interfacial electrochem.*, 1972, **39**, 163–184.
11 J. K. Nørskov, T. Bligaard, J. Rossmeisl and C. H. Christensen, *Nat. Chem.*, 2009, **1**, 37–46.
12 In *Fundamental Concepts in Heterogeneous Catalysis*, John Wiley & Sons, Ltd, 2014, pp. 1–5.
13 M. G. Evans and M. Polanyi, *Trans. Faraday Soc.*, 1936, **32**, 1333–1360.
14 B. Hammer and J. K. Nørskov, in *Advances in Catalysis*, Academic Press, 2000, vol. 45, pp. 71–129.
15 E. P. Alsaç, N. Bodappa, A. W. H. Whittingham, Y. Liu, A. de Lazzari and R. D. L. Smith, *Chem. Phys. Rev.*, 2021, **2**, 031306.
16 H. Dau, C. Limberg, T. Reier, M. Risch, S. Roggan and P. Strasser, *ChemCatChem*, 2010, **2**, 724–761.
17 Z.-F. Huang, J. Song, Y. Du, S. Xi, S. Dou, J. M. V. Nsanzimana, C. Wang, Z. J. Xu and X. Wang, *Nat Energy*, 2019, **4**, 329–338.
18 A. Damjanovic and B. Jovanovic, *J. Electrochem. Soc.*, 1976, **123**, 374.
19 J. O. Bockris and T. Otagawa, *J. Phys. Chem.*, 1983, **57**, 2960–2971.
20 M. Wohlfahrt-Mehrens and J. Heitbaum, *J. electroanal. chem. interfacial electrochem.*, 1987, **237**, 251–260.
21 T. Binninger, R. Mohamed, K. Waltar, E. Fabbri, P. Levecque, R. Kötz and T. J. Schmidt, *Sci Rep*, 2015, **5**, 12167.
22 D. Zhong, T. Li, D. Wang, L. Li, J. Wang, G. Hao, G. Liu, Q. Zhao and J. Li, *Nano Res.*, 2022, **15**, 162–169.
23 X. Wang, C. Xing, Z. Liang, P. Guardia, X. Han, Y. Zuo, J. Llorca, J. Arbiol, J. Li and A. Cabot, *J. Mater. Chem. A*, 2022, **10**, 3659–3666.
24 C. E. Beall, E. Fabbri and T. J. Schmidt, *ACS Catal.*, 2021, **11**, 3094–3114.
25 A. Zagalskaya, I. Evazzade and V. Alexandrov, *ACS Energy Lett.*, 2021, **6**, 1124–1133.
26 H. Ding, H. Liu, W. Chu, C. Wu and Y. Xie, *Chem. Rev.*, 2021, **121**, 13174–13212.
27 J. S. Yoo, X. Rong, Y. Liu and A. M. Kolpak, *ACS Catal.*, 2018, **8**, 4628–4636.

28 Z. W. Seh, J. Kibsgaard, C. F. Dickens, I. Chorkendorff, J. K. Nørskov and T. F. Jaramillo, *Science*, 2017, **355**, eaad4998.
29 J. Mohammed-Ibrahim, *J. Power Sources*, 2020, **448**, 227375.
30 J. Wang, Y. Gao, H. Kong, J. Kim, S. Choi, F. Ciucci, Y. Hao, S. Yang, Z. Shao and J. Lim, *Chem. Soc. Rev*, 2020, **49**, 9154–9196.
31 L. Gong, H. Yang, A. I. Douka, Y. Yan and B. Y. Xia, *Adv. Sustainable Syst.*, 2021, **5**, 2000136.
32 F. Song, L. Bai, A. Moysiadou, S. Lee, C. Hu, L. Liardet and X. Hu, *J. Am. Chem. Soc.*, 2018, **140**, 7748–7759.
33 S. Jung, C. C. L. McCrory, I. M. Ferrer, J. C. Peters and T. F. Jaramillo, *J. Mater. Chem. A*, 2016, **4**, 3068–3076.
34 Z. Chen, C. X. Kronawitter, Y. W. Yeh, X. Yang, P. Zhao, N. Yao and B. E. Koel, *J. Mater. Chem. A*, 2017, **5**, 842–850.
35 D. G. Evans and R. C. T. Slade, in *Layered Double Hydroxides*, eds. X. Duan and D. G. Evans, Springer, Berlin, Heidelberg, 2006, pp. 1–87.
36 L. Trotochaud, S. L. Young, J. K. Ranney and S. W. Boettcher, *J. Am. Chem. Soc.*, 2014, **136**, 6744–6753.
37 D. S. Hall, D. J. Lockwood, C. Bock and B. R. MacDougall, *Proc. R. Soc. A*, 2014, **471**, 20140792.
38 K. Momma and F. Izumi, *J Appl Cryst*, 2011, **44**, 1272–1276.
39 H. Bode, K. Dehmelt and J. Witte, *Electrochim. Acta*, 1966, **11**, 1079–1087.
40 D. E. Hall, *J. Electrochem. Soc.*, 1983, **130**, 317–317.
41 M. E. G. Lyons and M. P. Brandon, *Int. J. Electrochem. Sci.*, 2008, **3**, 1386–1424.
42 R. D. L. Smith, M. S. Prévot, R. D. Fagan, S. Trudel and C. P. Berlinguette, *J. Am. Chem. Soc.*, 2013, **135**, 11580–11586.
43 R. Subbaraman, D. Tripkovic, K. C. Chang, D. Strmcnik, A. P. Paulikas, P. Hirunsit, M. Chan, J. Greeley, V. Stamenkovic and N. M. Markovic, *Nat. Mater.*, 2012, **11**, 550–557.
44 S. Krehula, M. Ristić, C. Wu, X. Li, L. Jiang, J. Wang, G. Sun, T. Zhang, M. Perović, M. Bošković, B. Antić, L. K. Krehula, B. Kobzi, S. Kubuki and S. Musić, *J. Alloys Compd.*, 2018, **750**, 687–695.
45 T. Zhang, M. R. Nellist, L. J. Enman, J. Xiang and S. W. Boettcher, *ChemSusChem*, 2019, **12**, 2015–2021.
46 Y. He, X. Liu, G. Chen, J. Pan, A. Yan, A. Li, X. Lu, D. Tang, N. Zhang, T. Qiu, R. Ma and T. Sasaki, *Chem. Mater.*, 2020, **32**, 4232–4240.
47 Y. Zhou and N. López, *ACS Catal.*, 2020, **10**, 6254–6261.
48 Q. Chang, X. Zhang, B. Wang, J. Niu, Z. Yang and W. Wang, *Nanoscale*, 2022, **14**, 1107–1122.
49 Q. Dong, C. Shuai, Z. Mo, N. Liu, G. Liu, J. Wang, H. Pei, Q. Jia, W. Liu and X. Guo, *J. Solid State Chem.*, 2021, **296**, 121967.
50 H. Boumeriame, E. S. Da Silva, A. S. Cherevan, T. Chafik, J. L. Faria and D. Eder, *J. Energy Chem.*, 2022, **64**, 406–431.

51 A. C. Thenuwara, N. H. Attanayake, J. Yu, J. P. Perdew, E. J. Elzinga, Q. Yan and D. R. Strongin, *J. Phys. Chem. B*, 2018, **122**, 847–854.
52 E. Y. Tsui and T. Agapie, *Proc. Natl. Acad. Sci. U.S.A.*, 2013, **110**, 10084–10088.
53 D. E. Herbert, D. Lionetti, J. Rittle and T. Agapie, *J. Am. Chem. Soc.*, 2013, **135**, 19075–19078.
54 H. B. Lee and T. Agapie, *Inorg. Chem.*, 2019, **58**, 14998–15003.
55 E. Y. Tsui, R. Tran, J. Yano and T. Agapie, *Nat. Chem.*, 2013, **5**, 293–299.
56 D. A. Kuznetsov, B. Han, Y. Yu, R. R. Rao, J. Hwang, Y. Román-Leshkov and Y. Shao-Horn, *Joule*, 2018, **2**, 225–244.
57 Z. Lu, L. Qian, Y. Tian, Y. Li, X. Sun and X. Duan, *Chem. Commun.*, 2016, **52**, 908–911.
58 Y. Bi, Z. Cai, D. Zhou, Y. Tian, Q. Zhang(m), Q. Zhang(f), Y. Kuang, Y. Li, X. Sun and X. Duan, *Journal of Catalysis*, 2018, **358**, 100–107.
59 J. Chen, H. Li, S. Chen, J. Fei, C. Liu, Z. Yu, K. Shin, Z. Liu, L. Song, G. Henkelman, L. Wei and Y. Chen, *Adv. Energy Mater.*, 2021, **11**, 2003412.
60 X. Bo, Y. Li, R. K. Hocking and C. Zhao, *ACS Appl. Mater. Interfaces*, 2017, **9**, 41239–41245.
61 Z. Cai, D. Zhou, M. Wang, S.-M. Bak, Y. Wu, Z. Wu, Y. Tian, X. Xiong, Y. Li, W. Liu, S. Siahrostami, Y. Kuang, X.-Q. Yang, H. Duan, Z. Feng, H. Wang and X. Sun, *Angew.Chem.Int.Ed*, 2018, **57**, 9392–9396.
62 N. Li, D. K. Bediako, R. G. Hadt, D. Hayes, T. J. Kempa, F. Von Cube, D. C. Bell, L. X. Chen and D. G. Nocera, *Proc. Natl. Acad. Sci. U.S.A.*, 2017, **114**, 1486–1491.
63 Y. Xing, J. Ku, W. Fu, L. Wang and H. Chen, *Chem. Eng. J.*, 2020, **395**, 125149–125149.
64 W. T. Hong, R. E. Welsch and Y. Shao-Horn, *J. Phys. Chem. C*, 2016, **120**, 78–86.
65 J. Zaanen and G. A. Sawatzky, *J. Solid State Chem.*, 1990, **88**, 8–27.
66 J. Zhu, S. Li, Z. Zhuang, S. Gao, X. Hong, X. Pan, R. Yu, L. Zhou, L. V. Moskaleva and L. Mai, *Energy Environ. Sci.*, 2020, 1–7.
67 Y. Yang, Y. Ou, Y. Yang, X. Wei, D. Gao, L. Yang, Y. Xiong, H. Dong, P. Xiao and Y. Zhang, *Nanoscale*, 2019, **11**, 23296–23303.
68 M. Kuang, J. Zhang, D. Liu, H. Tan, K. N. Dinh, L. Yang, H. Ren, W. Huang, W. Fang, J. Yao, X. Hao, J. Xu, C. Liu, L. Song, B. Liu and Q. Yan, *Adv. Energy Mater.*, 2020, **10**, 2002215–2002215.
69 D. Drevon, M. Görlin, P. Chernev, L. Xi, H. Dau and K. M. Lange, *Sci. Rep.*, 2019, **9**, 1–11.
70 J. He, Y. Zou and S. Wang, *Dalton Trans.*, 2019, **48**, 15–20.
71 Y. Wang, P. Han, X. Lv, L. Zhang and G. Zheng, *Joule*, 2018, **2**, 2551–2582.
72 Y. Zhang, L. Tao, C. Xie, D. Wang, Y. Zou, R. Chen, Y. Wang, C. Jia and S. Wang, *Adv. Mater.*, 2020, **32**, 1–22.
73 N. Cheng, L. Zhang, K. Doyle-Davis and X. Sun, *Electrochem. Energy Rev.*, 2019, **2**, 539–573.
74 Y. Chen, S. Ji, C. Chen, Q. Peng, D. Wang and Y. Li, *Joule*, 2018, **2**, 1242–1264.
75 A. Banik, T. Famprikis, M. Ghidiu, S. Ohno, M. A. Kraft and W. G. Zeier, *Chem. Sci.*, , DOI:10.1039/d0sc06553f.

76 U. Costantino, F. Marmottini, M. Nocchetti and R. Vivani, *Eur. J. Inorg. Chem.*, 1998, **1998**, 1439–1446.
77 Q. Xie, Z. Cai, P. Li, D. Zhou, Y. Bi, X. Xiong, E. Hu, Y. Li, Y. Kuang and X. Sun, *Nano Res.*, 2018, **11**, 4524–4534.
78 L. Peng, N. Yang, Y. Yang, Q. Wang, X. Xie, D. Sun-Waterhouse, L. Shang, T. Zhang and G. I. N. Waterhouse, *Angew.Chem.Int.Ed*, 2021, **133**, 24817–24824.
79 R. Liu, Y. Wang, D. Liu, Y. Zou and S. Wang, *Adv. Mater.*, 2017, **29**, 1701546.
80 X. Zheng, J. Tang, A. Gallo, J. A. G. Torres, X. Yu, C. J. Athanitis, E. M. Been, P. Ercius, H. Mao, S. C. Fakra, C. Song, R. C. Davis, J. A. Reimer, J. Vinson, M. Bajdich and Y. Cui, *Proc. Natl. Acad. Sci. U.S.A.*, 2021, **118**, e2101817118.
81 W. Chen, B. Wu, Y. Wang, W. Zhou, Y. Li, T. Liu, C. Xie, L. Xu, S. Du, M. Song, D. Wang, Y. Liu, Y. Li, J. Liu, Y. Zou, R. Chen, C. Chen, J. Zheng, Y. Li, J. Chen and S. Wang, *Energy Environ. Sci.*, 2021, **14**, 6428–6440.
82 D. K. Bediako, Y. Surendranath and D. G. Nocera, *J. Am. Chem. Soc.*, 2013, **135**, 3662–3674.
83 A. S. Batchellor and S. W. Boettcher, *ACS Catal.*, 2015, **5**, 6680–6689.
84 C. Zou, Z. Li, C. Wang, J. Hong, J. Chen and S. Zhong, *Chem. Phys. Lett.*, 2022, **793**, 139471.
85 W. Rong, S. Stepan and R. D. L. Smith, *MRS Advances*, 2019, **4**, 1843–1850.
86 M. Cai, R. Pan, W. Liu, X. Luo, C. Chen, H. Zhang and M. Zhong, *J. Laser Appl.*, 2020, **32**, 022032.
87 S. Krehula, M. Ristić, C. Wu, X. Li, L. Jiang, J. Wang, G. Sun, T. Zhang, M. Perović, M. Bošković, B. Antić, L. K. Krehula, B. Kobzi, S. Kubuki and S. Musić, *J. Alloys Compd.*, 2018, **750**, 687–695.
88 T. Hibino and H. Ohya, *Appl. Clay Sci.*, 2009, **45**, 123–132.
89 Z. Lu, W. Xu, W. Zhu, Q. Yang, X. Lei, J. Liu, Y. Li, X. Sun and X. Duan, *Chem. Commun.*, 2014, **50**, 6479–6482.
90 A. M. P. Sakita, R. D. Noce, E. Vallés and A. V. Benedetti, *Appl. Surf. Sci.*, 2018, **434**, 1153–1160.
91 G. E. Buono-Core, M. Tejos, G. Cabello, N. Guzman and R. H. Hill, *Mater. Chem. Phys.*, 2006, **96**, 98–102.
92 B. M. Hunter, W. Hieringer, J. R. Winkler, H. B. Gray and A. M. Müller, *Energy Environ. Sci.*, 2016, **9**, 1734–1743.
93 B. M. Hunter, N. B. Thompson, A. M. Müller, G. R. Rossman, M. G. Hill, J. R. Winkler and H. B. Gray, *Joule*, 2018, **2**, 747–763.
94 A. Ambrosi and M. Pumera, *Chem. Soc. Rev*, 2018, **47**, 7213–7224.
95 Q. Wang and D. Ohare, *Chem. Rev.*, 2012, **112**, 4124–4155.
96 M. Adachi-Pagano, C. Forano and J.-P. Besse, *Chem. Commun.*, 2000, 91–92.
97 T. Hibino and W. Jones, *J. Mater. Chem.*, 2001, **11**, 1321–1323.
98 L. Li, R. Ma, Y. Ebina, N. Iyi and T. Sasaki, *Chem. Mater.*, 2005, **17**, 4386–4391.
99 F. Song and X. Hu, *Nat Commun*, 2014, **5**, 4477.
100 J. Yu, B. R. Martin, A. Clearfield, Z. Luo and L. Sun, *Nanoscale*, 2015, **7**, 9448–9451.

101 J. Yu, J. Liu, A. Clearfield, J. E. Sims, M. T. Speiegle, S. L. Suib and L. Sun, *Inorg. Chem.*, 2016, **55**, 12036–12041.
102 G. Hu, N. Wang, D. O'Hare and J. Davis, *Chem. Commun.*, 2006, 287–289.
103 T.-B. Hur, T. X. Phuoc and M. K. Chyu, *J. Appl. Phys.*, 2010, **108**, 114312.
104 D. Zhou, Z. Cai, Y. Bi, W. Tian, M. Luo, Q. Zhang, Q. Xie, J. Wang, Y. Li, Y. Kuang, X. Duan, M. Bajdich, S. Siahrostami and X. Sun, *Nano Res.*, 2018, **11**, 1358–1368.
105 L. Dang, H. Liang, J. Zhuo, B. K. Lamb, H. Sheng, Y. Yang and S. Jin, *Chem. Mater.*, 2018, **30**, 4321–4330.
106 J. A. Carrasco, R. Sanchis-Gual, A. Seijas-Da Silva, G. Abellan and E. Coronado, *Chem. Mater.*, 2019, **31**, 6798–6807.
107 M. Görlin, J. H. Stenlid, S. Koroidov, H. Wang, M. Börner, M. Shipilin, A. Kalinko, V. Murzin, O. V. Safonova, M. Nachtegaal, A. Uheida, J. Dutta, M. Bauer, A. Nilsson and O. Diaz-morales, *Nat Commun*, 2020, 1–12.
108 A. C. Garcia, T. Touzalin, C. Nieuwland, N. Perini and M. T. M. Koper, *Angew.Chem.Int.Ed*, 2019, **58**, 12999–13003.
109 J. D. Michael, E. L. Demeter, S. M. Illes, Q. Fan, J. R. Boes and J. R. Kitchin, *J. Phys. Chem. C*, 2015, **119**, 11475–11481.
110 J. Zaffran, M. B. Stevens, C. D. M. Trang, M. Nagli, M. Shehadeh, S. W. Boettcher and M. C. Toroker, *Chem. Mater.*, 2017, **29**, 4761–4767.
111 C. Yang, O. Fontaine, J.-M. Tarascon and A. Grimaud, *Angew.Chem.Int.Ed*, 2017, **56**, 8652–8656.
112 L. Bai, S. Lee and X. Hu, *Angew.Chem.Int.Ed*, 2021, **133**, 3132–3140.
113 F. Song, M. M. Busch, B. Lassalle-Kaiser, C. S. Hsu, E. Petkucheva, M. Bensimon, H. M. Chen, C. Corminboeuf and X. Hu, *ACS Cent. Sci.*, 2019, **5**, 558–568.
114 F. Song and X. Hu, *J. Am. Chem. Soc.*, 2014, **136**, 16481–16484.
115 Y. D. G. Edañol, J. A. O. Poblador, T. J. E. Talusan and L. M. Payawan, *Materials Today: Proceedings*, 2020, **33**, 1809–1813.
116 R. Xu and H. C. Zeng, *Chem. Mater.*, 2001, **13**, 297–303.
117 R. Li, J. Xu, Q. Pan, J. Ba, T. Tang and W. Luo, *ChemistryOpen*, 2019, **8**, 1027–1032.
118 J. Prince, A. Montoya, G. Ferrat and J. S. Valente, *Chem. Mater.*, 2009, **21**, 5826–5835.
119 P.-H. Chang, Y.-P. Chang, Y.-H. Lai, S.-Y. Chen, C.-T. Yu and Y.-P. Chyou, *J. Alloys Compd.*, 2014, **586**, S498–S505.
120 X. Lu and C. Zhao, *Nat Commun*, 2015, **6**, 6616.
121 R. D. L. Smith, C. Pasquini, S. Loos, P. Chernev, K. Klingan, P. Kubella, M. R. Mohammadi, D. González-Flores and H. Dau, *Energy Environ. Sci.*, 2018, **11**, 2476–2485.
122 X. Li, L. Yu, G. Wang, G. Wan, X. Peng, K. Wang and G. Wang, *Electrochimica Acta*, 2017, **255**, 15–22.
123 Z. Yang, J. Wei, G. Zeng, H. Zhang, X. Tan, C. Ma, X. Li, Z. Li and C. Zhang, *Coord. Chem. Rev.*, 2019, **386**, 154–182.
124 A. A. Avey and R. H. Hill, *J. Am. Chem. Soc.*, 1996, **118**, 237–238.

125 R. D. L. Smith, M. S. Prévot, R. D. Fagan, Z. Zhang, P. A. Sedach, M. K. J. Siu, S. Trudel and C. P. Berlinguette, *Science*, 2013, **340**, 60–63.
126 S. Tradel, G. Li, X. Zhang and R. H. Hill, *J. Photopolym. Sci. Technol.*, 2006, **19**, 467–475.
127 G. E. Buono-Core, G. Cabello, A. H. Klahn, A. Lucero, M. V. Nuñez, B. Torrejón and C. Castillo, *Polyhedron*, 2010, **29**, 1551–1554.
128 G. E. Buono-Core, M. Tejos, J. Lara, F. Aros and R. H. Hill, *Mater. Res. Bull.*, 1999, **34**, 2333–2340.
129 G. E. Buono-Core, M. Tejos, G. Alveal and R. H. Hill, *J. Mater. Sci.*, 2000, **35**, 4873–4877.
130 G. E. Buono-Core, G. Cabello, B. Torrejon, M. Tejos and R. H. Hill, *Mater. Res. Bull.*, 2005, **40**, 1765–1774.
131 R. D. L. Smith, C. Pasquini, S. Loos, P. Chernev, K. Klingan, P. Kubella, M. R. Mohammadi, D. Gonzalez-Flores and H. Dau, *Nat Commun*, 2017, **8**, 2022.
132 N. Bodappa, S. Stepan and R. D. L. Smith, *Inorg. Chem.*, 2021, **60**, 2304–2314.
133 M. V. Bukhtiyarova, *J. Solid State Chem.*, 2019, **269**, 494–506.
134 F. L. Theiss, G. A. Ayoko and R. L. Frost, *Appl. Surf. Sci.*, 2016, **383**, 200–213.
135 P. Sun, R. Ma, X. Bai, K. Wang, H. Zhu and T. Sasaki, *Sci. Adv.*, 2017, **3**, e1602629.
136 R. Ma, Z. Liu, L. Li, N. Iyi and T. Sasaki, *J. Mater. Chem.*, 2006, **16**, 3809–3813.
137 F. Song and X. Hu, *Nat Commun*, 2014, **5**, 4477.
138 J. A. Carrasco, R. Sanchis-Gual, A. Seijas-Da Silva, G. Abellan and E. Coronado, *Chem. Mater.*, 2019, **31**, 6798–6807.
139 G. Chen, H. Wan, W. Ma, N. Zhang, Y. Cao, X. Liu, J. Wang and R. Ma, *Adv. Energy Mater.*, 2020, **10**, 1902535–1902535.
140 D. Liang, W. Yue, G. Sun, D. Zheng, K. Ooi and X. Yang, *Langmuir*, 2015, **31**, 12464–12471.
141 J. Karthikeyan, H. Fjellvåg, S. Bundli and A. O. Sjåstad, *Materials*, 2021, **14**, 346.
142 L. Li, Y. Dai, Q. Xu, B. Zhang, F. Zhang, Y. You, D. Ma, S.-S. Li and Y.-X. Zhang, *J. Alloys Compd.*, 2021, **882**, 160752.
143 R. Gao and D. Yan, *Nano Res.*, 2018, **11**, 1883–1894.
144 C. Delmas and C. Tessier, *J. Mater. Chem.*, 1997, **7**, 1439–1443.
145 W. L. Bragg, *Nature*, 1912, **90**, 410–410.
146 W. H. Bragg, *Nature*, 1912, **90**, 360–361.
147 W. L. Bragg and W. H. Bragg, *Proceedings of the Royal Society of London. Series A, Containing Papers of a Mathematical and Physical Character*, 1913, **89**, 248–277.
148 J. Timoshenko and B. Roldan Cuenya, *Chem. Rev.*, 2021, **121**, 882–961.
149 M. Sahnoun, C. Daul and O. Haas, *J. Appl. Phys.*, 2007, **101**, 014911.
150 J. L. Bantignies, S. Deabate, A. Righi, S. Rols, P. Hermet, J. L. Sauvajol and F. Henn, *J. Phys. Chem. C*, 2008, **112**, 2193–2201.
151 Y. C. Cho and S. I. Ahn, *Sci Rep*, 2020, **10**, 11692.
152 P. Gütlich, *Z Anorg Allg Chem*, 2012, **638**, 15–43.
153 E. Ruska and M. Knoll, *Z. techn. Physik*, 1931, **12**, 389–400.
154 M. M. Freundlich, *Science*, 1963, **142**, 185–188.
155 S. Hwang, X. Chen, G. Zhou and D. Su, *Adv. Energy Mater.*, 2020, **10**, 1902105.

156 A. J. Bard and L. R. Faulkner, *Electrochemical Methods: Fundamentals and Applications*, WILEY-VCH Verlag, 2nd edn., 2001.
157 P. Giannozzi, S. Baroni, N. Bonini, M. Calandra, R. Car, C. Cavazzoni, D. Ceresoli, G. L. Chiarotti, M. Cococcioni, I. Dabo, A. D. Corso, S. de Gironcoli, S. Fabris, G. Fratesi, R. Gebauer, U. Gerstmann, C. Gougoussis, A. Kokalj, M. Lazzeri, L. Martin-Samos, N. Marzari, F. Mauri, R. Mazzarello, S. Paolini, A. Pasquarello, L. Paulatto, C. Sbraccia, S. Scandolo, G. Sclauzero, A. P. Seitsonen, A. Smogunov, P. Umari and R. M. Wentzcovitch, *J. Phys.: Condens. Matter*, 2009, **21**, 395502.
158 D. A. Corrigan and R. M. Bendert, *J. Electrochem. Soc.*, 1989, **136**, 723.
159 M. W. Louie and A. T. Bell, *J. Am. Chem. Soc.*, 2013, **135**, 12329–12337.
160 D. A. Corrigan, *J. Electrochem. Soc.*, 1987, **134**, 377–377.
161 D. Friebel, M. W. Louie, M. Bajdich, K. E. Sanwald, Y. Cai, A. M. Wise, M. J. Cheng, D. Sokaras, T. C. Weng, R. Alonso-Mori, R. C. Davis, J. R. Bargar, J. K. Nørskov, A. Nilsson and A. T. Bell, *J. Am. Chem. Soc.*, 2015, **137**, 1305–1313.
162 H. Xiao, H. Shin and W. A. Goddard, *Proc. Natl. Acad. Sci. U.S.A.*, 2018, **115**, 5872–5877.
163 N. Li, D. K. Bediako, R. G. Hadt, D. Hayes, T. J. Kempa, F. von Cube, D. C. Bell, L. X. Chen and D. G. Nocera, *Proc. Natl. Acad. Sci. U.S.A.*, 2017, **114**, 1486–1491.
164 J. Y. C. Chen, L. Dang, H. Liang, W. Bi, J. B. Gerken, S. Jin, E. E. Alp and S. S. Stahl, *J. Am. Chem. Soc.*, 2015, **137**, 15090–15093.
165 S. Klaus, Y. Cai, M. W. Louie, L. Trotochaud and A. T. Bell, *J. Phys. Chem. C*, 2015, **119**, 7243–7254.
166 Z. K. Goldsmith, A. K. Harshan, J. B. Gerken, M. Vörös, G. Galli, S. S. Stahl and S. Hammes-Schiffer, *Proc. Natl. Acad. Sci. U.S.A.*, 2017, **114**, 3050–3055.
167 D. González-Flores, K. Klingan, P. Chernev, S. Loos, M. Reza Mohammadi, C. Pasquini, P. Kubella, I. Zaharieva, R. D. L. Smith and H. Dau, *Sustain. Energy Fuels*, 2018, **2**, 1986–1994.
168 D. A. Corrigan and S. L. Knight, *J. Electrochem. Soc.*, 1989, **136**, 613.
169 M. Görlin, P. Chernev, J. F. De Araújo, T. Reier, S. Dresp, B. Paul, R. Krähnert, H. Dau and P. Strasser, *J. Am. Chem. Soc.*, 2016, **138**, 5603–5614.
170 H. Li, C. Tsai, A. L. Koh, L. Cai, A. W. Contryman, A. H. Fragapane, J. Zhao, H. S. Han, H. C. Manoharan, F. Abild-Pedersen, J. K. Nørskov and X. Zheng, *Nat. Mater.*, 2016, **15**, 48–53.
171 Rodriguez, J.A., and Goodman D.W., *Science*, 1992, **257**, 897–903.
172 B. Hammer and J. K. Nørskov, *Surface Science*, 1995, **343**, 211–220.
173 A. Ruban, B. Hammer, P. Stoltze, H. L. Skriver and J. K. Nørskov, *J. Mol. Catal. A: Chem.*, 1997, **115**, 421–429.
174 L. A. Kibler, A. M. El-Aziz, R. Hoyer and D. M. Kolb, *Angew.Chem.Int.Ed*, 2005, **44**, 2080–2084.
175 J. R. Petrie, V. R. Cooper, J. W. Freeland, T. L. Meyer, Z. Zhang, D. A. Lutterman and H. N. Lee, *J. Am. Chem. Soc.*, 2016, **138**, 2488–2491.
176 M. Du, L. Cui, Y. Cao and A. J. Bard, *J. Am. Chem. Soc.*, 2015, **137**, 7397–7403.
177 N. Muralidharan, R. Carter, L. Oakes, A. P. Cohn and C. L. Pint, *Sci Rep*, 2016, **6**, 27542.

178 R. Chattot, O. Le Bacq, V. Beermann, S. Kühl, J. Herranz, S. Henning, L. Kühn, T. Asset, L. Guétaz, G. Renou, J. Drnec, P. Bordet, A. Pasturel, A. Eychmüller, T. J. Schmidt, P. Strasser, L. Dubau and F. Maillard, *Nat. Mater.*, 2018, **17**, 827–833.
179 J. Greeley, T. F. Jaramillo, J. Bonde, I. Chorkendorff and J. K. Nørskov, *Nat. Mater.*, 2006, **5**, 909–913.
180 A. Vojvodic and J. K. Nørskov, *Natl. Sci. Rev.*, 2015, **2**, 140–149.
181 J. Suntivich, K. J. May, H. A. Gasteiger, J. B. Goodenough and Y. Shao-Horn, *Science*, 2011, **334**, 1383–1385.
182 L. C. Seitz, C. F. Dickens, K. Nishio, Y. Hikita, J. Montoya, A. Doyle, C. Kirk, A. Vojvodic, H. Y. Hwang, J. K. Norskov and T. F. Jaramillo, *Science*, 2016, **353**, 1011–1014.
183 M. W. Kanan and D. G. Nocera, *Science*, 2008, **321**, 1072–1075.
184 A. Bergmann, E. Martinez-Moreno, D. Teschner, P. Chernev, M. Gliech, J. F. De Araújo, T. Reier, H. Dau and P. Strasser, *Nat Commun*, , DOI:10.1038/ncomms9625.
185 K. J. May, C. E. Carlton, K. A. Stoerzinger, M. Risch, J. Suntivich, Y.-L. Lee, A. Grimaud and Y. Shao-Horn, *J. Phys. Chem. Lett.*, 2012, **3**, 3264–3270.
186 M. Risch, A. Grimaud, K. J. May, K. A. Stoerzinger, T. J. Chen, A. N. Mansour and Y. Shao-Horn, *J. Phys. Chem. C*, 2013, **117**, 8628–8635.
187 S. Arias, J. G. Eon, R. A. S. S. Gil, Y. E. Licea, L. A. Palacio and A. C. Faro, *Dalton Trans.*, 2013, **42**, 2084–2093.
188 K. Chakrapani, F. Özcan, K. F. Ortega, T. Machowski and M. Behrens, *ChemElectroChem*, 2018, **5**, 93–100.
189 R. D. Shannon, *Acta Cryst.*, 1976, **32**, 751–767.
190 M. Risch, V. Khare, I. Zaharieva, L. Gerencser, P. Chernev and H. Dau, *J. Am. Chem. Soc.*, 2009, **131**, 6936–6937.
191 M. Risch, K. Klingan, J. Heidkamp, D. Ehrenberg, P. Chernev, I. Zaharieva and H. Dau, *Chem. Commun.*, 2011, **47**, 11912–11914.
192 M. W. Kanan, J. Yano, Y. Surendranath, M. Dincă, V. K. Yachandra and D. G. Nocera, *J. Am. Chem. Soc.*, 2010, **132**, 13692–13701.
193 D. K. Bediako, B. Lassalle-Kaiser, Y. Surendranath, J. Yano, V. K. Yachandra and D. G. Nocera, *J. Am. Chem. Soc.*, 2012, **134**, 6801–6809.
194 Q. Tao, B. J. Reddy, H. He, R. L. Frost, P. Yuan and J. Zhu, *Mater. Chem. Phys.*, 2008, **112**, 869–875.
195 R. L. Frost, Z. Ding and J. T. Kloprogge, *Can. J. Anal. Sci. Spectrosc.*, 2000, **45**, 96–101.
196 T. Shinagawa, A. T. Garcia-Esparza and K. Takanabe, *Sci. Rep.*, 2015, **5**, 13801.
197 L. J. Enman, M. S. Burke, A. S. Batchellor and S. W. Boettcher, *ACS Catal.*, 2016, **6**, 2416–2423.
198 J. Gao, C.-Q. Xu, S.-F. Hung, W. Liu, W. Cai, Z. Zeng, C. Jia, H. M. Chen, H. Xiao, J. Li, Y. Huang and B. Liu, *J. Am. Chem. Soc.*, 2019, **141**, 3014–3023.
199 Z. Li, Y. Zhang, Y. Feng, C.-Q. Cheng, K.-W. Qiu, C.-K. Dong, H. Liu and X.-W. Du, *Adv. Funct. Mater.*, 2019, **29**, 1903444.

200 J. Liu, E. Jia, L. Wang, K. A. Stoerzinger, H. Zhou, C. S. Tang, X. Yin, X. He, E. Bousquet, M. E. Bowden, A. T. S. Wee, S. A. Chambers and Y. Du, *Adv. Sci.*, 2019, **6**, 1901073–1901073.
201 M. Görlin, P. Chernev, P. Paciok, C. W. Tai, J. Ferreira de Araújo, T. Reier, M. Heggen, R. Dunin-Borkowski, P. Strasser and H. Dau, *Chem. Commun.*, 2019, **55**, 818–821.
202 L. Francàs, S. Corby, S. Selim, D. Lee, C. A. Mesa, R. Godin, E. Pastor, I. E. L. Stephens, K. S. Choi and J. R. Durrant, *Nat Commun*, 2019, **10**, 1–10.
203 C. Kuai, C. Xi, A. Hu, Y. Zhang, Z. Xu, D. Nordlund, C.-J. Sun, C. A. Cadigan, R. M. Richards, L. Li, C.-K. Dong, X.-W. Du and F. Lin, *J. Am. Chem. Soc.*, , DOI:10.1021/jacs.1c07975.
204 C. Peng, N. Ran, G. Wan, W. Zhao, Z. Kuang, Z. Lu, C. Sun, J. Liu, L. Wang and H. Chen, *ChemSusChem*, 2020, **13**, 811–818.
205 Y. Wang and S. Wang, *ECS Trans.*, 2017, **80**, 1029.
206 M. A. W. Schoen, O. Calderon, N. M. Randell, S. Jimenez-Villegas, K. M. Daly, R. Chernikov and S. Trudel, *J. Mater. Chem. A*, 2021, **9**, 13252–13262.
207 M. B. Stevens, C. D. M. Trang, L. J. Enman, J. Deng and S. W. Boettcher, *J. Am. Chem. Soc.*, 2017, **139**, 11361–11364.
208 N. Li, T. P. Keane, S. S. Veroneau, R. G. Hadt, D. Hayes, L. X. Chen and D. G. Nocera, *Proc. Natl. Acad. Sci. U.S.A.*, 2020, 202001529–202001529.
209 E. P. Alsaç, A. Whittingham, Y. Liu and R. D. L. Smith, *Chem. Mater.*, 2019, **31**, 7522–7530.
210 D. Y. Chung, P. P. Lopes, P. Farinazzo Bergamo Dias Martins, H. He, T. Kawaguchi, P. Zapol, H. You, D. Tripkovic, D. Strmcnik, Y. Zhu, S. Seifert, S. Lee, V. R. Stamenkovic and N. M. Markovic, *Nat Energy*, 2020, **5**, 222–230.
211 M. R. Mohammadi, S. Loos, P. Chernev, C. Pasquini, I. Zaharieva, D. González-Flores, P. Kubella, K. Klingan, R. D. L. Smith and H. Dau, *ACS Catal.*, 2020, **10**, 7990–7999.
212 F. Dionigi and P. Strasser, *Adv. Energy Mater.*, 2016, **6**, 1600621.
213 X. Bo, Y. Li, X. Chen and C. Zhao, *Chem. Mater.*, 2020, **32**, 4303–4311.
214 A. Mavrič, M. Fanetti, Y. Lin, M. Valant and C. Cui, *ACS Catal.*, 2020, **10**, 9451–9457.
215 M. Yu, E. Budiyanto and H. Tüysüz, *Angew.Chem.Int.Ed*, 2021, **60**, 2–26.
216 W. Cai, R. Chen, H. Yang, H. B. Tao, H.-Y. Wang, J. Gao, W. Liu, S. Liu, S.-F. Hung and B. Liu, *Nano Lett.*, 2020, **20**, 4278–4285.
217 K. Klingan, F. Ringleb, I. Zaharieva, J. Heidkamp, P. Chernev, D. Gonzalez-Flores, M. Risch, A. Fischer and H. Dau, *ChemSusChem*, 2014, **7**, 1301–1310.
218 Y. Song, M. Song, P. Liu, W. Liu, L. Yuan, X. Hao, L. Pei, B. Xu, J. Guo and Z. Sun, *J. Mater. Chem. A*, 2021, **9**, 14372–14380.
219 Y.-Y. Dong, D.-D. Ma, X.-T. Wu and Q.-L. Zhu, *Inorg. Chem. Front.*, 2019, **7**, 270–276.
220 A. V. Radha, S. Weiß, I. Sanjuán, M. Ertl, C. Andronescu and J. Breu, *Chem. Eur. J.*, 2021, **27**, 16930–16937.
221 F. Menil, *J. Phys. Chem. Solids*, 1985, **46**, 763–789.
222 M. Akasaka and H. Ohashi, *Phys Chem Minerals*, 1985, **12**, 13–18.
223 P. Ravindran, R. Vidya, H. Fjellvåg and A. Kjekshus, *Phys. Rev. B*, 2008, **77**, 134448.

224 D. S. Hall, D. J. Lockwood, S. Poirier, C. Bock and B. R. MacDougall, *J. Phys. Chem. A*, 2012, **116**, 6771–6784.
225 L. Gourrier, S. Deabate, T. Michel, M. Paillet, P. Hermet, J.-L. Bantignies and F. Henn, *J. Phys. Chem. C*, 2011, **115**, 15067–15074.
226 S. S. Mitra, *Solid State Physics*, Academic Press: New York, 1962, vol. 13.
227 T. Ishikawa, K. Matsumoto, K. Kandori and T. Nakayama, *J. Solid State Chem.*, 2006, **179**, 1110–1118.
228 P. Dawson, C. D. Hadfield and G. R. Wilkinson, *J. Phys. Chem. Solids*, 1973, **34**, 1217–1225.
229 M. C. Bernard, R. Cortes, M. Keddam, H. Takenouti, P. Bernard and S. Senyarich, *J. Power Sources*, 1996, **63**, 247–254.
230 M. C. Bernard, P. Bernard, M. Keddam, S. Senyarich and H. Takenouti, *Electrochim. Acta*, 1996, **41**, 91–93.
231 B. C. Cornilsen, P. J. Karjala and P. L. Loyselle, *J. Power Sources*, 1988, **22**, 351–357.
232 S. Deabate, F. Fourgeot and F. Henn, *J. Power Sources*, 2000, **87**, 125–136.
233 M. Aghazadeh, A. N. Golikand and M. Ghaemi, *Int. J. Hydrog. Energy*, 2011, **36**, 8674–8679.
234 X. Xue, F. Yu, J. G. Li, G. Bai, H. Yuan, J. Hou, B. Peng, L. Chen, M. F. Yuen, G. Wang, F. Wang and C. Wang, *Int. J. Hydrog. Energy*, 2019, **45**, 1802–1809.
235 X. Li, X. Hao, Z. Wang, A. Abudula and G. Guan, *Journal of Power Sources*, 2017, **347**, 193–200.
236 H. C. Greenwell, W. Jones, S. L. Rugen-Hankey, P. J. Holliman and R. L. Thompson, *Green Chem.*, 2010, **12**, 688–695.
237 Z.-X. Shi, J.-W. Zhao, C.-F. Li, H. Xu and G.-R. Li, *Appl. Catal. B.*, 2021, **298**, 120558.
238 M. Liu, K.-A. Min, B. Han and L. Y. S. Lee, *Adv. Energy Mater.*, 2021, **11**, 2101281.
239 T. E. Westre, P. Kennepohl, J. G. DeWitt, B. Hedman, K. O. Hodgson and E. I. Solomon, *J. Am. Chem. Soc.*, 1997, **119**, 6297–6314.
240 M. Wilke, F. Farges, P.-E. Petit, G. E. Brown and F. Martin, *Am. Mineral.*, 2001, **86**, 714–730.
241 H. Dau, P. Liebisch and M. Haumann, *Anal Bioanal Chem*, 2003, **376**, 562–583.
242 S. Wang, J. Nai, S. Yang and L. Guo, *ChemNanoMat*, 2015, **1**, 324–330.
243 J. a. V. Butler, *Trans. Faraday Soc.*, 1924, **19**, 729–733.
244 T. Erdey-Grúz and M. Volmer, *Zeitschrift für Physikalische Chemie*, 1930, **150A**, 203–213.
245 L. Lv, Z. Yang, K. Chen, C. Wang and Y. Xiong, *2D Layered Double Hydroxides for Oxygen Evolution Reaction: From Fundamental Design to Application*, Wiley-VCH Verlag, 2019, vol. 9.
246 C. Kuai, Y. Zhang, L. Han, H. L. Xin, C.-J. Sun, D. Nordlund, S. Qiao, X.-W. Du and F. Lin, *J. Mater. Chem. A*, 2020, **8**, 10747.
247 M. Casas-Cabanas, M. R. Palacín and J. Rodríguez-Carvajal, *Powder Diffr.*, 2005, **20**, 334–344.
248 R. M. Badger, *J. Chem. Phys.*, 1935, **3**, 710–714.
249 M. T. Green, *J. Am. Chem. Soc.*, 2006, **128**, 1902–1906.
250 A. D. Spaeth, N. L. Gagnon, D. Dhar, G. M. Yee and W. B. Tolman, *J. Am. Chem. Soc.*, 2017, **139**, 4477–4485.

251 M. A. Boyer, O. Marsalek, J. P. Heindel, T. E. Markland, A. B. McCoy and S. S. Xantheas, *J. Phys. Chem. Lett.*, 2019, **10**, 918–924.
252 B. B. Gicha, L. T. Tufa, Y. Choi and J. Lee, *ACS Appl. Energy Mater.*, 2021, **4**, 6833–6841.
253 D. Zhou, S. Wang, Y. Jia, X. Xiong, H. Yang, S. Liu, J. Tang, J. Zhang, D. Liu, L. Zheng, Y. Kuang, X. Sun and B. Liu, *Angew.Chem.Int.Ed*, 2019, **58**, 736–740.
254 https://www.uni-due.de/~hm236ap/hoersten/home.html, (Accessed January 24, 2022).
255 B. Ravel and M. Newville, *J Synchrotron Rad*, 2005, **12**, 537–541.
256 S. Calvin, *XAFS for Everyone*, CRC Press, 2013.
257 A. Karmakar, K. Karthick, S. S. Sankar, S. Kumaravel, R. Madhu and S. Kundu, *J. Mater. Chem. A*, 2021, **9**, 1314–1352.
258 T. N. Ramesh and P. V. Kamath, *J. Power Sources*, 2006, **156**, 655–661.
259 H. Schäfer, S. Sadaf, L. Walder, K. Kuepper, S. Dinklage, J. Wollschläger, L. Schneider, M. Steinhart, J. Hardege and D. Daum, *Energy Environ. Sci.*, 2015, **8**, 2685–2697.
260 N. Yamada, S. Kitano, Y. Yato, D. Kowalski, Y. Aoki and H. Habazaki, *ACS Appl. Energy Mater.*, 2020, **3**, 12316–12326.
261 J. Fan, Z. Chen, H. Shi and G. Zhao, *Chem. Commun.*, 2016, **52**, 4290–4293.
262 T. Hibino and H. Ohya, *Appl. Clay Sci.*, 2009, **45**, 123–132.
263 C. Zhang, M. Shao, L. Zhou, Z. Li, K. Xiao and M. Wei, *ACS Appl. Mater. Interfaces*, 2016, **8**, 33697–33703.
264 S. Dresp, F. Luo, R. Schmack, S. Kühl, M. Gliech and P. Strasser, *Energy Environ. Sci.*, 2016, **9**, 2020–2024.
265 Y. Song, B. Xu, T. Liao, J. Guo, Y. Wu and Z. Sun, *Small*, 2021, **17**, 2002240.
266 Z. Zhang, D. Zhou, J. Liao, X. Bao and H. Yu, *Int. J. Energy Res.*, 2019, **43**, 1460–1467.
267 X. Luo, X. Wei, H. Zhong, H. Wang, Y. Wu, Q. Wang, W. Gu, M. Gu, S. P. Beckman and C. Zhu, *ACS Appl. Mater. Interfaces*, 2020, **12**, 3539–3546.
268 J. Zhang, J. Liu, L. Xi, Y. Yu, N. Chen, S. Sun, W. Wang, K. M. Lange and B. Zhang, *J. Am. Chem. Soc.*, 2018, **140**, 3876–3879.
269 M. Rinawati, Y.-X. Wang, K.-Y. Chen and M.-H. Yeh, *Chem. Eng. J.*, 2021, **423**, 130204.
270 D. A. Corrigan, *J. Electrochem. Soc.*, 1987, **134**, 377–377.
271 M. Steimecke, G. Seiffarth, C. Schneemann, F. Oehler, S. Förster and M. Bron, *ACS Catal.*, 2020, **10**, 3595–3603.
272 C. Qiao, Z. Usman, T. Cao, S. Rafai, Z. Wang, Y. Zhu, C. Cao and J. Zhang, *Chem. Eng. J.*, 2021, **426**, 130873.
273 Y. Zeng, X. Li, J. Wang, M. T. Sougrati, Y. Huang, T. Zhang and B. Liu, *Chem Catalysis*, 2021, **1**, 1215–1233.
274 D. Zhou, P. Li, X. Lin, A. McKinley, Y. Kuang, W. Liu, W.-F. Lin, X. Sun and X. Duan, *Chem. Soc. Rev*, 2021, **50**, 8790–8817.
275 S. Anantharaj, S. Kundu and S. Noda, *Nano Energy*, 2021, **80**, 105514.
276 K. Ma, J. P. Cheng, J. Zhang, M. Li, F. Liu and X. Zhang, *Electrochim. Acta*, 2016, **198**, 231–240.
277 Y. Sun, Y. Zhou, Z. Wang and X. Ye, *Appl. Surf. Sci.*, 2009, **255**, 6372–6377.

278 Y. P. Yew, K. Shameli, M. Miyake, N. Kuwano, N. B. Bt Ahmad Khairudin, S. E. Bt Mohamad and K. X. Lee, *Nanoscale Res. Lett*, 2016, **11**, 276.
279 M. Singh, P. Ulbrich, V. Prokopec, P. Svoboda, E. Šantavá and F. Štěpánek, *J. Solid State Chem.*, 2013, **200**, 150–156.
280 E. P. Alsaç, K. Zhou, W. Rong, S. Salamon, J. Landers, H. Wende and R. D. L. Smith, *Energy Environ. Sci.*, 2022, **15**, 2638–2652.
281 M. Hanesch, *Geophys. J. Int.*, 2009, **177**, 941–948.
282 I. Chourpa, L. Douziech-Eyrolles, L. Ngaboni-Okassa, J. F. Fouquenet, S. Cohen-Jonathan, M. Soucé, H. Marchais and P. Dubois, *Analyst*, 2005, **130**, 1395–1403.
283 T. Yamamoto, *X-Ray Spectrom.*, 2008, **37**, 572–584.
284 A. Boubnov, H. Lichtenberg, S. Mangold and J.-D. Grunwaldt, *J Synchrotron Rad*, 2015, **22**, 410–426.
285 A. Kontny, B. Reznik, A. Boubnov, J. Göttlicher and R. Steininger, *Geochem Geophys.*, 2018, **19**, 921–931.
286 D. K. Bora, A. Braun, S. Erat, O. Safonova, T. Graule and E. C. Constable, *Current Applied Physics*, 2012, **12**, 817–825.
287 Z. Xia, H. Zhang, K. Shen, Y. Qu and Z. Jiang, *Phys. B: Condens. Matter.*, 2018, **542**, 12–19.
288 H. Funke, M. Chukalina and A. C. Scheinost, *J Synchrotron Rad*, 2007, **14**, 426–432.
289 R. Farhat, J. Dhainy and L. I. Halaoui, *ACS Catal.*, 2020, **10**, 20–35.
290 O. N. Shebanova and P. Lazor, *J. Solid State Chem.*, 2003, **174**, 424–430.
291 C. Kuai, Z. Xu, C. Xi, A. Hu, Z. Yang, Y. Zhang, C.-J. Sun, L. Li, D. Sokaras, C. Dong, S.-Z. Qiao, X.-W. Du and F. Lin, *Nat Catal*, 2020, **3**, 743–753.
292 F. Dionigi, J. Zhu, Z. Zeng, T. Merzdorf, H. Sarodnik, M. Gliech, L. Pan, W.-X. Li, J. Greeley and P. Strasser, *Angew.Chem.Int.Ed*, 2021, **60**, 14446–14457.
293 J. O. Bockris, *J. Chem. Phys.*, 1956, **24**, 817–817.
294 M. C. Henstridge, N. V. Rees and R. G. Compton, *J. Electroanal. Chem.*, 2012, **687**, 79–83.
295 M. C. Henstridge, E. Laborda and R. G. Compton, *J. Electroanal. Chem.*, 2012, **674**, 90–96.
296 E. Laborda, M. C. Henstridge, C. Batchelor-McAuley and R. G. Compton, *Chem. Soc. Rev*, 2013, **42**, 4894–4905.
297 M. C. Henstridge, E. Laborda, N. V. Rees and R. G. Compton, *Electrochim. Acta*, 2012, **84**, 12–20.
298 M. G. Siebecker and D. L. Sparks, *J. Phys. Chem. A*, 2017, **121**, 6992–6999.
299 H.-Y. Wang, S.-F. Hung, H.-Y. Chen, T.-S. Chan, H. M. Chen and B. Liu, *J. Am. Chem. Soc.*, 2016, **138**, 36–39.
300 J. B. Gerken, J. G. McAlpin, J. Y. C. Chen, M. L. Rigsby, W. H. Casey, R. D. Britt and S. S. Stahl, *J. Am. Chem. Soc.*, 2011, **133**, 14431–14442.
301 J. G. McAlpin, Y. Surendranath, M. Dincă, T. A. Stich, S. A. Stoian, W. H. Casey, D. G. Nocera and R. D. Britt, *J. Am. Chem. Soc.*, 2010, **132**, 6882–6883.
302 P. Du, O. Kokhan, K. W. Chapman, P. J. Chupas and D. M. Tiede, *J. Am. Chem. Soc.*, 2012, **134**, 11096–11099.

303 C. L. Farrow, D. K. Bediako, Y. Surendranath, D. G. Nocera and S. J. L. Billinge, *J. Am. Chem. Soc.*, 2013, **135**, 6403–6406.
304 N. Li, R. G. Hadt, D. Hayes, L. X. Chen and D. G. Nocera, *Nat Commun*, 2021, **12**, 4218.
305 J. T. Mefford, A. R. Akbashev, M. Kang, C. L. Bentley, W. E. Gent, H. D. Deng, D. H. Alsem, Y.-S. Yu, N. J. Salmon, D. A. Shapiro, P. R. Unwin and W. C. Chueh, *Nature*, 2021, **593**, 67–73.
306 A. E. Thorarinsdottir, S. S. Veroneau and D. G. Nocera, *Nat Commun*, 2022, **13**, 1243.
307 A. Badreldin, A. E. Abusrafa and A. Abdel-Wahab, *ChemSusChem*, 2021, **14**, 10–32.
308 S. R. Shieh and T. S. Duffy, *Phys. Rev. B*, 2002, **66**, 134301.
309 F. Lyu, Y. Bai, Q. Wang, L. Wang, X. Zhang and Y. Yin, *Dalton Trans.*, 2017, **46**, 10545–10548.
310 Y. Zheng, R. Gao, Y. Qiu, L. Zheng, Z. Hu and X. Liu, *Inorg. Chem.*, 2021, **60**, 5252–5263.
311 M. S. Burke, S. Zou, L. J. Enman, J. E. Kellon, C. A. Gabor, E. Pledger and S. W. Boettcher, *J. Phys. Chem. Lett.*, 2015, **6**, 3737–3742.
312 L. J. Enman, M. B. Stevens, M. H. Dahan, M. R. Nellist, M. C. Toroker and S. W. Boettcher, *Angew.Chem.Int.Ed*, 2018, **57**, 12840–12844.
313 M. S. Burke, M. G. Kast, L. Trotochaud, A. M. Smith and S. W. Boettcher, *J. Am. Chem. Soc.*, 2015, **137**, 3638–3648.
314 S.-H. Ye, Z.-X. Shi, J.-X. Feng, Y.-X. Tong and G.-R. Li, *Angew.Chem.Int.Ed*, 2018, **57**, 2672–2676.
315 F. Yang, K. Sliozberg, I. Sinev, H. Antoni, A. Bähr, K. Ollegott, W. Xia, J. Masa, W. Grünert, B. R. Cuenya, W. Schuhmann and M. Muhler, *ChemSusChem*, 2017, **10**, 156–165.
316 F. Pertlik, *Monatshefte fuer Chemie*, 1999, **130**, 1083–1088.
317 R. G. Delaplane, J. A. Ibers, J. R. Ferraro and J. J. Rush, *J. Chem. Phys.*, 1969, **50**, 1920–1927.
318 E. Scavetta, B. Ballarin, M.Gazzano and D. Tonelli, *Electrochim. Acta*, 2009, **54**, 1027–1033.
319 F. Leroux, E. M. Moujahid, C. Taviot-Guého and J.-P. Besse, *Solid State Sci.*, 2001, **3**, 81–92.
320 M. Herrero, P. Benito, F. M. Labajos and V. Rives, *Catal. Today*, 2007, **128**, 129–137.
321 C. A. Serhal, R. El Khawaja, M. Labaki, I. Mallard, C. Poupin, R. Cousin and S. Siffert, *J. Solid State Chem.*, 2022, **309**, 122943.
322 M. E. Fleet, *Acta Cryst C*, 1984, **40**, 1491–1493.
323 C. Greaves, *J. Solid State Chem.*, 1983, **49**, 325–333.
324 B. Rivas-Murias and V. Salgueiriño, *J. Raman Spectrosc.*, 2017, **48**, 837–841.
325 C. Pasquini, I. Zaharieva and H. Dau, *J. Chem. Phys.*, 2020, **152**, 194202–194202.
326 J. Yang, H. Liu, W. N. Martens and R. L. Frost, *J. Phys. Chem. C*, 2010, **114**, 111–119.
327 J. Pérez-Ramírez, G. Mul, F. Kapteijn and J. A. Moulijn, *J. Mater. Chem.*, 2001, **11**, 821–830.
328 O. Bøckman, T. Østvold, G. A. Voyiatzis and G. N. Papatheodorou, *Hydrometallurgy*, 2000, **55**, 93–105.
329 H. B. Li, P. Liu, Y. Liang, J. Xiao and G. W. Yang, *RSC Adv.*, 2013, **3**, 26412–26417.
330 Y. Q. Gao, H. B. Li and G. W. Yang, *J. Appl. Phys.*, 2016, **119**, 034902.
331 C.-W. Tang, C.-B. Wang and S.-H. Chien, *Thermochim. Acta*, 2008, **473**, 68–73.

332 Á. Gallo-Cordova, A. Espinosa, A. Serrano, L. Gutiérrez, N. Menéndez, M. del P. Morales and E. Mazarío, *Mater. Chem. Front.*, 2020, **4**, 3063–3073.
333 H. Niwa, K. Higashiyama, K. Amaha, W. Kobayashi, K. Ishii and Y. Moritomo, *Appl. Phys. Express*, 2019, **12**, 052005.
334 E. Efimova, V. Efimov, D. Karpinsky, A. Kuzmin, J. Purans, V. Sikolenko, S. Tiutiunnikov, I. Troyanchuk, E. Welter, D. Zajac, V. Simkin and A. Sazonov, *J. Phys. Chem. Solids*, 2008, **69**, 2187–2190.
335 M. Risch, K. Klingan, F. Ringleb, P. Chernev, I. Zaharieva, A. Fischer and H. Dau, *ChemSusChem*, 2012, **5**, 542–549.
336 Y. Liu, Y. Li, G. Yuan, J. Zhang, X. Zhang and Q. Wang, *ChemElectroChem*, 2019, **6**, 2415–2422.
337 Y. Zhou, J. Hu, D. Li and Q. Gao, *Chem. Commun.*, 2021, **57**, 7653–7656.

Appendices

Appendix A: Supplementary Information for Chapter 3

Calculation of activation energy and electron transfer coefficients from reaction coordinate diagrams:

The Butler-Volmer model for electron transfer defines the standard rate constant, k^0, as the kinetics for electron transfer when the electrode voltage, E, is held at the formal potential for the redox couple of interest, $E^{0'}$. At this point the kinetics for oxidation (k_{ox}) and reduction (k_{red}) reactions are equivalent and defined as k^0, which can be described by the Arrhenius equation and the activation energy at the formal potential, $\Delta G_0^{\ddagger}$:

$$k^0 = Ae^{-\Delta G_0^{\ddagger}/RT} \qquad \textbf{(A. 1)}$$

The activation energy at the formal potential, $\Delta G_0^{\ddagger}$, thus provides a standardized measure of kinetic facility for electron transfer. Application of a positive overpotential ($\eta = E - E^{0'}$) induces a negative free energy shift in the potential energy surface (PES) describing the oxidized phase, lowering the activation energy for oxidation ($\Delta G_{ox}^{\ddagger}$) and increasing the activation energy for reduction ($\Delta G_{red}^{\ddagger}$). The electron transfer coefficient, η, is a fraction that describes the portion of this free energy change that affects $\Delta G_{red}^{\ddagger}$.

$$\Delta G_{ox}^{\ddagger} = \Delta G_0^{\ddagger} - (1-\alpha)F\eta \qquad \textbf{(A. 2)}$$

$$\Delta G_{red}^{\ddagger} = \Delta G_0^{\ddagger} - \alpha F\eta \qquad \textbf{(A. 3)}$$

The transfer coefficient represents the symmetry of the two PES: 0.5 indicates perfectly symmetric curves, α<0.5 indicates a relative broadening in the PES for the oxidized phase, and α>0.5 indicates a relative broadening for the reduced phase.

Nickel (oxy)hydroxide-based materials are known to undergo significant volume changes upon oxidation and reduction. Therefore, the spacing between metal atoms could be a reasonable parameter for the reaction coordinate diagrams. For the work presented here, reaction coordinate diagrams were created for each of the binary compositions by plotting DFT-calculated single point energies as a function of average Ni-M distances for both the oxidized and reduced phases (**Figure 3.10**). The data were mathematically fitted using parabolic function and the curves were shifted such that the minima were located at zero free energy to simulate the situation at $E^{0'}$. The standard activation energy, $\Delta G_0^{\ddagger}$, was taken as the intercept of the two parabolic PES. The electron transfer coefficient was then extracted by shifting the PES for the oxidized phase by -0.300 eV (blue curve in **Figure 3.10**), extracting $\Delta G_{ox}^{\ddagger}$ and $\Delta G_{red}^{\ddagger}$ from the new intercept, then using **equation A.2** or **A.3** to calculate α. The relevant activation energies and α values are provided in **Figure 3.10C-D**.

Table A. 1 Calculated energy for the reduced state of $Ni_9(OH)_{18}$, $Al_1Ni_8O_{18}H_{17}$, $Ga_1Ni_8O_{18}H_{17}$, and $Fe_1Ni_8O_{18}H_{17}$ under varied biaxial strain.

	Ni-Ni		**Al-Ni**		**Ga-Ni**		**Fe-Ni**	
a_{latt} **(Å)**	***E* (Ry)**	**Δ*E* (eV)**	***E* (Ry)**	**Δ*E* (eV)**	***E* (Ry)**	**Δ*E* (eV)**	***E* (Ry)**	**Δ*E* (eV)**
9.34	-2441.59459	0	-2294.63415	0	-2532.83237	0	-2583.93179	0
9.25	-2441.57246	0.3011	-2294.61909	0.2049	-2532.81328	0.2598	-2583.91160	0.2746
9.15	-2441.53971	0.7466	-2294.59410	0.5448	-2532.78377	0.6613	-2583.881126	0.6893
9.06	-2441.50262	1.2513	-2294.56384	0.9566	-2532.74942	1.1286	-2583.84617	1.1649
8.97	-2441.45801	1.8582	-2294.52592	1.4725	-2532.70739	1.7004	-2583.79404	1.8741
8.87	-2441.39931	2.6569	-2294.47444	2.1729	-2532.65134	2.4631	-2583.74790	2.5018
8.78	-2441.33791	3.4922	-2294.41928	2.9235	-2532.59212	3.2688	-2583.68901	3.3030
8.69	-2441.26808	4.4423	-2294.35565	3.7892	-2532.52436	4.1906	-2583.62217	4.2125
vc-relax[a]	-2441.62179	-0.3699	-2294.64436	-0.1390	-2532.85094	-0.2527	-2583.95320	-0.2913

[a] relaxation calculation with variable unit cell dimensions; structure outputs provided below.

Table A. 2 Calculated energy for the oxidized state of Ni_9O_{18}, $[Al_1Ni_8O_{18}]^-$, $[Ga_1Ni_8O_{18}]^-$, and $[Fe_1Ni_8O_{18}]^-$ under varied biaxial strain.

	Ni-Ni		**Al-Ni**		**Ga-Ni**		**Fe-Ni**	
a_{latt} **(Å)**	***E* (Ry)**	**Δ*E* (eV)**	***E* (Ry)**	**Δ*E* (eV)**	***E* (Ry)**	**Δ*E* (eV)**	***E* (Ry)**	**Δ*E* (eV)**
8.62	-2418.02896	0	-2272.59901	0	-2510.78452	0	-2561.88583	0.0000
8.71	-2418.00313	0.3515	-2272.57934	0.2677	-2510.77h	0.1620	-2561.865187	0.2809
8.79	-2417.97561	0.7258	-2272.55501	0.5986	-2510.75430	0.4112	-2561.84794	0.5155
8.88	-2417.93329	1.3017	-2272.51919	1.0860	-2510.72499	0.8100	-2561.82055	0.8882
8.96	-2417.89016	1.8885	-2272.48028	1.6153	-2510.69169	1.2630	-2561.79327	1.2594
9.05	-2417.83454	2.6452	-2272.42919	2.3104	-2510.64668	1.8754	-2561.759132	1.7238
9.14	-2417.77203	3.4956	-2272.37093	3.1031	-2510.59428	2.5884	-2561.72225	2.2256
9.22	-2417.711191	4.3234	-2272.31361	3.8830	-2510.54196	3.3002	-2561.69028	2.6606
vc-relax[a]	-2418.04395	-0.2039	-2272.60580	-0.0924	-2510.78564	-0.0152	-2561.891451	-0.0765

[a] relaxation calculation with variable unit cell dimensions; structure outputs provided below.

Structural outputs from VC-Relax Calculations:

Reduced phase: $Ni_9O_{18}H_{18}$

Ni	7.985771574	2.766676524	7.500389579
O	7.985909174	4.610679824	8.520389245
H	7.986323035	4.610918766	9.487255457
Ni	6.388900702	5.532534820	7.500389579
Ni	9.582616519	5.532519852	7.500070820
O	7.985802563	0.922907695	6.480229953
H	7.986093130	0.923184384	5.513177577
Ni	6.388890316	0.000865178	7.500051085
O	9.582850847	1.844751183	8.519885815
H	9.583435209	1.844808770	9.487175628
O	9.582433108	3.688620808	6.480118412
H	9.582117647	3.688741396	5.512907740
O	11.179498680	4.610431281	8.519863653
H	11.179416006	4.610161766	9.486872888
O	11.179506829	6.454465513	6.480091066
H	11.179288862	6.454339671	5.513274958
O	12.776560947	7.376560725	8.520159120
H	12.777333973	7.377007032	9.486755808
Ni	4.791932892	2.766620558	7.500023077
O	4.791988646	0.922775494	6.479934491
H	4.791671745	0.923074380	5.512758500
Ni	3.195096996	0.000770766	7.499577892
O	6.388754037	1.844723092	8.520177879
H	6.388551370	1.844918244	9.487287629
O	6.388916153	3.688619885	6.480563777
H	6.388926122	3.688625642	5.513422965
O	7.985675429	6.454283048	6.480118412
H	7.985622131	6.453949557	5.512907740
O	9.582488685	7.376530547	8.519863653
H	9.582213940	7.376593709	9.486872888

Reduced phase: $Al_1Ni_8O_{18}H_{17}$

Al	7.992526868	2.684358386	7.529317560
O	7.922430791	4.394520176	8.489715488
H	8.071263357	4.315106615	9.442144161
Ni	6.318777749	5.475954012	7.552321192
Ni	9.472582220	5.467253342	7.470634922
O	7.842866904	1.071812816	6.416485436
H	7.834853413	1.076410910	5.450261114
Ni	6.322345085	0.011074543	7.470617756
O	9.338078172	1.907480469	8.446675029
O	9.314210521	3.620096719	6.416394667
H	9.306185133	3.624853657	5.450162648
O	11.023200027	4.566146998	8.499133620
H	10.954464388	4.513014584	9.462391837
O	11.051900036	6.390771989	6.444826660
H	11.067574553	6.381687099	5.478016054
O	12.617664976	7.327961810	8.499177052
H	12.629097369	7.413988999	9.462451503
Ni	4.738030152	2.737963302	7.552275214
O	4.740230626	0.934982648	6.497550237
H	4.722671923	0.963189652	5.531295239
Ni	3.144560035	0.010395641	7.517210352
O	6.476363834	1.889971919	8.489724396
H	6.619480178	1.800764073	9.442171982
O	6.467511599	3.564796890	6.562854608
H	6.466535285	3.565451603	5.596370229
O	7.881337734	6.375451629	6.497615769
H	7.848147633	6.376681876	5.531351707
O	9.487966984	7.293712371	8.516572584
H	9.506093812	7.283308926	9.483387864
Ni	1.496761965	2.699014597	7.537950360

Ni	1.598216002	2.766646595	7.499577892
O	1.598083724	0.922634682	6.479619279
H	1.597473735	0.922282504	5.512472266
Ni	0.001497889	0.000864807	7.499999127
O	3.194934647	1.844612578	8.519510930
H	3.194734769	1.844497178	9.486474654
Ni	3.195194424	5.532502351	7.500051085
O	3.195158133	3.688563885	6.479934491
H	3.195258526	3.688139999	5.512758500
O	4.791940049	4.610482860	8.520177879
H	4.792007721	4.610209770	9.487287629
O	4.792179580	6.454418585	6.480229953
H	4.792564485	6.454531879	5.513177577
O	6.389012783	7.376634607	8.519885815
H	6.389354835	7.377111887	9.487175628
O	1.597323060	0.903631411	6.444766105
H	1.595816126	0.904513104	5.478025128
Ni	-0.007869331	0.093137748	7.538078873
O	3.151387216	1.825507296	8.553745898
H	3.081786979	1.801821936	9.518093614
Ni	3.154489160	5.477457824	7.517334556
O	3.155158408	3.636644026	6.511971399
H	3.160969432	3.624688962	5.544869267
O	4.747647726	4.557680840	8.554063084
H	4.749380398	4.556683625	9.521066972
O	4.749021659	6.397339564	6.512087166
H	4.762232050	6.398347903	5.545002982
O	6.315677365	7.306200861	8.553853335
H	6.301421979	7.378188111	9.518205226

Reduced phase: $Ga_1Ni_8O_{18}H_{17}$

Ga	8.048535716	2.700202567	7.579071591
O	7.968498181	4.527691022	8.527650131
H	8.091793237	4.456299491	9.485463662
Ni	6.353164769	5.527543984	7.554013140
Ni	9.539712748	5.525809361	7.469873131
O	7.886068265	0.985906307	6.406460770
H	7.871372662	1.037311089	5.440035776
Ni	6.347333950	-0.003437051	7.469899978
O	9.465944569	1.882304260	8.473508130
O	9.452154850	3.698548221	6.406435807
H	9.400588082	3.685814951	5.439987672
O	11.095656619	4.599812519	8.487421524
H	11.034956861	4.542778186	9.451128679
O	11.123191589	6.434833949	6.446009071
H	11.134917787	6.428213674	5.479301757
O	12.698630032	7.376283434	8.487539774

Reduced phase: $Fe_1Ni_8O_{18}H_{17}$

Fe	8.082532078	2.680729306	7.612213479
O	7.964814892	4.561825945	8.546047526
H	8.033741361	4.552968101	9.511508072
Ni	6.356716001	5.512040821	7.519316970
Ni	9.542566440	5.527337038	7.486140316
O	7.913225999	0.941064161	6.421814737
H	7.887027400	0.993387989	5.456042999
Ni	6.347293473	-0.007126024	7.486230059
O	9.493309427	1.866001718	8.508324628
O	9.504156998	3.697166748	6.421672989
H	9.445975338	3.693153851	5.455913267
O	11.107704006	4.597930806	8.496350292
H	11.057828687	4.549441760	9.461092857
O	11.122853127	6.434480894	6.455841021
H	11.121247799	6.435486308	5.488759792
O	12.705328292	7.365353820	8.496831700

H	12.717618852	7.457254051	9.451258097
Ni	4.752556371	2.755451380	7.553857032
O	4.762817752	0.942060850	6.499820083
H	4.739138446	0.968849598	5.533554873
Ni	3.161825042	0.012657789	7.513251246
O	6.426036070	1.856310466	8.527694832
H	6.549599738	1.785391302	9.485506734
O	6.463562803	3.615658921	6.575397066
H	6.513681820	3.586903612	5.609231724
O	7.928686344	6.425415249	6.499955220
H	7.893659504	6.432570317	5.533691961
O	9.541195156	7.348163635	8.512003666
H	9.562254996	7.336073881	9.478721359
Ni	1.533517110	2.721333665	7.510296638
O	1.611761939	0.907582207	6.433765488
H	1.622318570	0.901485719	5.466691464
Ni	0.001960555	0.068372774	7.510455488
O	3.162416032	1.836691949	8.540444880
H	3.076596546	1.821964673	9.503596202
Ni	3.178837390	5.512206434	7.510094255
O	3.186232120	3.665086357	6.504968263
H	3.197747966	3.654912615	5.537911090
O	4.774357853	4.590976745	8.548814396
H	4.763866680	4.597019700	9.515787539
O	4.782277853	6.429348870	6.505144070
H	4.796768683	6.424557217	5.538087139
O	6.353796154	7.364059957	8.540633630
H	6.323667734	7.445800517	9.503785811

H	12.721822892	7.432989505	9.461682134
Ni	4.767610442	2.759453817	7.519342337
O	4.770975272	0.927020486	6.491520677
H	4.773113264	0.928469030	5.524579780
Ni	3.170927580	0.007294923	7.509352462
O	6.394457791	1.841845042	8.545476023
H	6.436346539	1.785803945	9.511002868
O	6.409761984	3.646614059	6.516571230
H	6.397493648	3.653647537	5.549320832
O	7.945308692	6.425257671	6.491319268
H	7.944313312	6.422934212	5.524389906
O	9.538962174	7.348783247	8.526048192
H	9.552555870	7.341287441	9.492957409
Ni	1.569699447	2.732586155	7.508868074
O	1.606475048	0.910568253	6.452058673
H	1.610346296	0.907786928	5.484995623
Ni	0.010087157	0.031313301	7.508872952
O	3.180051282	1.835595388	8.532610551
H	3.107606302	1.826728259	9.497195460
Ni	3.180972249	5.510380452	7.500897021
O	3.180648201	3.667623848	6.488465225
H	3.168603398	3.658278507	5.521522816
O	4.773820367	4.590813159	8.529837369
H	4.769349502	4.593172747	9.496765839
O	4.776608183	6.432306355	6.488411296
H	4.779513080	6.447187374	5.521477688
O	6.363122056	7.348782791	8.532006168
H	6.334817867	7.415745745	9.496572263

Oxidized phase: Ni_9O_{18}

Ni	7.019796843	2.426828764	6.900577891
O	7.019724270	4.052851149	7.855373977

Oxidized phase: $[Al_1Ni_8O_{18}]^-$

Al	7.059347033	2.440512410	6.900642181
O	7.059307800	4.096106621	7.860342810

Ni	5.611596210	4.865901002	6.900577891	Ni	5.646067203	4.888393714	6.900623190
Ni	8.427875180	4.865830394	6.900507426	Ni	8.472565982	4.888344144	6.900574728
O	7.019839339	0.800753664	5.945791934	O	7.059382815	0.784921435	5.940913874
Ni	5.611640637	-0.012143256	6.900726585	Ni	5.646103381	-0.007287151	6.900730622
O	8.427851591	1.613965084	7.855778798	O	8.493072315	1.612804266	7.860669803
O	8.428053004	3.239710034	5.945675998	O	8.493191195	3.268217536	5.940843617
O	9.835930085	4.053002124	7.855654572	O	9.889845031	4.074872757	7.852948929
O	9.836047250	5.678821856	5.945668754	O	9.896301790	5.708061084	5.945309368
O	11.244138980	6.491815312	7.855713488	O	11.307537627	6.530200823	7.852991902
Ni	4.203540747	2.426912578	6.900850828	Ni	4.232869124	2.440571120	6.900815142
O	4.203475842	0.800926040	5.945939885	O	4.228738254	0.806342823	5.948606826
Ni	2.795387102	-0.012057892	6.900937813	Ni	2.811130424	-0.012143354	6.905298741
O	5.611750377	1.613872416	7.855654593	O	5.625647723	1.612753990	7.860551079
O	5.611575791	3.239824928	5.945657381	O	5.625510944	3.268325334	5.940809768
O	7.019714898	5.679020384	5.945675998	O	7.059299498	5.709142404	5.948412984
O	8.427957927	6.491678633	7.855654572	O	8.470656163	6.531063808	7.856047598
Ni	1.387251110	2.426902384	6.900937813	Ni	1.389390202	2.440561192	6.900892258
O	1.387292652	0.800936725	5.946081681	O	1.393504238	0.806352422	5.948718981
Ni	-0.020927142	-0.012082291	6.900886348	Ni	-0.023874922	-0.007246284	6.900849476
O	2.795464964	1.613976706	7.855972028	O	2.811183654	1.617476917	7.856293219
Ni	2.795303951	4.865889367	6.900726585	Ni	2.811082761	4.893289684	6.896304609
O	2.795374994	3.239825447	5.945939885	O	2.811111817	3.263630236	5.945502971
O	4.203517352	4.053000756	7.855654593	O	4.228785300	4.074865672	7.852950650
O	4.203407461	5.678951163	5.945791934	O	4.222331793	5.708151008	5.945394767
O	5.611648214	6.491766809	7.855778798	O	5.648069203	6.531122604	7.856147958

***Oxidized phase:* [$Ga_1Ni_8O_{18}$]$^-$**

Ga	7.110181092	2.458098699	6.900367338
O	7.110144971	4.203226112	7.877360596
Ni	5.677564634	4.939435846	6.900674601
Ni	8.542735725	4.939395599	6.900633305
O	7.110203569	0.712805159	5.923810129
Ni	5.677618705	-0.023188213	6.900758106
O	8.621453433	1.585580412	7.877620479
O	8.621712206	3.330691939	5.923727236
O	9.966097925	4.107069257	7.850334317
O	9.973254937	5.745881520	5.949118320
O	11.388957715	6.571427454	7.850366932
Ni	4.245035961	2.458139392	6.900823173
O	4.254153702	0.809222769	5.951282210
Ni	2.831363113	-0.012250065	6.904372651
O	5.598921102	1.585565365	7.877524146
O	5.598656302	3.330759516	5.923738181
O	7.110135768	5.756042795	5.951129789
O	8.525947467	6.581408993	7.852380245
Ni	1.417676727	2.458141611	6.900868252
O	1.408558402	0.809238396	5.951356321
Ni	-0.014908930	-0.023145768	6.900840224
O	2.831385031	1.622540771	7.852564763
Ni	2.831321991	4.928526753	6.897309580
O	2.831340425	3.293706407	5.949258339
O	4.254199671	4.107085026	7.850341067
O	4.247049020	5.745961279	5.949176259
O	5.694393282	6.581459820	7.852451491

***Oxidized phase:* [$Fe_1Ni_8O_{18}$]$^-$**

Fe	7.079589786	2.447504073	6.901759127
O	7.079565084	4.118632545	7.848895197
Ni	5.658395551	4.909168840	6.900634220
Ni	8.500719474	4.909151399	6.900580597
O	7.079614140	0.777210786	5.953424056
Ni	5.658330488	-0.014047181	6.900702768
O	8.526763347	1.612009744	7.849108234
O	8.526141844	3.282604497	5.953349485
O	9.922749940	4.089173487	7.860902111
O	9.929235114	5.721786000	5.948268947
O	11.339935574	6.543671321	7.860930980
Ni	4.237177503	2.447528812	6.900786360
O	4.236565350	0.806187056	5.940248874
Ni	2.819174066	-0.012179825	6.896291957
O	5.632406803	1.611989455	7.849037014
O	5.633023893	3.282661516	5.953341992
O	7.079541188	5.730426157	5.940089061
O	8.490160674	6.552553601	7.852473252
Ni	1.401181202	2.447524104	6.900823588
O	1.401778416	0.806189027	5.940323366
Ni	-0.019992993	-0.014031988	6.900790446
O	2.819208269	1.616631258	7.852679404
Ni	2.819141454	4.907320522	6.904477650
O	2.819169181	3.278297930	5.948438912
O	4.236340404	4.089164560	7.860925913
O	4.229879346	5.721824602	5.948346940
O	5.669009202	6.552578924	7.852557596

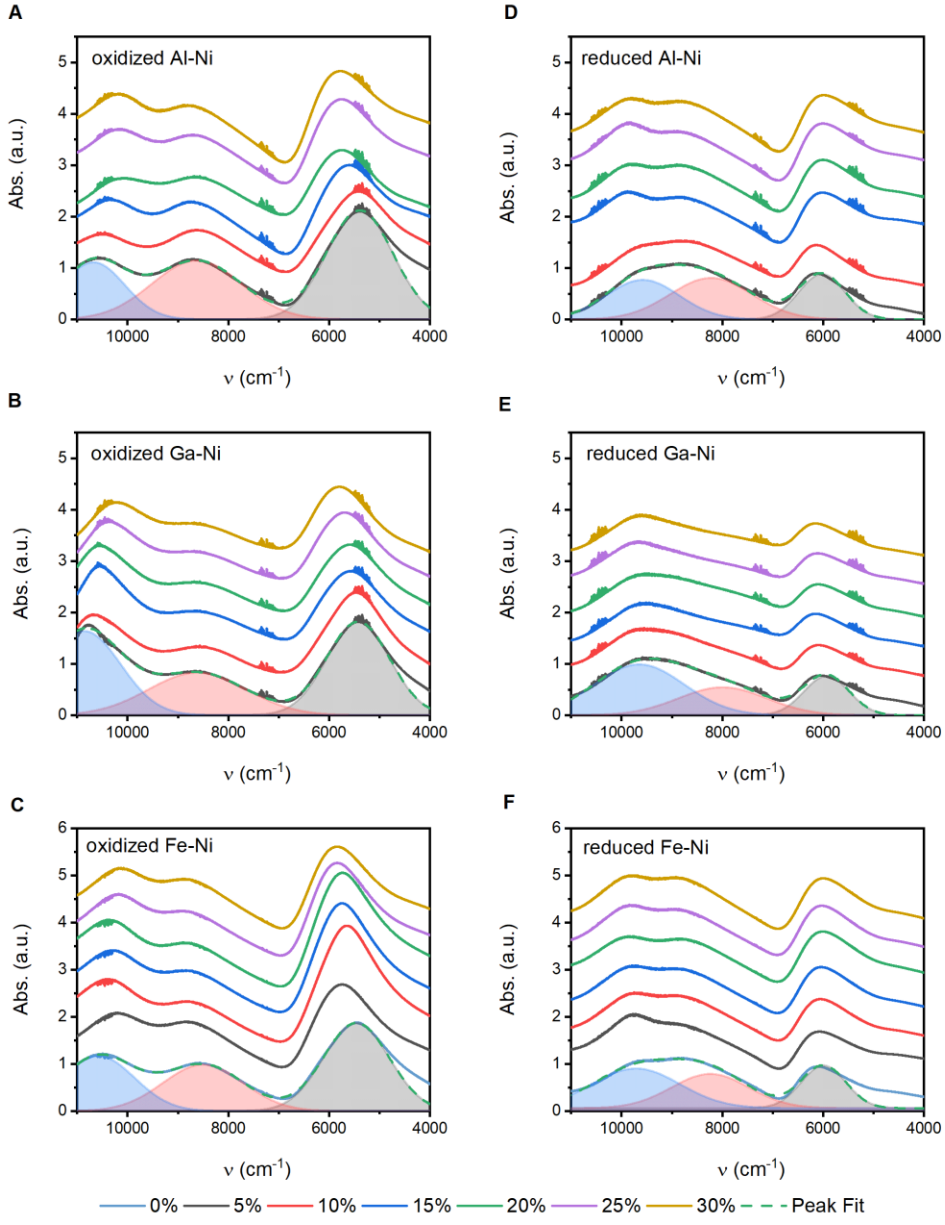

Figure A.1 Near infrared spectra for the **(A-C)** oxidized and **(D-F)** reduced forms of $M_yNi_{100-y}O_x$. Peak locations were extracted from the curves by peak-fitting; components of sample fits are shown as shaded peaks for each panel and total fit as a dashed green line. NiO_x (*i.e.*, M = Ni) is shown in Panels **C** and **F**.

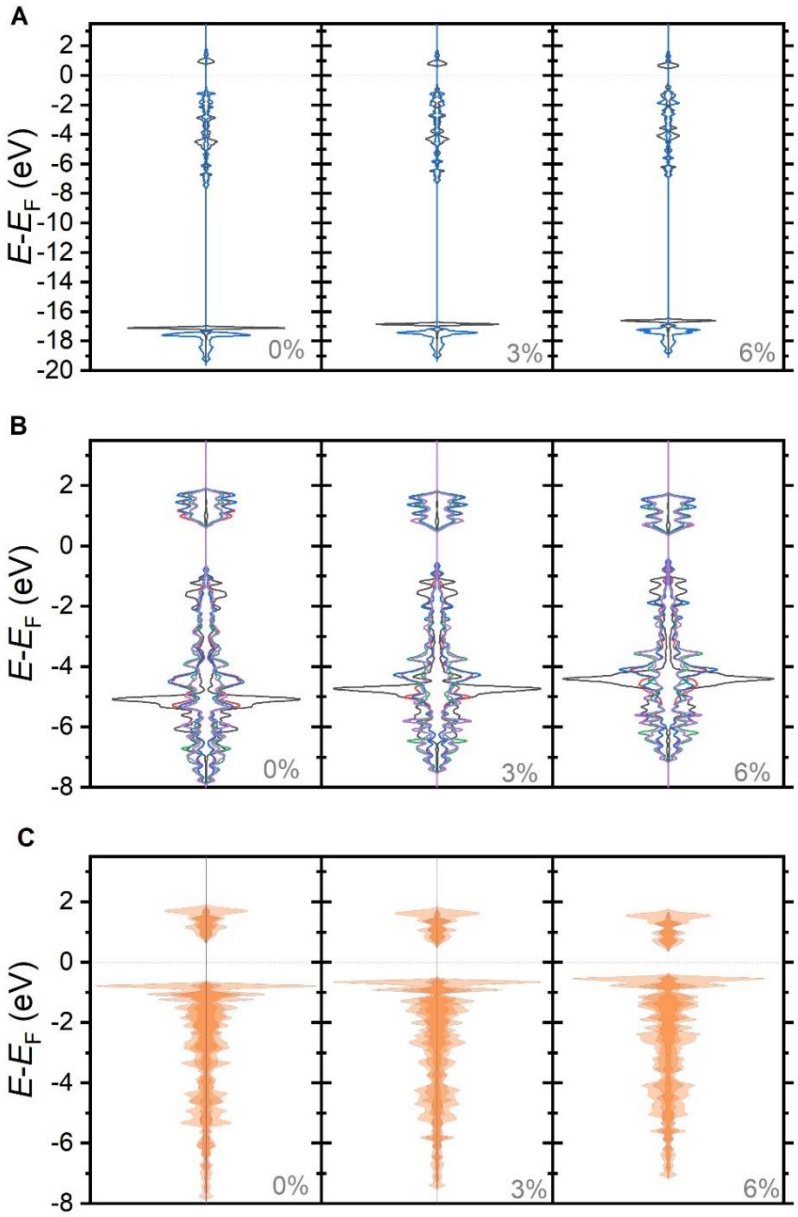

Figure A.2 Projected density of states for **(A)** Al 2p, **(B)** Ni 3d and **(C)** O 2p orbitals in the oxidized model for $[AlNi_8O_{18}]^-$. Values are shown for 0%, 3% and 6% tensile strain, defined relative to the crystalline nickel hydroxide lattice.

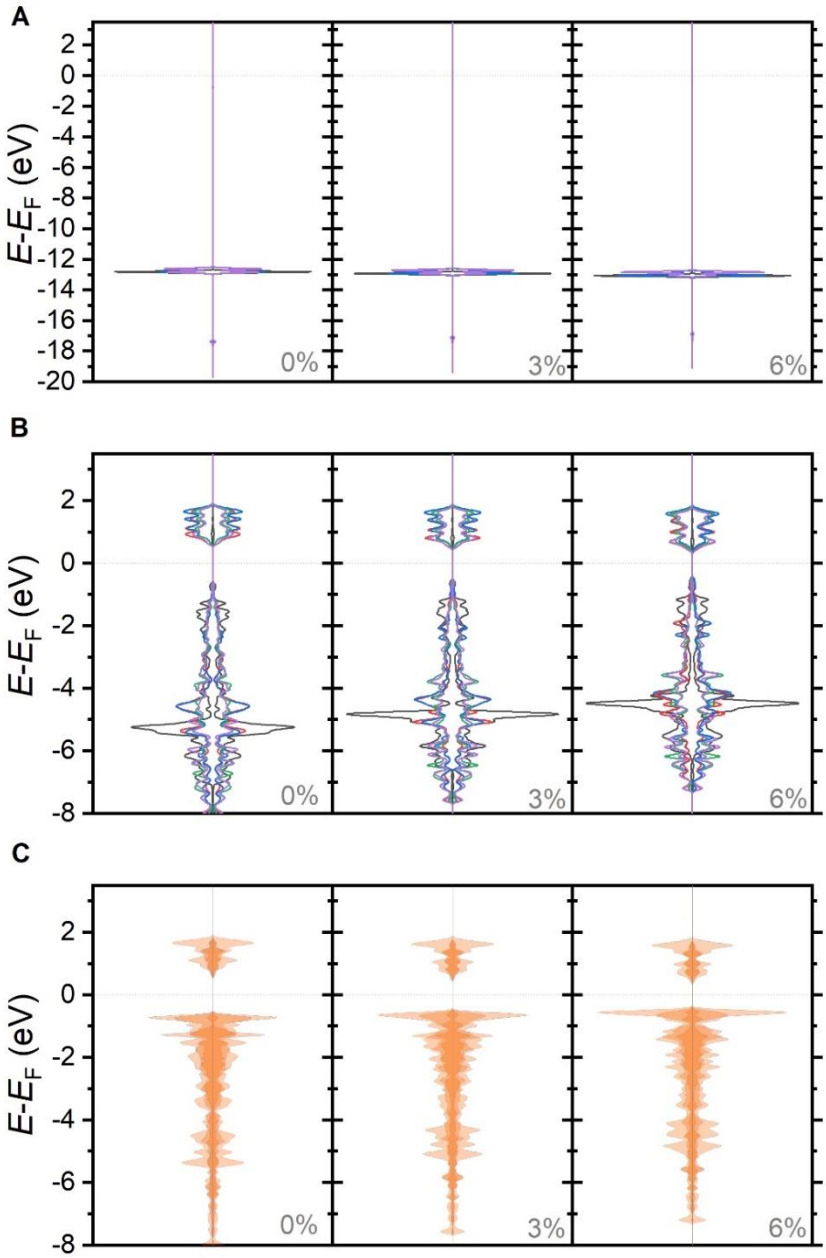

Figure A.3 Projected density of states for **(A)** Ga 3d, **(B)** Ni 3d and **(C)** O 2p orbitals in the oxidized model for $[GaNi_8O_{18}]^-$. Values are shown for 0%, 3% and 6% tensile strain, defined relative to the crystalline nickel hydroxide lattice.

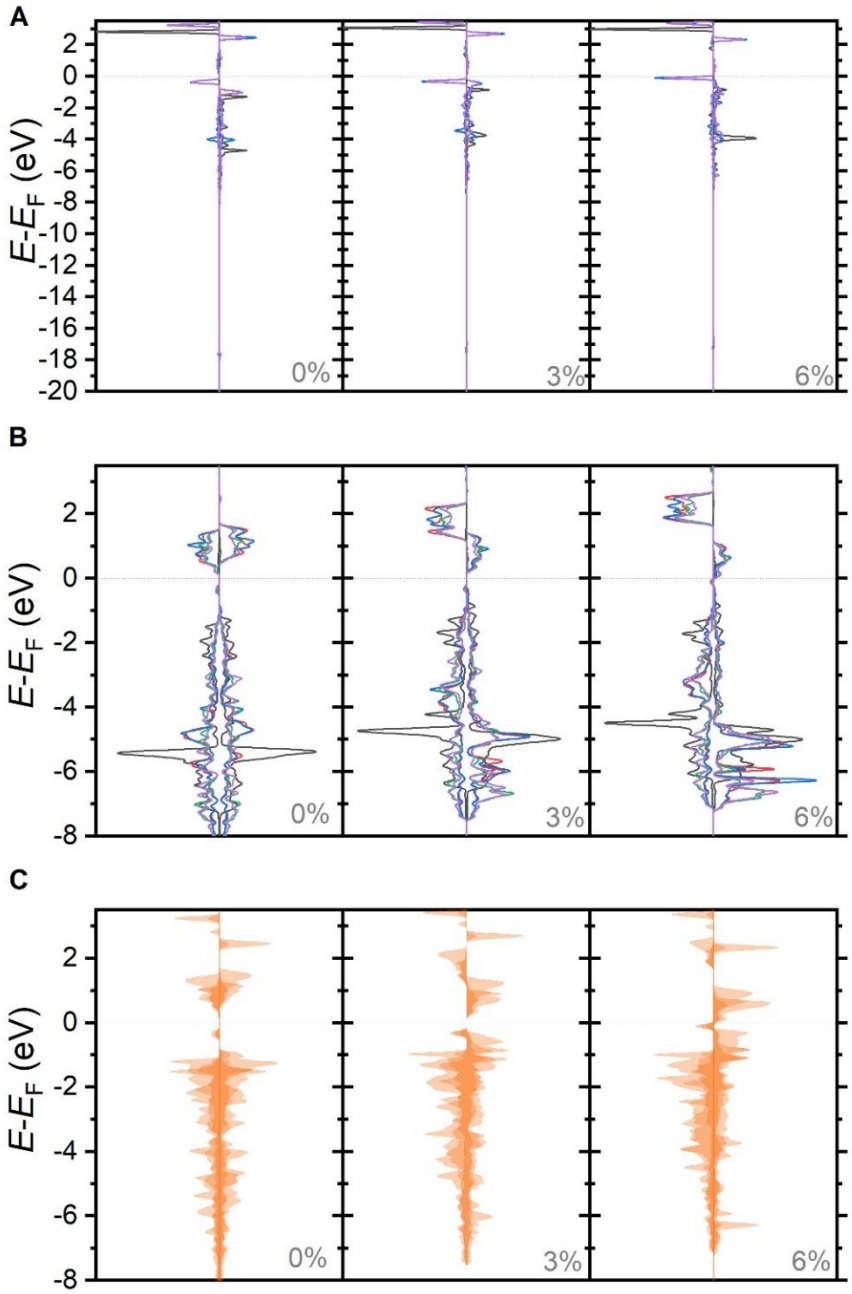

Figure A.4 Projected density of states for **(A)** Fe 3d, **(B)** Ni 3d and **(C)** O 2p orbitals in the oxidized model for $[FeNi_8O_{18}]^-$. Values are shown for 0%, 3% and 6% tensile strain, defined relative to the crystalline nickel hydroxide lattice.

Appendix B: Supplementary Information for Chapter 4

Table B. 1 Charges passed in the pre-catalytic cathodic redox peaks in cyclic voltammograms that are used to normalize current flow in electrochemical experiments.

	Water (mC)	**Formamide (mC)**
0% Fe	22.61	23.11
0.5% Fe	22.99	22.58
2.7% Fe	23.43	16.34
5.7% Fe	18.81	13.36
8.7% Fe	15.60	26.05
11.9% Fe	12.43	19.03
15.3% Fe	2.838	4.982
18.9% Fe	12.12	18.84
21.4% Fe	18.32	12.44

Table B. 2 Location of the Ni and Fe K-edges from XANES spectra on the two sample series

	Formamide Sample Series		Water Sample Series	
	Ni K-edge	**Fe K-edge**	**Ni K-edge**	**Fe K-edge**
0% Fe	8341.33 (0.002)		8341.39 (0.035)	
5% Fe	8341.38 (0.004)	7124.97 (0.054)	8341.26 (0.006)	7124.58 (0.067)
10% Fe	8341.39 (0.068)	7124.63 (0.041)	8341.53 (0.006)	7124.56 (0.024)
15% Fe	8341.46 (0.004)	7124.47 (0.025)	8341.38 (0.006)	7124.39 (0.042)
20% Fe	8341.44 (0.027)	7124.33 (0.025)	8341.34 (0.009)	7124.30 (0.023)
25% Fe	8341.49 (0.004)	7124.17 (0.011)	8341.42 (0.003)	7124.06 (0.011)
30% Fe	8341.48 (0.009)	7124.93 (0.014)	8341.43 (0.009)	7123.90 (0.026)

[a] parentheses are estimated errors are standard deviation from all individual spectra per sample

Table B. 3 EXAFS preliminary simulation parameters of Ni K-edge of water series

Sample	σ_O^2	σ_{Ni}^2	E_o	R_{Ni-O}	R_{Ni-M}	***R-factor***
0% Fe	0.0057	0.0071	8.174	2.065	3.116	0.006
	(0.0005)	(0.0005)	(0.476)	(0.0057)	(0.0053)	
5% Fe	0.0069	0.0077	8.328	2.068	3.116	0.007
	(0.0005)	(0.0004)	(0.421)	(0.0052)	(0.0048)	
10% Fe	(0.0053)	0.0070	8.290	2.065	3.110	0.010
	(0.0006)	(0.0006)	(0.599)	(0.007)	(0.007)	
15% Fe	0.0061	0.0073	8.097	2.063	3.103	0.007
	(0.0005)	(0.0005)	(0.516)	(0.006)	(0.005)	
20% Fe	0.0073	0.0078	8.133	2.062	3.098	0.014
	(0.0006)	(0.0005)	(0.582)	(0.007)	(0.006)	
25% Fe	0.0065	0.0075	8.329	2.065	3.095	0.019
	(0.0008)	(0.0008)	(0.767)	(0.009)	(0.008)	
30% Fe	0.0058	0.0074	8.146	2.061	3.090	0.012
	(0.0007)	(0.0007)	(0.679)	(0.008)	(0.007)	

N_{Ni-O}, N_{Ni-M}= 6, S_0^2=0.75, $E_{0,Ni}$= 8333 eV

Table B. 4 EXAFS preliminary simulation parameters of Fe K-edge of water series.

Sample	σ_O^2	σ_{Fe}^2	E_o	R_{Fe-O}	R_{Fe-M}	*R-factor*
5% Fe	0.0039	0.0065	12.362	2.000	3.112	0.015
	(0.0006)	(0.0007)	(0.555)	(0.007)	(0.007)	
10% Fe	0.0041	0.0068	12.342	2.000	3.108	0.013
	(0.0005)	(0.0007)	(0.492)	(0.006)	(0.006)	
15% Fe	0.0047	0.0071	12.163	1.998	3.100	0.015
	(0.0005)	(0.0007)	(0.500)	(0.006)	(0.007)	
20% Fe	0.0062	0.0078	12.181	1.996	3.090	0.023
	(0.0006)	(0.0007)	(0.521)	(0.007)	(0.007)	
25% Fe	0.0080	0.0090	12.054	1.991	3.086	0.027
	(0.0008)	(0.0009)	(0.641)	(0.008)	(0.009)	
30% Fe	0.0089	0.0103	11.883	1.989	3.076	0.044
	(0.0008)	(0.0012)	(0.715)	(0.010)	(0.011)	

N_{Fe-O}, N_{Fe-M}= 6, S_0^2=0.80, $E_{0,Fe}$= 7112 eV

Table B. 5 EXAFS preliminary simulation parameters of Ni K-edge of formamide series.

Sample	σ_O^2	σ_{Ni}^2	E_o	R_{Ni-O}	R_{Ni-M}	***R-factor***
0% Fe	0.0061	0.0074	8.196	2.064	3.118	0.012
	(0.0005)	(0.0005)	(0.497)	(0.006)	(0.005)	
5% Fe	0.0060	0.0074	8.005	2.061	3.110	0.009
	(0.0005)	(0.0005)	(0.501)	(0.006)	(0.005)	
10% Fe	0.0057	0.0072	7.996	2.058	3.102	0.013
	(0.0006)	(0.0006)	(0.598)	(0.007)	(0.006)	
15% Fe	0.0056	0.0071	8.185	2.059	3.099	0.013
	(0.0007)	(0.0007)	(0.648)	(0.008)	(0.007)	
20% Fe	0.0058	0.0070	8.100	2.059	3.095	0.013
	(0.0007)	(0.0007)	(0.686)	(0.008)	(0.007)	
25% Fe	0.0052	0.0070	8.145	2.057	3.092	0.016
	(0.0007)	(0.0007)	(0.717)	(0.008)	(0.008)	
30% Fe	0.0050	0.0074	8.312	2.060	3.092	0.020
	(0.0007)	(0.0008)	(0.736)	(0.009)	(0.009)	

N_{Ni-O}, N_{Ni-M}= 6, S_0^2=0.75, $E_{0,Ni}$= 8333 eV

Table B. 6 EXAFS preliminary simulation parameters of Fe K-edge of formamide series.

Sample	σ_O^2	σ_{Fe}^2	E_o	R_{Fe-O}	R_{Fe-M}	***R-factor***
5% Fe	0.0037	0.0053	13.085	2.002	3.111	0.012
	(0.0006)	(0.0006)	(0.521)	(0.006)	(0.006)	
10% Fe	0.0042	0.0051	12.755	1.998	3.096	0.010
	(0.0005)	(0.0005)	(0.473)	(0.006)	(0.005)	
15% Fe	0.0049	0.0060	12.623	1.997	3.089	0.013
	(0.0006)	(0.0006)	(0.561)	(0.007)	(0.006)	
20% Fe	0.0065	0.0070	12.704	1.998	3.089	0.017
	(0.0007)	(0.0007)	(0.590)	(0.008)	(0.007)	
25% Fe	0.0079	0.0082	12.472	1.994	3.081	0.015
	(0.0007)	(0.0007)	(0.560)	(0.007)	(0.007)	
30% Fe	0.0093	0.0092	12.623	1.995	3.077	0.023
	(0.0009)	(0.0010)	(0.708)	(0.010)	(0.009)	

N_{Fe-O}, N_{Fe-M}= 6, S_0^2=0.80, $E_{0,Fe}$= 7112 eV

Table B. 7 EXAFS final simulation parameters of Ni K-edge of water series

Sample	σ_O^2	σ_{Ni}^2	R_{Ni-O}	R_{Ni-M}	***R-factor***
0% Fe	0.0058	0.0072	2.065	3.116	0.0064
	(0.0005)	(0.0005)	(0.003)	(0.004)	
5% Fe	0.0069	0.0077	2.066	3.115	0.0072
	(0.0004)	(0.0004)	(0.002)	(0.003)	
10% Fe	0.0053	0.0070	2.063	3.109	0.010
	(0.0006)	(0.0006)	(0.003)	(0.005)	
15% Fe	0.0061	0.0073	2.063	3.104	0.008
	(0.0005)	(0.0005)	(0.003)	(0.004)	
20% Fe	0.0073	0.0078	2.062	3.098	0.014
	(0.0006)	(0.0005)	(0.003)	(0.004)	
25% Fe	0.0064	0.0075	2.063	3.093	0.018
	(0.0008)	(0.0007)	(0.004)	(0.006)	
30% Fe	0.0058	0.0074	2.061	3.090	0.012
	(0.0007)	(0.0006)	(0.004)	(0.005)	

N_{Ni-O}, N_{Ni-M}= 6, S_0^2=0.75, $E_{0,Ni}$= 8333 eV, E_0= 8.15 eV

Table B. 8 EXAFS final simulation parameters of Fe K-edge of water series.

Sample	σ_O^2	σ_{Fe}^2	R_{Fe-O}	R_{Fe-M}	***R-factor***
5% Fe	0.0039	0.0065	1.998	3.110	0.016
	(0.0006)	(0.0007)	(0.003)	(0.006)	
10% Fe	0.0041	0.0068	1.998	3.106	0.014
	(0.0005)	(0.0006)	(0.003)	(0.005)	
15% Fe	0.0047	0.0071	1.998	3.100	0.015
	(0.0005)	(0.0006)	(0.003)	(0.005)	
20% Fe	0.0062	0.0078	1.995	3.090	0.023
	(0.0006)	(0.0007)	(0.003)	(0.005)	
25% Fe	0.0080	0.0090	1.993	3.087	0.027
	(0.0007)	(0.0009)	(0.004)	(0.007)	
30% Fe	0.0089	0.0103	1.992	3.078	0.042
	(0.0008)	(0.0011)	(0.004)	(0.008)	

N_{Fe-O}, N_{Fe-M}= 6, S_0^2=0.80, $E_{0,Fe}$= 7112, E_o:12.15 eV

Table B. 9 EXAFS final simulation parameters of Ni K-edge of formamide series.

Sample	σ_O^2	σ_{Ni}^2	R_{Ni-O}	R_{Ni-M}	***R-factor***
0% Fe	0.061	0.0074	2.064	3.118	0.012
	(0.0005)	(0.0005)	(0.003)	(0.004)	
5% Fe	0.006	0.0074	2.062	3.111	0.009
	(0.0005)	(0.0005)	(0.003)	(0.004)	
10% Fe	0.0057	0.0072	2.060	3.104	0.013
	(0.0006)	(0.0006)	(0.003)	(0.005)	
15% Fe	0.0056	0.0071	2.059	3.099	0.013
	(0.0006)	(0.0006)	(0.004)	(0.005)	
20% Fe	0.0058	0.0070	2.059	3.095	0.014
	(0.0007)	(0.0007)	(0.004)	(0.005)	
25% Fe	0.0052	0.0069	2.057	3.092	0.016
	(0.0007)	(0.0007)	(0.004)	(0.006)	
30% Fe	0.0050	0.0075	2.058	3.090	0.020
	(0.0007)	(0.0008)	(0.004)	(0.007)	

N_{Ni-O}, N_{Ni-M}= 6, S_0^2=0.75, $E_{0,Ni}$= 8333 eV, E_0= 8.15 eV

Table B. 10 EXAFS final simulation parameters of Fe K-edge of formamide series.

Sample	σ_O^2	σ_{Fe}^2	R_{Fe-O}	R_{Fe-M}	***R-factor***
5% Fe	0.0036	0.0053	1.992	3.104	0.017
	(0.0006)	(0.0006)	(0.004)	(0.005)	
10% Fe	0.0042	0.0052	1.992	3.092	0.012
	(0.0005)	(0.0005)	(0.003)	(0.004)	
15% Fe	0.0049	0.0060	1.992	3.085	0.014
	(0.0006)	(0.0006)	(0.003)	(0.005)	
20% Fe	0.0065	0.0070	1.992	3.085	0.019
	(0.0007)	(0.0007)	(0.004)	(0.006)	
25% Fe	0.0078	0.0082	1.990	3.078	0.015
	(0.0006)	(0.0007)	(0.003)	(0.005)	
30% Fe	0.0092	0.0092	1.989	3.073	0.024
	(0.0008)	(0.0009)	(0.004)	(0.007)	

N_{Fe-O}, N_{Fe-M}= 6, S_0^2=0.80, $E_{0,Fe}$= 7112, E_o:12.15 eV

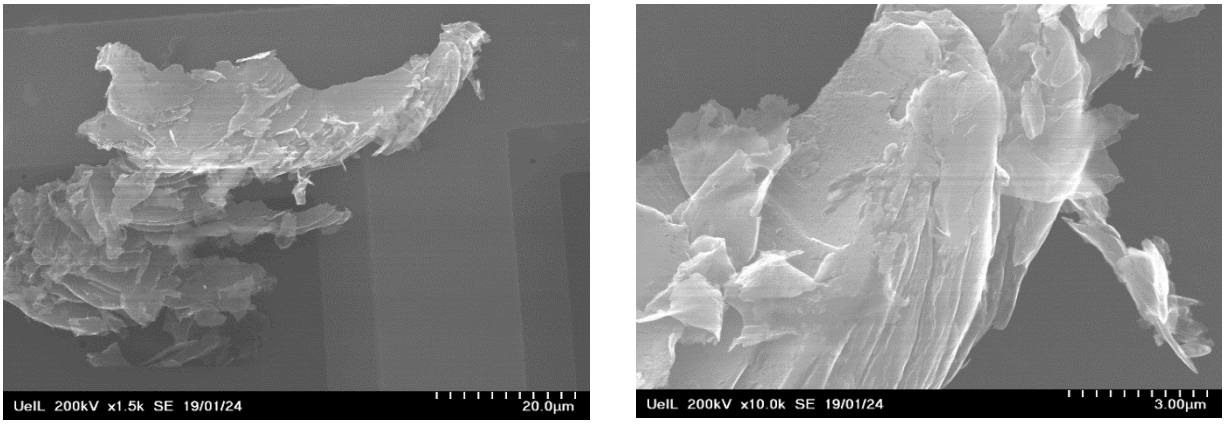

Figure B.1 Electron micrographs obtained on $Fe_{0.214}Ni_{0.786}(OH)_2$ synthesized in the presence of formamide.

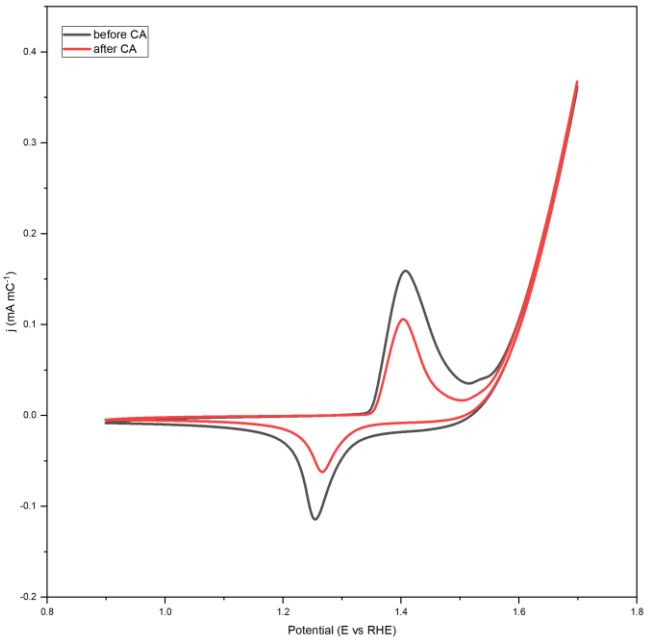

Figure B.2 Sample cyclic voltammograms of $Fe_{0.05}Ni_{0.095}(OH)_2$ in water series recorded before and after chronoamperometry experiment.

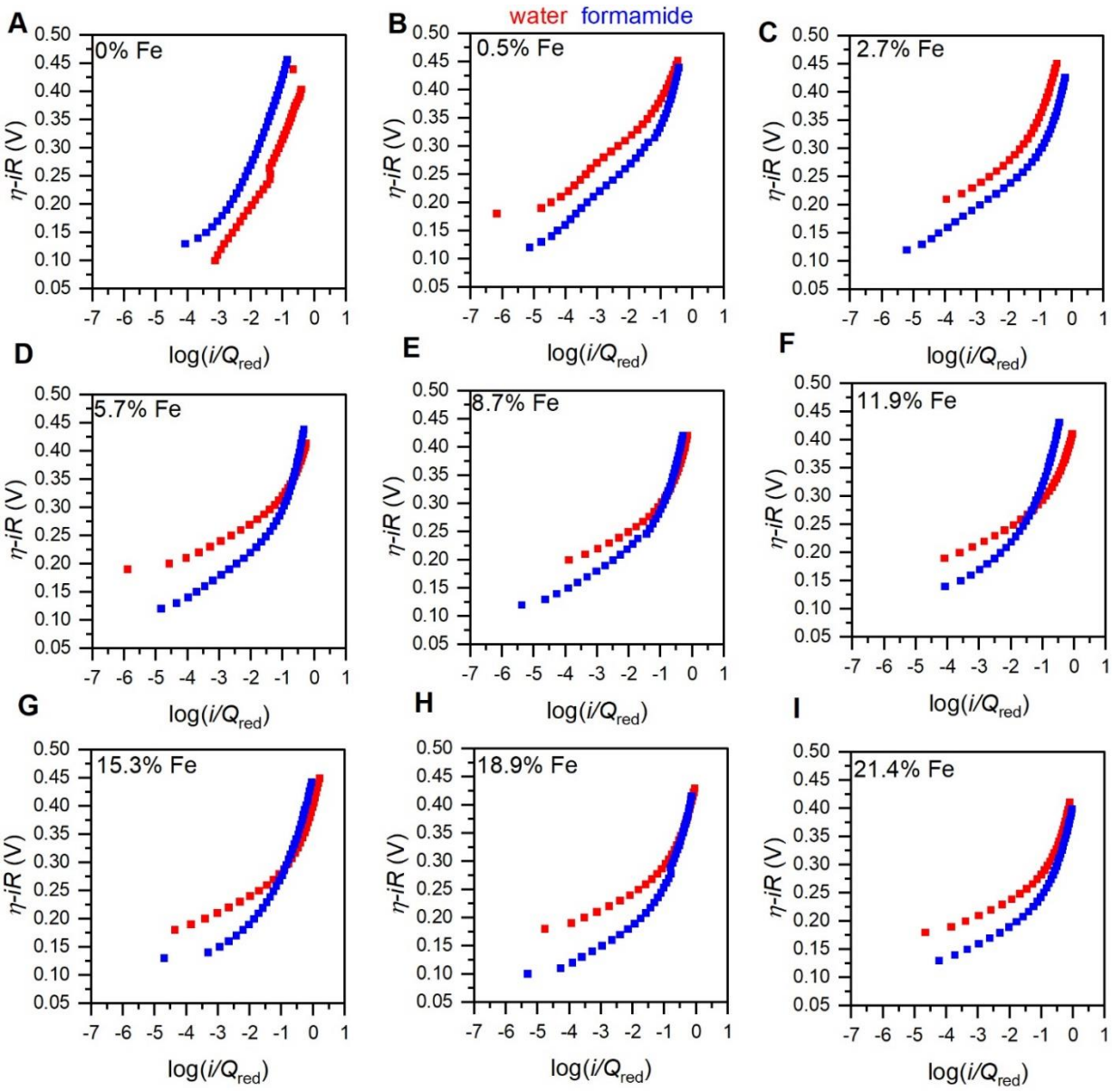

Figure B.3 Electron transfer kinetics of water (red) and formamide(blue) series. Synthesis dependent Tafel plots for **(A)** 0% Fe, **(B)** 0.5% Fe, **(C)** 2.7% Fe, **(D)** 5.7% Fe, **(E)** 8.7% Fe, **(F)** 11.9% Fe, **(G)** 15.3% Fe**, (H)** 18.9% Fe, **(I)** 21.4% Fe.

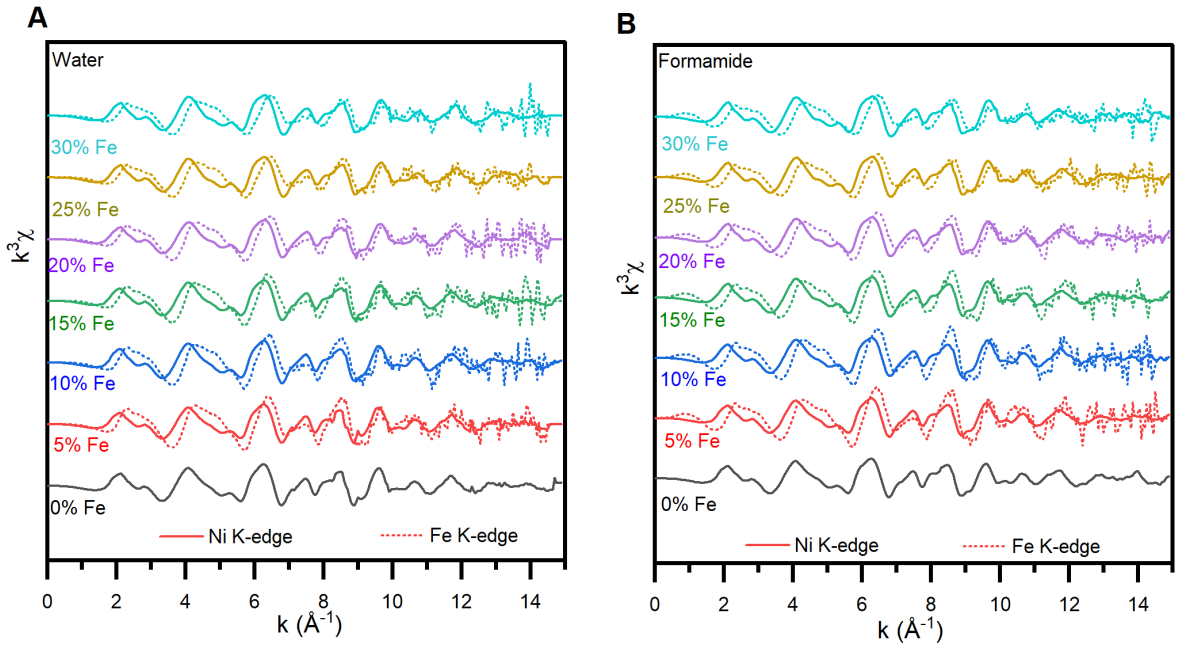

Figure B.4 k-space X-ray absorption fine-structure spectra of **(A)** water and **(B)** formamide series at the Ni K-edge (solid lines) and Fe K-edge (dotted lines).

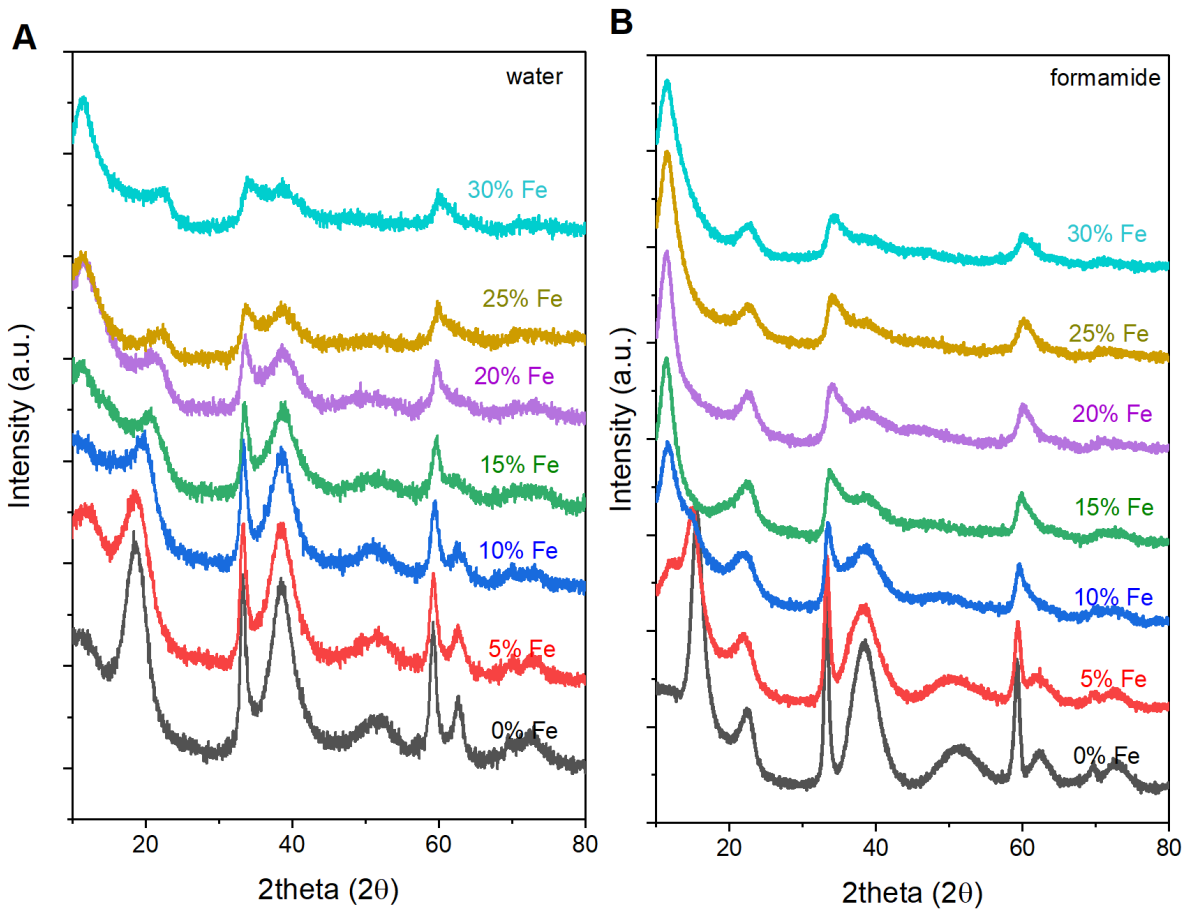

Figure B.5 XRD patterns of the samples used in EXAFS analysis of **(A)** water series **(B)** formamide series.

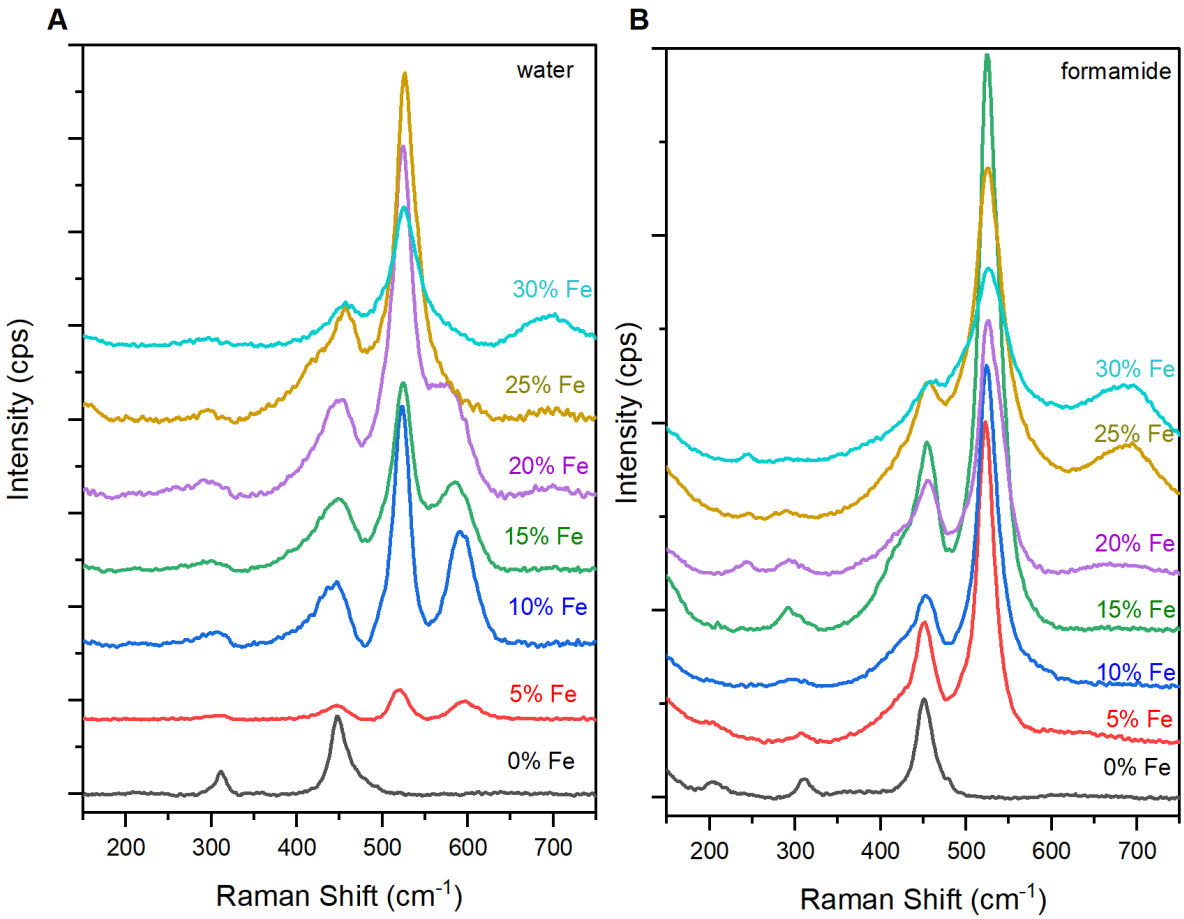

Figure B.6 Low wavenumber Raman spectra on $Fe_xNi_{1-x}(OH)_2$ samples used in EXAFS analysis. Data for the **(A)** water and **(B)** formamide sample series.

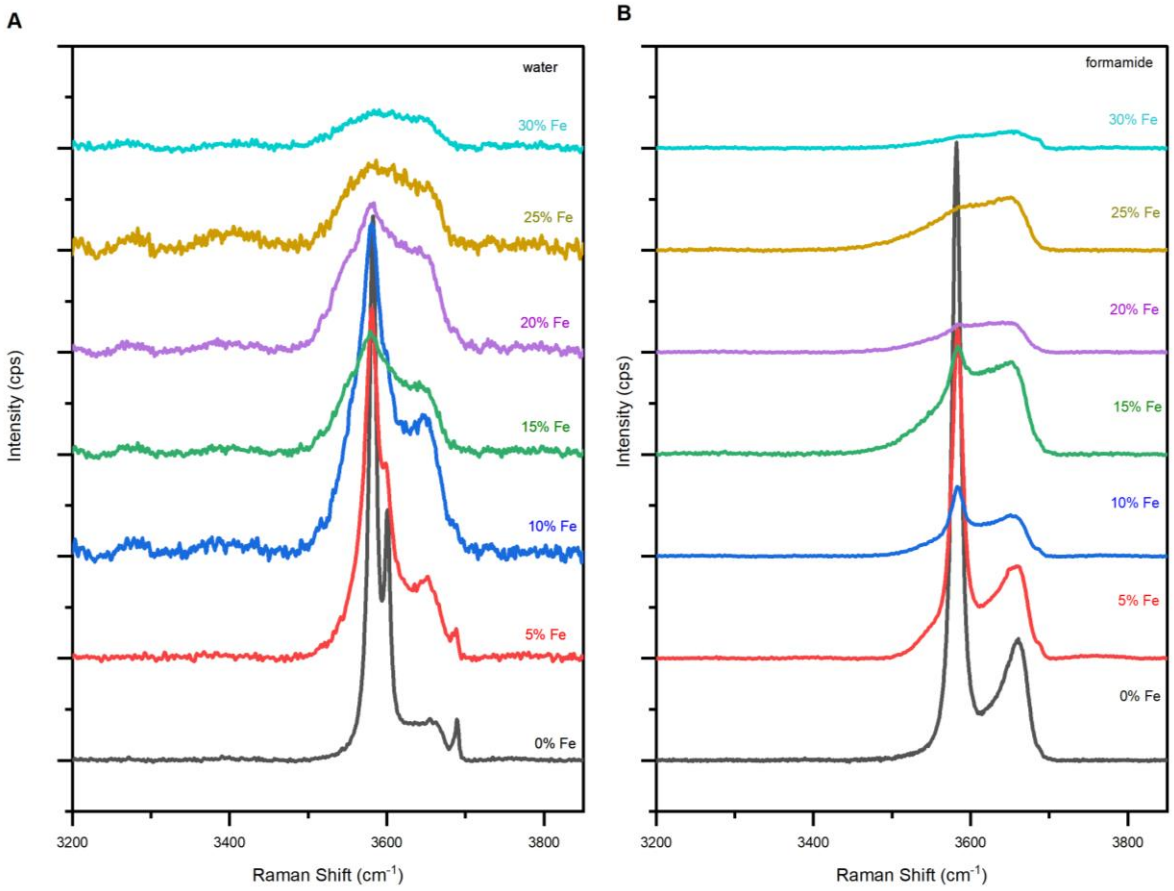

Figure B.7 High wavenumber Raman spectra on $Fe_xNi_{1-x}(OH)_2$ samples used in EXAFS analysis. Data for the **(A)** water and **(B)** formamide sample series.

Appendix C: Supplementary Information for Chapter 5

Table C. 1 Ni and Fe K-edge locations extracted from half-height method of hydrothermally synthesized NiFe hydroxides.

	Ni K-edge	**Estimated error**	**Fe K-edge**	**Estimated error**
0% Fe	8342.137	0.003		
5% Fe	8341.966	0.003	7124.148	0.062
10% Fe	8342.015	0.044	7123.977	0.102
15% Fe	8341.878	0.026	7123.733	0.156
20% Fe	8341.959	0.051	7123.830	0.206
25% Fe	8342.907	0.034	7123.503	0.107
30% Fe	8341.808	0.002	7123.337	0.016

Table C. 2 Extended X-ray absorption fine-structure spectroscopy (EXAFS) modeling parameters for Ni K-edge of hydrothermally synthesized NiFe hydroxides.

Sample	$\mathbf{E_o}$	$\boldsymbol{R_{Ni\text{-}O}}$	$\boldsymbol{R_{Ni\text{-}M}}$	***R-factor***
0% Fe	8.354	2.068	3.128	0.019
	(0.828)	(0.009)	(0.008)	
5% Fe	8.185	2.063	3.122	0.018
	(0.700)	(0.007)	(0.007)	
10% Fe	8.441	2.067	3.119	0.016
	(0.692)	(0.008)	(0.007)	
15% Fe	8.375	2.067	3.117	0.021
	(0.668)	(0.007)	(0.007)	
20% Fe	8.628	2.069	3.115	0.017
	(0.756)	(0.009)	(0.007)	
25% Fe	8.938	2.073	3.112	0.044
	(0.916)	(0.011)	(0.009)	
30% Fe	9.221	2.074	3.108	0.049
	(0.964)	(0.011)	(0.010)	

$N_{O\text{-}M}$, $N_{Ni\text{-}M}$= 6, S_o^2= 0.8, σ^2_{Ni}= 0.006, σ^2_O= 0.004, $E_{0,Ni}$= 8333 eV. Brackets indicate uncertainties in values.

Table C. 3 Extended X-ray absorption fine-structure spectroscopy (EXAFS) modeling parameters for Fe K-edge of hydrothermally synthesized NiFe hydroxides (brucite).

Sample	**E_0**	**N_{FeA-O}**	**R_{FeA-O}**	**N_{FeA-M}**	**R_{FeA-M}**	**R-factor**
5% Fe	12.362 (0.687)	6.00	2.019 (0.009)	6.00	3.124 (0.011)	0.024
10% Fe	11.229 (0.807)	4.50	1.975 (0.010)	4.50	3.106 (0.013)	0.011
15% Fe	11.308 (0.945)	4.32	1.965 (0.011)	4.32	3.081 (0.014)	0.019
20% Fe	10.124 (0.835)	4.10	1.953 (0.010)	4.10	3.079 (0.013)	0.018
25% Fe	12.291 (1.202)	4.10	1.955 (0.015)	4.10	3.077 (0.018)	0.024
30% Fe	12.585 (0.918)	4.00	1.952 (0.011)	4.00	3.069 (0.014)	0.020

S_o^2= 0.8 σ^2_{FeA}= 0.011, σ^2_O= 0.007, $E_{0,Fe}$= 7112 eV. Brackets indicate uncertainties in values.

Table C. 4 Extended X-ray absorption fine-structure spectroscopy (EXAFS) modeling parameters for Fe K-edge of hydrothermally synthesized NiFe hydroxides (magnetite).

Sample	**E_0**	**R_{FeC}** oct-O	**R_{FeC}** oct-oct	**R_{FeC}** oct-tet	**R_{FeC}** tet-O	**R_{FeC}** tet-tet	**N_{FeC}** oct-oct, oct-O, tet-tet	**N_{FeC}** oct-tet	**R-factor**
5% Fe	12.362								0.024
10% Fe	11.229	2.095 (0.033)	2.951 (0.013)	3.462 (0.013)	1.925 (0.033)	3.618 (0.013)	1	2	0.011
15% Fe	11.816	2.090 (0.032)	2.929 (0.012)	3.438 (0.012)	1.946 (0.032)	3.591 (0.012)	1.12	2.24	0.025
20% Fe	10.124	2.103 (0.025)	2.924 (0.010)	3.436 (0.010)	1.933 (0.025)	3.591 (0.010)	1.266	2.533	0.018
25% Fe	12.291	2.148 (0.036)	2.948 (0.014)	3.460 (0.014)	1.978 (0.036)	3.615 (0.014)	1.266	2.533	0.024
30% Fe	12.585	2.145 (0.025)	2.949 (0.010)	3.461 (0.010)	1.975 (0.025)	3.616 (0.011)	1.32	2.64	0.020

S_o^2= 0.8 , σ^2_{FeC}= 0.002, σ^2_O= 0.0035, $E_{0,Fe}$= 7112 eV. Brackets indicate uncertainties in values.

Calculation of Phase Fraction from EXAFS Simulations

The total number of iron and nickel sites are denoted as N_{Fe}.and N_{Ni}. The proportion between the total iron and nickel amount in the intended synthesis of $Fe_xNi_{1-x}(OH)_2$ is:

$$\frac{N_{Fe}}{N_{Ni}} = \frac{x}{1-x} \quad \textbf{(C. 1)}$$

The total amount of iron is the combination of the magnetite and $Fe_xNi_{1-x}(OH)_2$:

$$N_{Fe} = 3N_{Fe_3O_4} + yN_{Fe_xNi_{1-x}(OH)_2} \quad \textbf{(C. 2)}$$

where y is the actual Fe concentration successfully incorporated in brucite lattice.

The total amount of nickel sites at y% Fe:

$$N_{Ni} = (1-y)N_{NiFe(OH)_2} \quad \textbf{(C. 3)}$$

The fraction of Fe incorporated in the $Fe_xNi_{1-x}(OH)_2$ is the proportion between the incorporated Fe amount at a specific iron percentage and total iron amount and is denoted as *a* in **equation C.4**:

$$a = \frac{yN_{NiFe(OH)_2}}{3N_{Fe_3O_4} + yN_{NiFe(OH)_2}} \text{ at y \%Fe} \quad \textbf{(C. 4)}$$

The number of iron sites in terms of a is represented in **equation C.5**:

$$N_{Fe} = \frac{yN_{NiFe(OH)_2}}{a} = \frac{yN_{Ni}}{a(1-y)} \quad \textbf{(C. 5)}$$

The proportion between total iron and nickel amounts can be written as:

$$\frac{N_{Fe}}{N_{Ni}} = \frac{x}{1-x} = \frac{y}{a(1-y)} \quad \textbf{(C. 6)}$$

Rearrangement of this equation yields the amount of actual incorporated iron sites in nickel hydroxide:

$$y = \frac{ax}{1-x+ax} \quad \textbf{(C. 7)}$$

Calculation of Phase Fraction from XRD

The total number of iron and nickel sites are denoted as N_{Fe}.and N_{Ni}. The proportion between the total iron and nickel amount in the intended synthesis of $Fe_xNi_{1-x}(OH)_2$ is:

$$\frac{N_{Fe}}{N_{Ni}} = \frac{x}{1-x} \quad \textbf{(C. 8)}$$

The number of nickel sites in $Fe_xNi_{1-x}(OH)_2$ is represented as:

$$N_{Ni} = (1-y)N_{NiFe(OH)_2} = (1-x) \quad \textbf{(C. 9)}$$

where y is the actual iron amount successfully incorporated in brucite lattice.

According to **equation C.9**, the number of $NiFe(OH)_2$ is:

$$N_{NiFe(OH)_2} = \frac{N_{Ni}}{1-y} \quad \textbf{(C. 10)}$$

The number of Fe sites are the total number of iron sites in $Fe_3O_4$and $NiFe(OH)_2$

$$N_{Fe} = \frac{3N_{Fe_3O_4}}{8} + yN_{NiFe(OH)_2} = x \quad \textbf{(C. 11)}$$

where 3 accounts for stoichiometry within the formula and 8 is the number of formula units within the Fe_3O_4 unit cell. The amount of Fe_3O_4:

$$N_{Fe_3O_4} = \frac{8\,[N_{Fe} - yN_{NiFe(OH)_2}]}{3} \quad \textbf{(C. 12)}$$

$$phase\ fraction\ (p) = \frac{N_{NiFe(OH)_2}}{N_{Fe_3O_4} + N_{NiFe(OH)_2}} \quad \textbf{(C. 13)}$$

where N is the number of nickel and iron sites according to the unit cells of nickel hydroxide ($NiFe(OH)_2$) and magnetite (Fe_3O_4). After substitution of N_{Ni} and N_{Fe} to **equation C.13** becomes:

$$p = \frac{\frac{N_{Ni}}{(1-y)}}{\frac{N_{Ni}}{(1-y)} + \frac{8N_{Fe}}{3} - \frac{8y[\frac{N_{Ni}}{(1-y)}]}{3}} \quad \textbf{(C. 14)}$$

Rearrangement of **equation C.14** yields the amount of actual incorporated iron sites in nickel hydroxide:

$$y = \frac{3p+3x+5px-3}{8p} \quad \textbf{(C. 15)}$$

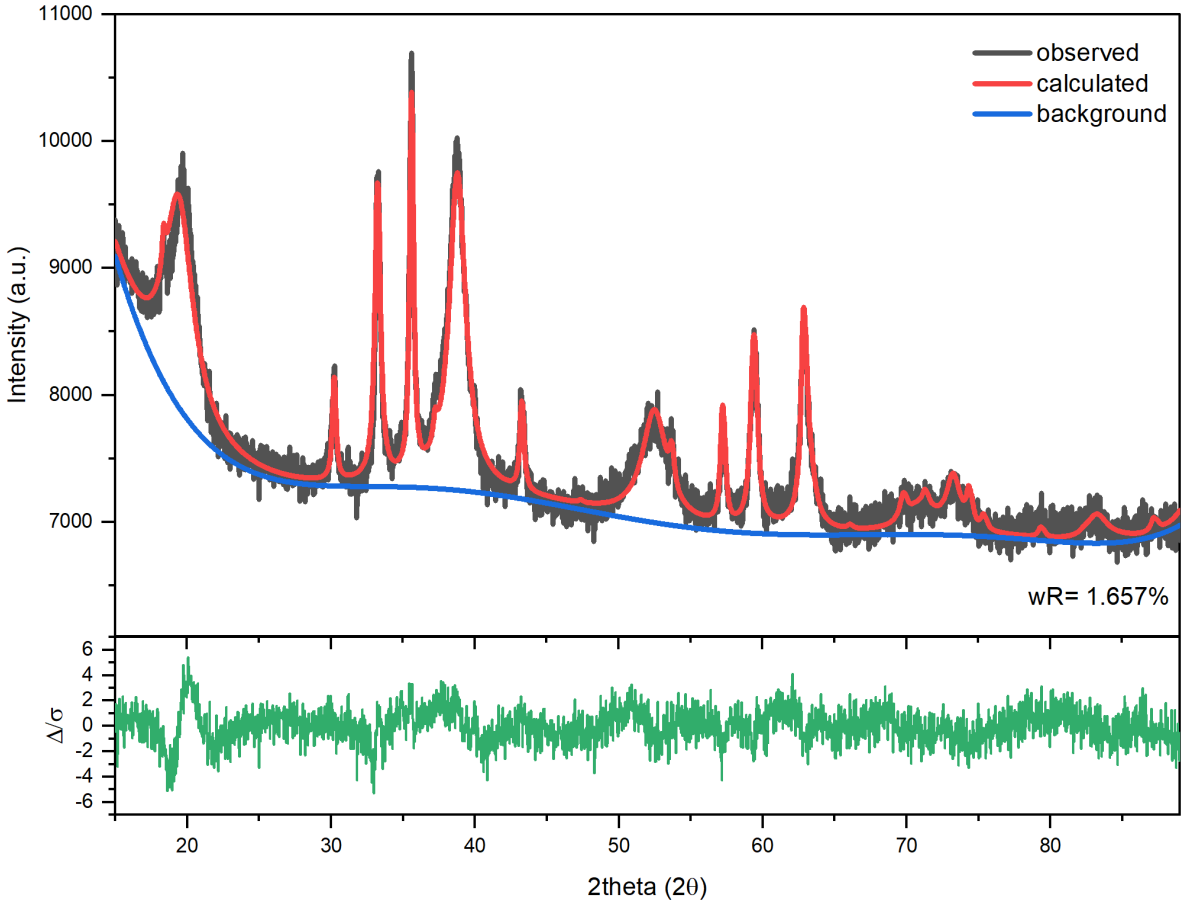

Figure C.1 Sample Rietveld refinement on the $Fe_{0.3}Ni_{0.7}(OH)_2$.

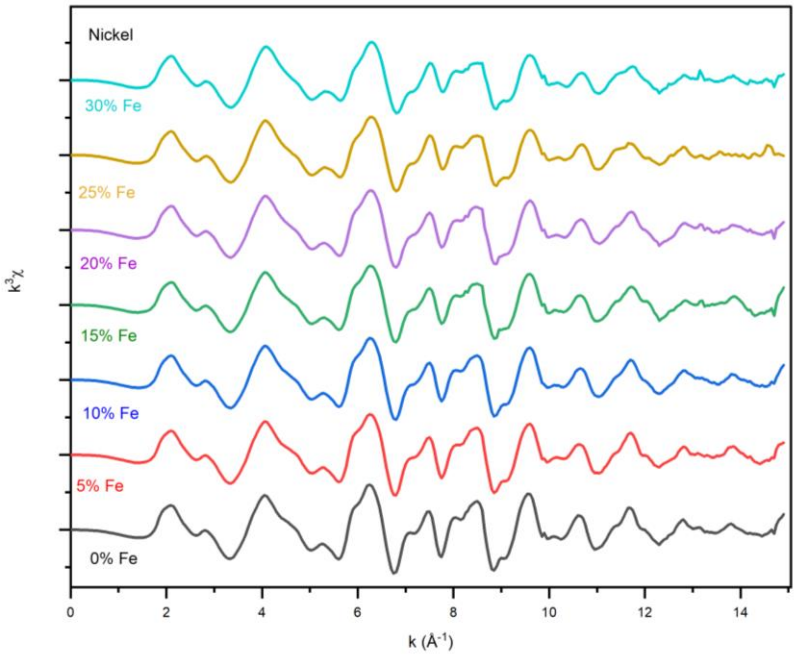

Figure C.2 k-space X-ray absorption fine-structure spectra of Ni K-edge of $Fe_xNi_{1-x}(OH)_2$ sample series.

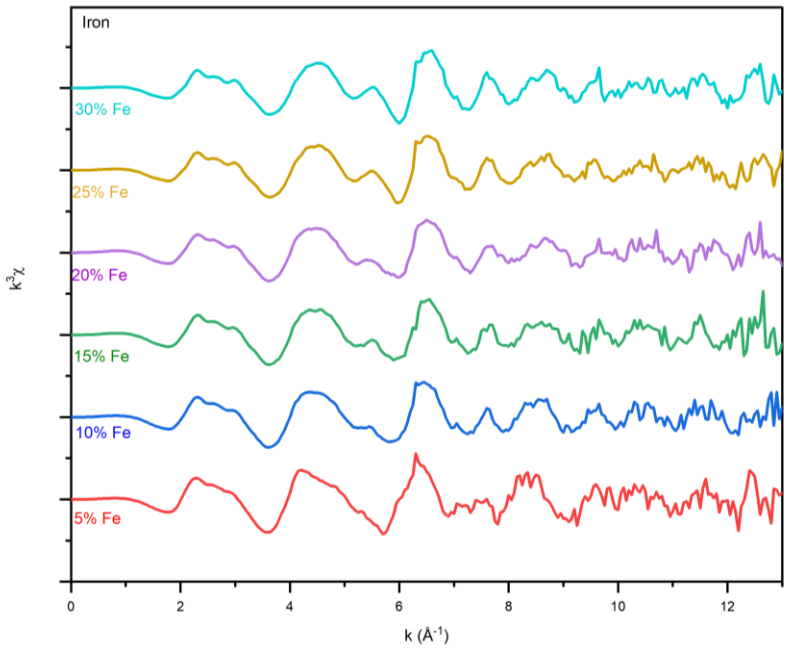

Figure C.3 k-space X-ray absorption fine-structure spectra of Fe K-edge of $Fe_xNi_{1-x}(OH)_2$ sample series.

Appendix D: Supplementary Information for Chapter 6

Table D. 1 Co and Fe edge locations derived from XANES

	Hydrothermal Series		**Water Series**		**Formamide Series**	
	Co K-edge	***Fe K-edge***	***Co K-edge***	***Fe K-edge***	***Co K-edge***	***Fe K-edge***
0% Fe	7718.03 (0.005)		7720.90 (0.006)		7718.19 (0.003)	
5% Fe	7719.999 (0.009)	7123.74 (0.047)	7719.89 (0.040)	7124.21 (0.032)	7717.93 (0.087)	7124.58 (0.050)
10% Fe	7718.05 (0.068)	7123.64 (0.015)	7719.33 (0.031)	7124.22 (0.047)	7718.08 (0.076)	7124.55 (0.020)
15% Fe	7717.98 (0.107)	7123.60 (0.026)	7719.25 (0.197)	7124.21 (0.047)	7718.09 (0.093)	7124.36 (0.027)
20% Fe	7717.93 (0.159)	7123.52 (0.038)	7718.12 (0.119)	7124.14 (0.031)	7718.03 (0.072)	7124.03 (0.018)
25% Fe	7717.98 (0.112)	7123.48 (0.042)	7718.12 (0.131)	7124.08 (0.029)	7718.03 (0.021)	7123.78 (0.012)
30% Fe	7718.14 (0.006)	7123.30 (0.010)	7718.11 (0.003)	7123.82 (0.010)	7718.07 (0.003)	7123.60 (0.005)

Table D. 2 Extended X-ray absorption fine-structure spectroscopy (EXAFS) modeling parameters for Co K-edge of formamide series.

	$N_{M\text{-}O}$	$R_{M\text{-}O}$	$N_{M\text{-}M}$	$R_{M\text{-}M}$	*R-factor*
0	5.47 (0.343)	2.045 (0.007)	6.021 (0.549)	3.08768 (0.006)	0.0297
5	4.51 (0.365)	2.051 (0.009)	5.122 (0.555)	3.0867 (0.007)	0.037836
10	5.49 (0.328)	2.062 (0.006)	5.566 (0.517)	3.10406 (0.006)	0.030047
15	5.02 (0.282) 1.414 (0.644)	2.083 (0.016) 1.932	4.57814 (0.588) 1.0691 (0.51)	3.11012 (0.007) 2.8546	0.0188
20	4.782 (0.242) 1.515 (0.561)	2.085 (0.015) 1.932	3.965 (0.55) 1.1692 (0.48)	3.1083 (0.008) 2.8546	0.0194
25	4.873 (0.345) 1.842 (0.697)	2.098 (0.019) 1.932	3.739 (0.71) 0.7828 (0.62)	3.10618 (0.011) 2.854	0.0334
30	5.728 (1.1537) 1.1537 (1.042)	2.091 (0.023) 1.932	5.154 (0.98) 1.2 (0.86)	3.110 (0.011) 2.8546	0.0439

E_0=12.0 eV, $S_O^2 = 0.78$, $\sigma_{M-O}^2 = 0.01$, $\sigma_{M-M}^2 = 0.007$

Table D. 3 Extended X-ray absorption fine-structure spectroscopy (EXAFS) modeling parameters for Fe K-edge of formamide series.

	$N_{M\text{-}O}$	$R_{M\text{-}O}$	$N_{M\text{-}M}$	$R_{M\text{-}M}$	E_0	*R-factor*
5	6.3191 (0.22)	2.004 (0.006)	6.44 (0.50)	3.124 (0.006)	15.6	0.027
10	6.1588 (0.22)	2.003 (0.006)	6.3895 (0.50)	3.121 (0.006)	15.6	0.012
15	5.723 (0.25)	2.003 (0.008)	5.324 (0.57)	3.122 (0.009)	15.7	0.018
20	5.149 (0.24)	2.000 (0.009)	3.595 (0.54)	3.112 (0.012)	15.7	0.023
25	4.37411 (0.32)	2.004 (0.014)	3.082 (0.63)	3.102 (0.016)	16.3	0.049
30	4.307 (0.297)	1.995 (0.013)	2.838 (0.64)	3.091 (0.0175)	15.7	0.061

$S_O^2 = 0.78,\ \sigma_{M-O}^2 = 0.004, \sigma_{M-M}^2 = 0.006$

Table D. 4 Extended X-ray absorption fine-structure spectroscopy (EXAFS) modeling parameters for Co K-edge of hydrothermal series.

	N_{M-O}	R_{M-O}	N_{M-M}	R_{M-M}	R-factor
0	6.592 (0.384)	2.105 (0.006)	5.453 (0.55)	3.186 (0.006)	0.029
5	5.135 (0.290)	1.925 (0.006)	5.054 (0.401)	2.861 (0.005)	0.017
10	5.721 (0.372)	2.091 (0.006)	4.107 (0.551)	3.181 (0.008)	0.034
15	6.443 (0.383)	2.098 (0.006)	4.408 (0.544)	3.176 (0.008)	0.031
20	6.317 (0.353)	2.097 (0.006)	4.194 (0.523)	3.171 (0.008)	0.029
25	6.128 (0.52)	2.096 (0.016)	3.621 (0.682)	3.169 (0.015)	0.035
30	5.587 (0.33)	2.109 (0.010)	3.976 (0.722)	3.157 (0.013)	0.027
	1.565 (0.47)	1.932	1.208 (0.601)	2.982 (0.03)	

E_0=12.0 eV, $S_O^2 = 0.78$, $\sigma_{M-O}^2 = 0.006$, $\sigma_{M-M}^2 = 0.005$

Table D. 5 Extended X-ray absorption fine-structure spectroscopy (EXAFS) modeling parameters for Fe K-edge of hydrothermal series.

	$N_{M\text{-}O}$	$R_{M\text{-}O}$	$N_{M\text{-}M}$	$R_{M\text{-}M}$	$N_{magnetite}$	$R_{M\text{-}O}$	$R_{M\text{-}M}$	R-factor
5	4.442	1.941	1.069	2.889	0.663	2.010	2.926	0.016
	(0.40)	(0.010)	(0.501)	(0.029)		1.731	3.434	
						(0.031)	3.588	
							(0.012)	
10	3.718	1.941	0.554	2.986	0.671	2.068	2.966	0.020
	(0.343)	(0.007)	(0.455)	(0.045)		1.789	3.474	
						(0.025)	3.628	
							(0.008)	
15	3.478	1.943	0.750	3.029	0.688	2.065	2.9549	0.016
	(0.282)	(0.007)	(0.432)	(0.031)		1.786	3.4632	
						(0.021)	3.6168	
							(0.009)	
20	3.372	1.943	0.615	3.027	0.676	2.066	2.95471	0.015
	(0.271)	(0.007)	(0.395)	(0.035)		1.787	3.463	
						(0.020)	3.61661	
							(0.008)	
25	3.378	1.936	0.563	3.021	0.735	2.071	2.95622	0.014
	(0.298)	(0.007)	(0.397)	(0.038)		1.792	3.46452	
						(0.019)	3.61812	
							(0.008)	
30	3.026	1.929	0.921	3.041	0.799	2.052	2.94937	0.015
	(0.273)	(0.008)	(0.381)	(0.023)		1.773	3.45767	
						(0.017)	3.61127	
							(0.007)	

E_0=11.0 eV, $S_O^2 = 0.78$, $\sigma_{M-O}^2 = 0.005$, $\sigma_{M-M}^2 = 0.003$

Table D. 6 Extended X-ray absorption fine-structure spectroscopy (EXAFS) modeling parameters for Co K-edge of water series.

	N_{M-O}	R_{M-O}	N_{M-M}	R_{M-M}	R-factor
0	6.114	1.896	6.030	2.851	0.009
	(0.231)	(0.003)	(0.311)	(0.003)	
5	4.501	1.918	4.136	2.847	0.0195
	(0.289)	(0.006)	(0.365)	(0.005)	
10	4.125	1.914	3.006	2.860	0.004
	(0.174)	(0.005)	(0.216)	(0.004)	
	2.209	2.128	1.541 (0.264)	3.133	
	(0.219)	(0.011)		(0.010)	
15	4.375	1.914	3.561	2.859	0.003
	(0.162)	(0.004)	(0.222)	(0.003)	
	1.525	2.200	1.618 (0.267)	3.101	
	(0.202)	(0.0150		(0.009)	
20	5.334	2.073	3.845	3.140	0.086
	(0.523)	(0.010)	(0.762)	(0.012)	
25	5.031	2.067	3.669	3.131	0.090
	(0.486)	(0.010)	(0.746)	(0.013)	
30	2.962	2.125	2.505	3.116	0.014
	(0.342)	(0.014)	(0.417)	(0.009)	
	2.759	1.945	1.249 (0.347)	2.896	
	(0.303)	(0.012)		(0.009)	

E_0=11.5 eV, $S_O^2 = 0.78$, $\sigma_{M-O}^2 = 0.004$, $\sigma_{M-M}^2 = 0.004$

Table D. 7 Extended X-ray absorption fine-structure spectroscopy (EXAFS) modeling parameters for Fe K-edge of water series.

	$N_{M\text{-}O}$	$R_{M\text{-}O}$	$N_{M\text{-}M}$	$R_{M\text{-}M}$	R-factor
5	4.070	1.962	3.188	2.884	0.013
	(0.747)	(0.011)	(0.0106)	(0.011)	
	2.008	2.029	3.658	3.0997	
	(0.831)	(0.009)	(0.009)	(0.009)	
10	4.332	1.972	2.826	2.894	0.032
	(1.052)	(0.014)	(0.707)	(0.142)	
	1.437	2.035	4.592	3.106	
	(1.232)	(0.011)	(0.851)	(0.011)	
15	3.349	1.958	2.317	2.880	0.016
	(0.793)	(0.014)	(0.576)	(0.138)	
	2.420	2.027	5.409	3.097	
	(0.919)	(0.008)	(0.696)	(0.0078)	
20	6.324	1.986	5.098	3.095	0.024
	(0.268)	(0.004)	(0.628)	(0.009)	
25	6.192	1.986	4.653	3.090	0.028
	(0.291)	(0.005)	(0.651)	(0.010)	
30	4.356	1.857	4.657	2.891	0.023
	(0.544)	(0.013)	(0.794)	(0.0255)	
	1.453	2.012	1.951	3.0872	
	(0.512)	(0.014)	(0.669)	(0.036)	

E_0=14 eV, $S_O^2 = 0.78,\ \sigma_{M-O}^2 = 0.007$, $\sigma_{M-M}^2 = 0.008$

Table D. 8 Charges (in mC) passed in the first (C_1) and second (C_2) pre-catalytic cathodic redox peaks in cyclic voltammograms

	Water		Hydrothermal		Formamide	
	C_1	C_2	C_1	C_2	C_1	C_2
0% Fe	-0.517	-0.414	-0.017	-0.122	-18.08	-2.915
5% Fe	-0.806	-0.630	-0.137	-0.194	-14.75	-1.928
10% Fe	-3.453	-1.382	-0.164	-0.656	-6.814	-4.297
15% Fe	-5.087	-1.565	-0.162	-0.727	-1.409	-2.911
20% Fe	-9.070	-2.632	-0.062	-0.338	-10.24	-3.885
25% Fe	-11.61	-2.114	-0.024	-0.216	-5.255	-2.341
30% Fe	-2.122	-0.958	-0.029	-1.957	-7.283	-2.777

Table D. 9 Charges (in mC) passed in the first (A_1) and second (A_2) pre-catalytic anodic redox peaks in cyclic voltammograms

	Water		Hydrothermal		Formamide	
	A_1	A_2	A_1	A_2	A_1	A_2
0% Fe	0.521	0.030	0.028	0.010	62.54	
5% Fe	1.289	0.015	0.171	0.006	22.30	
10% Fe	5.644	0.003	0.237	0.076	12.06	
15% Fe	7.474		0.203	0.015	6.903	
20% Fe	11.93		0.077	0.015	10.38	
25% Fe	14.73		0.018	0.011	4.69	
30% Fe	2.714		0.038	0.0127	5.284	

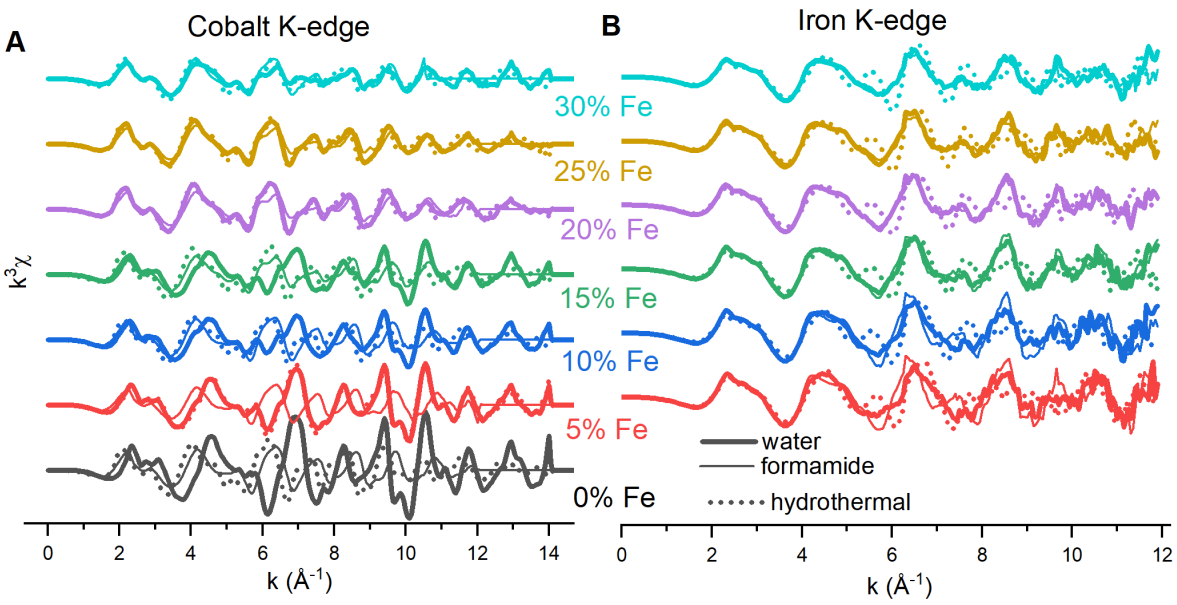

Figure D.1 k-space X-ray absorption fine-structure spectra of **(A)** Co K-edge and **(B)** Fe K-edge of $Fe_xCo_{1-x}(OH)_2$ sample series.

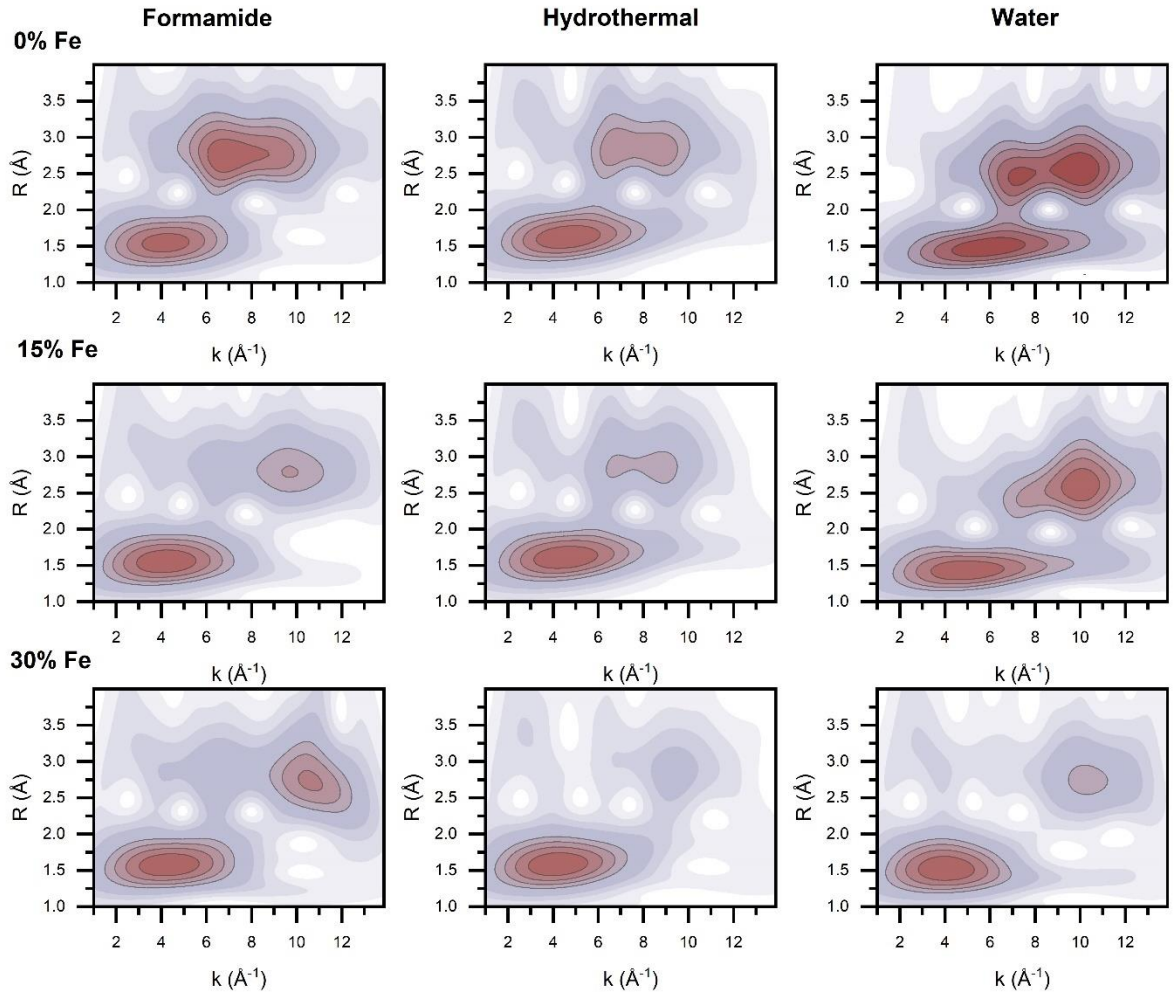

Figure D.2 Wavelet transform analysis of $Fe_xCo_{1-x}(OH)_2$. Continuous wavelet transforms performed using a Morlet wavelet on k^3 weighted data for the Co K-edge in **(A)** 0% Fe, **(B)** 15% Fe, **(C)** 30% Fe.

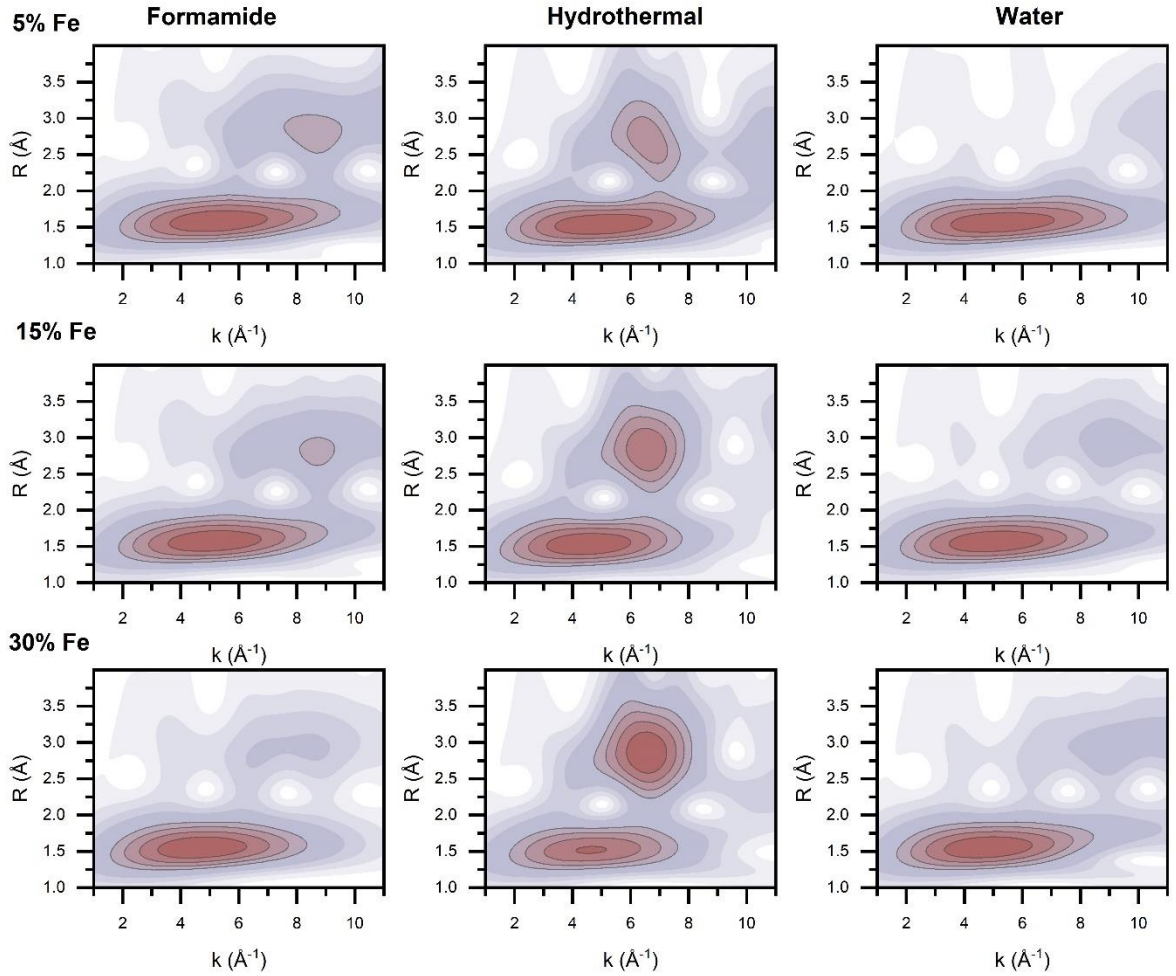

Figure D.3 Wavelet transform analysis of $Fe_xCo_{1-x}(OH)_2$. Continuous wavelet transforms performed using a Morlet wavelet on k^3 weighted data for the Fe K-edge in **(A)** 5% Fe, **(B)** 15% Fe, **(C)** 30% Fe.

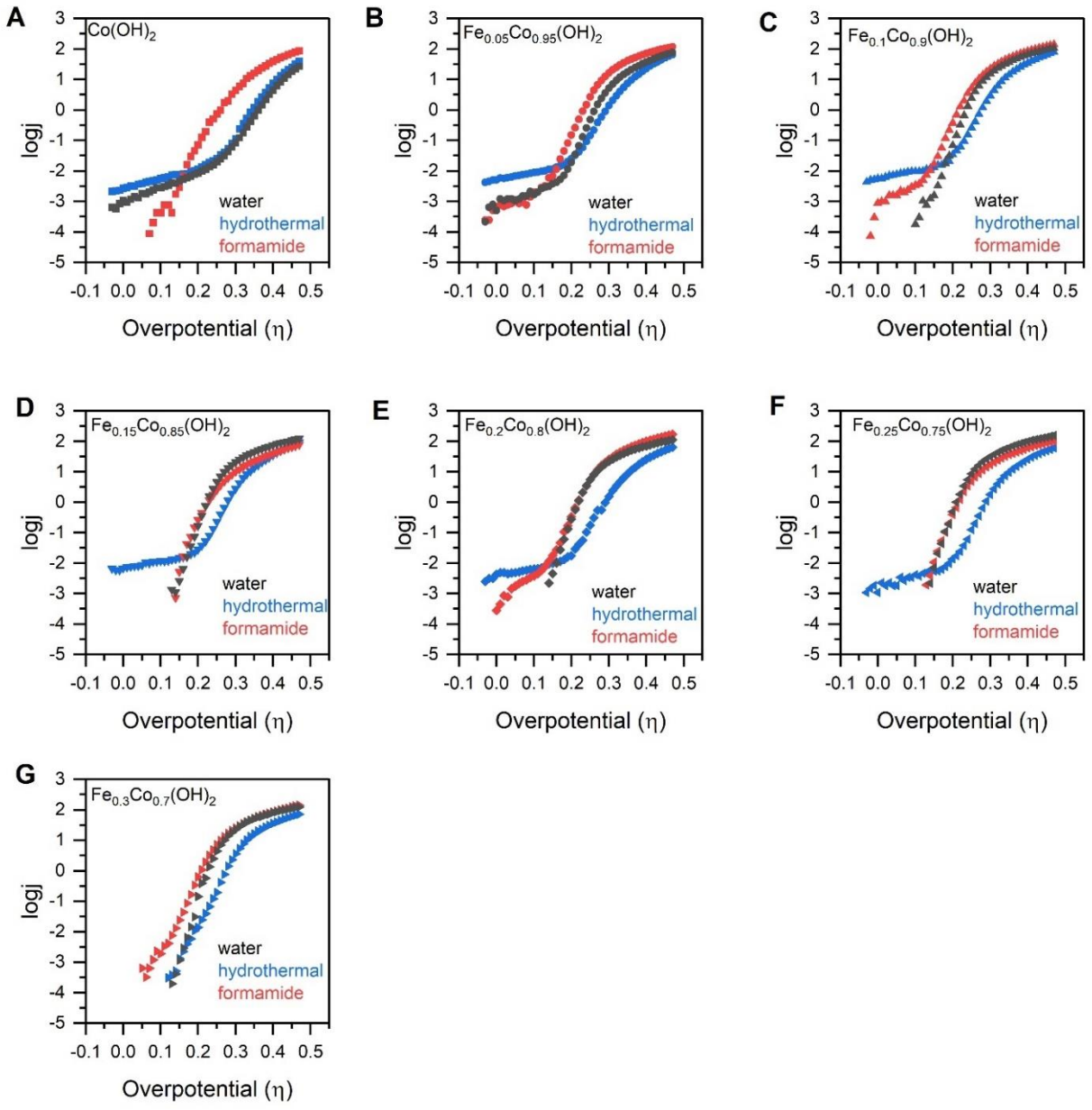

Figure D.4 Electron transfer kinetics of water (black), formamide (red), and hydrothermal (blue) series. Synthesis dependent Tafel plots for **(A)** 0% Fe, **(B)** 5% Fe, **(C)** 10% Fe, **(D)** 15% Fe, **(E)** 20% Fe, **(F)** 25% Fe, **(G)** 30% Fe.